

Nonequilibrium Dynamics of Correlated Fermi Gases

Dissertation
zur
Erlangung des Doktorgrades (Dr. rer. nat.)
der
Mathematisch-Naturwissenschaftlichen Fakultät
der
Rheinischen Friedrich-Wilhelms-Universität Bonn

vorgelegt von
Johannes Amani Kombe
aus
Münster, Deutschland

Bonn 2020

Angefertigt mit Genehmigung der Mathematisch-Naturwissenschaftlichen Fakultät
der Rheinischen Friedrich-Wilhelms-Universität Bonn

1. Gutachterin: Prof. Dr. Corinna Kollath
2. Gutachter: Prof. Dr. Sebastian Diehl

Tag der Promotion: 29.09.2020
Erscheinungsjahr: 2020

To my parents.

Abstract

Strongly correlated quantum systems display a myriad of complex, fascinating behaviour. The competition between charge, spin, orbital, or lattice degrees of freedom and their respective energy scales gives rise to rich and complex emergent phases. More recently, the non-equilibrium properties of correlated quantum many-body systems have come into the focus of active research, with remarkable advances. While the advent of tensor network based simulations on the theoretical side has allowed access to the full time-evolution of the quantum state as it traverses the Hilbert space, the experimental progress in the ultracold atom community has allowed physicists to enter the paradigm of analog quantum simulation. Their tunability and isolation from the environment makes them ideal platforms to emulate and study open problems in condensed matter physics and go beyond the simulational capabilities of state of the art classical simulations.

In this thesis, we explore the dynamics of correlated Fermi gases. We develop and present different facets of applicability of radiofrequency modulation techniques to drive the system out of equilibrium. We begin by considering a homogeneous, three-dimensional Fermi gas in the BCS-BEC crossover and develop an off-resonant radiofrequency transfer scheme to excite the Higgs mode of the superfluid. In a subsequent study we investigate the tunability of the coherence between Cooper pairs by tuning the duration of interaction ramps of the internal interaction strength. These works highlight the possibility to externally tune and stabilise complex quantum many-body states away from equilibrium. Using quasi-exact matrix product state simulations, we study the response of an attractively interacting, one-dimensional Fermi-Hubbard model to weak radiofrequency perturbations. We reveal the emergence of two distinct dynamical regimes in the time evolution and are able to relate it back to the underlying excitation spectrum of the system. Finally, we explore the possibility to perform quantum quenches through radiofrequency π -pulses, achieving nearly complete population transfer between different interacting fermionic states. We reveal non-trivial dynamical effects in the pair correlation of the final state, as well as the excitation of a collective trap mode of the system.

Zusammenfassung

Stark korrelierte Quantensysteme bringen eine Vielzahl komplexer, faszinierender Phänomene hervor. Die feine Balance zwischen Ladungs-, Spin-, Orbital- oder Gitterfreiheitsgraden und ihren jeweiligen Energieskalen führt zu reichen und komplexen Quantenphasen. In den letzten Jahren sind die Nichtgleichgewichtseigenschaften korrelierter Vielteilchen-Quantensystemen mit bemerkenswerten Fortschritten in den Fokus der aktiven Forschung gerückt. Während auf der theoretischen Seite die auf Tensornetzwerken basierenden numerischen Simulationen den Zugang zur vollständigen Zeitentwicklung eines Quantenzustands im Hilbertraum ermöglicht haben, erlaubten es die experimentellen Fortschritte im Bereich ultrakalter Quantengase Physikern, diese als analoge Quantensimulatoren zu benutzen. Ihre genaue Kontrolle, Manipulation und Isolierung von der Umgebung machen sie zu idealen Plattformen, um offene Probleme der Physik der kondensierten Materie zu emulieren und befähigen sie darüber hinaus, über die Grenzen klassischer Simulationen hinauszugehen.

In dieser Arbeit untersuchen wir die Dynamik korrelierter Fermi-Gase. Wir entwickeln und präsentieren verschiedene Facetten der Anwendbarkeit von Radiofrequenzmodulationstechniken, um das System aus dem Gleichgewicht zu bringen. Wir beginnen mit der Betrachtung eines homogenen, dreidimensionalen Fermi-Gases im BCS-BEC-Crossover und entwickeln eine rotverstimmte Radiofrequenzmethode zur Anregung der Higgs-Mode des Superfluids. In einer anschließenden Studie untersuchen wir die Modulation der Kohärenz zwischen Cooper-Paaren, indem wir die Dauer der Änderung der internen Wechselwirkungsstärke variieren. Diese Arbeiten heben die Möglichkeit hervor komplexe Vielteilchen-Quantenzustände im Nichtgleichgewicht zu stabilisieren. Mit quasi-exakten Matrix-Produktzustand-Simulationen untersuchen wir die Reaktion des attraktiven, eindimensionalen Fermi-Hubbard-Modells auf schwache Radiofrequenzstörungen. Wir zeigen die Entstehung zweier dynamischer Regime in der Zeitentwicklung und sind in der Lage, diese mit dem zugrundeliegenden Anregungsspektrum des Systems in Beziehung zu setzen. Schließlich untersuchen wir die Möglichkeit einen Quantenquench durch einen Radiofrequenz- π -Puls durchzuführen, wodurch ein nahezu vollständiger Populationstransfer zwischen unterschiedlichen wechselwirkenden, fermionischen Zuständen erreicht wird. Hier demonstrieren wir nichttriviale, dynamische Effekte in der Paar-Korrelation des Endzustandes sowie die Anregung einer kollektiven Fallenmode des Systems.

List of publications related to this thesis

1. *Higgs mode in a strongly interacting fermionic superfluid*
A. Behrle, T. Harrison, **J. Kombe**, K. Gao, M. Link, J.-S. Bernier, C. Kollath, and M. Köhl
Nat. Phys. **14**, 781–785 (2018)
2. *Finite-duration interaction quench in dilute attractively interacting Fermi gases: Emergence of preformed pairs*
J. Kombe, J.-S. Bernier, M. Köhl, and C. Kollath
Phys. Rev. A **100**, 013604 (2019)
3. *Decay and revival of a transient trapped Fermi condensate*
T. Harrison, M. Link, A. Behrle, K. Gao, A. Kell, **J. Kombe**, J.-S. Bernier, C. Kollath, and M. Köhl
arXiv:1411.4831, (2020)
4. *Radiofrequency spectroscopy for the attractive, one-dimensional Fermi-Hubbard model*
J. Kombe, J.-S. Bernier, and C. Kollath
in preparation

Acknowledgements

First, I must thank Corinna Kollath for giving me the possibility to work in her group. I am very grateful for her supportive, sincere, and insightful supervision. It has been a pleasure working with you, and I have benefited greatly from all the knowledgeable discussions.

Over the years I have had the great opportunity to collaborate very closely with members of the experimental group of Michael Köhl on more than one occasion. I would especially like to thank my co-authors on the publications contained in this thesis, Alexandra Behrle, Tim Harrison, Kuiyi Gao, Martin Link, Andreas Kell, and Michael Köhl for their part in these projects, all the stimulating and fruitful discussions, their patience in explaining an experimentalist's view on the problems at hand, and finding all the missing factors of 2π .

A group wouldn't be a group without its group members. Ameneh, Catalin, Karla, Jean-Sébastien, and Stefan, I cherish these last four years in Bonn in large parts because of you. Whether it's everyone's welcoming, unassuming, and happy spirit, our ongoing lunch conundrums, or our great conversations and discussions (some were actually physics related) over the years, they all made it so easy to arrive and now so hard to leave. I would like to especially express my gratitude to Jean-Sébastien, with whom I have worked together on all projects contained in this thesis, and without whom it would not have come together like this. The numerous discussions we have had over the years (I say discussions, but I fear it was rather a one-way Q&A session), as well as his meticulous, clear way of thinking and working on problems, have formed and shaped my physical understanding and my approach to this work. Fortunately, it wasn't only physics during this time so what is left to say is this - thank you so much for the last four years.

I would like to also thank Tina Naggert and Lisa Takacs for their work and support in all administrative matters, and Harald van Pee for his help to get my simulations actually running on our HPC cluster.

I would like to thank all my friends for their open arms, and enduring support, for their tolerance when I needed to work, and their intervention when I needed not to work.

My love, my gratitude to you I cannot put into words. You have been there from the very first moment until the very last. Thank you for believing in me, believing in us, and making my life so much more special. You are my home.

Mwisho, nawashukuru wazazi wangu kwa uvumilivu wao, ukarimu wao, mapenzi yao ya dhiti, na ushirikiano walionipa ama kunionesha. Nguvu zenu, na imani yenu kwangu, zimenisaidia kutafuta na kupata njia yangu binafsi maishani. Bila ninyi pengine nisingekua hapa leo, nimebahatika kuwa sehemu ya familia hii yenye kipaji na upendo mkubwa. Napendekeza nadharia hii kwenu. Aika Mbe, aika Mae.

Johannes Kombe, October 12, 2020.

Contents

1	Introduction	1
2	Properties of Ultracold Fermi Gases	5
2.1	Scattering Theory of Ultracold Atoms	6
2.2	Tuning Interactions and Feshbach Resonances	8
2.3	The BCS-BEC crossover	10
2.3.1	Molecular BEC	12
2.3.2	BCS Pairing and the Cooper Problem	13
2.4	Fermionic Atoms in Optical Lattices	20
2.4.1	Trapping of Neutral Atoms	22
2.4.2	Towards Strongly Correlated Fermions: The Fermi-Hubbard Model	23
2.5	Radiofrequency Driving of Ultracold Fermions	27
2.5.1	Modelling the Radiofrequency Drive	27
2.5.2	The non-interacting system	30
3	Methods	33
3.1	Bardeen-Cooper-Schrieffer Theory away from Equilibrium	33
3.2	Matrix Product State Techniques for one-dimensional Quantum Systems	35
3.2.1	Matrix Product State Formalism and Graphical Representation	35
3.2.2	Ground State Search	43
3.2.3	Time Evolution	45
3.2.4	Abelian Quantum Numbers	48
3.3	Linear Response Theory	50
3.4	Bethe Ansatz and Exact Solution of the one-dimensional, attractive Fermi-Hubbard Model	53
4	Observation of the Higgs Mode in a Strongly Interacting Superfluid	58
4.1	Ginzburg-Landau Theory and the Anderson-Higgs Mechanism	59
4.2	Exciting the Higgs Mode	62
4.3	Calibration Procedure	62
4.4	Activation of the Higgs	64
4.4.1	Convergence of the Numerical Simulations	65
4.4.2	The Effective Rabi Problem	68
4.4.3	The Higgs Mode as a Collective Excitation	73
4.5	Experimental Signature and Observation	75
4.6	Conclusion and Outlook	79
5	Finite-Duration Interaction Quench in Dilute Attractively Interacting Fermi Gases: Emergence of Pre-Formed Pairs	81
5.1	Quench Dynamics in the BCS Model	82

Contents

5.2	Finite-Duration Quenches: Emergence of Pre-Formed Pairs	84
5.3	Numerical Convergence	92
5.4	Conclusion and Outlook	93
6	Radiofrequency Spectroscopy of Ultracold Fermions: Probing the Excitations of the Fermi-Hubbard Model	95
6.1	Weakly attractive Fermi-Hubbard model	96
6.1.1	Momentum-resolved Transfer to the third level	97
6.1.2	Finite Size Effects	102
6.1.3	Evolution of the Momentum Distributions	102
6.1.4	Evolution of the Pair Distribution	110
6.1.5	Total Transfer to the third state	111
6.2	Strongly attractive Fermi-Hubbard model	113
6.2.1	Momentum-resolved Transfer to the third state	114
6.2.2	Evolution of the Momentum Distribution	118
6.2.3	Evolution of the Pair Distribution	120
6.2.4	Total Transfer to the third state	120
6.3	Conclusions	124
7	Decay and Revival of a Transient Fermi Condensate	126
7.1	Non-Equilibrium Dynamics through Population Quenches	126
7.2	Calibration	127
7.3	Density Dynamics and Breathing Mode Excitation	130
7.4	Characterising the Pairing State	134
7.5	Summary and Convergence of Results	135
7.6	Connection to Experiment	137
7.7	Conclusion	139
8	Conclusion	140
A	Appendix for Chapter 2	143
A.1	Bound state of two particles interacting attractively	143
A.2	Self-consistent solution of the BCS gap and number equation	145
B	Appendix for Chapter 5	146
B.1	Quasiparticle weight in a sudden Quench	146
B.2	Free Evolution of the BCS Equations	147
	Bibliography	154

Chapter 1

Introduction

The intricate balance of competing energy scales and degrees of freedom in interacting quantum many-body systems leads to the emergence of complex phases and phenomena. In particular, in strongly correlated materials we can no longer understand the system as a whole by thinking about the individual particles it is comprised of, but rather have to understand the *collective* behaviour of all its constituents. The emergent quasiparticles behave in their own right and bear no resemblance to the underlying electrons or atoms the system is comprised of; they are thus truly a collective many-body quantum effect. To theoretically capture and understand these quantum systems is a notoriously difficult task to tackle, first and foremost because of the exponentially large Hilbert space of any real material with a macroscopic number of individual particles. With even the most sophisticated supercomputers in the world, we are limited to study a few tens of particles interacting with each other exactly. Hence various analytical and numerical approaches have been developed to study these systems in certain limits and under careful approximations [1–16].

One example highlighting the breadth, complexity, and potential for future applications of correlated quantum systems is the phenomenon of superconductivity [17, 18]. The superconducting state is now understood to originate from the condensation of Cooper pairs akin to a Bose-Einstein condensate [19–21], and culminated, almost 50 years after its experimental discovery in 1911 [17], in the remarkably successful microscopic theory of superconductivity (and Nobel prize) of Bardeen, Cooper and Schrieffer (BCS) [18, 22–24]. In 1986 a new class of superconductors with unprecedented high critical temperatures, henceforth termed *high-temperature superconductors*, was discovered by Bednorz and Müller [25, 26]. Their discovery has led to a proliferation of discoveries of new materials with ever increasing transition temperatures, with a broad range of applications. While much has been learned about these correlated electron systems and they seem to follow the general phenomenology of conventional superconductors, the basic mechanism giving rise to the superconducting state and a quantitative understanding is still eluding physicists to this day [18, 27].

Ultracold atomic quantum gases have emerged as immensely versatile, very successful platforms to explore the physics of interacting quantum many-body systems. Advances in cooling, and trapping of atoms with laser light have led to a remarkable control and tunability of cold atomic gases [28, 29]. Experimental progress has been rapid and exciting, with the first reali-

CHAPTER 1. INTRODUCTION

sation of Bose-Einstein condensation (BEC) in dilute quantum gases in 1995 [30, 31], and the realisation of a degenerate quantum gas of fermions shortly thereafter [32]. The observation of quantised vortices demonstrated the superfluid character of the BEC [33, 34], while the successful confinement of ultracold fermions to a three-dimensional optical lattice [35] opened up the possibility to study quantum lattice systems in a cold atom setup. Ultracold atomic quantum gases have proven to be extremely versatile, with exceptional control of the system’s internal parameters and their almost complete isolation from the environment. As such they can be considered clean, highly controlled quantum systems to be used e.g. for analogue quantum simulation of condensed matter systems [36–38]. Furthermore, the low temperatures required for quantum degeneracy result in long coherence times, which facilitate the experimental observation of *dynamics* in these systems [39–44]. These advances have allowed experiments to address and uncover some of the processes underlying the physics of non-equilibrium phenomena [45, 46].

Systems away from equilibrium are of great interest and ubiquitous in nature for the simple reason that “a living system in equilibrium is oxymoronic (or dead)” [47]. Examples range from the various forms of transport phenomena, over active matter [48], to the study of quenches in quantum many-body systems [43, 49]. Understanding their dynamical, non-equilibrium properties requires knowledge of the full evolution of the system. With an exponentially growing dimension of the Hilbert space, exact approaches are scarce and numerically only available for relatively small system sizes beyond which it becomes impossible to store the full wave function in memory. Furthermore, to understand the non-equilibrium dynamics of these systems it does not suffice to identify the ground state (or a few low-lying excited states), but one needs to consider the full spectrum of the Hamiltonian. Tensor network based methods allow to efficiently parametrise and reduce the Hilbert space to only the most important degrees of freedom, thereby achieving machine precision in the full numerical simulation of such driven systems, provided the entanglement entropy remains sufficiently small [50]. For short and intermediate time scales these methods are therefore the method of choice for low-dimensional quantum systems, being able to capture large systems with several hundred sites [42, 51–54].

In light of the recent advances, physicists are thus in the very promising position to address non-equilibrium dynamics in a comprehensive way. With a continued and combined effort from experiment and theory, one can imagine engineered non-equilibrium states with novel properties and vast potential. In this thesis we will investigate the non-equilibrium dynamics of correlated Fermi gases, both in the BCS-BEC crossover, and confined to a one-dimensional optical lattice, subject to a radiofrequency (rf) drive. In the following chapters we aim to give a comprehensive account of using an rf-drive to bring the systems out of equilibrium, focussing on their dynamical evolution, and exploring the multifaceted nature of the rf-drive to probe and stabilise complex many-body quantum states.

This dissertation is organised as follows.

Chapter 2 We begin with a concise introduction to the field of ultracold Fermi gases and their theoretical description. To understand the way interactions are mediated, we review the scat-

tering theory of two particles and discuss the tunability of interactions via Feshbach resonances. Engineering attractive interactions in this way between two different fermionic species of the degenerate Fermi gas thus realises the celebrated Bardeen-Cooper-Schrieffer (BCS) Hamiltonian and gives rise to a phase transition to a superfluid state. We will discuss the BCS theory and its mean-field solution in detail, and outline the phases of the gas as the interaction between the particles are tuned throughout the BCS-BEC crossover, relevant to the results presented in chapters 4 and 5.

By creating a crystal of light with pair-wise interfering laser beams, it is possible to study quantum lattice models in ultracold atom setups. We will detail the trapping of atoms and their confinement to an optical lattice geometry and introduce the Fermi-Hubbard model, a hallmark model in condensed matter physics for over 50 years since its conception in 1963 [55].

Finally, we introduce and discuss the method of radiofrequency driving, which we will use throughout this thesis to excite and probe the fermionic quantum gases in subsequent chapters. In particular we highlight the rf-drive applied to a non-interacting system as our starting point for the subsequent discussions of interacting systems.

Chapter 3 In this chapter we introduce the different numerical and analytical methods used to study the response of the Fermi gas to the rf-drive. We outline our numerical approach to the time-dependent BCS problem, and discuss in detail the quasi-exact time-dependent matrix product state (t-MPS) algorithm to unravel the full time evolution of one-dimensional, interacting quantum systems. The t-MPS algorithm is used in chapters 6 and 7 to investigate the dynamics of the attractive, one-dimensional Hubbard model. We supplement our numerical approach with the analytical Bethe ansatz technique, which we outline in the latter part of this chapter.

Chapter 4 Here, we investigate the evolution of a three-dimensional Fermi gas in the BCS-BEC crossover, while the interaction strength is effectively modified in time. We propose a novel time-dependent excitation mechanism, based on radiofrequency modulation of the effective underlying interaction, to activate the Higgs mode, a collective excitation of the system. We use this rf-modulation to transfer small amounts of atoms to a different internal state, thereby exciting the system. We simulate the system using the mean-field BCS model, explicitly including the time-dependent drive in our description. We show that the rf-drive directly couples to the order parameter and activates the Higgs mode, which is identified as the stable, collective oscillation of the amplitude of the Cooper pairs. This chapter is based upon a publication coming out of a fruitful collaboration with the experimental group on Michael Köhl [56].

Chapter 5 Driven away from equilibrium by a rapid quench of an internal parameter, quantum systems will subsequently undergo complex dynamics and non-trivial states may emerge in the long-time limit. However, any experimental quench will inevitably be conducted over a finite window of time. In this chapter we therefore address the non-equilibrium behaviour of dilute, attractively interacting Fermi gases subjected to finite-duration ramps of their internal interaction strength. By changing the duration of the ramp time in our numerical protocol,

CHAPTER 1. INTRODUCTION

we identify and characterise three dynamical regimes exhibiting distinct features in their long-time steady state. This work demonstrates the possibility to dynamically tune the coherence between Cooper pairs, the magnitude of the superconducting order parameter, and even to stabilise a non-equilibrium steady state made of preformed pairs. This chapter is based upon results published in [57].

Chapter 6 In this chapter, we investigate the radiofrequency (rf) technique for an ultracold gas of interacting fermions moving in a one-dimensional lattice. We study the full dynamics of the fermionic gas under the rf-drive, taking three internal states of the fermions into account. Our numerical results show how the rf-technique not only offers direct access to the single-particle spectral function, but also can be employed to probe the coupling mechanisms to the underlying excitations in the many-body system.

Chapter 7 Finally, we study the response of a harmonically trapped Fermi condensate in the strongly-interacting regime to a fast quench of the interaction strength, by a complete population transfer. We use our lattice model to gain insights into the condensate dynamics of a fully interacting fermionic gas in the low density limit. We observe non-trivial pairing dynamics influenced by the excitation of a collective mode of the trap. This work, submitted for publication [58], is another example of a collaboration with the experimental group of Michael Köhl, exploring a novel route to realise quench experiments on time scales, so far inaccessible with current magnetic field ramps via Feshbach resonances.

We conclude our discussions in chapter 8 with a brief summary of our results and an outlook onto future directions.

Chapter 2

Properties of Ultracold Fermi Gases

Strongly correlated Fermi gases are ubiquitous in nature, from the quark-gluon plasma of the early universe, via the structure of nuclear matter, and the electronic degrees of freedom of solids, to the extreme conditions present in white dwarfs and neutron stars. Table 2.1 gives an overview of the superfluid transition and Fermi temperatures in a variety of Fermi systems. We see that examples of systems comprised of strongly interacting fermions span across all length and temperature scales encountered in nature.

Examples of degenerate Fermi Gases			
	T_c	T_F	T_c/T_F
Ultracold Quantum Gases	200nK	$1\mu\text{K}$	0.2
conventional Superconductors	1 – 10K	$10^5 - 10^6\text{K}$	$10^{-5} - 10^{-4}$
high- T_c Superconductors	35 – 140K	10^3K	10^{-2}
Neutron Star	10^{10}K	10^{11}K	$10^{-2} - 10^{-1}$

Table 2.1: Examples of degenerate Fermi gases, adapted from [59].

While there are similarities and analogies between the different fermionic systems, in this thesis we are concerned with the physics of ultracold Fermi gases. To this end, this chapter reviews the necessary theoretical background for the discussion of ultracold fermionic quantum gases. Due to the remarkable progress and rapid advancement of the field, this chapter by no means aims to give a complete overview over the field, but rather we focus on the central themes relevant for the discussion of our results in subsequent chapters. In section 2.1 we review the scattering properties in order to understand the way interactions are mediated in ultracold gases, and will highlight the use of Feshbach resonances in section 2.2. Section 2.3 is devoted to the BCS-BEC crossover of an ultracold Fermi gas, which sets the theoretical background for the results presented in chapters 4 and 5. The introduction of optical lattices in section 2.4 leads us to the celebrated Fermi-Hubbard model, which is extensively studied in the context of radiofrequency (rf) spectroscopy (see section 2.5) in chapters 6 and 7.

2.1 Scattering Theory of Ultracold Atoms

2.1 Scattering Theory of Ultracold Atoms

To bring atomic gases into the quantum degenerate regime the de-Broglie wavelength λ_{dB} of the atoms must be increased to be comparable to the interparticle spacing $d = n^{-1/3}$ (n being the number density of the gas), giving the general criterion

$$\lambda_{dB} \sim \frac{1}{n^{1/3}} \longrightarrow n\lambda_{dB}^3 \sim 1, \quad (2.1)$$

where $\lambda_{dB} = \sqrt{2\pi\hbar^2/(mk_B T)}$ with m the mass of the considered particle, and T the temperature. There are now two ways one can go about achieving quantum degeneracy, namely by increasing either the particle density n or the de-Broglie wavelength λ_{dB} . The former is not practicable as an increased density leads to an enhancement of three-body losses, reducing the lifetime of the atomic gas¹. Therefore one is left with the task of *significantly* reducing the temperature T of the system, in order to increase the particles de-Broglie wavelength. With the significant advances in the field of ultracold atoms [60–62], the first realisation of a Bose-Einstein condensate (BEC) was achieved in 1995 [30, 31]. However cooling fermionic atoms into the quantum degenerate regime presented the next great challenge, since the Pauli exclusion principle prohibits s -wave collisions for identical fermions and as such prevents thermalisation. It took another four years until a degenerate quantum gas of fermionic atoms was finally realised [32].

In the following, we consider an atomic gas in a balanced mixture of two different fermionic atoms, such that s -wave collisions between different species are allowed. These gases are extremely dilute (see Table 2.1), so the atoms predominantly interact by undergoing pairwise collisions, described by a central potential $V(r)$, which at large distances is given by the van der Waals potential. We will briefly outline the necessary background of scattering theory as applicable to these quantum gases, following [59].

Since the interaction potential of the two-body scattering process is centro-symmetric, the Schrödinger equation decouples completely into the centre of mass motion and the relative motion of a reduced particle of mass $\mu = m/2$. The relative motion for the reduced particle is described by

$$(\nabla^2 + k^2)\Psi_{\mathbf{k}}(\mathbf{r}) = v(r)\Psi_{\mathbf{k}}(\mathbf{r}), \quad (2.2)$$

with $k^2 = 2\mu E/\hbar^2$, $v(r) = 2\mu V(r)/\hbar^2$ and E the energy of the particle. An incident plane wave $e^{i\mathbf{k}\cdot\mathbf{r}}$ interacts with the potential $v(r)$ and is scattered off as an outgoing (spherical) wave, such that the total wave function at large distances takes the superposition of the two as its asymptotic form

¹At densities $n > 10^{14}\text{cm}^{-3}$ inelastic three-body collisions start to contribute, leading to molecule formation and the release of their binding energy, which ultimately drives the system into its stable ground state: a solid. In fact ultracold atom experiments are all performed in a metastable state, on route to solidification. Due to the low temperatures the time scale until the atomic vapour forms a solid is long enough such that experiments can be performed in this metastable regime [45].

$$\Psi_{\mathbf{k}}(\mathbf{r}) \sim e^{i\mathbf{k}\cdot\mathbf{r}} + f(\mathbf{k}', \mathbf{k}) \frac{e^{ikr}}{r}. \quad (2.3)$$

Here $f(\mathbf{k}', \mathbf{k})$ is the scattering amplitude for an incident wave of wave vector \mathbf{k} to scatter into the direction \mathbf{k}' , where $k = k'$ due to energy conservation (elastic collisions). In the low momentum limit applicable to cold gases ($kr_0 \ll 1$, where r_0 is the range of the interatomic potential) a partial wave expansion into states with angular momentum l shows that s -wave collisions ($l = 0$) are the only significant contribution in the absence of resonance phenomena, and we can neglect higher order angular momenta in what is to follow. The scattering amplitude now reads

$$f \approx f_s = \frac{e^{2i\delta_s} - 1}{2ik} = \frac{1}{k \cot(\delta_s) - ik}. \quad (2.4)$$

δ_s is the phase shift acquired during the scattering event and f_s the s -wave scattering amplitude [63]. We then *define* the scattering length a as

$$a = - \lim_{kr_0 \ll 1} \frac{\tan(\delta_s)}{k}, \quad (2.5)$$

which is a measure of the interaction strength and closely related to the phase shift δ_s . Since atomic gases are ultra dilute and are cooled to very low temperatures, both the thermal de-Broglie wavelength and the interparticle distance are much larger than the range of the interaction potential r_0 . A typical scattering process will therefore not resolve or probe the fine details of $v(r)$, allowing for a simpler description of the collision by the use of a contact pseudopotential. We replace the interaction by the contact potential $\delta(\mathbf{r})$, with the condition, that it must reproduce the correct s -wave scattering results (i.e. $f \rightarrow -a$ in the s -wave limit).

To this end, we evaluate the Green's function of the Schrödinger equation 2.2 and find

$$G_k(\mathbf{r}) = \int \frac{d^3\mathbf{p}}{(2\pi)^3} \frac{e^{i\mathbf{p}\cdot\mathbf{r}}}{k^2 - p^2 + i\eta} = -\frac{1}{4\pi} \frac{e^{ikr}}{r}. \quad (2.6)$$

The exact solution to Eq. 2.2 far away from the origin can then be written down as

$$\begin{aligned} \Psi_{\mathbf{k}}(\mathbf{r}) &= e^{i\mathbf{k}\cdot\mathbf{r}} + \int d^3\mathbf{r}' G_{\mathbf{k}}(\mathbf{r} - \mathbf{r}') v(\mathbf{r}') \Psi_{\mathbf{k}}(\mathbf{r}') \\ &= e^{i\mathbf{k}\cdot\mathbf{r}} - \frac{e^{ikr}}{4\pi r} \int d^3\mathbf{r}' e^{i\mathbf{k}'\cdot\mathbf{r}'} v(\mathbf{r}') \Psi_{\mathbf{k}}(\mathbf{r}'), \end{aligned} \quad (2.7)$$

from which one can straightforwardly derive the following expression for the scattering amplitude by comparison with Eq. 2.3,

$$f(\mathbf{k}', \mathbf{k}) = -\frac{1}{4\pi} \int d^3\mathbf{r}' e^{i\mathbf{k}'\cdot\mathbf{r}'} v(\mathbf{r}') \Psi_{\mathbf{k}}(\mathbf{r}'). \quad (2.8)$$

2.2 Tuning Interactions and Feshbach Resonances

Reinserting the exact solution of $\Psi_{\mathbf{k}}(\mathbf{r})$, Eq. 2.7, into the above expression, yields the Lippmann-Schwinger equation for the scattering amplitude [59]

$$f(\mathbf{k}', \mathbf{k}) = -\frac{v(\mathbf{k}' - \mathbf{k})}{4\pi} + \int \frac{d^3\mathbf{p}}{(2\pi)^3} \frac{v(\mathbf{k}' - \mathbf{p})f(\mathbf{p}, \mathbf{k})}{k^2 - p^2 + i\eta}. \quad (2.9)$$

The Lippmann-Schwinger equation gives an exact integral equation for the scattering amplitude in terms of the Fourier transform of the scattering potential, $v(\mathbf{k})$, which makes it very amenable to perturbative calculations. For low-energy s -wave collisions the scattering amplitude only depends on the magnitude $k = |\mathbf{k}|$ of the scattering wave vector. In the low-momentum limit and assuming a contact potential $V(\mathbf{r}) = V_0\delta(\mathbf{r})$, we obtain

$$V_0 = \frac{4\pi\hbar^2 a}{m}, \quad (2.10)$$

the Born approximation (first order expansion in V_0) for the scattering length. However already the second order term would diverge in the calculations. The origin of the divergence is the contact potential we assumed, since it does not decay at high momentum values. Any physical potential will of course decay, and we can remedy this by replacing the contact potential with the pseudo-potential $V(\mathbf{r})\psi(\mathbf{r}) = V_0\delta(\mathbf{r})\frac{\partial}{\partial r}(r\psi(\mathbf{r}))$ [64]. It acts as an effective interaction potential, is independent of the microscopic properties of the system, and exactly reproduces the s -wave result for the scattering amplitude $f(k) = -\frac{a}{1+ika}$, if Eq. 2.10 holds. To make the second order term in the expansion converge, we impose a high-momentum cutoff q_c , and assume $v(\mathbf{q}) = mV_0/\hbar^2$ for $|q| < q_c$ and else zero. In the low-momentum limit $k \ll 1/r_0$ we then find

$$\frac{1}{V_0} = \frac{m}{4\pi\hbar^2 a} - \frac{m}{\hbar^2} \int_{|\mathbf{q}| < q_c} \frac{d^3\mathbf{q}}{(2\pi)^3} \frac{1}{q^2}. \quad (2.11)$$

Making connection to experiments, we henceforth follow the formal prescription to replace the strength of the potential V_0 by the right hand side of Eq. 2.11 in terms of the measurable s -wave scattering length a .

To conclude this discussion we briefly comment on the effect of quantum statistics on the scattering problem. Since the orbital wave function is symmetric for s -wave collisions, considering two interacting fermions requires an anti-symmetric wave function in the spin-sector such that their overall wave function is anti-symmetric. This immediately rules out s -wave collisions for indistinguishable fermions (i.e. a single species Fermi gases), and means that thermalisation is not possible (at least in the s -wave channel). We therefore require a Bose-Fermi mixture or different fermionic species to allow for s -wave interactions, which is the experimental basis for the systems considered in the remainder of this thesis. In the following section we now want to focus on the tunability of the interaction strength between the fermions, by employing the tool of Feshbach resonances.

2.2 Tuning Interactions and Feshbach Resonances

As we have seen in the previous discussion interactions in an ultracold quantum gas are mediated by collisions between the atomic species comprising the gas. At the low temperatures

necessary to reach quantum degeneracy s -wave collisions are the dominant contribution in the scattering process. In a dilute, ultracold quantum gas, the s -wave scattering length a can be tuned, by the means of Feshbach resonances [65], to arbitrary repulsive or attractive values [66], allowing experimental access to the strongly correlated regime in these systems.

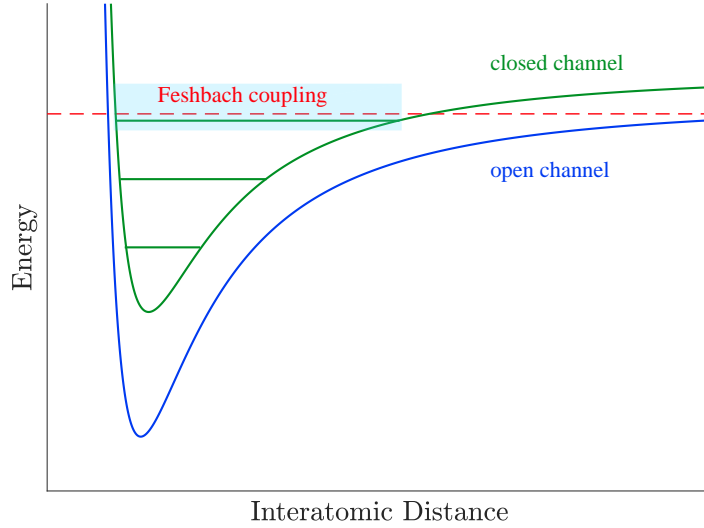


Figure 2.1: Illustration of interatomic potentials in the open (triplet) and closed (singlet) channel of a scattering event. By tuning an external magnetic field, a bound state in the closed channel can be brought into resonance with the incident energy of the particles.

Whenever a bound state in a closed scattering channel is coupled resonantly to the energy of the open channel in a two-particle collision, a resonance behaviour occurs. The particles can briefly form a quasi bound state, their interaction is strongly enhanced, and their scattering length diverges. If the open and closed scattering channels have different magnetic moments (e.g. spin singlet and spin triplet states), the relative shift between the open channel energy and the closed channel bound state can be tuned simply by adjusting an external magnetic field B , as shown in Fig. 2.1 [66, 67]. Within second order perturbation theory, the scattering length takes the functional form [68]

$$a(B) = a_{bg} \left(1 - \frac{\Delta B}{B - B_0} \right), \quad (2.12)$$

where a_{bg} denotes the background scattering length, and B_0 and ΔB are the position and width of the Feshbach resonance. In ultracold quantum gases the fermionic pseudo-spin can be encoded into the different hyperfine levels of the electronic ground state manifold of the atoms. Fig. 2.2 shows the hyperfine level structure of ${}^6\text{Li}$. We highlighted the lowest three hyperfine levels which are used to encode the three fermionic species discussed in section 2.5.

Fig. 2.3 shows the Feshbach resonance of ${}^6\text{Li}$ between the three lowest hyperfine levels of the electronic ground state manifold. We see the clear divergence of the scattering length and

2.3 The BCS-BEC crossover

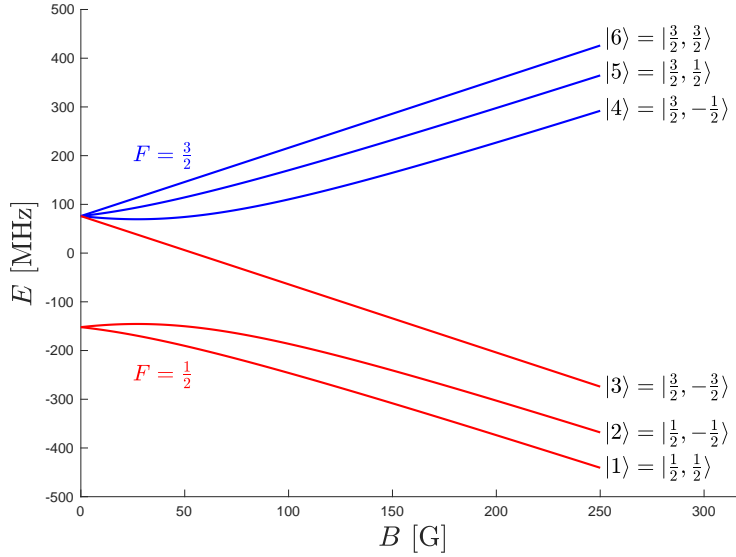


Figure 2.2: Electronic ground state $2^2S_{\frac{1}{2}}$ of ${}^6\text{Li}$ in a magnetic field with hyperfine coupling ($I = 1$). Zeeman and Paschen-Back regime are shown. The lowest three hyperfine states (marked in red) are used to encode the fermionic spin in our model.

its change in sign, giving rise to near arbitrary control of the scattering properties and therefore interactions of cold atomic gases.

2.3 The BCS-BEC crossover

In this section we want to discuss the properties of quantum gases comprised of *paired* fermions. Fermionic pairing is a subtle effect, but ultimately arises from an underlying effective, attractive interaction between fermions of different species as dictated by the Pauli exclusion principle. The interaction is parametrised by the dimensionless coupling parameter $1/(k_F a)$, where k_F is the Fermi wave vector of the system, and a the s -wave scattering length. We have seen that the scattering length can be tuned by the means of Feshbach resonances and k_F depends on the number density of atoms n (and trapping frequencies for a harmonically trapped gas). Thus, by changing any one of temperature T , magnetic field B , or density n , $1/(k_F a)$ can be varied almost at will between $\pm\infty$.

Whilst for $1/(k_F a) \gg 1$ the system realises a Bose-Einstein condensate (BEC) of bosonic molecules, $1/(k_F a) \ll -1$ is described by the Bardeen-Cooper-Schrieffer (BCS) theory of superconductivity. The two regimes realise two seemingly different pictures of Fermi condensates: a BEC of composite bosons with pairing occurring in real space, and a BCS superfluid of spatially-overlapping Cooper pairs (paired in momentum space), as depicted schematically in Fig. 2.4. In between these two regimes, for $1/(k_F a) \sim 0$, the scattering length diverges, the fermionic pair size is comparable to the interparticle spacing, and the only relevant energy scale is the Fermi energy E_F .

While the BCS superfluid is *not* simply a BEC of fermionic pairs [24], the two are however

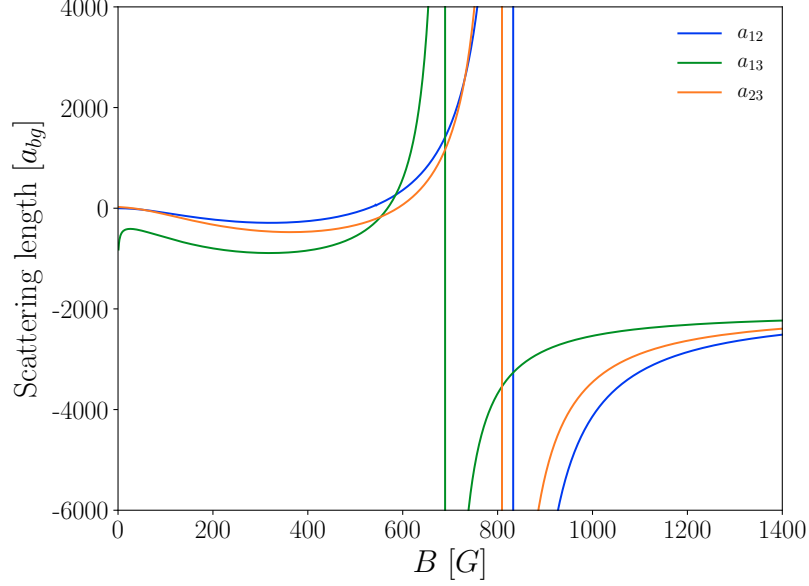


Figure 2.3: Feshbach resonances in ${}^6\text{Li}$. Shown is the s -wave scattering length a as a function of magnetic field for the lowest three hyperfine states. We clearly see the resonances around 834G in a_{12} , 690G in a_{13} , and 811G in a_{23} . The data is taken from the supplementary material of [69].

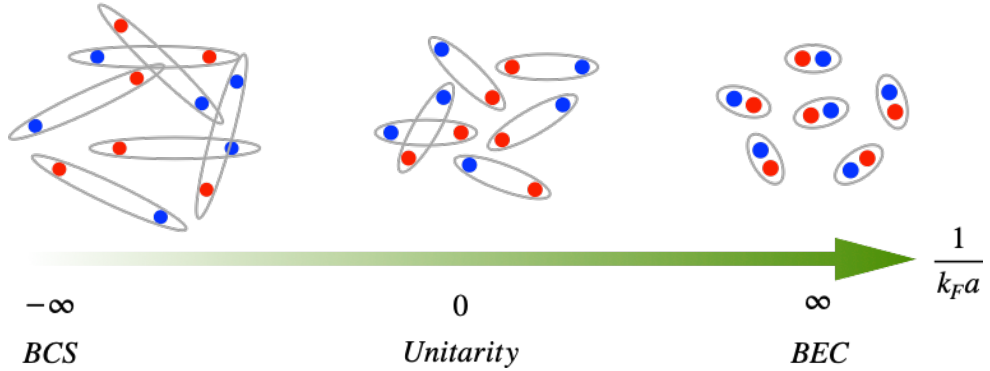


Figure 2.4: By varying the dimensionless interaction parameter $1/(k_F a)$ between two fermionic species (here denoted in red and blue), the system smoothly interpolates between a molecular BEC of tightly bound bosonic dimers, and a BCS superfluid of spatially extended Cooper pairs. The plot is adapted from [70].

2.3 The BCS-BEC crossover

intimately related. Building upon works in the 1960s [71–73], Leggett showed in 1980 that the distinct regimes of BEC and BCS superfluidity are in fact connected by a smooth crossover [74]. The phase diagram of an interacting, two component Fermi gas in the BCS-BEC crossover is shown in Fig. 2.5 as a function of temperature and interaction strength. For $T \gg T^*$, the fermions are unpaired and the system is simply a mixture of both fermionic species on either side of the resonance. For $T \lesssim T^*$, pairs start to form which condense below T_c to form a superfluid condensate. A detailed account of the BCS-BEC crossover can be found in [59, 70, 75–77] (and references therein). In the following we will discuss the different regimes in the crossover in more detail, with a focus on BCS pairing, as this will be particularly relevant for the discussion of our results in chapters 4 and 5.

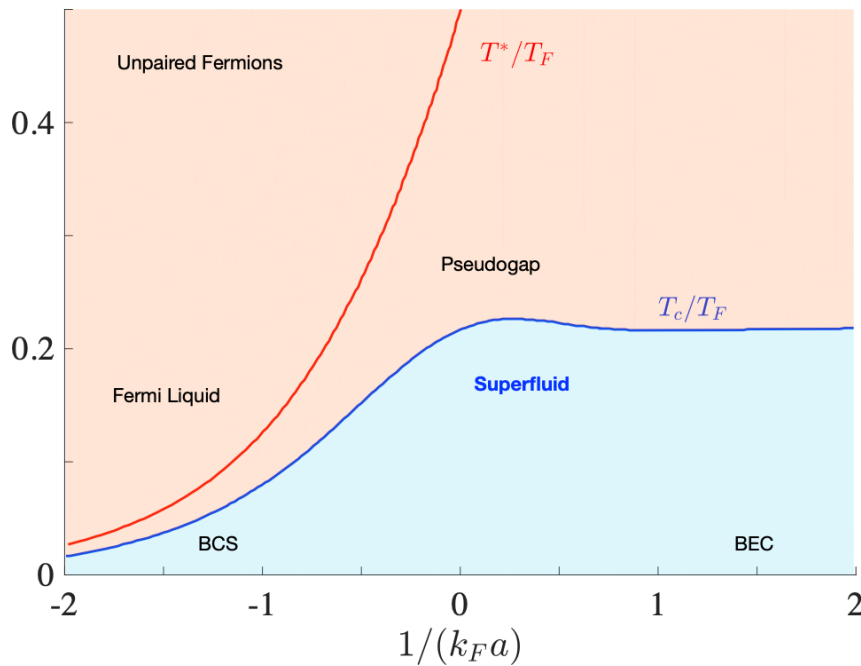


Figure 2.5: Qualitative phase diagram of the BCS-BEC crossover as a function of temperature and interaction $1/(k_F a)$. Below the transition temperature T_c (blue shaded region), the system is superfluid, and interpolates smoothly between a molecular BEC of tightly bound dimers, and a BCS superfluid of Cooper pairs. The solid red line, T^* , marks the onset of pairing. The Figure is adapted from [75].

2.3.1 Molecular BEC

For $1/(k_F a) \gg 1$ the interaction between fermions is so strong, that they form bosonic dimers with a size much smaller than $1/k_F$ and a binding energy given by [59]

$$E_b = -\frac{\hbar^2}{ma^2}, \quad (2.13)$$

where m is the mass of the fermions. For temperatures below the binding energy, and for sufficiently strong attraction between the fermions, bosonic dimers are formed and behave as

point-like particles. These dimers in turn interact repulsively and for $T < T_c$ undergo a quantum phase transition to a superfluid Bose-Einstein condensate (BEC). It should be emphasised, that the underlying interaction between the different fermionic species is *attractive* and monotonically growing from the BCS to the BEC regime, but that in the BEC limit there remains a weak residual repulsion between dimers, $a_{dd} = 0.6a$, giving rise to superfluidity in this regime [59, 75].

2.3.2 BCS Pairing and the Cooper Problem

For $1/(k_F a) \ll -1$ the fermions feel a weak attraction between the two different species, which leads to the formation of Cooper pairs and their condensation into a BCS superfluid. In three dimensions however, there is no two-body bound state for arbitrarily weak interactions between two isolated fermions. This poses the question regarding the nature of the pairing underlying the BCS condensate and the structure of the ground state. In this section we want to elucidate the nature of the pairing mechanism for attractive interactions. To this end we will review the formation of a two-body bound state of isolated particles, which will lead us to the famous Cooper problem [23]. Building upon this, we give an overview over the BCS theory of superconductivity, discussing the nature of its ground state and excitation spectrum. There are many comprehensive reviews on the subject and our discussion will follow in particular [18, 59].

To understand the pairing mechanism in BCS superconductors, it is instructive to look at the corresponding two-particle problem, and to see why no bound state exists for arbitrarily weak interactions in three dimensions. We start with the Schrödinger equation of the reduced particle of mass $\mu = m/2$,

$$\left(-\frac{\hbar^2}{2\mu} \nabla^2 + V(\mathbf{r}) \right) \psi(\mathbf{r}) = E \psi(\mathbf{r}). \quad (2.14)$$

Here, $m_1 = m_2 = m$ is the mass of the two fermions, and $V(\mathbf{r})$ is the (attractive) interaction potential between them. We are looking for bound state solutions, i.e. $E = -\frac{\hbar^2 \kappa^2}{2\mu}$. Rewriting the problem in momentum space yields for an n-dimensional system

$$\psi(\mathbf{q}) = -\frac{2\mu}{\hbar^2} \frac{1}{q^2 + \kappa^2} \int \frac{d^n \mathbf{p}}{(2\pi)^n} V(\mathbf{q} - \mathbf{p}) \psi(\mathbf{p}). \quad (2.15)$$

For short-range interactions, the potential is approximately constant $V(\mathbf{q}) \approx V_0$ over a range $q \lesssim 1/R$ and then quickly falls to zero beyond this (where R is the range of the potential in real space). By integrating on both side of the equation, the self-consistent equation 2.15 can then be rewritten as

$$-\frac{1}{V_0} = \frac{2\mu}{\hbar^2} \int_{q \lesssim \frac{1}{R}} \frac{d^n \mathbf{q}}{(2\pi)^n} \frac{1}{q^2 + \kappa^2} = \frac{1}{\Omega} \int_{\epsilon < E_R} d\epsilon \frac{\rho_n(\epsilon)}{2\epsilon + |E|}, \quad (2.16)$$

where Ω is the volume of the system, $\rho_n(\epsilon)$ the density of states in n dimensions, $\epsilon = \frac{\hbar^2 q^2}{2m}$ the energy of a free particle of mass m , and $E_R = \frac{\hbar^2}{mR^2}$ the energy cutoff [59]. The problem of the

2.3 The BCS-BEC crossover

existence of a bound state therefore translates into finding a consistent solution to the above equation for a given interaction V_0 . In particular for very weak attractive interactions $|V_0| \rightarrow 0$ the left hand side of the equation diverges, so we need to analyse the integral on the right hand side in different dimensions. The density of states for free fermions is given by

$$\rho(\epsilon) = \sum_{\mathbf{k}} \delta(\epsilon - \epsilon_{\mathbf{k}}) \sim \begin{cases} \frac{1}{\sqrt{\epsilon}}, & n = 1 \\ \Theta(\epsilon), & n = 2 \\ \sqrt{\epsilon}, & n = 3 \end{cases} . \quad (2.17)$$

Eq. 2.16 only has a solution, if the integral on the right hand side diverges for a vanishing bound state energy $E \rightarrow 0$. These integrals can be solved exactly (c.f. appendix section A.1) and one finds that in one dimension the integral diverges as $1/\sqrt{|E|}$, whilst in two dimensions it diverges logarithmically. This means that for $n \leq 2$ we can always find a bound state solution for any attractive potential. In 3D however, the integral is finite as $|E| \rightarrow 0$, which implies a *threshold* on the interaction for the binding of two particles. This however raises the questions, how a paired superfluid in the BCS regime of the crossover comes about. In 1956 Cooper presented a mechanism by which two fermions could pair into a bound state even at weak attractive interactions [23]. We shall now briefly revisit his argument before proceeding to discuss the celebrated BCS theory of superconductivity.

The Cooper Problem

Consider two attractively interacting fermions on top of a non-interacting, filled Fermi sphere. Due to Pauli blocking all states below the Fermi surface are occupied and hence not available as potential final states for the two interacting fermions above the Fermi surface. In particular the fermions deep inside the Fermi sea are, to a very good approximation, ‘frozen’ inside the Fermi sphere and they do not take part in any microscopic processes. It is only the fermions close to the Fermi surface which can be excited as particle-hole pairs. Hence for weak interactions the only available scattering states of the two fermions are the states in the immediate vicinity of the Fermi surface, i.e. a shallow momentum shell around k_F . The density of states at the Fermi surface is constant, $\rho_{3D}(E_F)$, just like the density of states of the two dimensional problem discussed above. We can therefore expect, that pairing can happen even for arbitrarily weak interactions, as long as the two fermions sit on top of a filled Fermi sea. From appendix A.1, we found that the binding energy of two particles in two dimensions is given by

$$E = -2E_R e^{-\frac{4\pi\hbar^2}{m|V_0|}} = -2E_R e^{-\frac{2\Omega}{\rho_2|V_0|}} . \quad (2.18)$$

Thus the binding energy depends exponentially on the inverse density of states of the two dimensional problem. In the case considered here, $\rho_2 = \rho_{3D}(E_F)$. Now in all generality fermion pairs can form at any momentum. However the number of available scattering states for zero-momentum pairing is much larger than for any finite momentum. For zero-momentum pairing, the two fermions have to have equal and opposite momenta, which means the entire Fermi surface is available. On the other hand, pairs with finite momentum $2\mathbf{q}$ can only scatter into the

ring of radius $\sqrt{k_F^2 - q^2}$, offering significantly fewer states to scatter into. With regard to Eq. 2.18 we see that a larger effective density of states gives rise to a larger absolute binding energy. Therefore we conclude that the fermions with zero net momentum experience stronger pairing. Up until now we have assumed the fermions inside the Fermi sea to be non-interacting. If we imagine to slowly turn on the interactions between the fermions (starting from the Fermi surface and moving successively further into the core of the Fermi sphere), we conclude that the entire system will reorganise into a new, paired state, comprised of these spatially extended Cooper pairs. The Fermi liquid therefore has an instability towards pairing in the presence of attractive interactions (Cooper instability). In 1957 Bardeen, Cooper, and Schrieffer (BCS) presented their celebrated microscopic theory, which takes the interacting many-body problem as well as the proper antisymmetrisation of the wave function fully into account. In the following we will detail the ideas relevant to the results presented in chapters 4 and 5.

BCS Theory

We start our discussion with the Hamiltonian for an interacting many-body system of two fermionic species $\sigma = \{\uparrow, \downarrow\} = \{1, 2\}$ (e.g. the two spin species of electrons in a solid or two different hyperfine levels of fermionic atoms in a cold atom experiment), given by

$$H = \sum_{\sigma} \int d^3\mathbf{r} \Psi_{\sigma}^{\dagger}(\mathbf{r}) \left(-\frac{\hbar^2 \nabla^2}{2m} + \epsilon_{\sigma}^0 - \mu_{\sigma} \right) \Psi_{\sigma}(\mathbf{r}) + \frac{1}{2} \sum_{\sigma \neq \tau} \int d^3\mathbf{r} d^3\mathbf{r}' \Psi_{\sigma}^{\dagger}(\mathbf{r}) \Psi_{\tau}^{\dagger}(\mathbf{r}') V(\mathbf{r} - \mathbf{r}') \Psi_{\tau}(\mathbf{r}') \Psi_{\sigma}(\mathbf{r}). \quad (2.19)$$

Here $\Psi_{\sigma}^{(\dagger)}(\mathbf{r})$ is the fermionic field operator annihilating (creating) a fermion of species σ and mass m at position \mathbf{r} , $V(\mathbf{r} - \mathbf{r}') = g\delta(\mathbf{r} - \mathbf{r}')$ is the contact interaction between the different (pseudo-)spin species, and $\mu_1 = \mu_2 = \mu$ the chemical potential. ϵ_{σ}^0 is a potential spin-dependent energy offset e.g. the hyperfine splitting in cold atoms. Since the Hamiltonian is conserving the different spin species separately, the different hyperfine levels can be shifted on top of each other, $\epsilon_2^0 \rightarrow \epsilon_1^0 = 0$, using a suitable unitary transformation (and we will neglect them from here onwards as they just give rise to a global phase).

BCS theory applies in the parameter regime $1/(k_F a) \ll -1$ of the crossover, where two fermions of different (pseudo-)spin feel a weakly attractive interaction ($g < 0$). In the cold atom context the attractive interaction can be engineered in this way by the means of Feshbach resonances as we have seen above in section 2.2. In solid state superconductors however, spin up and down electrons interact through the Coulomb potential *repulsively*. The works of Fröhlich, and of Bardeen and Pines addressed this issue and showed that an attractive potential arises as an effective interaction, when the coupling between the electrons and the phononic modes of the crystal lattice is taken into account [22, 78–80].

We have seen from Eq. 2.18 that the bound state energy of paired fermions is lowest, if the fermions have zero momentum in the centre of mass frame. The Pauli exclusion principle enforces the fermions forming a pair to be of opposite (pseudo-)spin species, and going to

2.3 The BCS-BEC crossover

momentum space with $\Psi_\sigma(\mathbf{r}) = \frac{1}{\sqrt{V}} \sum_{\mathbf{k}} e^{i\mathbf{k}\cdot\mathbf{r}} c_{\mathbf{k},\sigma}$, the BCS Hamiltonian can be written as

$$H_{BCS} = \sum_{\mathbf{k},\sigma} \xi_{\mathbf{k},\sigma} c_{\mathbf{k},\sigma}^\dagger c_{\mathbf{k},\sigma} + \frac{g}{V} \sum_{\mathbf{k},\mathbf{q}} c_{\mathbf{k},1}^\dagger c_{-\mathbf{k},2}^\dagger c_{-\mathbf{q},2} c_{\mathbf{q},1}, \quad (2.20)$$

where $\xi_{\mathbf{k},\sigma} = \epsilon_{\mathbf{k}} - \mu_\sigma$ and $\epsilon_{\mathbf{k}} = \frac{\hbar^2 k^2}{2m}$ is the (free) single-particle dispersion. The chemical potential of species σ is μ_σ , V the volume of the system, and $c_{\mathbf{k},\sigma}^{(\dagger)}$ are the annihilation (creation) operators of a fermion in spin state σ at momentum \mathbf{k} . The first term represents the kinetic energy of the different fermions, whilst the second term accounts for the interaction between different zero-momentum Cooper pairs. In writing this Hamiltonian we have already invoked the approximation that pairs of net zero-momentum have the largest binding energy, therefore we explicitly neglected interactions between pairs at finite momentum here, which is a great simplification to the full many-body problem, as density fluctuations are no longer captured by the model. In charged superfluids these are in any case suppressed by the Coulomb repulsion, whereas in neutral superfluids sound waves are not taken into account [59].

Guided by the intuition of the previous section, we anticipate the Fermi gas to be unstable to the formation of Cooper pairs. In this case, the pair correlator $\Delta_{\mathbf{k}} = \langle c_{-\mathbf{k},2} c_{\mathbf{k},1} \rangle$ acquires a non-zero finite expectation value. To study the phase transition from a Fermi liquid to a BCS superconductor, we therefore introduce the superconducting (*s*-wave) order parameter²,

$$\Delta = \frac{g}{V} \sum_{\mathbf{k}} \langle c_{-\mathbf{k},2} c_{\mathbf{k},1} \rangle. \quad (2.21)$$

It is designed in such a way that it is zero in the (high temperature) normal phase, and non-zero below the transition temperature to the superconducting phase. As such it is a clear indicator of the system's phase and will be the center of our investigations in chapters 4 and 5. It is worth noting that in any practical computation the discrete sum over momentum in Eq. 2.21 is replaced by an integral, and the interaction strength is replaced by applying the renormalisation procedure outlined in 2.1, giving $1/(k_F a) = (8\pi E_F)/(g k_F^3) + \sqrt{(4E_c)/(\pi^2 E_F)}$.

Since in typical superconductors and superfluids a macroscopic number of particles is involved in the pairing, the fluctuations around $\langle c_{-\mathbf{k},2} c_{\mathbf{k},1} \rangle$ can be expected to be small, which allows us to use a mean-field decoupling³ to simplify Eq. 2.20 into a quadratic (and thereby solvable) Hamiltonian

$$H_{BCS}^{mf} = \sum_{\mathbf{k},\sigma} \xi_{\mathbf{k}} c_{\mathbf{k},\sigma}^\dagger c_{\mathbf{k},\sigma} + \sum_{\mathbf{k}} \left(\Delta c_{\mathbf{k},1}^\dagger c_{-\mathbf{k},2}^\dagger + \text{h.c.} \right), \quad (2.22)$$

where we have neglected constant shifts to the Hamiltonian and assumed a balanced superfluid ($N_1 = N_2$, i.e. $\mu_1 = \mu_2 = \mu$). Note that, whilst we have simplified the quartic interaction term of the Hamiltonian, Eq. 2.22 is no longer particle number conserving. For a Fermi gas in the BCS regime, the BCS order parameter is expressed in experimentally measurable quantities as

²In the literature it is also commonly called the superconducting gap function or simply the gap.

³The mean-field decoupling of two operators A and B is given by: $\langle AB \rangle \approx \langle A \rangle B + A \langle B \rangle - \langle A \rangle \langle B \rangle$.

[59] (for more details we refer the reader to appendix A.2),

$$\Delta = \frac{8}{e^2} e^{-\pi/(2k_F|a|)}. \quad (2.23)$$

The BCS Hamiltonian, Eq. 2.22, is quadratic in the fermionic operators, and readily diagonalised by a canonical Bogoliubov-Valatin transformation to a new set of fermionic quasiparticle operators [18, 81, 82]

$$\begin{pmatrix} \gamma_{\mathbf{k},0} \\ \gamma_{\mathbf{k},1}^\dagger \end{pmatrix} = \begin{pmatrix} u_{\mathbf{k}} & -v_{\mathbf{k}} \\ v_{\mathbf{k}}^* & u_{\mathbf{k}}^* \end{pmatrix} \begin{pmatrix} c_{\mathbf{k},1} \\ c_{-\mathbf{k},2}^\dagger \end{pmatrix} \text{ and } \begin{pmatrix} c_{\mathbf{k},1} \\ c_{-\mathbf{k},2}^\dagger \end{pmatrix} = \begin{pmatrix} u_{\mathbf{k}}^* & v_{\mathbf{k}} \\ -v_{\mathbf{k}}^* & u_{\mathbf{k}} \end{pmatrix} \begin{pmatrix} \gamma_{\mathbf{k},0} \\ \gamma_{\mathbf{k},1}^\dagger \end{pmatrix}, \quad (2.24)$$

where $|u_{\mathbf{k}}|^2 + |v_{\mathbf{k}}|^2 = 1$. The unitary transformation preserves the fermionic anticommutation relations (by the virtue that it is unitary). The coefficients $u_{\mathbf{k}}, v_{\mathbf{k}}$ are determined by enforcing, that the BCS Hamiltonian is diagonal with respect to the new quasiparticle operators in this new basis. The Bogoliubov amplitudes are found to be given by $|u_{\mathbf{k}}|^2 = 1 - |v_{\mathbf{k}}|^2 = \frac{1}{2}(1 + \frac{\xi_{\mathbf{k}}}{E_{\mathbf{k}}})$ and $E_{\mathbf{k}} = \sqrt{\xi_{\mathbf{k}}^2 + |\Delta|^2}$, where the latter is the dispersion of the quasiparticles. Up to constant shifts in energy, the Hamiltonian in the quasiparticle basis now reads

$$H_{BCS}^{mf} = \sum_{\mathbf{k}} E_{\mathbf{k}} (\gamma_{\mathbf{k},0}^\dagger \gamma_{\mathbf{k},0} + \gamma_{\mathbf{k},1}^\dagger \gamma_{\mathbf{k},1}). \quad (2.25)$$

The quasiparticle dispersion $E_{\mathbf{k}}$ as a function of momentum is shown in Fig. 2.6. It exhibits a gapped dispersion, with the size of the gap given by the superconducting order parameter Δ . It costs at least this amount of energy to excite quasiparticles on top of the BCS ground state and thereby break Cooper pairs.

The ground state is then constructed as the vacuum of quasiparticles $\gamma_{\mathbf{k},0}|\psi_{BCS}\rangle = \gamma_{\mathbf{k},1}|\psi_{BCS}\rangle = 0$ and found to be given by the celebrated BCS wave function

$$|\psi_{BCS}\rangle = \prod_{\mathbf{k}} (u_{\mathbf{k}} + v_{\mathbf{k}} c_{\mathbf{k},1}^\dagger c_{-\mathbf{k},2}^\dagger) |0\rangle. \quad (2.26)$$

Interestingly, the BCS wave function is not only the ground state of the mean-field Hamiltonian, Eq. 2.22, but can be shown to be the *exact* solution to the BCS Hamiltonian in Eq. 2.20. It is a coherent superposition of empty and occupied Cooper pair states and as such does not conserve the total particle number. It is made of a superposition of states of differing particle number sectors and describes a condensate of Cooper pairs⁴. An example of the Cooper pair amplitudes as a function of momentum is shown in Fig. 2.7. We note that the BCS wave function in Eq. 2.26 contains, in the limit of vanishing interactions, the ground state of a gas of fermions, the Fermi sea. It is recovered for $u_{\mathbf{k}} = 0, v_{\mathbf{k}} = 1$ for $k \leq k_F$ and vice versa for $k > k_F$. Turning

⁴One can think of the BCS wave function as a coherent state of Cooper pairs, for $|\psi_{BCS}\rangle \sim \prod_{\mathbf{k}} \exp(\frac{v_{\mathbf{k}}}{u_{\mathbf{k}}} c_{\mathbf{k},1}^\dagger c_{-\mathbf{k},2}^\dagger) |0\rangle$

2.3 The BCS-BEC crossover

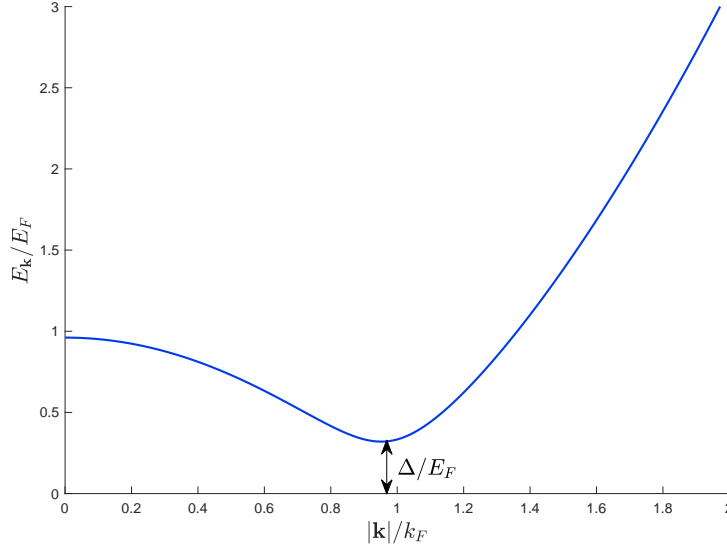


Figure 2.6: Quasiparticle dispersion as a function of momentum for a BCS gap parameter of $\Delta = 0.32E_F$. The dispersion is gapped, it therefore costs a *finite* amount of energy to break Cooper pairs (by the creation of a quasiparticle). The energy gap is exactly given by the superconducting order parameter, hence it is also often called the superconducting gap (marked here by a black arrow).

on attractive interactions and tuning through the BCS regime of the crossover, the Bogoliubov amplitudes smoothly evolve from the Heaviside step function behaviour to a smooth function of momentum as shown in Fig. 2.7 for an interaction $1/(k_F a) \sim -0.6$.

Using the BCS wave function, we can now evaluate the the superconducting gap as

$$\Delta = \frac{g}{V} \sum_{\mathbf{k}} \langle c_{-\mathbf{k},2} c_{\mathbf{k},1} \rangle = \frac{g}{V} \sum_{\mathbf{k}} u_{\mathbf{k}}^* v_{\mathbf{k}} . \quad (2.27)$$

We have an additional constraint imposed by the total number of particles in our system, and the equation for the particle density $n = N/V$ reads

$$n = \frac{1}{V} \sum_{\mathbf{k},\sigma} \langle n_{\mathbf{k},\sigma} \rangle = \frac{2}{V} \sum_{\mathbf{k}} |v_{\mathbf{k}}|^2 . \quad (2.28)$$

This is an implicit equation for the chemical potential μ , and the two equations (for the gap and particle density Eq. 2.27 - 2.28) need to be evaluated self-consistently to yield Δ and μ for a given interaction $1/(k_F a)$ [59]. Appendix A.2 gives more details on the self-consistent solution of the two equations, the result of which is shown in Fig. 2.8. In the BCS regime, $1/(k_F a) \ll -1$, $\mu \approx E_F$ and the superconducting gap is given by Eq. 2.23. In the BEC regime on the other hand, $1/(k_F a) \gg 1$, $\mu = -\frac{\hbar^2}{2ma^2} + \frac{\pi\hbar^2 a n}{m}$, while $\Delta \approx \sqrt{\frac{16}{3\pi}} \frac{E_F}{\sqrt{k_f a}}$. The chemical potential term consists of the energy of the formed bound state *per particle* and a mean-field correction arising from the repulsive interaction between the molecules. Δ is neither related

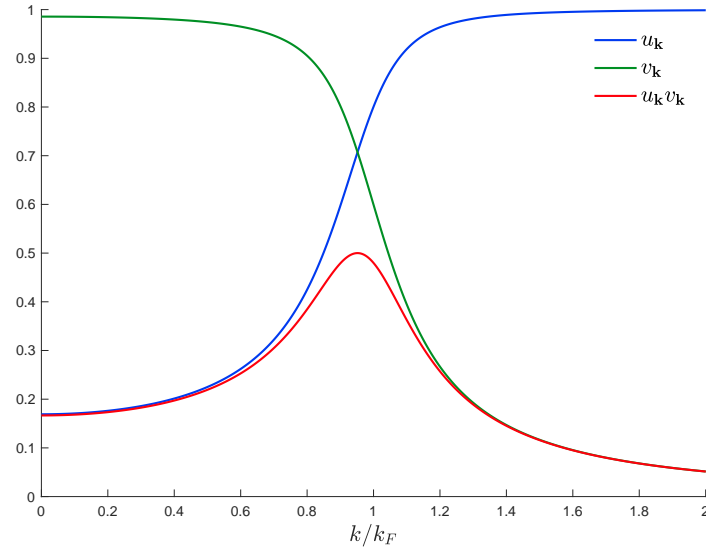


Figure 2.7: Cooper pair amplitudes as a function of momentum. Shown are the Bogoliubov amplitudes for a BCS gap parameter of $\Delta = 0.32E_F$.

to the binding energy nor the gap in the spectrum (which in the BEC regime occurs at $|\mathbf{k}| = 0$, since $\mu < 0$) [59].

BCS theory at finite Temperature

Up to now we have discussed the BCS theory, its ground state wave function and the dispersion of quasiparticle excitations at zero temperature. In chapter 5 we will also discuss briefly some thermal properties of the BCS state, so we here want to very briefly outline the necessary ideas for the aforementioned chapter.

The excitation of a fermionic quasiparticle $\gamma_{\mathbf{k},\sigma}^\dagger$ costs an energy $E_{\mathbf{k}} \geq |\Delta|$ in the BCS regime. At finite inverse temperature $\beta = 1/(k_B T)$, the probability that such a quasiparticle is thermally activated *on top of the BCS ground state* is given by the Fermi-Dirac distribution

$$f(E_{\mathbf{k}}) = \frac{1}{e^{\beta E_{\mathbf{k}}} + 1}. \quad (2.29)$$

Therefore the momentum distribution of quasiparticles is given by $\langle \gamma_{\mathbf{k},\sigma}^\dagger \gamma_{\mathbf{k},\sigma} \rangle = f(E_{\mathbf{k}})$. With this, the finite temperature gap equation (c.f. Eq. 2.27) reads

2.4 Fermionic Atoms in Optical Lattices

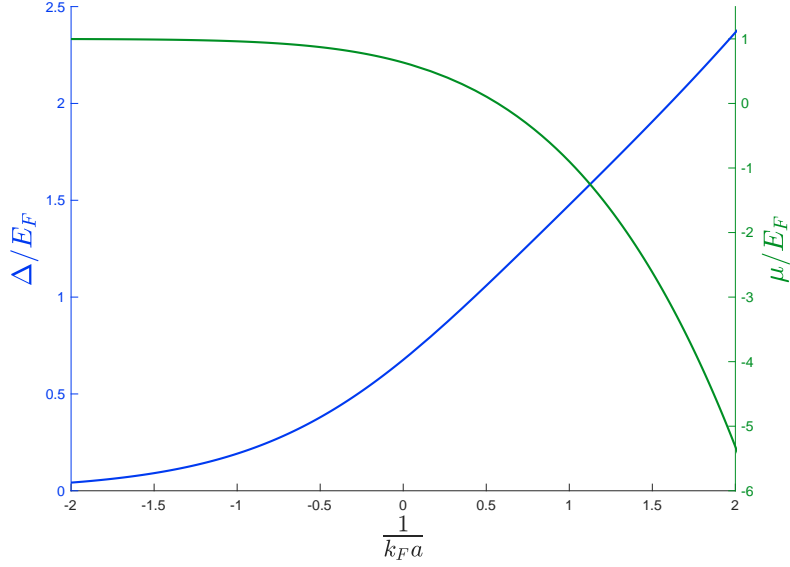


Figure 2.8: The superconducting gap Δ and chemical potential μ as a function of the dimensionless coupling $1/(k_F a)$, obtained from solving Eq. 2.27 and 2.28 self-consistently (details in appendix A.2). The plot is adapted from [59].

$$\begin{aligned}
 \Delta &= \frac{g}{V} \sum_{\mathbf{k}} u_{\mathbf{k}}^* v_{\mathbf{k}} \langle 1 - \gamma_{\mathbf{k},0}^\dagger \gamma_{\mathbf{k},0} - \gamma_{\mathbf{k},1}^\dagger \gamma_{\mathbf{k},1} \rangle \\
 &= \frac{g}{V} \sum_{\mathbf{k}} u_{\mathbf{k}}^* v_{\mathbf{k}} (1 - 2f(E_{\mathbf{k}})) \\
 &= \frac{g}{V} \sum_{\mathbf{k}} \frac{\Delta}{2E_{\mathbf{k}}} \tanh\left(\frac{\beta E_{\mathbf{k}}}{2}\right), \tag{2.30}
 \end{aligned}$$

which can be solved numerically.

2.4 Fermionic Atoms in Optical Lattices

The interplay of the various degrees of freedom in interacting many-body quantum systems opens up the possibility to observe and study a multitude of complex, emergent phenomena. Examples include the observation of the superfluid to Mott insulator transition in the Bose-Hubbard model [83], the collapse and revival of the macroscopic matter wave field of a Bose-Einstein condensate [39], the realisation of the BCS-BEC crossover [84–89] or the generation of artificial gauge field in optical lattice systems to study topological quantum matter [90], to name a few. These complex phases arise from the subtle competition between different energy scales and degrees of freedom of the system. The richness and complexity that can arise from their fundamental constituents, ultimately makes strongly correlated many-body quantum system the fascinating and active research field it is today. Major milestones achieved in

the field of quantum optics and ultracold quantum gases have since led to a further acceleration of the research activity. We have already seen how Feshbach resonances can be used to tune the interactions properties of atomic vapours at will. Another route to realise strongly correlated systems is by changing their kinetic energy to *effectively* enhance the interactions. Experimentally this can be achieved, by subjecting the atomic particles to a crystal potential and confining them to the crystal's lattice sites. Motion of the particles is possible, if desired, by allowing hopping process of the atoms to nearby sites. By confining the atoms to a lattice, their kinetic energy can be varied over several orders of magnitude, allowing access to the strongly correlated regime. Note that in this way of tuning the system, the interaction energy has not been changed physically, so that strong interactions are accessible without risking the stability of the atomic cloud due to three-body loss processes. The exceptional tunability of the systems' parameters and their excellent isolation from the environment means that degenerate quantum gases are extremely versatile systems with long coherence times, offering the possibility to control and explore novel phenomena in quantum many-body physics in and away from equilibrium.

In solid state systems, the electrons feel the electrostatic potential of the ionic cores, and the underlying lattice structure is key to understanding these systems [2, 91]. In the cold atom context, the atoms experience an optical lattice potential created from standing waves of retro-reflected laser fields due to the interaction of the induced dipole moment with the laser field (see 2.4.1). Correlated quantum gases in optical lattices are a highly controlled, tuneable experimental platform, with excellent isolation from the environment and the added advantage, that complications due to lattice phonons or impurities do not arise. These systems realise Hamiltonians which have traditionally been studied extensively in condensed matter physics [92], and can be considered as realisations of analogue quantum simulators [93–95]. Furthermore, by superposing several laser fields, the lattice structure and even the whole dimensionality of the system can be altered. Whilst a single retro-reflected laser beam creates a single standing wave and produces a series of planar, two-dimensional quantum systems [96], adding a further laser field results in an array of one-dimensional tubes of atoms [97]. With yet another intersecting laser, a three-dimensional cubic lattice is realised [35].

The Hubbard model [55] is one of the hallmark models in condensed matter physics when studying the behaviour of electrons in solids. Within a single-band tight-binding approximation, it has two key ingredients: the kinetic energy of electrons hopping between adjacent lattice sites, and a local interactions between electrons of opposite spin. The Fermi-Hubbard model captures these two competing energy scales in the Hamiltonian

$$H = -J \sum_{\langle i,j \rangle, \sigma} c_{i,\sigma}^\dagger c_{j,\sigma} + U \sum_i n_{i,\uparrow} n_{i,\downarrow}, \quad (2.31)$$

where J is the tunnelling matrix element between adjacent sites ($\langle i, j \rangle$ denotes the sum over nearest neighbours), and U is the on-site interaction between fermions of opposite spin. Ultracold quantum gases have been proposed as ideal candidates to study the physics of this model [98, 99], which, despite its apparent simplicity, remains elusive and has not been fully solved. The Hubbard model hosts a wide range of phases and phenomena, its wealth stemming from

2.4 Fermionic Atoms in Optical Lattices

the intricate interplay between interaction, delocalisation, and magnetic ordering. Confining fermionic atoms to an optical lattice, the tunnelling matrix element J , and on-site interaction U can be tuned experimentally by varying the depth of the optical lattice. Employing Feshbach resonances then allows to further refine and influence the interactions of the system. Their versatility makes cold atoms in optical lattices ideal quantum simulators, where the atoms in the optical lattice mimic the dynamics of electrons in solid state systems [95].

In section 2.4.1 we will introduce the key ideas of how atoms can be trapped by laser light, and will then go on to introduce the theoretical description of an atomic cloud of fermionic atoms in an optical lattice, described by the Fermi-Hubbard model (section 2.4).

2.4.1 Trapping of Neutral Atoms

Experiments on ultracold quantum gases are only possible because of the advances made in cooling and trapping neutral atoms using laser light. The directed absorption and spontaneous re-emission of the laser photons gives rise to a dissipative contribution, the atoms are slowed down due to the momentum exchange with the photons, and the cloud of atoms is cooled [29]. Furthermore, the laser field induces a dipole moment in the atoms which in turn interacts with the light field. An effective, conservative potential via the AC Stark shift is created to confine and trap the atoms in the intensity maxima or minima of the laser (for a red or blue detuning respectively) [100, 101].

To illustrate the trapping mechanism we follow the dressed atom approach as detailed in [102]. We consider a two-level atom, $H_a = \frac{1}{2}\hbar\omega_0\sigma_z$, interacting with a single-mode quantised light-field, $H_p = \hbar\omega(a^\dagger a + 1/2)$ via the electric dipole interaction $H_{int} = -\mathbf{d} \cdot \mathbf{E}$. We label the atomic states by $|g\rangle$ and $|e\rangle$ (ground state and excited state) and the photonic mode by its occupation $|n\rangle$. The atomic raising and lowering operators are then given by $\sigma^\pm = \sigma_x \pm i\sigma_y$. Within the electric dipole approximation, we can write the interaction Hamiltonian as $H = \hbar g(\sigma^+ + \sigma^-)(a^\dagger + a)$, where g is the coupling strength and related to the dipole operator of the atom. In the limit of small detunings $|\omega - \omega_0| \ll \omega + \omega_0$ we use a rotating wave approximation to finally obtain the Jaynes-Cummings Hamiltonian [103]

$$H = \frac{\hbar\omega_0}{2}\sigma_z + \hbar\omega(a^\dagger a + \frac{1}{2}) + \hbar g(\sigma^+ a + \sigma^- a^\dagger), \quad (2.32)$$

where $\sigma_z = |e\rangle\langle e| - |g\rangle\langle g|$. For $g = 0$ the basis states can be labelled by $|\{g, e\}, n\rangle$ with eigenenergies $E = \pm \frac{\hbar\omega_0}{2} + \hbar\omega(n + \frac{1}{2})$. The Jaynes-Cummings model is the hallmark model in quantum optics to study the quantised light-matter interaction. A finite interaction leads to a coupling of the atomic and photonic degrees of freedom between states $|g, n\rangle \leftrightarrow |e, n-1\rangle$ and in this reduced two-dimensional space the Hamiltonian reads

$$H = \hbar \begin{pmatrix} -\delta/2 & g\sqrt{n} \\ g\sqrt{n} & \delta/2 \end{pmatrix} + n\hbar\omega\mathbb{1}, \quad (2.33)$$

where $\delta = \omega - \omega_0$ and we have identified $|e, n-1\rangle = \begin{pmatrix} 1 \\ 0 \end{pmatrix}$ and $|g, n\rangle = \begin{pmatrix} 0 \\ 1 \end{pmatrix}$. In section 2.5.2 we will see that this kind of Hamiltonian gives rise to Rabi oscillations in the population

2.4.2 Towards Strongly Correlated Fermions: The Fermi-Hubbard Model

dynamics. For our purposes here we are more interested in the exact energy spectrum, which can be obtained by diagonalising Eq. 2.33, giving

$$E_{\pm}(\delta, g) = \hbar \left(n\omega \pm \frac{1}{2} \sqrt{\delta^2 + (2g)^2 n} \right), \quad (2.34)$$

for the *dressed states* $|n, \pm\rangle$. The energy shift between the levels for zero and non-zero coupling is then given by

$$\Delta E = E_{\pm}(\delta, g) - E_{\pm}(\delta, g = 0) \stackrel{\delta \gg 2g\sqrt{n}}{\approx} \pm \frac{\hbar \Omega_R^2}{4\delta}, \quad (2.35)$$

where we have defined the Rabi frequency $\Omega_R = 2g\sqrt{n} \sim \sqrt{I(\mathbf{r})}$, where $I(\mathbf{r})$ is the intensity of the light field. We observe that for a red-detuned laser field ($\delta < 0$) atoms in the ground state experience a force towards regions of low intensity (e.g. the nodes of a standing wave), whilst atoms in the excited state are drawn to regions of high intensity (the opposite holds for blue detuning $\delta > 0$). In this way it is possible to trap neutral atoms in light fields. By superposing several intersecting beams various lattice arrangements can be realised and even the dimensionality of the system (by e.g. tightly confining the atoms in a particular direction through a highly anisotropic intensity of the laser beams) tuned.

2.4.2 Towards Strongly Correlated Fermions: The Fermi-Hubbard Model

In one dimension, for distances much smaller than the waist of the Gaussian laser beams, the trapping potential can be approximated by

$$V(z) = V_0 \sin^2(kz), \quad (2.36)$$

where $k = \frac{2\pi}{\lambda} = \frac{\pi}{a}$ is the wave vector of the lattice potential. If we restrict ourselves to time-scales, where spontaneous emission events can be neglected, the coherent dynamics of an atom trapped in this potential is described by the Hamiltonian

$$H = -\frac{\hbar^2}{2m} \frac{\partial^2}{\partial z^2} + V(z). \quad (2.37)$$

Since the potential, created by the retro-reflected laser beams, is periodic with the lattice constant a (size of the unit cell), $V(z + a) = V(z)$, the eigenfunctions of the system are given by Bloch eigenstates [91].

Band structure

The periodic nature of the potential gives rise to allowed energy bands separated by energy gaps. The solution of the Schrödinger equation for a particle in a periodic potential is given by Bloch's theorem. The eigenfunctions are Bloch wave functions, which read

$$\phi_q^{(n)}(z) = e^{iqz} u_q^{(n)}(z), \quad (2.38)$$

2.4 Fermionic Atoms in Optical Lattices

where $u_q^{(n)}(z)$ is labelled by the band index n and quasi-momentum $q \in (-\pi/a, \pi/a]$ living in the first Brillouin zone. The envelope function $u_q^{(n)}(z)$ are the eigenfunctions of the Hamiltonian

$$\left[\frac{1}{2m} (\hbar q - i\hbar \frac{\partial}{\partial z})^2 + V(z) \right] u_q^{(n)}(z) = E_q^{(n)} u_q^{(n)}(z), \quad (2.39)$$

and themselves periodic function of the lattice. Therefore we can expand them in a Fourier series over the reciprocal lattice

$$u_q^{(n)}(z) = \sum_G u_G^{(n,q)} e^{iGz} \quad (2.40)$$

$$V(z) = \sum_G V_G e^{iGz}, \quad (2.41)$$

where the reciprocal lattice is understood as the set of all reciprocal lattice vectors $G = \frac{2\pi}{a} \mathbb{Z}$. For the periodic potential given in Eq. 2.36, the time-independent Schrödinger equation then becomes

$$\sum_{G'} H_{G,G'}^q u_{G'}^{(n,q)} = E_q^{(n)} u_G^{(n,q)}, \quad (2.42)$$

where $H_{G,G'}^q = \frac{\hbar^2}{2m} (q + G)^2 \delta_{G,G'} + V_{G'-G}$.

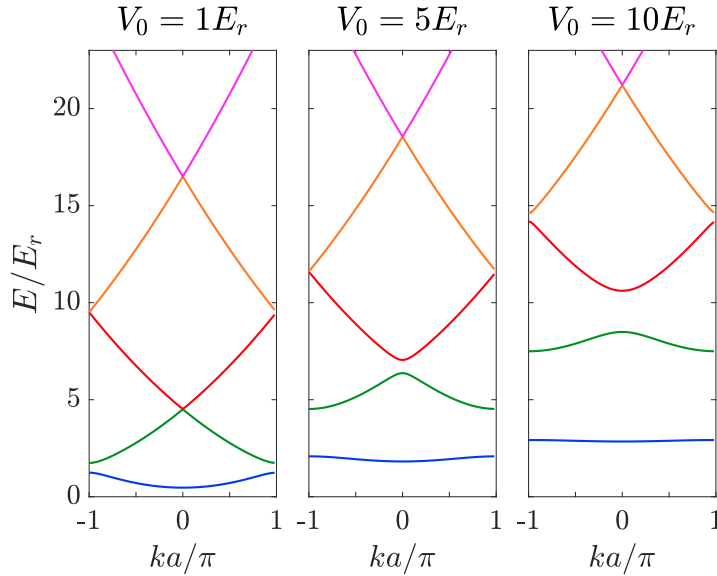


Figure 2.9: Band structure of a one-dimensional optical lattice in units of recoil energy E_r . We have shown the lowest five Bloch bands in the first Brillouin zone, for three different lattice depths.

This problem can be efficiently solved numerically by truncating the effective Hamiltonian. Fig. 2.9 shows the energy bands in units of the recoil energy $E_r = \frac{\hbar^2 k^2}{2m} = \frac{\hbar^2 \pi^2}{2ma^2}$. For weak poten-

2.4.2 Towards Strongly Correlated Fermions: The Fermi-Hubbard Model

tials and upon unfolding the Brillouin zone, we recover approximately the parabolic dispersion of a free particle. However, for any finite potential $V_0 \neq 0$, band gaps open up at the Brillouin zone edge at $k = \pm\pi/a$, whose size increases with increasing lattice depth. We thus see how the presence of a periodic potential gives rise to *energy bands* in the allowed energy spectrum. Finally, for very deep lattices, the different bands flatten and become more and more equidistant, reflecting the fact that in this limit we can approximate each lattice well by a harmonic oscillator with a lattice spacing of $\hbar\omega = 2\sqrt{V_0/E_r E_r}$.

Derivation of the Fermi-Hubbard Hamiltonian

Consider a gas of fermionic atoms confined to a one-dimensional optical lattice geometry. Theoretically the system is described by the many-body Hamiltonian

$$H = \sum_{\sigma} \int d^3\mathbf{r} \Psi_{\sigma}^{\dagger}(\mathbf{r}) \left(-\frac{\hbar^2}{2m} \nabla^2 + V_0(\mathbf{r}) \right) \Psi_{\sigma}(\mathbf{r}) + \frac{1}{2} \sum_{\sigma \neq \sigma'} \int d^3\mathbf{r} d^3\mathbf{r}' \Psi_{\sigma}^{\dagger}(\mathbf{r}) \Psi_{\sigma'}^{\dagger}(\mathbf{r}') V(\mathbf{r} - \mathbf{r}') \Psi_{\sigma'}(\mathbf{r}') \Psi_{\sigma}(\mathbf{r}), \quad (2.43)$$

where $\Psi_{\sigma}(\mathbf{r})$ is the field operator annihilating a fermion in spin state $\sigma = \{\uparrow, \downarrow\}$ on site \mathbf{r} , and where the interaction is given by $V(\mathbf{r} - \mathbf{r}') = g\delta(\mathbf{r} - \mathbf{r}')$ and $g = \frac{4\pi\hbar a}{m}$, with a the s -wave scattering length. The first term describes the kinetic energy of the atoms, whilst the second term captures the short-range interaction (s -wave collisions) of fermions in different spin states. If the relevant energy scales (recoil energy E_r , temperature T and interaction strength g) are small compared to the band gap, to a good approximation, the fermions are confined to the lowest energy band of the system. This is for instance true for sufficiently deep lattices, where the corresponding fermionic wave function extends only over a few lattice sites. In this situation it is favourable to work in the orthonormal basis of localised Wannier states [104, 105]

$$\Psi_{\sigma}(\mathbf{r}) = \sum_i w_{\sigma}^{(n)}(\mathbf{r} - \mathbf{R}_i) c_{i,n,\sigma}, \quad (2.44)$$

where $c_{i,n,\sigma}$ annihilates a fermion on site i in band n of spin σ . The Wannier functions are constructed from the spin dependent Bloch wave functions as

$$w_{\sigma}^{(n)}(\mathbf{r} - \mathbf{R}_i) = \frac{1}{\sqrt{\Omega}} \sum_{\mathbf{k}} e^{-i\mathbf{k}\cdot\mathbf{R}_i} \phi_{\mathbf{k},\sigma}^{(n)}(\mathbf{r}), \quad (2.45)$$

where Ω is the volume of the system. At low temperatures, we can neglect higher-order energy bands and restrict our discussion to the lowest band $n = 0$. In this approximation we can reduce Eq. 2.43 to the single-band Fermi-Hubbard model with the parameters

2.4 Fermionic Atoms in Optical Lattices

$$J_{i,j} = - \int d^3\mathbf{r} w_\sigma^*(\mathbf{r} - \mathbf{R}_i) \left(-\frac{\hbar^2}{2m} \nabla^2 + V_0(\mathbf{r}) \right) w_\sigma(\mathbf{r} - \mathbf{R}_j), \quad i \neq j \quad (2.46)$$

$$\epsilon_j = \int d^3\mathbf{r} w_\sigma^*(\mathbf{r} - \mathbf{R}_j) \left(-\frac{\hbar^2}{2m} \nabla^2 + V_0(\mathbf{r}) \right) w_\sigma(\mathbf{r} - \mathbf{R}_j) \quad (2.47)$$

$$U_{j,k,l,m} = g \int d^3\mathbf{r} w_\sigma^*(\mathbf{r} - \mathbf{R}_j) w_{\bar{\sigma}}^*(\mathbf{r} - \mathbf{R}_k) w_{\bar{\sigma}}(\mathbf{r} - \mathbf{R}_l) w_\sigma(\mathbf{r} - \mathbf{R}_m). \quad (2.48)$$

Here $V_0(\mathbf{r})$ denotes the optical lattice potential and $\bar{\sigma}$ the opposite spin state to σ . To derive Eq. 2.31, we further assume the tunnelling amplitude between next-nearest neighbours (and further) to be much smaller than the nearest neighbour hopping ($J_{i,j} \neq 0$ only for $i = j \pm 1$), and we neglected all interactions between fermions that are not occupying the same site $U = U_{i,i,i,i}$ [98]. A band structure calculation, as shown in Fig. 2.10, indeed confirms this assertion. We find the tunnelling matrix element to exponentially decrease as a function of hopping distance and lattice depth.

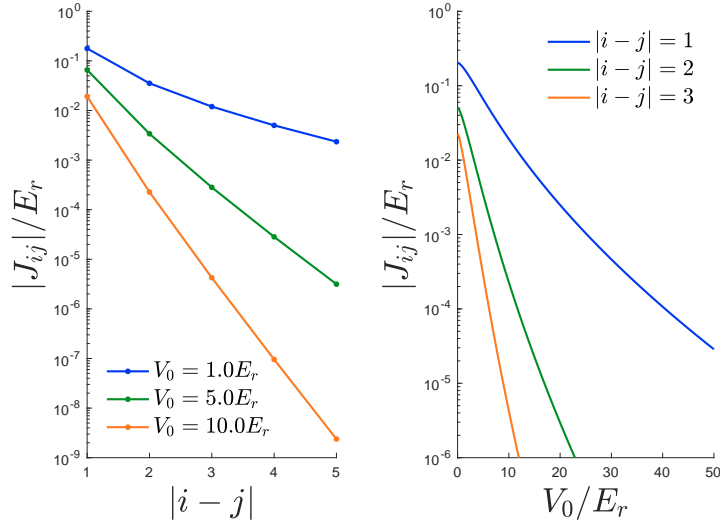


Figure 2.10: Hopping amplitude as a function of distance for three different lattice depths (left). We see that the tunnelling matrix elements exponentially decrease with increasing distance, justifying the nearest-neighbour approximation to derive the Fermi-Hubbard model. The right panel shows the tunnelling matrix element for three different distances as a function of lattice depth V_0/E_r . All calculations were performed for a one-dimensional lattice.

Generically, these integrals have to be solved numerically. For sufficiently deep lattices however, we can approximate the Wannier functions by harmonic oscillator states, which allows for an analytic solution to said integrals [68], giving

$$\frac{J}{E_r} = \frac{4}{\sqrt{\pi}} \left(\frac{V_0}{E_r} \right)^{\frac{3}{4}} e^{-2\sqrt{V_0/E_r}} \quad (2.49)$$

$$\frac{U}{E_r} = \sqrt{\frac{8}{\pi}} ka \left(\frac{V_0}{E_r} \right)^{\frac{3}{4}}. \quad (2.50)$$

For our simulations in this thesis, we will use a finite chain with open boundary conditions. The Fermi gas consists of two internal species which can move on a one-dimensional lattice structure and are attractively interacting. The unperturbed Hamiltonian is given by,

$$H_0 = -J \sum_{i=1, \sigma}^{L-1} (c_{i, \sigma}^\dagger c_{i+1, \sigma} + \text{h.c.}) + U \sum_{i=1}^L n_{i,1} n_{i,2}, \quad (2.51)$$

where $c_{i, \sigma}^{(\dagger)}$ are the fermionic annihilation (creation) operators of spin $\sigma = \{1, 2\}$ on site i , and $n_{i, \sigma}$ the corresponding number operator. J denotes the hopping amplitude, $U < 0$ the attractive on-site interaction, and L the number of lattice sites. The Fermi-Hubbard model in one dimension can be solved *exactly* by Bethe ansatz. We will discuss its ground state phase diagram, together with a brief summary of the Bethe ansatz solution in chapter 3 along with the other numerical and analytical methods used throughout this thesis.

2.5 Radiofrequency Driving of Ultracold Fermions

In chapter 4 we study the collective amplitude excitation of the superconducting order parameter in the BCS-BEC crossover. There we develop a novel approach to excite and detect the amplitude mode of the system, which relies upon the well known method of radiofrequency (rf) spectroscopy [106–114]. We use the rf-transfer to drive far red-detuned transitions between different hyperfine states of the fermionic atoms to couple directly to the superconducting order parameter. Chapter 6 investigates the detailed dynamical response of a strongly correlated fermionic quantum gas in a one-dimensional lattice geometry subject to rf-driving. Finally, in chapter 7 we make use of the coherent transfer of fermions between different hyperfine states, to realise fast, effective interaction quenches in the one-dimensional Fermi-Hubbard model.

In this section we will therefore summarise the rf-spectroscopy background necessary for the following chapters. We start by discussing the basic properties of rf-photons and then detail the theoretical modelling of the rf-driving both in the case of a homogeneous three-dimensional Fermi gas (chapter 4) as well as for a one-dimensional Fermi-Hubbard lattice model (chapters 6 and 7).

2.5.1 Modelling the Radiofrequency Drive

The rf-field couples different hyperfine levels of the atoms and induces transitions between them. Referring back to the hyperfine level structure of ${}^6\text{Li}$, Fig. 2.2, in this thesis we will consider rf-coupling between the second and third lowest hyperfine levels $|2\rangle$ and $|3\rangle$. The wavelength of rf-field is very long ($\lambda \sim 1\text{m}$), so the rf-photon transfers negligible momentum and the transition is ‘vertical’ in momentum space. Furthermore, since the wavelength is large

2.5 Radiofrequency Driving of Ultracold Fermions

compared to the atomic cloud, we can also safely assume that the rf-field couples to the entire cloud equally strongly, i.e. the Rabi frequency associated with the transition is constant throughout the sample, $\Omega_R = q|\mathbf{E}_0|\langle 3|\mathbf{r}|2\rangle$ (matrix element of dipole operator which induces transitions between $|2\rangle$ and $|3\rangle$).

Homogeneous, three-dimensional BCS model for three fermionic species

For the three-state system in chapter 4, by driving Rabi oscillations on the $|2\rangle \rightarrow |3\rangle$ hyperfine transition, we effectively break the Cooper pairs and thereby drive the system out of equilibrium. The interaction within the $|12\rangle = |1\rangle \otimes |2\rangle$ manifold is treated at the mean-field level as outlined before, Eq. 2.22. To add the third state, we include the rf-driving of the form $\Omega(t) = \hbar\Omega_R \cos(\omega_{\text{rf}}t)$. Since momentum is conserved in the transfer, we can model the rf-drive as $H'(t) = \Omega(t) \sum_{\mathbf{k}} (c_{\mathbf{k},3}^\dagger c_{\mathbf{k},2} + \text{h.c.})$. We assume the upper state $|3\rangle$ to be non-interacting, hence the full Hamiltonian describing the system reads $H = H_{\text{BCS}}^{\text{mf}} + H_3 + H'(t)$, where

$$H_3 = \sum_{\mathbf{k}} \left(\epsilon_{\mathbf{k}} + \epsilon_3^0 - \mu_3 \right) n_{\mathbf{k},3}. \quad (2.52)$$

Upon a unitary transformation $|\tilde{\Psi}\rangle = e^{-i\gamma\hat{O}t}|\Psi\rangle$, the effective Hamiltonian, H_{eff} , governing the dynamics of the transformed state is given by,

$$i\hbar \frac{\partial |\tilde{\Psi}\rangle}{\partial t} = \{e^{-i\gamma\hat{O}t} H e^{i\gamma\hat{O}t} + \hbar\gamma\hat{O}\} |\tilde{\Psi}\rangle \equiv H_{\text{eff}} |\tilde{\Psi}\rangle. \quad (2.53)$$

Since, $[H, N_1] = [H, N_2 + N_3] = 0$, choosing $\hbar\gamma\hat{O} = [(\epsilon_2^0 - \mu_2) - (\epsilon_1^0 - \mu_1)]N_1$, and, in a second transformation $\hbar\gamma\hat{O} = -\epsilon_2^0 N$ (where N is the total particle number), allows us to shift the hyperfine levels $|1\rangle$ and $|2\rangle$ on top of each other and move the hyperfine splitting fully into the Hamiltonian describing the upper level. Since initially the upper level is empty, we can take the chemical potential of the upper level to be zero. Furthermore, initially the system is prepared in a balanced mixture of states $|1\rangle$ and $|2\rangle$, and once their populations are set, the net particle number does not change anymore (within the theoretical modelling; there is no decay channel present). In our numerical simulations we therefore initialise our system in the grand canonical ensemble with $\mu_1 = \mu_2 = \mu$ (taking the chemical potential into account to set the correct particle number according to Fig. 2.8). During the evolution however, we describe the dynamics in the canonical ensemble and set $\mu = 0$, therefore the chemical potential does *not* explicitly appear in our equations of motion as we will see later in Eq. 3.3.

In order to eliminate the fast oscillating terms in the driving we evoke the rotating-wave approximation, taking the operator $\gamma\hat{O} = -\omega_{\text{rf}}N_3$. In this case $[\hat{O}, H_{\text{BCS}}^{\text{mf}}] = [\hat{O}, N_{\mathbf{k}\sigma}] = 0$ but importantly the driving term does *not* commute with \hat{O} . Defining the rf-detuning from the atomic resonance to be $\delta = \omega_{\text{rf}} - \omega_a$ with $\hbar\omega_a = \epsilon_3^0 - \mu_3 - \epsilon_2^0 = \epsilon_3^0 - \epsilon_2^0$ ⁵, we find

⁵ $\mu_3 = 0$ at $t = 0$ and remains zero for $t > 0$ since we are driving the system far red-detuned from the resonance so the transfer rate to the upper level is very low.

$$\begin{aligned}
 H_{\text{eff}} &= H_{\text{BCS}}^{\text{mf}} + \sum_{\mathbf{k}} (\epsilon_{\mathbf{k}} + \hbar\omega_a - \hbar\omega_{\text{rf}}) n_{\mathbf{k},3} + \frac{\hbar\Omega_R}{2} [e^{i\omega_{\text{rf}}t} + e^{-i\omega_{\text{rf}}t}] \sum_{\mathbf{k}} \left(e^{-i\gamma t} c_{\mathbf{k},3}^\dagger c_{\mathbf{k},2} + e^{i\gamma t} c_{\mathbf{k},2}^\dagger c_{\mathbf{k},3} \right) \\
 &\approx H_{\text{BCS}}^{\text{mf}}(\mu = 0) + \sum_{\mathbf{k}} (\epsilon_{\mathbf{k}} - \hbar\delta) n_{\mathbf{k},3} + \frac{\hbar\Omega_R}{2} \sum_{\mathbf{k}} \left(c_{\mathbf{k},3}^\dagger c_{\mathbf{k},2} + c_{\mathbf{k},2}^\dagger c_{\mathbf{k},3} \right), \quad (2.54)
 \end{aligned}$$

where in the last line we dropped the fast rotating terms $\sim e^{\pm 2i\omega_{\text{rf}}t}$ ⁶. For notational simplicity we will, in all subsequent chapters, refer to the effective Hamiltonian simply as the Hamiltonian of the system. This concludes our theoretical modelling of the system. The numerical simulation of the model is discussed in section 3.1.

Three-species Fermi-Hubbard model in a one-dimensional lattice geometry

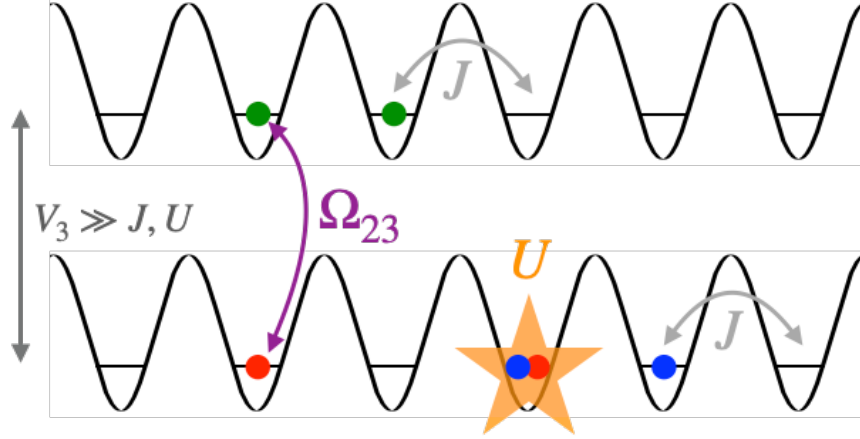


Figure 2.11: Sketch of the underlying Fermi-Hubbard model with the rf-coupling of the different internal (hyperfine) states $\sigma = \{1, 2, 3\}$ (here depicted in blue, red and green respectively). The hopping amplitude J is taken to be the same in the lower and upper bands, and the hyperfine splitting to the final state is denoted by V_3 .

Just as in the homogeneous BCS system, the rf-field induces vertical transitions in momentum space between the different hyperfine levels of the atom. The difference is the presence of an optical lattice, which breaks the translational symmetry of the system such that ‘real’ momentum is no longer a good quantum number and states are instead labelled by their quasi-momentum living in the first Brillouin zone. The attractive, one-dimensional Fermi-Hubbard model was introduced in section 2.4.2 and is sketched in Fig. 2.11 for clarity. We model the rf-coupling as a perturbation $H'(t)$ to the total Hamiltonian of the system (Eq. 2.51), given by

⁶This procedure is commonly known as a rotating-wave approximation.

2.5 Radiofrequency Driving of Ultracold Fermions

$$\begin{aligned}
H'(t) &= \overbrace{\hbar\Omega_{23} \cos(\omega_{\text{rf}}t)}^{\Omega(t)} \sum_{i=1}^L (c_{i,3}^\dagger c_{i,2} + \text{h.c.}) \\
&= \Omega(t) \sum_{m=1}^L (c_{k_m,3}^\dagger c_{k_m,2} + \text{h.c.}), \tag{2.55}
\end{aligned}$$

where Ω_{23} is the Rabi frequency of the transition, ω_{rf} the frequency of the rf-field, and $k_m = \frac{m\pi}{L+1}$ ($m = 1, \dots, L$) the momentum of the particle, where we have used the Fourier transform for open boundary conditions for numerical convenience. We take the third level of the Hamiltonian to be a free band,

$$H_3 = -J \sum_{i=1}^{L-1} (c_{i,3}^\dagger c_{i+1,3} + \text{h.c.}) + V_3 \sum_{i=1}^L n_{i,3}. \tag{2.56}$$

This neglects interactions in the final state, which for many atoms can be dominant. However, e.g. for ${}^6\text{Li}$, any mixture of the lowest three hyperfine states exhibits a broad Feshbach resonance. Choosing the $|13\rangle = |1\rangle \otimes |3\rangle$ manifold as the initial mixture and driving rf-transitions to the initially empty $|2\rangle$ state indeed realises a system with a small scattering length in the final $|12\rangle = |1\rangle \otimes |2\rangle$ state [115], thus the final state interaction is small and we are mainly interested in the dynamics induced by the rf-driving. The energetic splitting V_3 between the state $|2\rangle$ and $|3\rangle$ is usually much larger than the kinetic and interaction energy scales, i.e. $V_3 \gg J, U$. Finally, the full model is given by $H(t) = H_0 + H_3 + H'(t)$. In chapters 6 and 7 we will present results of the quasi-exact solution of the full, interacting many-body problem $H(t)$ using the time-dependent matrix product state algorithm (see section 3.2 for details).

2.5.2 The non-interacting system

In this subsection, we describe the response of a non-interacting Fermi gas to the rf-drive. The BCS Hamiltonian (Eq. 2.54) and the Fermi-Hubbard model (Eqs. 2.51, 2.55, 2.56) become diagonal in momentum space in the absence of interactions.

$$H_{\text{BCS}}(t) \rightarrow \sum_{\mathbf{k}} \left[\epsilon_{\mathbf{k}} (n_{\mathbf{k},1} + n_{\mathbf{k},2}) + (\epsilon_{\mathbf{k}} + \hbar\omega_a) n_{\mathbf{k},3} + \Omega(t) (c_{\mathbf{k},3}^\dagger c_{\mathbf{k},2} + \text{h.c.}) \right] \tag{2.57}$$

$$H_{\text{FH}}(t) \rightarrow \sum_{m=1}^L \left[\epsilon_{\mathbf{k}_m} (n_{k_m,1} + n_{k_m,2}) + (\epsilon_{\mathbf{k}_m} + V_3) n_{k_m,3} + \Omega(t) (c_{k_m,3}^\dagger c_{k_m,2} + \text{h.c.}) \right], \tag{2.58}$$

where $\epsilon_{\mathbf{k}} = \hbar^2 k^2 / (2m)$ for the BCS model, and $\epsilon_{\mathbf{k}} = -2J \cos(k_m a)$ for the Fermi-Hubbard model. We see that the individual momenta fully decouple, and the system can be understood as a series of three-level quantum systems, subject to a periodic drive,

$$H(t) = \sum_k \Psi_k^\dagger \begin{pmatrix} \epsilon_{\mathbf{k}} & 0 & 0 \\ 0 & \epsilon_{\mathbf{k}} & \Omega(t) \\ 0 & \Omega(t) & \epsilon_{\mathbf{k}} + \epsilon_{23} \end{pmatrix} \Psi_k, \quad (2.59)$$

where $\Psi_k^\dagger = (c_{k,1}^\dagger, c_{k,2}^\dagger, c_{k,3}^\dagger)$ ⁷ and $\epsilon_{23} = \hbar\omega_a$ ($\epsilon_{23} = V_3$) for the BCS (Fermi-Hubbard) model. Level $|1\rangle$ is fully decoupled, and the non-trivial dynamics takes place in the two-dimensional $\{|k, 2\rangle, |k, 3\rangle\}$ subspace. The transition is ‘vertical’ in momentum space, as exemplary depicted in Fig. 2.12 for the non-interacting Fermi-Hubbard model dispersion.

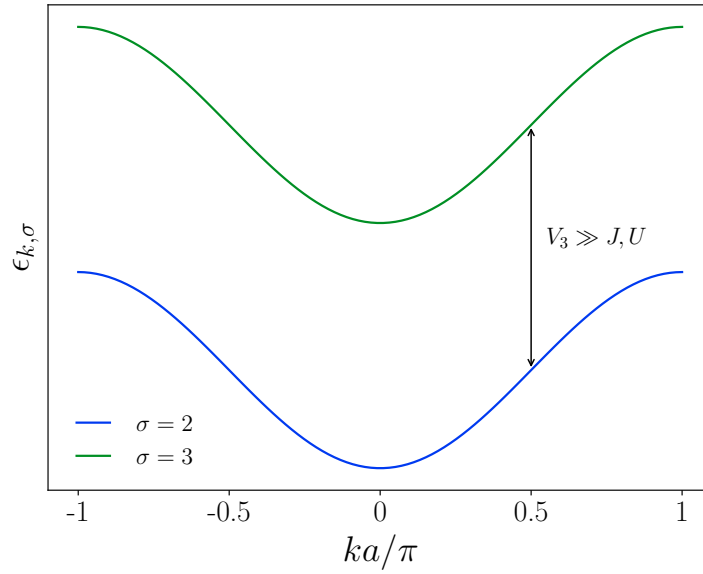


Figure 2.12: The lower and upper bands of the non-interacting system in the $|23\rangle = |2\rangle \otimes |3\rangle$ manifold. The two free bands are separated by the hyperfine splitting $\epsilon_{23} = V_3 \gg J, U$.

Up to overall constant terms, the effective Hamiltonian of this two-level system takes the form $H_{23} = -\frac{1}{2}\epsilon_{23}\sigma_z + \Omega(t)\sigma_x$, which we recognise as the Hamiltonian describing a two-level atom driven by a laser field. Within the rotating-wave approximation, the dynamics can be solved analytically⁸. The drive induces (off)resonant Rabi oscillations given by

$$\langle n_{k,3}(t) \rangle = \frac{\Omega_{23}^2}{\Omega_{\text{eff}}^2} \sin^2\left(\frac{1}{2}\Omega_{\text{eff}}t\right), \quad (2.60)$$

where $\Omega_{\text{eff}} = \sqrt{\Omega_{23}^2 + \delta^2}$ is the generalised, effective Rabi frequency and $\hbar\delta = \hbar\omega_{\text{rf}} - \epsilon_{23}$ the detuning of the rf-field from the bare 2-3 transition. Fig 2.13 shows the evolution of the

⁷To keep the notation as simple as possible, and for this section only, we will label the momentum as k , to mean either \mathbf{k} (BCS) or k_m (Fermi-Hubbard).

⁸One can go beyond the rotating wave approximation, applying Floquet theory to this time-periodic problem. For more details we refer the reader to [116].

2.5 Radiofrequency Driving of Ultracold Fermions

upper level population $\langle n_{k,3}(t) \rangle$ for various detunings. On resonance $\delta = 0$ and the population *coherently* oscillates between the states $\{|k, 2\rangle, |k, 3\rangle\}$. After a time $t = \pi/\Omega_{\text{eff}} = \pi/\Omega_{23}$, for a system initialised in the lower $|2\rangle$ level, the populations are completely reversed and $\langle n_{k,3} \rangle = 1$ (π -pulse). At finite detuning the Rabi oscillations become faster, $\Omega_{\text{eff}} > \Omega_{23}$, albeit with a reduced amplitude. The overall amplitude of the oscillations has a Lorentzian dependence on the detuning, where its width is given by the bare Rabi frequency Ω_{23} of the problem⁹. Finally, it is important to stress the coherent nature of the transfer. Starting initially in the $|k, 2\rangle$ state, the Hamiltonian evolves the system into a coherent *superposition* of states $\psi(t) = \alpha(t)|k, 2\rangle + \beta(t)|k, 3\rangle$ at time t . As we will see in the later part of this thesis (chapters 6 and 7) adding interactions to the system allows for decoherence and dephasing effects, which reduce or even hinder the coherent transfer of particles between the levels.

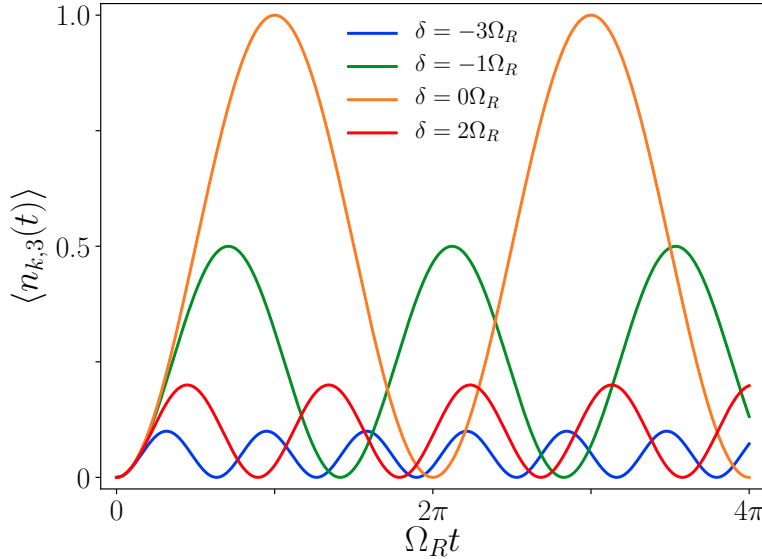


Figure 2.13: Time evolution of the upper level population $\langle n_{k,3}(t) \rangle$. The population undergoes coherent Rabi oscillations. Shown are curves for both red ($\delta < 0$) and blue ($\delta > 0$) detunings. For off-resonant driving, $\delta \neq 0$, we observe an increase in the effective modulation frequency accompanied with a reduction in the amplitude of the oscillations, in accordance with Eq. 2.60.

⁹Note that in section 2.5 we introduced the Rabi frequency as Ω_R (BCS) and Ω_{23} (Fermi-Hubbard). Here we choose the latter notation but the equations hold nonetheless for *both* systems discussed in this thesis.

Chapter 3

Methods

In this chapter we will detail the numerical and analytical methods used throughout this thesis to study the non-equilibrium dynamics of correlated Fermi gases. In section 3.1 we introduce the time-dependent BCS theory and derive its equations of motion. Supplemented by a global self-consistency condition the coupled, non-linear equations of motion are solved with a fourth-order Runge-Kutta method, which allows us to explore the time evolution of the BCS state in chapters 4 and 5. Section 3.2 is devoted to the theoretical background of matrix product state techniques and how they can be used to simulate low-dimensional, interacting quantum many-body systems. We will discuss their range of validity and highlight its algorithmic strength, allowing us access to the quasi-exact time-evolution of driven Hubbard models, as studied in chapters 6 and 7. In these chapters, we study the response of the system to an rf-drive, by monitoring the transfer and population of the final state. Within linear response theory, discussed in section 3.3, the transfer rate to the final state can be related to the spectral function of the correlated, initial state, which we use to gain insight into the underlying excitation spectrum of the Fermi-Hubbard model. Our findings are corroborated by exact results from the Bethe ansatz technique, applied to the attractive Fermi-Hubbard model, which is introduced in section 3.4. While the full theoretical framework of Bethe ansatz technique is not part of this thesis, we will briefly discuss the central ideas and highlight the obtained excitation spectrum, relevant for our analytical understanding of the central results of chapter 6.

3.1 Bardeen-Cooper-Schrieffer Theory away from Equilibrium

We employ an rf-field to drive the BCS state away from equilibrium and study a collective excitation of the system. In this section we want to briefly comment on the numerical simulation of the model. The full Hamiltonian describing the system (including the rf-drive) is given by Eq. 2.54,

$$H = \sum_{\mathbf{k}} \left\{ \epsilon_{\mathbf{k}}(n_{\mathbf{k},1} + n_{\mathbf{k},2}) + \left(\Delta c_{\mathbf{k},1}^{\dagger} c_{-\mathbf{k},2}^{\dagger} + \text{h.c.} \right) + (\epsilon_{\mathbf{k}} - \hbar\delta)n_{\mathbf{k},3} + \frac{\hbar\Omega_R}{2} \left(c_{\mathbf{k},3}^{\dagger} c_{\mathbf{k},2} + \text{h.c.} \right) \right\}. \quad (3.1)$$

The arising equations of motion for this system in the canonical ensemble are obtained

3.1 Bardeen-Cooper-Schrieffer Theory away from Equilibrium

from the Heisenberg equation of motion. In the Heisenberg picture $\hat{O}_H(t) = e^{iHt/\hbar}\hat{O}e^{-iHt/\hbar}$ and the operators' dynamics is governed by

$$\frac{\partial \hat{O}_H}{\partial t} = \frac{i}{\hbar}[H, \hat{O}_H] + \left(\frac{\partial \hat{O}}{\partial t}\right)_H. \quad (3.2)$$

The commutators are readily evaluated and we obtain the following closed set of six coupled differential equations,

$$\begin{aligned} \frac{\partial \langle c_{-\mathbf{k},2} c_{\mathbf{k},1} \rangle}{\partial t} &= \frac{i}{\hbar} \left[-2\epsilon_{\mathbf{k}} \langle c_{-\mathbf{k},2} c_{\mathbf{k},1} \rangle - \frac{\hbar\Omega_R}{2} \langle c_{-\mathbf{k},3} c_{\mathbf{k},1} \rangle + \Delta(n_{\mathbf{k},1} + n_{-\mathbf{k},2} - 1) \right] \\ \frac{\partial \langle c_{-\mathbf{k},3} c_{\mathbf{k},1} \rangle}{\partial t} &= \frac{i}{\hbar} \left[-\frac{\hbar\Omega_R}{2} \langle c_{-\mathbf{k},2} c_{\mathbf{k},1} \rangle - (2\epsilon_{\mathbf{k}} - \hbar\delta) \langle c_{-\mathbf{k},3} c_{\mathbf{k},1} \rangle + \Delta \langle c_{-\mathbf{k},2}^\dagger c_{-\mathbf{k},3} \rangle \right] \\ \frac{\partial \langle c_{-\mathbf{k},2}^\dagger c_{-\mathbf{k},3} \rangle}{\partial t} &= \frac{i}{\hbar} \left[\Delta^* \langle c_{-\mathbf{k},3} c_{\mathbf{k},1} \rangle + \hbar\delta \langle c_{-\mathbf{k},2}^\dagger c_{-\mathbf{k},3} \rangle - \frac{\hbar\Omega_R}{2} (n_{-\mathbf{k},2} - n_{-\mathbf{k},3}) \right] \\ \frac{\partial \langle n_{\mathbf{k},1} \rangle}{\partial t} &= \frac{1}{\hbar} \Im \left[-2\Delta^* \langle c_{-\mathbf{k},2} c_{\mathbf{k},1} \rangle \right] \\ \frac{\partial \langle n_{-\mathbf{k},2} \rangle}{\partial t} &= \frac{1}{\hbar} \Im \left[-2\Delta^* \langle c_{-\mathbf{k},2} c_{\mathbf{k},1} \rangle + \hbar\Omega_R \langle c_{-\mathbf{k},2}^\dagger c_{-\mathbf{k},3} \rangle \right] \\ \frac{\partial \langle n_{-\mathbf{k},3} \rangle}{\partial t} &= \frac{1}{\hbar} \Im \left[-\hbar\Omega_R \langle c_{-\mathbf{k},2}^\dagger c_{-\mathbf{k},3} \rangle \right], \end{aligned} \quad (3.3)$$

supplemented by the self-consistency condition for the superconducting gap,

$$\frac{\Delta}{E_F} = \frac{4}{\pi} \frac{1}{\frac{1}{k_F a} - \frac{2}{\pi} \sqrt{\frac{E_c}{E_F}}} \int_0^{\tilde{k}_c} d\tilde{k} \tilde{k}^2 \Delta_{\tilde{k}}. \quad (3.4)$$

Here $\tilde{k} = |\mathbf{k}|/k_F$, and we imposed an energy cutoff $E_c = \hbar^2 k_c^2 / (2m)$ for the numerical evaluation of the integral. This numerical cutoff on the momentum sums yields a renormalised value of the contact interaction g in terms of the experimentally measurable quantity $1/(k_F a) = (8\pi E_F)/(gk_F^3) + \sqrt{(4E_c)/(\pi^2 E_F)}$ [59]. It is important to point out that in Eq. 3.3, *all* momentum states are coupled implicitly through Δ .

We numerically solve these equations employing a 4th order Runge-Kutta method [117, 118], discretising both time t and momentum \mathbf{k} . We carefully ensure the self-consistency condition at each point in time, and the convergence of the simulation with the time-step dt and the momentum spacing dk . Typical values taken are $dk/k_F = 5 \times 10^{-4}$, $dt = 5 \times 10^{-4} \hbar/E_F$ and the cutoff for the momentum sum is $E_c = 100E_F$. Unless stated otherwise, we run the simulations up to a final time $T = 400\hbar/E_F$ both for chapters 4 and 5.

3.2 Matrix Product State Techniques for one-dimensional Quantum Systems

Here we develop the formalism and theoretical background of matrix product states, which will allow us to simulate low-dimensional many-body quantum systems with remarkable accuracy. Originally formulated by S. R. White as the density matrix renormalisation group (DMRG) to study the static ground state properties of one-dimensional quantum systems [13], understanding its intimate connection to matrix product states (MPS) has led to great progress and a rapid development of the field. With its extension to time-dependent phenomena [14, 15, 119], its versatile nature is highlighted by the breadth of topics investigated using this framework, such as superconductivity and quantum magnetism. The success of the MPS technique and its time-dependent (t-MPS) version lies in the fact, that ground states of one-dimensional local, gapped Hamiltonians obey an *area law* entanglement spectrum [120], and we will see that this implies that they can be efficiently represented using matrix product states. Matrix product states are a certain class of variational quantum states, which can be parameterised efficiently and constitute a smaller sub-manifold of the full Hilbert space. If the targeted quantum state of interest is only moderately entangled upon any bipartition of the system, it can be faithfully represented by a matrix product space using polynomial rather than exponential resource scaling with the system size. This efficient compression scheme makes MPS algorithms so powerful and successful.

In the following we will begin by introducing the basic building blocks of MPS and their corresponding graphical representation, to make the subsequent discussions more transparent. An algorithm to find the ground state of a one-dimensional quantum system is discussed and extensions to obtain the full time evolution are presented. Making use of symmetries of the Hamiltonian will save computational resources and improve run times. Therefore, we conclude this section with a brief outline of how to make use of abelian quantum numbers to speed up the computational protocol. There exist a number of open source tensor network packages to simulate MPS, such as ALPS [121], TeNPy [122], and ITensor [123, 124], where we use the latter library for all our simulations presented in chapters 6 and 7.


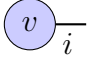
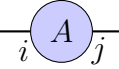
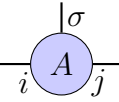
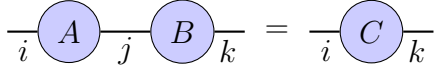
3.2.1 Matrix Product State Formalism and Graphical Representation

Before discussing the matrix product state (MPS) formalism and applying it to study the non-equilibrium dynamics of low-dimensional quantum many-body systems, we begin by introducing a convenient representation of the algebraic building blocks required for the subsequent discussions. Matrix product states are special cases of tree tensor networks. Graphically a tensor network is a collection of vertices (tensors) which are interconnected along their edges (index contraction). Table 3.1 shows the most common building blocks found in a tensor network diagram along with its formal linear algebra operation. Scalars (rank-0 tensors) are represented by circles, vectors (rank-1 tensors) by a circle with a single edge, and a generic rank- n tensor by a circle with n edges (representing its n indices). Index contraction, i.e. the summation over a common index of two tensors is then depicted by connecting the shared edges (indices) of the two tensors graphically as shown in the bottom row of the table. For more complicated diagrams, writing down the mathematical expression quickly becomes very

3.2 Matrix Product State Techniques for one-dimensional Quantum Systems

cumbersome and usually is not very illuminating, so the graphical representation adds clarity and intuition. In the following we will present the idea of tensor network based algorithms and show, where possible, the formal mathematical expression and its graphical representation in parallel to familiarise the reader with the latter.

Table 3.1: Example of common tensor diagram elements.

Diagram	Operation	Equation
	scalar	s
	vector	v_i
	matrix	A_{ij}
	rank-3 tensor	A_{ij}^σ
	matrix multiplication	$\sum_j A_{ij} B_{jk} = C_{ik}$

The great success of matrix-product state methods to solve quantum many-body problems ultimately stems from its clever way of representing the many-body wave function in a highly efficient and compact form. Whilst formally being an exact representation, its power comes from allowing for a very controlled (and usually very accurate) approximation scheme, to reduce the computational effort from exponential to polynomial complexity. Physically this approximation is based upon the intimate connection between the ‘size’ of a matrix product state and the entanglement entropy it can represent¹. There are many great articles on the subject [16, 125–129], and our discussions will loosely follow Schollwöck’s review article [16].

The starting point of our discussion is a one-dimensional quantum system of L sites and local dimension d . The total Hilbert space of the quantum many-body system is $\mathcal{H} = \bigotimes_{i=1}^L \mathcal{H}_i$, where $\dim(\mathcal{H}_i) = d$ and therefore $\dim(\mathcal{H}) = d^L$. Thus the dimension of the Hilbert space grows exponentially with system size, which necessitates an efficient truncation method when trying to numerically study even medium-sized systems. Consider bipartitioning the system into two subsystems A and B . The most general quantum state can then be written as

$$|\psi\rangle = \sum_{i,j} \psi_{i,j} |i\rangle_A \otimes |j\rangle_B, \quad (3.5)$$

¹In the following we will precisely define what exactly is meant by the ‘size’ of an MPS.

3.2.1 Matrix Product State Formalism and Graphical Representation

where $|i\rangle_A$ and $|j\rangle_B$ form an orthonormal basis of subsystem A and B respectively. We can interpret the quantum amplitude $\psi_{i,j}$ as a matrix, which we decompose using a singular-value decomposition (SVD) to find

$$\begin{aligned}
|\psi\rangle &= \sum_{i,j} \psi_{i,j} |i\rangle_A \otimes |j\rangle_B \\
&= \sum_{i,j,\alpha} U_{i,\alpha} S_{\alpha,\alpha} V_{\alpha,j}^\dagger |i\rangle_A \otimes |j\rangle_B \\
&= \sum_{\alpha=1}^r \sqrt{\lambda_\alpha} \left(\sum_i U_{i,\alpha} |i\rangle_A \right) \otimes \left(\sum_j V_{j,\alpha}^* |j\rangle_B \right) \\
&= \sum_{\alpha=1}^r \sqrt{\lambda_\alpha} |\alpha\rangle_A \otimes |\alpha\rangle_B.
\end{aligned} \tag{3.6}$$

Here r is the rank of the matrix $\psi_{i,j}$ (i.e. the number of non-zero singular values λ_α), and S is a diagonal matrix of singular values $\sqrt{\lambda_\alpha}$. Assuming $\psi_{i,j}$ to have the dimensions $(m \times n)$, the matrices U and V^\dagger have dimensions $(m \times p)$ and $(p \times n)$ respectively, where $p = \min(m, n) \geq r$. Furthermore, the two matrices satisfy the unitarity conditions $U^\dagger U = \mathbb{1}$ and $V^\dagger V = \mathbb{1}$. This representation, known as the Schmidt decomposition of the quantum state, is intimately connected to the von-Neumann entropy of the system, an entanglement measure of two subsystems A and B . The entanglement entropy is calculated from the reduced density matrix of one subsystem $\rho_A = \text{tr}_B(|\psi\rangle\langle\psi|)$ as

$$S_{vN} = -\text{tr}(\rho_A \log(\rho_A)) = -\sum_{\alpha=1}^r \lambda_\alpha \log(\lambda_\alpha). \tag{3.7}$$

We thus see that the von-Neumann entanglement entropy is constructed from the non-zero singular values of the original matrix. If we order λ_α in descending order and provided the singular values decay quickly enough, we can approximate the state $|\psi\rangle$ of Eq. 3.6 by a *truncated* state $|\tilde{\psi}\rangle$, where we impose an upper cutoff D on the sum over the singular values. The difference between the original and the truncated state is then given by

$$\| |\psi\rangle - |\tilde{\psi}\rangle \|^2 = 2 \left(1 - \sum_{\alpha=1}^D \lambda_\alpha \right), \tag{3.8}$$

so it is *exact* for $D \geq r$. Since U and V^\dagger are unitary matrices, $\{|\alpha\rangle_A, |\alpha\rangle_B\}$ form another orthonormal set. To construct a matrix product state we apply these ideas now to a generic quantum many-body state

$$|\psi\rangle = \sum_{\{\sigma_i\}} c_{\sigma_1 \dots \sigma_L} |\boldsymbol{\sigma}\rangle. \tag{3.9}$$

3.2 Matrix Product State Techniques for one-dimensional Quantum Systems

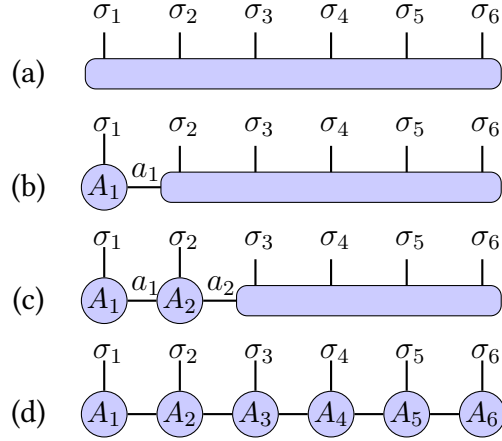


Figure 3.1: Construction of a left-canonical matrix product state by iterative applications of the singular value decomposition (SVD), c.f. Eq. 3.10

The quantum amplitude is a rank- L tensor or equivalently a d^L dimensional vector and $|\sigma\rangle = |\sigma_1 \dots \sigma_L\rangle$. Reshaping it into a (d, d^{L-1}) matrix $c_{(\sigma_1),(\sigma_2 \dots \sigma_L)}$ and applying successive SVDs we obtain

$$\begin{aligned}
 c_{\sigma_1 \dots \sigma_L} &= c_{(\sigma_1),(\sigma_2 \dots \sigma_L)} \\
 &= \sum_{a_1=1}^{r_1} U_{\sigma_1, a_1} S_{a_1, a_1} V_{a_1, (\sigma_2 \dots \sigma_L)}^\dagger \\
 &= \sum_{a_1=1}^{r_1} A_{1, a_1}^{\sigma_1} c_{a_1, (\sigma_2 \dots \sigma_L)} \\
 &= \sum_{a_1=1}^{r_1} A_{1, a_1}^{\sigma_1} c_{(a_1 \sigma_2), (\sigma_3 \dots \sigma_L)} \\
 &= \sum_{a_1=1}^{r_1} \sum_{a_2=1}^{r_2} A_{1, a_1}^{\sigma_1} U_{(a_1 \sigma_2), a_2} S_{a_2, a_2} V_{a_2, (\sigma_3 \dots \sigma_L)}^\dagger \\
 &= \sum_{a_1=1}^{r_1} \sum_{a_2=1}^{r_2} A_{1, a_1}^{\sigma_1} A_{a_1, a_2}^{\sigma_2} c_{(a_2 \sigma_3), (\sigma_4 \dots \sigma_L)} \\
 &= \dots \\
 &= \sum_{\{a_i\}} A_{1, a_1}^{\sigma_1} A_{a_1, a_2}^{\sigma_2} \dots A_{a_{L-2}, a_{L-1}}^{\sigma_{L-1}} A_{a_{L-1}, a_L}^{\sigma_L} .
 \end{aligned} \tag{3.10}$$

We have deconstructed the quantum amplitude into a product over local matrices A^{σ_i} (for $\sigma_i \in \{1, \dots, d\}$). The corresponding graphical representation is shown in Fig. 3.1 for a system of $L = 6$ sites and the generic matrix product state reads

3.2.1 Matrix Product State Formalism and Graphical Representation

$$|\psi\rangle = \sum_{\boldsymbol{\sigma}} A^{\sigma_1} A^{\sigma_2} \dots A^{\sigma_{L-1}} A^{\sigma_L} |\boldsymbol{\sigma}\rangle. \quad (3.11)$$

The dimensions of the local tensors are inherited from the unitaries in the SVD and grow towards the centre of the lattice, after which they start to decrease. Explicitly, for an even number of lattice sites the matrix dimensions evolve as $(1 \times d), (d \times d^2), \dots, (d^{\frac{L}{2}-1} \times d^{\frac{L}{2}}), \dots, (d^2 \times d), (d \times 1)$. It is important to note that at this point we haven't made any approximation, so this representation is *exact*. However this does not help us with overcoming the problem of an exponentially growing Hilbert space dimension, since the local tensors in turn also grow exponentially if we wanted to have an exact representation of any given state. The power of the MPS formulation stems from the fact, that with the matrix dimension of the local tensors A^{σ_i} we have a well controlled handle on the approximation made by truncating the matrices to some finite maximal bond dimension. Physically, as we have seen above, this approximation is well justified for states which have a relatively low entanglement entropy (i.e. the singular values decay sufficiently fast). The truncation error ϵ_i on a given site i measures the quality of this truncation scheme. Referring back to Eq. 3.8, we see that the quality is directly related to the amount of truncated singular values not considered in the approximate wave function. The truncation error is therefore given by

$$\epsilon_i = \sum_{a_i > D} \lambda_{a_i}. \quad (3.12)$$

For typical simulations the global truncation error, i.e. the maximum of $\{\epsilon_i\}$, is kept on the order of 10^{-10} or less.

Finally, since we constructed the local MPS tensors from the matrices U of the SVD they inherit their unitarity property which can be rewritten as

$$U^\dagger U = \mathbb{1} \longrightarrow \sum_{\sigma_k} A^{\sigma_k \dagger} A^{\sigma_k} = \mathbb{1}. \quad (3.13)$$

An MPS whose tensors satisfy this criterion is called 'left-canonical' or 'left-normalised' (in this chapter we will denote a left-canonical MPS by blue vertices, see Fig. 3.1).

Simple Examples of MPS states

To gain some intuition for this construction we briefly want to discuss explicit matrix product state representations for two spins living on two sites ($L = 2$ and $\sigma = \{\uparrow, \downarrow\}$). A basis of the Hilbert space is formed by the triplet and singlet subspaces. Two of the triplet states are simple product states and therefore show no entanglement. Their MPS representation is thus particularly simple and reads $A_1^\uparrow = A_2^\uparrow = 1$ for $|1, 1\rangle = |\uparrow_1, \uparrow_2\rangle$ and $A_1^\downarrow = A_2^\downarrow = 1$ for $|1, -1\rangle = |\downarrow_1, \downarrow_2\rangle$ (the other tensors are all zero). The non-trivial states are the remaining triplet state $|1, 0\rangle = \frac{1}{\sqrt{2}} \left(|\uparrow_1, \downarrow_2\rangle + |\downarrow_1, \uparrow_2\rangle \right)$ which can be encoded using the MPS tensors

3.2 Matrix Product State Techniques for one-dimensional Quantum Systems

$$A_1^\uparrow = \begin{pmatrix} 1 & 0 \end{pmatrix} \qquad A_1^\downarrow = \begin{pmatrix} 0 & 1 \end{pmatrix} \qquad (3.14)$$

$$A_2^\uparrow = \frac{1}{\sqrt{2}} \begin{pmatrix} 0 \\ 1 \end{pmatrix} \qquad A_2^\downarrow = \frac{1}{\sqrt{2}} \begin{pmatrix} 1 \\ 0 \end{pmatrix}. \qquad (3.15)$$

Similarly the singlet state $|0, 0\rangle = \frac{1}{\sqrt{2}}(|\uparrow_1, \downarrow_2\rangle - |\downarrow_1, \uparrow_2\rangle)$ is given by

$$A_1^\uparrow = \begin{pmatrix} 1 & 0 \end{pmatrix} \qquad A_1^\downarrow = \begin{pmatrix} 0 & -1 \end{pmatrix} \qquad (3.16)$$

$$A_2^\uparrow = \frac{1}{\sqrt{2}} \begin{pmatrix} 0 \\ 1 \end{pmatrix} \qquad A_2^\downarrow = \frac{1}{\sqrt{2}} \begin{pmatrix} 1 \\ 0 \end{pmatrix}. \qquad (3.17)$$

We see that if a given state is simply a product state of the two subsystems, there is no entanglement between them, and the only non-zero singular value at the bipartition bond $(i, i + 1)$ is $\lambda_1 = 1$. Consequently the entanglement entropy, Eq. 3.7, is zero. The non-trivial triplet and singlet states however are examples of *maximally* entangled states, since the singular values are all equal, $\lambda_\alpha = \frac{1}{2}$, for $\alpha = \{1, 2\}$, giving a von-Neumann entropy of $S_{vN} = \log(2)$.

Right and Mixed canonical representation

Similarly, building up the MPS from the right,

$$\begin{aligned} c_{\sigma_1 \dots \sigma_L} &= c_{(\sigma_1 \dots \sigma_{L-1}), (\sigma_L)} \\ &= \sum_{b_{L-1}} U_{(\sigma_1 \dots \sigma_{L-1}), b_{L-1}} S_{b_{L-1}, b_{L-1}} V_{b_{L-1}, \sigma_L}^\dagger \\ &= \sum_{b_{L-1}} c_{(\sigma_1 \dots \sigma_{L-2}), (\sigma_{L-1} b_{L-1})} B_{b_{L-1}, 1}^{\sigma_L} \\ &= \sum_{b_{L-1}, b_{L-2}} U_{(\sigma_1 \dots \sigma_{L-2}), b_{L-2}} S_{b_{L-2}, b_{L-2}} V_{b_{L-2}, (\sigma_{L-1} b_{L-1})}^\dagger B_{b_{L-1}, 1}^{\sigma_L} \\ &= \sum_{b_{L-1}, b_{L-2}} c_{(\sigma_1 \dots \sigma_{L-3}), (\sigma_3 b_{L-2})} B_{b_{L-2}, b_{L-1}}^{\sigma_{L-1}} B_{b_{L-1}, 1}^{\sigma_L} \\ &= \dots \\ &= B_{1, b_1}^{\sigma_1} B_{b_1, b_2}^{\sigma_2} \dots B_{b_{L-2}, b_{L-1}}^{\sigma_{L-1}} B_{b_{L-1}, b_L}^{\sigma_L}, \end{aligned} \qquad (3.18)$$

yields a ‘right-canonical’ MPS, as seen in Fig. 3.2 (marked by red vertices). The right-canonical tensors obey the property

$$V^\dagger V = \mathbb{1} \longrightarrow \sum_{\sigma_k} B^{\sigma_k} B^{\sigma_k \dagger} = \mathbb{1}. \qquad (3.19)$$

Hence, the MPS construction is not unique, there exists a gauge freedom in choosing the

3.2.1 Matrix Product State Formalism and Graphical Representation

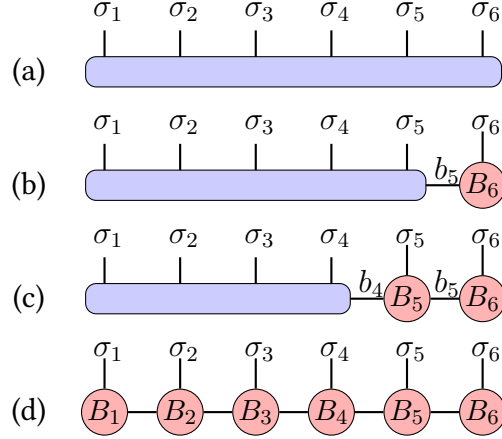


Figure 3.2: Construction of a right-canonical matrix product state by iterative applications of the singular value decomposition (SVD).

matrices M^{σ_i} . Take an invertible matrix X , we can insert XX^{-1} between matrices M^{σ_i} and $M^{\sigma_{i+1}}$ on adjacent sites $(i, i+1)$ in the MPS. Under this transformation the local tensors change as $M^{\sigma_i} \rightarrow M^{\sigma_i} X$ and $M^{\sigma_{i+1}} \rightarrow X^{-1} M^{\sigma_{i+1}}$ and the MPS does not change.

Finally, starting the normalisation procedure from *both* ends of the chain, we obtain a ‘mixed-canonical’ matrix product state

$$|\psi\rangle = \sum_{\boldsymbol{\sigma}} A^{\sigma_1} A^{\sigma_2} \dots A^{\sigma_{l-1}} M^{\sigma_l} B^{\sigma_{l+1}} \dots B^{\sigma_L} |\boldsymbol{\sigma}\rangle, \quad (3.20)$$

which will be extremely useful when computing expectation values of local observables as we will discuss in the following.

Measurements and Matrix Product Operators

The simplest measurement one can perform is a local one. As the name says, the corresponding operator only acts non-trivially on a single site, all other sites are left untouched by it, $\mathcal{O}_l = \sum_{\sigma_l, \sigma'_l} O_{\sigma_l, \sigma'_l} |\sigma_l\rangle \langle \sigma'_l|$. In this case the computation becomes particularly simple, using the *mixed-canonical* MPS representation. Making use of the unitary properties of the left and right canonical tensors, Eq. 3.13 and Eq. 3.19, most tensor contractions resolve in identities and the computation reduces to simple tensor contractions on the corresponding site of the local operator, as exemplified in Fig. 3.3.

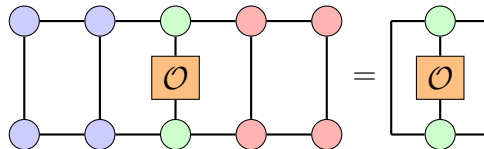


Figure 3.3: Measurement of a local observable for an MPS in the mixed-canonical representation. The blue (red) circles mark left (right) normalised tensors, while the central green tensor is *not* normalised.

3.2 Matrix Product State Techniques for one-dimensional Quantum Systems

A local observable is an example of a one-point measurement. A lot of information about a system can be gained by performing multipoint non-local measurements, the most common of which is the two-point correlator $\langle \mathcal{O}_i \mathcal{O}_j \rangle$. Fig 3.4 shows a generic example of such an operation. It is most convenient to gauge the MPS into mixed-canonical form, such that one can cancel the left- and right-most tensors, due to their unitarity condition, Eq. 3.13 and Eq. 3.19, and we are left with evaluating the reduced MPS diagram involving only all sites between and including the measurement sites.

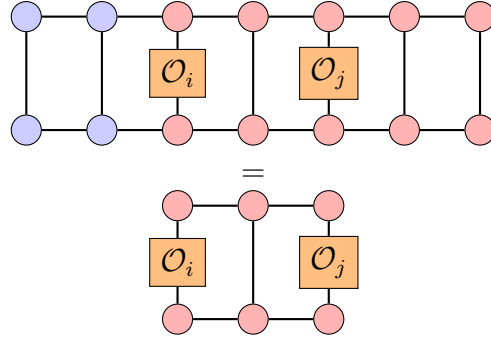


Figure 3.4: Measurement of a non-local two-point correlator in a mixed-canonical representation. The blue (red) circles mark left (right) normalised tensors. The lower diagram is the simplified, reduced measurement operation needed to perform the above correlation measurement.

A general matrix product operator (MPO) can be defined in the same way as we derived the MPS representation for a generic quantum state above, and reads

$$\begin{aligned}
 \mathcal{O} &= \sum_{\{\sigma_i, \tau_i\}} c_{(\sigma_1 \dots \sigma_L), (\tau_1 \dots \tau_L)} |\sigma_1 \dots \sigma_L\rangle \langle \tau_1 \dots \tau_L| \\
 &= \sum_{\{\sigma_i, \tau_i\}} c_{(\sigma_1 \tau_1) \dots (\sigma_L \tau_L)} |\sigma_1 \dots \sigma_L\rangle \langle \tau_1 \dots \tau_L| \\
 &= \sum_{\{\sigma_i, \tau_i\}} W^{\sigma_1, \tau_1} W^{\sigma_2, \tau_2} \dots W^{\sigma_L, \tau_L} |\sigma_1 \dots \sigma_L\rangle \langle \tau_1 \dots \tau_L|. \tag{3.21}
 \end{aligned}$$

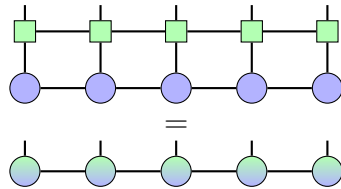


Figure 3.5: Application of a matrix product operator, to a matrix product state.

Applying an MPO, like the Hamiltonian, to an MPS is shown graphically in Fig. 3.5. We have to contract over the physical $\{\sigma_i\}$ indices common to both the MPS and MPO. If we start

with an MPS of a given bond dimension D and an MPO of bond dimension χ , the resulting new MPS will have an increased bond dimensions of χD . In practice the maximal bond dimension is limited by the desired accuracy and a truncation sweep, the successive truncation after each local application of the MPO tensors W^{σ_i, τ_i} , is required to limit the growth of the MPS bond dimension.

3.2.2 Ground State Search

We are now in the position to discuss the application of the MPS formalism to find the ground state of an interacting quantum many-body system. Ground states of one-dimensional, gapped Hamiltonians with local interactions can be efficiently represented by matrix product states, where the bond dimension only grows polynomially with the system size [50, 120]. Fundamentally, the theorem comes from the fact, that these systems obey an *area law* [130]: the entanglement entropy between two subsystems, upon bipartition of the system, is only dependent on the *area* of the boundary between the two subregions, and not - as is usually the case - on the volume of the system (i.e. the total system size). For a one-dimensional system, the boundary of any bipartition is a single bond, and therefore the entanglement entropy is bounded from above by a constant. As we have seen before, the bond dimension is directly related to the amount of entanglement between bipartitions of the system along a bond², which makes the MPS formulation the natural and convenient representation of such low-entangled states, and yields a reduction to polynomial complexity.

In 1992 S. R. White introduced the density matrix renormalisation group (DMRG) method to study the static properties of one-dimensional quantum systems [13], which has become one of the most powerful methods to study correlated lattice systems. Originally formulated as an iterative, variational algorithm on density matrices, it is now understood that matrix product states naturally arise in its formulation and we will present the key ideas in the language of matrix product states for clarity.

To find the ground state of the system we have to minimise the expectation value of the Hamiltonian with respect to the wave function

$$\min \frac{\langle \psi | H | \psi \rangle}{\langle \psi | \psi \rangle} . \quad (3.22)$$

We can rewrite this as a constrained problem by introducing the Lagrange multiplier λ , to ensure the normalisation of the wave function. We are then looking at the optimisation problem

$$\frac{\partial}{\partial \psi} \left\{ \langle \psi | H | \psi \rangle - \lambda (\langle \psi | \psi \rangle - 1) \right\} = 0 . \quad (3.23)$$

This is still a very complicated optimisation, because in principle we have to optimise *all* elements of the tensors at once and as the individual tensor elements appear as products in the

²For maximally entangled subsystems, the singular values are all equal, $\lambda_\alpha = \frac{1}{D}$, such that the von-Neumann entropy is given by $S_{vN} = \log(D)$ or equivalently $D \sim e^{S_{vN}}$, where D is the bond dimension of the MPS/Schmidt decomposition. For $S \sim \text{const.}$, the required bond dimension to represent (in this case) the ground state faithfully, is thus *independent* of system size.

3.2 Matrix Product State Techniques for one-dimensional Quantum Systems

expression this represents a highly non-linear optimisation problem. Instead we fix all but one tensor on a single site. It is then variationally updated and we iteratively move on to the next site. By ‘sweeping’ through the lattice we optimise, one by one, all local tensors in the MPS and gradually approach the minimum of the optimisation problem. This iterative sweeping procedure is at the heart of the original DMRG algorithm. Each local update reduces to an effective eigenvalue equation, given by

$$\frac{\partial \langle \psi | H | \psi \rangle}{\partial M_{a_{l-1}, a_l}^{\sigma_l^*}} \stackrel{!}{=} \lambda \frac{\partial \langle \psi | \psi \rangle}{\partial M_{a_{l-1}, a_l}^{\sigma_l^*}} \quad (3.24)$$

$$\sum_{\sigma'_l} \sum_{a'_{l-1}, a'_l} \sum_{b'_{l-1}, b'_l} L_{b_{l-1}}^{a_{l-1}, a'_{l-1}} W_{b_{l-1}, b'_l}^{\sigma_l, \sigma'_l} R_{b'_l}^{a_l, a'_l} M_{a'_{l-1}, a'_l}^{\sigma'_l} = \lambda M_{a_{l-1}, a_l}^{\sigma_l} \quad (3.25)$$

$$\sum_{\sigma'_l} \sum_{a'_{l-1}, a'_l} H_{(\sigma_l, a_{l-1}, a_l), (\sigma'_l, a'_{l-1}, a'_l)}^{eff} M_{\sigma'_l, a'_{l-1}, a'_l} = \lambda M_{\sigma_l, a_{l-1}, a_l} \quad (3.26)$$

$$H_{eff} \mathbf{v} = \lambda \mathbf{v}, \quad (3.27)$$

where we recognise the last equation as an eigenvalue equation for the reshaped vector $\mathbf{v} = M_{a_{l-1}, a_l}^{\sigma_l}$. The reduction of the optimisation to a local eigenvalue problem is depicted in Fig. 3.6. Here we have graphically represented the left (L) and right (R) tensors, in purple and red colours, and the orthogonality centre (green) is the vector \mathbf{v} . H_{eff} then combines both the left and right tensors and the original Hamiltonian in MPO form. The lowest eigenvalue of Eq. 3.27 is then the current ground state energy estimation at this position in the sweep and the corresponding eigenvalue the update for the local tensor $M_{a_{l-1}, a_l}^{\sigma_l}$. The dimension of the effective Hamiltonian is $(dD^2 \times dD^2)$ which can become large, but since we are usually only interested in the lowest eigenvalue, we can employ an iterative Lanczos-type algorithm to solve the eigenvalue problem and only target the lowest eigenvalue of the spectrum. Once we have updated the local tensor on this given site, we iterate to the next site along and repeat these steps until we have reached the end of the chain. Then we invert the procedure, optimising the tensor on site L and then iterating back to site 1 which then completes one ‘sweep’.

Commonly the MPS is initialised randomly to a fixed bond dimension and the tensors then iteratively updated until e.g. the energy is sufficiently well converged from one sweep to the next (in this work we use an energy convergence threshold of 10^{-9} between consecutive sweeps). The bond dimension of the MPS does not change in this case, which means that, having chosen a bond dimension D , the MPS is searching for the optimal approximation to the ground state within this manifold of all MPS of said bond dimension. This makes the single-site algorithm prone to get stuck in local minima of the constrained problem. This can be remedied by employing a two-site optimisation algorithm. Here, two sites are joined together and optimised in pairs. This comes at the cost of a larger H_{eff} of size $(d^2 D^2 \times d^2 D^2)$. This implies that the updated local tensors on sites $(l, l+1)$ now have an *increased* bond dimension of up to dD , which usually will need to be truncated down to D in a subsequent step. The advantage of this two-site algorithm is, that it allows the bond dimension to grow. Thereby the algo-

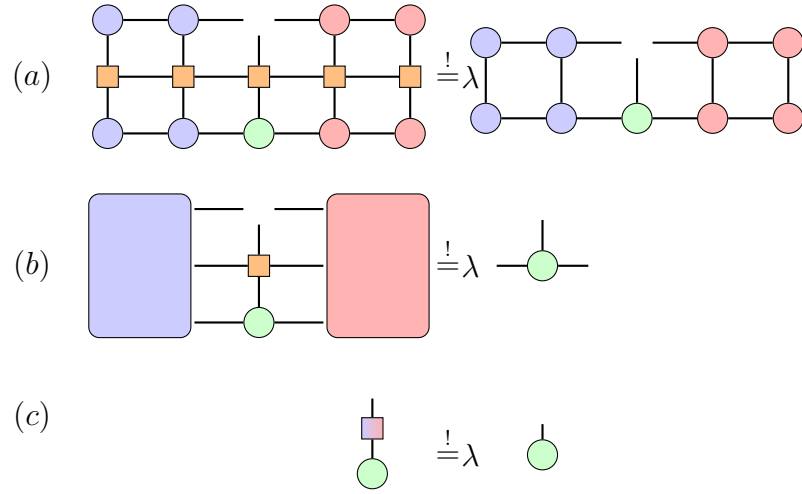


Figure 3.6: Single site optimisation during the ground state search algorithm, which reduces to an effective eigenvalue problem. (a) The original optimisation problem of Eq. 3.24. (b) Constructing the left and right tensors (L and R in blue and red respectively), using the normalisation conditions of left- (blue) and right-canonical (red) tensors, Eq. 3.25. (c) Reshaping the tensor $M_{a_{l-1}, a_l}^{\sigma_l}$ into a vector $\mathbf{v} = M_{\sigma_l, a_{l-1}, a_l}$ and rewriting the optimisation into an effective eigenvalue problem $H_{eff} \mathbf{v} = \lambda \mathbf{v}$, Eqs. 3.26 and 3.27.

rithm searches in the higher-dimensional manifold of MPS states for the optimal MPS to the eigenvalue problem. Despite the increased computational cost, the two-site algorithm usually converges faster, and is less likely to get stuck in a local minimum. It is therefore used throughout this thesis to find the ground state of the interacting Fermi-Hubbard model in chapters 6 and 7.

3.2.3 Time Evolution

If one is interested in the thermal or dynamical properties of a quantum system, one is faced with the challenging task of computing the (imaginary) time-evolution $e^{-iHt/\hbar}$ ($e^{-\beta H}$) of a given initial state $|\psi\rangle$, where the inverse temperature $\beta = \frac{1}{k_B T} = it$ plays to role of imaginary time in quantum statistical mechanics. Exponentiating an exponentially large matrix is clearly unfeasible, so the common method of dealing with such an evolution is to deconstruct the time-evolution operator into smaller, more ‘manageable’ pieces which *can* be implemented numerically via the Trotter-Suzuki decomposition [131–134]. In the following discussion we will restrict ourselves to time-independent Hamiltonians H , but since the wave function is only evolved in small, infinitesimal time steps, time-dependent Hamiltonians (as e.g. considered in chapters 6 and 7) can be modelled by a sequence of Hamiltonians which change from one time-step to the next. The time evolution is then performed using the time-dependent matrix product (t-MPS) approach [14–16, 119].

For systems with sufficiently local iterations, only adjacent sites in the lattice are coupled by bond Hamiltonians h_j acting on sites $(j, j + 1)$, so that the full Hamiltonian of the system is given by

3.2 Matrix Product State Techniques for one-dimensional Quantum Systems

$$H = \sum_j h_j = \underbrace{\sum_{j \text{ odd}} h_j}_{H_{\text{odd}}} + \underbrace{\sum_{j \text{ even}} h_j}_{H_{\text{even}}}, \quad (3.28)$$

where H_{odd} and H_{even} do *not*, but all terms within them respectively do *commute* amongst each other³. We then discretise the time as $t = Ndt$, where N is the number of time-steps required to evolve the system up to the final time t , and $U(t) = e^{-iHt/\hbar} = (e^{-iHdt/\hbar})^N$. The second-order Suzuki-Trotter decomposition for a single-time step reads

$$U(t + dt, t) = e^{-i(H_{\text{odd}} + H_{\text{even}})dt/\hbar} = e^{-iH_{\text{odd}}dt/2\hbar} e^{-iH_{\text{even}}dt/\hbar} e^{-iH_{\text{odd}}dt/2\hbar} + \mathcal{O}(Ldt^3). \quad (3.29)$$

Since the bond Hamiltonians of the same type (*odd* or *even*) commute with each other, the evolution under the odd or even Hamiltonian can be reduced *exactly* to the successive application of two-site evolution gates as $e^{-iH_{\text{odd}}dt/\hbar} = \prod_{j \text{ odd}} e^{-ih_j t/\hbar}$ and $e^{-iH_{\text{even}}dt/\hbar} = \prod_{j \text{ even}} e^{-ih_j t/\hbar}$. The unitary single bond evolution operator for a single time step dt is given by

$$U_j(t) = e^{-ih_j t/\hbar}, \quad (3.30)$$

and is shown graphically in Fig. 3.7. The matrix h_j acting on sites $(j, j + 1)$, and its corresponding unitary evolution operator have dimensions $(d^2 \times d^2)$. For the three-species Fermi-Hubbard model considered in chapters 6 and 7, $d = 8$ and we numerically diagonalise the resulting (64×64) matrix exactly to construct the bond evolution gates. Note that, in the absence of e.g. a trapping potential, we can exploit the translational invariance of the Hamiltonian by only constructing the evolution gates at the edges and a single one for the bulk to reduce the computational cost and memory requirements of the algorithm (since it is the same on all bonds in the bulk of the lattice). For the time-dependent Hamiltonian considered in this thesis, $h_j \rightarrow h_j(t)$, and we need to reconstruct these bond evolution gates at each time-step in the evolution.

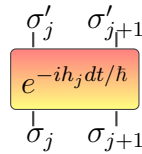


Figure 3.7: Bond evolution operator $U_j(dt)$, where the bond Hamiltonian h_j acts on sites $(j, j + 1)$.

Alternatively to the odd-even splitting of the Hamiltonian, we achieve the same numerical accuracy by the following deconstruction,

³This is in fact not a very big restriction since many paradigmatic, hallmark models of condensed matter physics (e.g. the spin interaction in the Heisenberg model $\mathbf{S}_i \cdot \mathbf{S}_{i+1}$, or the hopping term $\sum_{i,\sigma} (c_{i,\sigma}^\dagger c_{i+1,\sigma} + \text{h.c.})$ in the Hubbard model) fall into this category.

$$\begin{aligned}
U(t + dt, t) &= \prod_{j=1}^{L-1} \left(e^{-ih_j dt/2\hbar} \right) \prod_{j=L-1}^1 \left(e^{-ih_j dt/2\hbar} \right) + \mathcal{O}(Ldt^3) \\
&= \prod_{j=1}^{L-1} U_j(dt/2) \prod_{j=L-1}^1 U_j(dt/2) + \mathcal{O}(Ldt^3). \tag{3.31}
\end{aligned}$$

The entire time evolution for a second-order Suzuki-Trotter decomposition is then reproduced by applying the bond evolution operator on consecutive bonds, followed by a suitable truncation on the bond, and sweeping through the lattice back and forth to complete one time step. This procedure, for a single time step, is shown in Fig. 3.8.

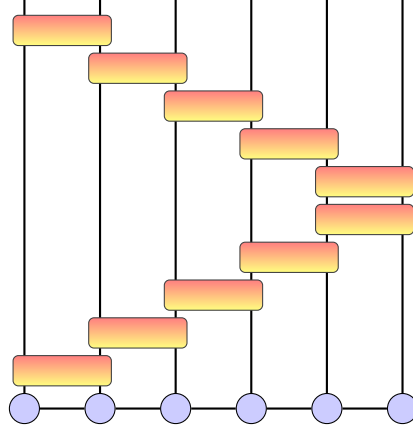


Figure 3.8: The full evolution for one time step $U(t + dt, t)$ deconstructed into its fundamental bond evolution operators $U_j(dt/2)$ for a second order Trotterisation scheme.

The error incurred from choosing a second-order Trotterisation scheme scales as dt^3 per time step, so at the end of the evolution after N time steps the error is linear in time $\sim tdt^2$. To keep the same accuracy but to be able to evolve to a longer time, one would thus expect to simply reduce the time step dt . However, this in turn increases the number gate applications of the bond evolution operator and therefore the total number of truncations. If the evolved wave function $|\psi(t + dt)\rangle$ could be represented with the same accuracy (bond dimension D), this would not be a big problem, but unfortunately this is not the case. Based on the Lieb-Robinson theorem [135], it can be shown that the entanglement growth in a time-evolved quantum system is bounded linearly in time, $S_{vN}(t) \leq S_{vN}(0) + \nu t$, for some constant ν [136, 137]. An MPS with fixed bond dimension D can encode at most an entanglement of $S_{vN} = \log(D)$, which implies that in the worst case, the bond dimension of the MPS has to grow *exponentially* in time, $D \sim e^{S_{vN}}$ [138], to accurately capture the quantum state at time t . Thus there exists an upper cutoff on the possible evolution time beyond which the MPS of a given bond dimension cannot faithfully capture the entanglement of the quantum state $|\psi(t)\rangle$. This upper wall is often large enough, to study the physics of interest, with examples including spin-charge separation [139], the propagation of bosonic correlations in ultracold atom gases [43], or the relaxation of

3.2 Matrix Product State Techniques for one-dimensional Quantum Systems

a density wave in strongly interacting ultracold atoms [42, 140]. Therefore in any simulation *both* convergence parameters, the MPS bond dimension D and the Suzuki-Trotter time step dt , must be chosen carefully to avoid a reduction in net accuracy of the simulation.

3.2.4 Abelian Quantum Numbers

Any MPS simulation can be improved significantly by exploiting the symmetries of the underlying Hamiltonian. If a system is invariant under a particular symmetry transformation, the Hamiltonian commutes with the generator of said symmetry and we can find a common basis to diagonalise both operators. In this new basis, the Hamiltonian is block-diagonal where each block corresponds to a different symmetry sector associated with a unique, conserved quantum number. Examples include the total magnetisation in spin chains, or the total number of particles in Hubbard models (both of these being examples of an abelian $U(1)$ symmetry), or the (non-abelian) spin-rotational $SU(2)$ symmetry of quantum spin systems. Implementing conserved quantum numbers into the algorithm allows the local MPS tensors to be block-sparse which can reduce the computational effort significantly. The ITensor open source libraries [123] provide the necessary quantum number conservation features natively in their implementation. Here we will follow their documentation and explain the encoding of conserved quantum numbers following a concrete example for illustrative purposes.

Consider a spin- $\frac{1}{2}$ system of $L = 4$ sites, described by a Hamiltonian which conserves the overall magnetisation $S^z = \sum_i S_i^z = 0$. Consider further an entangled quantum state

$$|\psi\rangle = \frac{1}{\sqrt{2}} \left(|\uparrow\downarrow\uparrow\downarrow\rangle + i |\downarrow\uparrow\downarrow\uparrow\rangle \right). \quad (3.32)$$

Following the SVD procedure outlined above the local MPS tensors $A^\sigma[i]$ are given by

$$\begin{aligned} A^\uparrow[1] &= \begin{pmatrix} 1 & 0 \end{pmatrix} & A^\downarrow[1] &= \begin{pmatrix} 0 & 1 \end{pmatrix} \\ A^\uparrow[2] &= \begin{pmatrix} 0 & 0 & 1 & 0 \\ -i & 0 & 0 & 0 \end{pmatrix} & A^\downarrow[2] &= \begin{pmatrix} 0 & 1 & 0 & 0 \\ 0 & 0 & 0 & 0 \end{pmatrix} \\ A^\uparrow[3] &= \begin{pmatrix} 0 & 0 \\ 0 & -1 \\ 0 & 0 \\ 0 & 0 \end{pmatrix} & A^\downarrow[3] &= \begin{pmatrix} 1 & 0 \\ 0 & 0 \\ 0 & 0 \\ 0 & 0 \end{pmatrix} \\ A^\uparrow[4] &= \frac{1}{\sqrt{2}} \begin{pmatrix} -1 \\ 0 \end{pmatrix} & A^\downarrow[4] &= \frac{1}{\sqrt{2}} \begin{pmatrix} 0 \\ -1 \end{pmatrix}. \end{aligned} \quad (3.33)$$

Multiplying out these matrices, it is easy to check that we indeed recover the quantum state defined above. However at this level we did not make use of the fact that we *know* that our

quantum state must conserve the total magnetisation and lives in the subspace of the full Hilbert space with quantum number $q = \langle S^z \rangle = 0$. For instance if we try to build up the state $|\psi\rangle$ and have a configuration $|\uparrow\downarrow\uparrow\dots\rangle$, we know with certainty that the spin on the final lattice site must be $|\downarrow\rangle$, else the state would violate our $q = 0$ condition and not be part of the considered subspace. Keeping track of the quantum numbers implies that many elements of our tensors will be identically zero, relieving us of the necessity to store those elements in memory or to iterate over them during tensor contractions.

To keep track of the different quantum numbers in the implementation, we supply our MPS tensors with two additional, symmetry aware quantum labels (an incoming and outgoing one) with the following convention

$$\begin{array}{c} \uparrow q(\sigma_i) \\ \circlearrowleft A[i] \\ \leftarrow q_{i-1} \quad \leftarrow q_i \end{array} = A_{q_{i-1}, q_i}^{\sigma_i}[i]. \quad (3.34)$$

Here a quantum number is assigned to each index and the quantum number ‘flow’ is indicated by the arrows. The incoming quantum number q_i is changed by the state of the local spin on site i by an amount $q(\sigma_i) = \pm 1$ (corresponding to $|\uparrow\rangle$ or $|\downarrow\rangle$ respectively) and results in an outgoing quantum number q_{i-1} (the absolute direction of the arrows is not important to the implementation and we have chosen a formulation that naturally follows from matrix multiplications of linear algebra). The arithmetic for abelian quantum numbers thus reduces to simple addition through the local quantum number fusion rule $q_i - q(\sigma_i) = q_{i-1}$. By convention, we initialise the first quantum number to zero, $q_0 = 0$, and require the final outgoing quantum number of the state to match the overall symmetry sector considered, here $q_4 = q = 0$. It is useful to think of building up the desired quantum state from the final, rightmost tensor, with the overall constraint that we need to end up at a tensor on site $i = 1$ which has as its outgoing quantum number $q_0 = 0$. For the considered system the intermediate quantum numbers are then given by $q_1 = \{1, -1\}$, $q_2 = \{2, 0, -2\}$, and $q_3 = \{1, -1\}$ ⁴. As an example, the tensor on site $i = 2$ decouples into different quantum number sectors and is depicted in Fig. 3.9.

$$\begin{array}{c} q_2 \\ \downarrow \\ A_{q_1, q_2}^{\sigma_2}[2] = q_1 \leftarrow \begin{pmatrix} A_{1,0}^{\sigma_2}[2] & A_{1,2}^{\sigma_2}[2] & A_{1,-2}^{\sigma_2}[2] \\ A_{-1,0}^{\sigma_2}[2] & A_{-1,2}^{\sigma_2}[2] & A_{-1,-2}^{\sigma_2}[2] \end{pmatrix} \end{array}$$

Figure 3.9: For site i we show the block structure of the MPS tensor $A_{q_{i-1}, q_i}^{\sigma_i}[i]$ on site $i = 2$. For the considered system, the quantum numbers at site $i = 1$ and $i = 2$ can take the values $q_1 = \{1, -1\}$ and $q_2 = \{2, 0, -2\}$.

Using this block structure, the only non-trivial tensors that we need to keep track of are

⁴Note that we have neglected the quantum numbers $q_1 = \{3, -3\}$ one *formally* obtains from the fusion rule, but a state with $q_1 = \pm 3$ *cannot* bring us to $q_0 = 0$, therefore these quantum numbers are not compatible with the overall symmetry sector we are considering here.

3.3 Linear Response Theory

$$\begin{aligned}
A_{0,1}^\uparrow[1] &= (1) & A_{0,-1}^\downarrow[1] &= (1) \\
A_{1,2}^\uparrow[2] &= (1) & A_{-1,0}^\uparrow[2] &= (-i \ 0) & A_{1,0}^\downarrow[2] &= (0 \ 1) & A_{-1,-2}^\downarrow[2] &= (1) \\
A_{0,1}^\uparrow[3] &= \begin{pmatrix} 0 \\ -1 \end{pmatrix} & A_{0,-1}^\downarrow[3] &= \begin{pmatrix} 1 \\ 0 \end{pmatrix} \\
A_{-1,0}^\uparrow[4] &= \left(-\frac{1}{\sqrt{2}}\right) & A_{1,0}^\downarrow[4] &= \left(-\frac{1}{\sqrt{2}}\right) .
\end{aligned} \tag{3.35}$$

Note that the $q_2 = 0$ subspace is two-fold degenerate (the states $|\uparrow\downarrow\rangle$ and $|\downarrow\uparrow\rangle$ contributing equally), hence in these cases the tensors are not simply scalar values. Reassembling the tensors of Eq. 3.35 as depicted in Fig. 3.9, we recover the matrices of Eq. 3.33. We thus see very clearly, how the use of conserved quantum numbers reduces the *size* of the underlying tensors in the MPS, at the expense of needing *more* tensors. For small systems this does not necessarily constitute a computational advantage, as the larger number of tensors needs to be constructed and initialised. However, already for very moderate and certainly for large system sizes, the reduction of the size of the tensors will speed up the numerical algorithm and required memory demands significantly⁵.

3.3 Linear Response Theory

In this section we discuss the linear response theory often employed to analyse rf-experiments. In general, an experimental measurement corresponds to computing quantum mechanical expectation values of an interacting many-body system. If we were able to diagonalise the Hamiltonian describing the system, this would not be a challenging task, but this is usually not the case. A generic experiment would subject the system to some external perturbation and measure the response of the system with an appropriate detection scheme. The response will in general be a functional of the exerted generalised ‘force’ on the system, and for a sufficiently weak perturbation, we can hope to compute the response of the system in a perturbation series. Keeping terms to linear order in the perturbation is known as *linear response theory* [141] and will be discussed in the following. Response theory has been successfully applied to radiofrequency spectroscopy experiments in cold atoms [109–114], and in chapter 6 we will employ the formalism to extract the spectral properties of an interacting quantum many-body system from its response to an rf-drive.

We consider the Fermi-Hubbard model introduced in section 2.4, which is additionally coupled to a free upper level via the rf-driving term $H'(t)$, Eq. 2.55. The following derivation is best done in the interaction picture representation, where states and operators transform as

⁵The diagonalisation of a $(N \times N)$ matrix requires $\mathcal{O}(N^3)$ operations, while the diagonalisation of m blocks of size $\frac{N}{m}$ requires only $\mathcal{O}(m(\frac{N}{m})^3) = \mathcal{O}(\frac{N^3}{m^2})$ operations.

$$\begin{aligned}
|\psi_I(t)\rangle &= e^{i(H_0+H_3)t/\hbar}|\psi(t)\rangle \\
\mathcal{O}_I(t) &= e^{i(H_0+H_3)t/\hbar}\mathcal{O}(t)e^{-i(H_0+H_3)t/\hbar},
\end{aligned} \tag{3.36}$$

where $|\psi(t)\rangle$ and $\mathcal{O}(t)$ are the quantum state and the observable in the Schrödinger picture. The full Hamiltonian is given by $H(t) = H_0 + H_3 + H'(t)$, with H_0 and H_3 defined in Eqs. 2.51 and 2.56. In the interaction picture the Schrödinger equation is given by $i\hbar\partial_t|\psi_I(t)\rangle = H'_I(t)|\psi_I(t)\rangle$, i.e. the dynamics is governed by the perturbing Hamiltonian $H'_I(t)$. Its formal integration yields

$$|\psi_I(t)\rangle = |\psi_0\rangle - \frac{i}{\hbar} \int_{-\infty}^t dt' H'_I(t') |\psi_I(t')\rangle, \tag{3.37}$$

where $|\psi_0\rangle$ is the initial ground state of the system. We see that the time evolved state $|\psi_I(t)\rangle$ depends on the state of the system at all previous times $t' \leq t$. We can view this integral equation as a recursion relation for $|\psi_I(t)\rangle$, which upon iteration becomes the Dyson series for the time evolution operator

$$\begin{aligned}
U(t) &= \mathbb{1} - \frac{i}{\hbar} \int_{-\infty}^t dt' H'_I(t') + \left(\frac{-i}{\hbar}\right)^2 \int_{-\infty}^t dt_1 \int_{-\infty}^{t_1} dt_2 H'_I(t_1) H'_I(t_2) + \dots \\
&\equiv \mathcal{T} \exp\left(-\frac{i}{\hbar} \int_{-\infty}^t dt' H'_I(t')\right),
\end{aligned} \tag{3.38}$$

where \mathcal{T} is the time-ordering operator and $|\psi_I(t)\rangle = U(t)|\psi_0\rangle$. We can now use this formal expansion to obtain an expansion for the upper level population in powers of the perturbing Hamiltonian $\langle n_{k,3}^I(t) \rangle = \langle n_{k,3}^I(t) \rangle^{(0)} + \langle n_{k,3}^I(t) \rangle^{(1)} + \langle n_{k,3}^I(t) \rangle^{(2)} + \dots$, whose individual terms can be related to equilibrium expectation values of the unperturbed model⁶. To first-order we obtain

$$\langle n_{k,3}^I(t) \rangle^{(0)} = \langle \psi_0 | n_{k,3} | \psi_0 \rangle = 0 \tag{3.39}$$

$$\langle n_{k,3}^I(t) \rangle^{(1)} = -\frac{i}{\hbar} \int_{-\infty}^t dt' \langle [n_{k,3}^I(t), H'_I(t')] \rangle = 0. \tag{3.40}$$

Both contributions are zero since we start with an initially empty upper level, i.e. $n_{k,3}|\psi_0\rangle = 0$. The first non-zero contribution appears at second-order,

⁶In the following, for notational simplicity we will denote the expectation value with respect to the initial ground state $|\psi_0\rangle$ simply by $\langle \dots \rangle$. The extension to finite-temperature is straightforward. The ground state expectation value becomes a trace over the thermal state $\langle \dots \rangle = \text{tr}(\dots \rho)$, where $\rho = e^{-\beta H}/Z$ is the thermal density matrix of the system, β the inverse temperature, and Z the partition function.

3.3 Linear Response Theory

$$\langle n_{k,3}^I(t) \rangle^{(2)} = \left(-\frac{i}{\hbar} \right)^2 \int_{-\infty}^t dt_1 \int_{-\infty}^{t_1} dt_2 \left\langle \left[\left[n_{k,3}^I(t), H'_I(t_1) \right], H'_I(t_2) \right] \right\rangle. \quad (3.41)$$

It turns out to be algebraically simpler to look at the equivalent first-order response of the transfer rate

$$\dot{n}_{k,3}(t) = -\frac{i}{\hbar} \left[n_{k,3}, H(t) \right] = -\frac{i}{\hbar} \Omega(t) \{ \alpha_k^\dagger - \alpha_k \}, \quad (3.42)$$

with $\alpha_k^\dagger = c_{k,3}^\dagger c_{k,2}$. From Eq. 3.40 we can now compute the first-order response of the momentum-resolved transfer rate

$$\begin{aligned} \langle \dot{n}_{k,3}^I(t) \rangle &= -\frac{i}{\hbar} \int_{-\infty}^t dt' \langle \left[\dot{n}_{k,3}^I(t), H'_I(t') \right] \rangle \\ &= \left(\frac{-i}{\hbar} \right)^2 \Omega(t) \sum_q \int_{-\infty}^{\infty} dt' \Theta(t-t') \Omega(t') \langle \left[\alpha_{k,I}^\dagger - \alpha_{k,I}, \alpha_{q,I}^\dagger + \alpha_{q,I} \right] \rangle \\ &= -\frac{i}{\hbar} \Omega(t) \sum_q \int_{-\infty}^{\infty} dt' \Omega(t') \left\{ \chi_{\alpha_{k,I}^\dagger, \alpha_{q,I}}(t, t') - \text{c.c.} \right\}, \end{aligned} \quad (3.43)$$

where the susceptibility is given by

$$\chi_{\alpha_{k,I}^\dagger, \alpha_{q,I}}(t, t') = -\frac{i}{\hbar} \Theta(t-t') \langle \left[\alpha_{k,I}^\dagger(t), \alpha_{q,I}(t') \right] \rangle. \quad (3.44)$$

Note that the Heaviside function $\Theta(t-t')$ ensures causality, physically expressed by the fact that a response at time t can only have been evoked by a perturbation at an *earlier* time $t' < t$. Since χ is computed in equilibrium, it is invariant under time translations and thus can only depend on the time difference between perturbation and measurement, $\chi(t, t') = \chi(t-t')$. Lastly, the response in the momentum-resolved transfer rate is a convolution of the susceptibility with the coupling strength $\Omega(t')$, so the expression will be diagonal in Fourier space,

$$\begin{aligned} \langle \dot{n}_{k,3}^I(t) \rangle &= \hbar \Omega_{23}^2 \sum_q \left\{ \frac{1 + \cos(2\omega_{\text{rf}}t)}{2} \Im \left[\chi_{\alpha_{k,I}^\dagger, \alpha_{q,I}}(\omega_{\text{rf}}) + \chi_{\alpha_{k,I}^\dagger, \alpha_{q,I}}(-\omega_{\text{rf}}) \right] \right. \\ &\quad \left. - \frac{\sin(2\omega_{\text{rf}}t)}{2} \Re \left[\chi_{\alpha_{k,I}^\dagger, \alpha_{q,I}}(\omega_{\text{rf}}) - \chi_{\alpha_{k,I}^\dagger, \alpha_{q,I}}(-\omega_{\text{rf}}) \right] \right\}. \end{aligned} \quad (3.45)$$

The latter term averages to zero, whereas the former oscillates around 1/2, giving rise to an observable constant background slope in the upper level transfer. We will now look at the susceptibility in more detail. Since the $|12\rangle = |1\rangle \otimes |2\rangle$ and $|3\rangle$ subspaces only couple via the perturbation $H'(t)$ and $[H_0, H_3] = 0$, we choose $|n_{12}\rangle \otimes |m_3\rangle = |n\rangle|m\rangle$ as a valid basis for the

full Hilbert space. Note that $(H_0 + H_3)|\psi_0\rangle = \hbar\omega_0|\psi_0\rangle$ and $\alpha_k|\psi_0\rangle = 0$. Explicitly writing out the time-dependence of the interaction picture we find

$$\begin{aligned}\chi_{\alpha_{k,I}^\dagger, \alpha_{q,I}}(\omega) &= \int_{-\infty}^{\infty} dt e^{i\omega t} \chi_{\alpha_{k,I}^\dagger, \alpha_{q,I}}(t) \\ &= -\frac{i}{\hbar} \int_0^{\infty} dt e^{i\omega t} \langle [\alpha_{k,I}^\dagger(t), \alpha_{q,I}(0)] \rangle \\ &= \frac{i}{\hbar} \int_0^{\infty} dt \sum_{\{n\}} e^{i(\omega + \omega_n + \omega_q - \omega_0)t} |\langle n|c_{q,2}|\psi_0\rangle|^2 \delta_{k,q}.\end{aligned}\quad (3.46)$$

Finally, putting everything together, the rate of particles transferred from $|2\rangle$ to $|3\rangle$ can be related to the single-particle spectral function $A(k, \omega)$, as

$$\langle \dot{n}_{k,3}^I \rangle^{(1)} \sim \frac{\pi \Omega_{23}^2}{2} \left[A(k, \omega_{\text{rf}}) + A(k, -\omega_{\text{rf}}) \right], \quad (3.47)$$

with $A(k, \omega_{\text{rf}}) = \sum_n |\langle n|c_{k,2}|\psi_0\rangle|^2 \delta(\omega_n + \omega_k - \omega_0 - \omega_{\text{rf}})$, $|\psi_0\rangle$ is the initial ground state of the system, and $|n\rangle$, $\hbar\omega_n$ the eigenstates and eigenenergies of H_0 respectively [109]. The upper level $|3\rangle$ is modelled as a free band, $\hbar\omega_k = \epsilon_{\mathbf{k}} + V_3$, with $\epsilon_{\mathbf{k}} = -2J \cos(k)$. The δ -function ensures that excitations are created resonantly: the photon energy of the rf-field, $\hbar\omega_{\text{rf}}$, has to match the energy difference between ground and excited state. Additionally, a transition can only occur if there is a finite matrix element of the perturbing operator $c_{k,2}$ between the initial and final states. The required energy for an excitation is comprised of two parts: the energy of a free particle in the upper band and the energy of an excitation in the lower band, created by the removal of a fermion of species $|2\rangle$. The spectrum of the lower band, the attractively interacting Fermi-Hubbard model, can be obtained analytically from Bethe Ansatz, $\hbar\omega_{\text{rf}} = \hbar(\omega_n - \omega_0) + \hbar\omega_{k,3} = \epsilon_{\text{Bethe}} + \hbar\omega_k$.

Note that the Rabi oscillations of Eq. 2.60 *cannot* be obtained within linear response calculations. Fundamentally, it is the coupling to a continuous band of levels, which makes Rabi oscillations give way to the linear response regime. We expect stronger interactions to increase the level mixing and thus, to make it easier to reach the linear regime. Since the rf-excitation scheme directly couples to both spin and charge degrees of freedom, the transfer is anticipated to be dominated by Rabi oscillations when driving outside of the spin-charge continuum of the final state, whilst sufficient coupling should give rise to a net linear transfer when driving inside the continuum. A detailed analysis of the response of the system in the different driving regimes is given in chapter 6.

3.4 Bethe Ansatz and Exact Solution of the one-dimensional, attractive Fermi-Hubbard Model

The one-dimensional Fermi-Hubbard model H_0 , Eq. 2.51, is integrable and exactly solvable using the nested Bethe Ansatz [142, 143]. Before concluding this chapter, here we briefly review the central results. We will discuss its ground state and the dispersion of different excitations

3.4 Bethe Ansatz and Exact Solution of the one-dimensional, attractive Fermi-Hubbard Model

on top of it, as these will become important in the analysis of the weak rf-drive (c.f. chapter 6). A detailed account of the one-dimensional Fermi-Hubbard model is given by Essler et al. [143] (and references therein) whom we will follow in our discussion here.

Since we study a Fermi-Hubbard model at half-filling in chapter 6 we here consider the same model with N fermions and $N_1 = N_2 = M = N/2$ fermions per spin state and zero chemical potential $\mu = 0$. Then, up to a constant shift in the energy, Eq. 2.51 is equivalent to the Hamiltonian⁷

$$H_0 = - \sum_{j=1}^L \sum_{\sigma} (c_{j,\sigma}^{\dagger} c_{j+1,\sigma} + \text{h.c.}) + 4u \sum_{j=1}^L (n_{j,1} - \frac{1}{2})(n_{j,2} - \frac{1}{2}), \quad (3.48)$$

where we have absorbed the hopping amplitude into the interaction strength and set $4u = U/J$.

Using the Bethe ansatz for the many-body wave function, the solution of the stationary Schrödinger equation can be reduced to a set of coupled, non-linear, algebraic equations which can be solved in the thermodynamic limit. The eigenstates of the attractive Fermi-Hubbard model are parameterised by the roots of these algebraic equations, namely two sets of quantum numbers $\{k_j\}$ and $\{\lambda_m\}$, known as charge momenta and spin rapidities respectively, with energy and momentum,

$$E = -2J \sum_{j=1}^N \cos(k_j), \quad (3.49)$$

$$P = \left(\sum_{j=1}^N k_j \right) \text{ mod } 2\pi, \quad (3.50)$$

where $N = N_1 + N_2 = 2M$ is the total number of fermions. In general (in particular for attractive interactions), the parameters $\{k_j, \lambda_m\}$ are complex and satisfy the Lieb-Wu equations,

$$\begin{aligned} e^{ik_j L} &= \prod_{m=1}^M \frac{\lambda_m - \sin(k_j) - iu}{\lambda_m - \sin(k_j) + iu} \\ \prod_{j=1}^N \frac{\lambda_m - \sin(k_j) - iu}{\lambda_m - \sin(k_j) + iu} &= \prod_{n \neq m}^M \frac{\lambda_m - \lambda_n - 2iu}{\lambda_m - \lambda_n + 2iu}, \end{aligned} \quad (3.51)$$

where $j = \{1, \dots, N\}$ in the first and $m = \{1, \dots, M\}$ in the second line of the Lieb-Wu

⁷For a state with a fixed number of particles $N = N_1 + N_2$, the shift is given by $2uN - uL$. Since the rf-drive effectively probes the single-particle spectral function, we compare an initial state with N fermions to a final state with $N - 1$ fermions. The net shift, as it appears in the linear-response rf-spectrum, is thus given by $\omega_n - \omega_0 \rightarrow (\omega_n + 2u(N - 1) - uL) - (\omega_0 + 2uN - uL) = \omega_n - \omega_0 - 2u$. Therefore to properly compare the results of our t-MPS simulations with the excitation spectrum obtained from Bethe ansatz, we need to shift the Bethe ansatz spectrum by $-2u$.

equations. The roots of these equations encode the complete information about the system.

Generally, for the N -particle case their solution is not explicitly known. However, in the thermodynamic limit only the distribution of these roots in the complex plane is important and the problem becomes tractable, because they arrange themselves into regular ‘string’ patterns in the complex plane. This conjecture, known as the ‘string hypothesis’, was first formulated by Takahashi [144], and leads to Takahashi’s equations, which in the thermodynamic limit become coupled integral equations. For our case of half-filling (and zero magnetic field), the integral equations decouple fully, and one obtains closed-form equations for the elementary spin- and charge-wave excitations

$$\begin{aligned}
\epsilon_{sw}(k) &= 2|u| - 2J \cos(k) + \\
&\quad 2 \int_0^\infty \frac{d\omega}{\omega} \frac{J_1(\omega) \cos(\omega \sin(k)) e^{-\omega|u|}}{\cosh(\omega u)} \\
p_{sw}(k) &= k - \int_0^\infty \frac{d\omega}{\omega} \frac{J_0(\omega) \cos(\omega \sin(k)) e^{-\omega|u|}}{\cosh(\omega u)} \\
\epsilon_{cw}(\lambda) &= 2 \int_0^\infty \frac{d\omega}{\omega} \frac{J_1(\omega) \cos(\omega \lambda)}{\cosh(\omega u)} \\
p_{cw}^p(\lambda) &= \pi - \int_0^\infty \frac{d\omega}{\omega} \frac{J_0(\omega) \sin(\omega \lambda)}{\cosh(\omega u)} = \pi - p_{cw}^h, \tag{3.52}
\end{aligned}$$

where $J_n(\omega)$ are Bessel functions [143]. The spin-wave *only* carries spin 1/2 and corresponds to a spinon, whilst the charge-wave excitations are spinless charge carriers (also known as holons cw_h , and antiholons cw_p).

We solve the above integral equations numerically and the results are depicted in Fig. 3.10 and Fig. 3.11. Here, we show the single and two-particle excitations of the attractive Hubbard model at half-filling for weak and strong attraction respectively. We note that the spin-wave is gapped, while the charge-wave remains gapless as shown in the top panels of the two plots. Physical excitations are constructed from even combinations of elementary excitations, and we find the charge singlet and triplet excitations to be gapless (central panels), while the spin singlet, triplet and the spin-charge continua remain gapped (bottom panels).

Ground state properties of the attractive Hubbard model

At half-filling the ground state of the Hubbard model undergoes a quantum phase transition at $U = 0$, where the system is a Mott insulator for all $U > 0$ and metallic for $U \leq 0$ [143] (and references therein). For half-filling and $U < 0$, conformal field theory and bosonization predict superconducting (SC) and charge density wave (CDW) correlations both to decay algebraically as $|x|^{-\nu}$ ($\nu = 1$), while spin density wave (SDW) correlations are exponentially suppressed (and vice versa for $U > 0$). Below half-filling, SC and CDW decay algebraically, but the SC correlations dominate for attractive interactions [143, 145].

3.4 Bethe Ansatz and Exact Solution of the one-dimensional, attractive Fermi-Hubbard Model

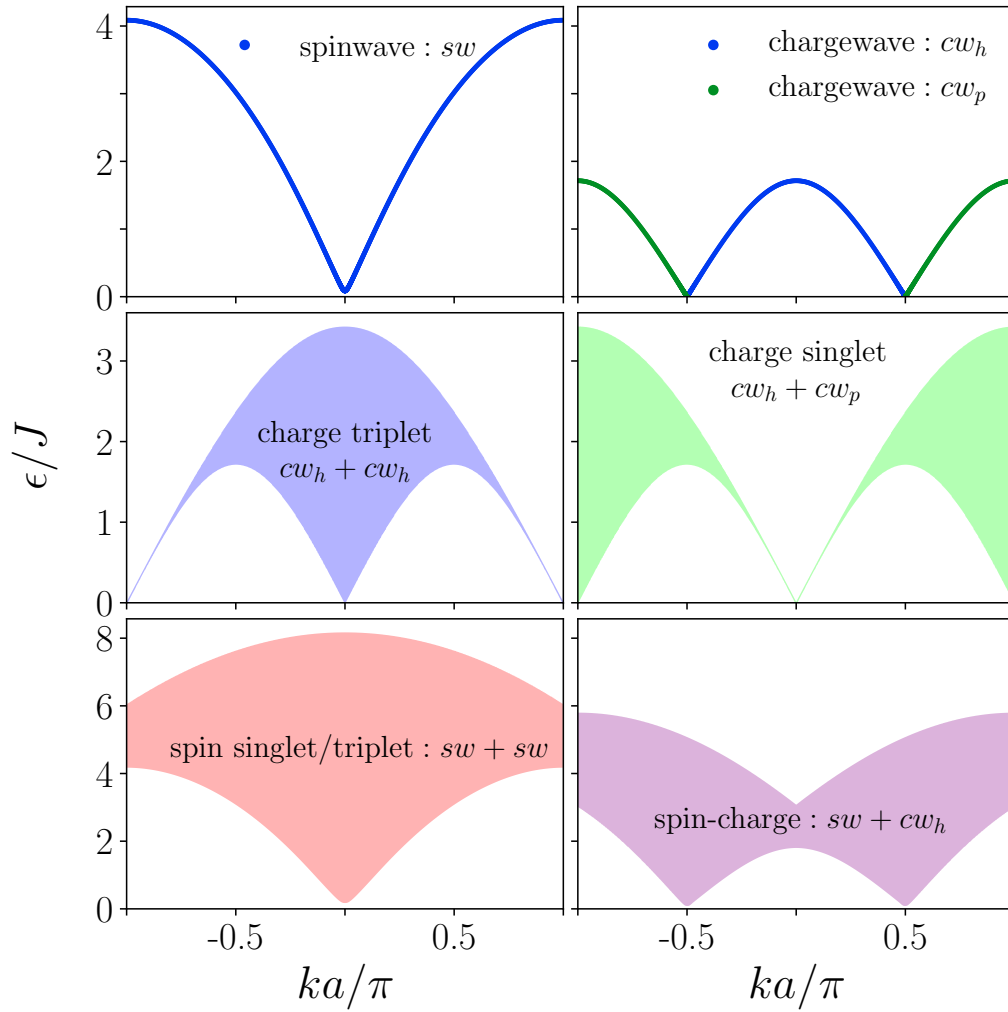


Figure 3.10: Single and two-particle excitation spectrum for the attractive, $U = -2J$, Fermi-Hubbard model. The excitations have charge (charge-wave, cw_h) and spin (spin-wave, sw) character. Physical excitations are constructed from *even* combinations of these elementary excitations, giving rise to singlet, triplet, as well as spin-charge excitation bands.

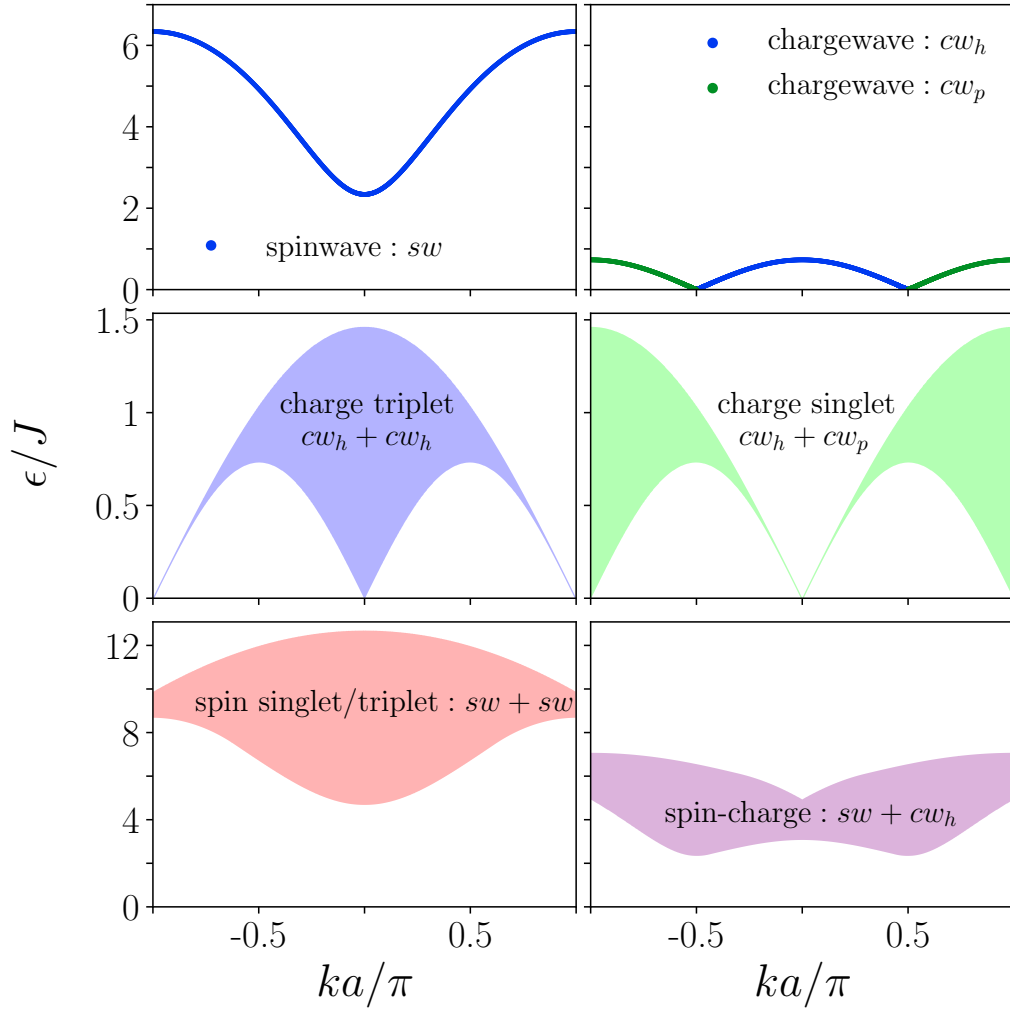


Figure 3.11: Single and two-particle excitation spectrum for the attractive, $U = -8J$, Fermi-Hubbard model. The excitations have charge (charge-wave, cw_h) and spin (spin-wave, sw) character. Physical excitations are constructed from *even* combinations of these elementary excitations, giving rise to singlet and triplet, as well as a spin-charge excitation bands.

Observation of the Higgs Mode in a Strongly Interacting Superfluid

In this work we theoretically investigate the evolution of a three-dimensional Fermi gas in the BCS-BEC crossover. The superfluid can be understood in the framework of spontaneous symmetry breaking and is described by the phenomenological Ginzburg-Landau theory of phase transitions. Upon lowering the temperature of the system below some critical value, the system spontaneously orders into a superfluid or superconducting state with long-range phase coherence, where the order parameter acquires a finite value. The breaking of the underlying $U(1)$ symmetry goes hand in hand with the emergence of long-wavelength Nambu-Goldstone modes [146, 147]. Yet another, gapped, collective excitation of the order parameter exists which is the Higgs mode. Within Ginzburg-Landau theory, Higgs and Nambu-Goldstone modes are possible collective excitations of an order parameter upon spontaneously breaking a continuous symmetry. These collective modes in turn correspond to phase and amplitude oscillations of the order parameter.

In principle they do not need to be independent, and couple so that the Higgs (amplitude) mode rapidly decays into the low-energy Goldstone (phase) mode, unless prevented by additional symmetries of the system. In high energy and particle physics the stability of the Higgs mode is ensured by the Lorentz invariance of the theory, whereas in the condensed matter setting this is effectively achieved by the particle-hole symmetry of the BCS Hamiltonian near the Fermi momentum [148]. The amplitude mode has been observed in various experimental settings including weakly interacting superconductors [149–151], antiferromagnets [152], liquid ^3He [153], ultracold bosonic quantum gases near the superfluid/Mott-insulator transition [154, 155], spinor Bose gases [156], and Bose gases strongly coupled to optical fields [157].

Here we propose a novel time-dependent excitation mechanism, based on radiofrequency modulation of the effective underlying interaction, to activate the Higgs mode in an interacting Fermi gas. By a direct reduction of the superconducting order parameter Δ through pair breaking, the drive directly couples to Δ and activates the Higgs mode, which we identified as the stable, momentum-independent, and collective oscillation of the amplitude of the Cooper pairs. Theoretically we simulate the system using the mean-field BCS model, explicitly including the

time-dependent drive to a third level in our description.

Our proposal has been experimentally realised in [56] and we compare our theoretical to the experimentally measured results. In the experiment, an excitation resonance at the Higgs' characteristic frequency was observed, as well as its broadening and eventual disappearance when the Cooper pairs turn into tightly bound molecules on the BEC side of the Feshbach resonance.

This work was done in collaboration with the experimental group on Michael Köhl in Bonn, who conducted the experiment and where we performed the theoretical modelling and numerical simulations of the system. The results of this chapter, together with the experimental investigation, are published in [56], which we will follow in our subsequent presentation.

4.1 Ginzburg-Landau Theory and the Anderson-Higgs Mechanism

An early, comprehensive theory describing superfluids and superconductors was presented by Ginzburg and Landau in their seminal work of 1950 [158]. It is a phenomenological theory, based upon Landau's theory of second-order phase transitions. They argued that the free energy of the superconductor near the transition temperature can be expressed in terms of a complex order parameter Δ . It is constructed in such a way that it is zero in the high temperature, disordered phase and non-zero in the superconducting state. The microscopic BCS theory of superconductivity, as detailed in section 2.3, was published in 1957 and it did not take long until Gor'kov derived the Ginzburg-Landau Lagrangian from BCS theory in the static, low energy limit in 1959 [159]. Here we want to review the key ideas of the *time-dependent* Ginzburg-Landau theory, necessary to treat dynamical properties, in particular the collective excitations occurring in the superconducting state. Our derivation of the equations of motion for the (gaussian) amplitude and phase fluctuations will follow the review of Pekker and Varma closely [160].

We start with the action given by,

$$S = \int dt d^3\mathbf{r} \mathcal{L} , \quad (4.1)$$

with $\mathcal{L} = \mathcal{L}_{static} + \mathcal{L}_{dynamic}$ being the Lagrangian density, comprised of a static and dynamic term given by

$$\mathcal{L}_{static} = -r|\Delta|^2 + \frac{u}{2}|\Delta|^4 + \xi^2(\nabla\Delta^*)(\nabla\Delta) \quad (4.2)$$

$$\mathcal{L}_{dynamic} = iK_1\Delta^*(\partial_t\Delta) - K_2(\partial_t\Delta^*)(\partial_t\Delta) . \quad (4.3)$$

r , u , and ξ are phenomenological parameters, which have been derived from the microscopic theory in the static, long-wavelength limit [159]. In the low-temperature limit we ignore energy dissipation in the degrees of freedom of Δ , which means our theory must be time-reversal invariant. The first two terms respecting this symmetry are the K_1 and K_2 terms in $\mathcal{L}_{dynamic}$. Their importance will become clear in the subsequent discussion, but we note here, that the K_1 term breaks Lorentz-invariance (space and time derivatives are not treated on an equal footing).

4.1 Ginzburg-Landau Theory and the Anderson-Higgs Mechanism

It is worth mentioning that while the Schrödinger equation is not Lorentz invariant, particle-hole symmetry around the Fermi momentum of a superfluid/superconductor acts as an effective Lorentz symmetry since it requires the equations of motion to be symmetric under conjugation, implying $K_1 \rightarrow 0$ [160].

Static, equilibrium solution

In the static ($\partial_t \Delta = 0$) limit in equilibrium we assume the order parameter $\Delta(\mathbf{r}, t) = \Delta$ to be time independent and homogeneous in space ($\nabla \Delta = 0$), which reduces the action to

$$S = \int dt d^3 \mathbf{r} \left[-r|\Delta|^2 + \frac{u}{2}|\Delta|^4 \right], \quad (4.4)$$

On physical grounds we require $u > 0$ (the energy must be bounded from below) and for low temperatures $T < T_c$ the system is in the ordered phase, i.e. $r > 0$. The ground state configuration is the stationary point of the action, i.e. we look for $\delta S = 0$ and find

$$\frac{\partial S}{\partial \Delta^*} = \int dt d^3 \mathbf{r} \left[-r\Delta + u|\Delta|^2 \Delta \right] = 0. \quad (4.5)$$

Besides the trivial solution $\Delta = 0$, we find $|\Delta|^2 = \Delta_0^2 = \frac{r}{u}$. A finite order parameter implies that the system has undergone a phase transition into the ordered phase of lower symmetry. In doing so it broke the original (global) $U(1)$ symmetry of the system (here by choosing Δ_0 to be real, i.e. of zero phase) spontaneously.

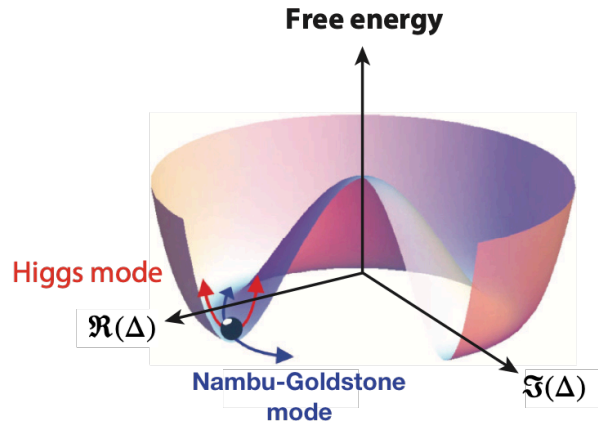


Figure 4.1: Mexican hat potential of the free energy as a function of $\Re(\Delta)$ and $\Im(\Delta)$. Blue and red arrows mark the collective phase and amplitude fluctuations (Nambu-Goldstone and Higgs mode) of the theory. Adapted with permission, conveyed through Copyright Clearance Center Inc., from [161].

The potential corresponding to Eq. 4.5 is shown in Fig. 4.1. We can see that by perturbing the system away from its ground state, we can excite two distinct collective modes of the system. The Nambu-Goldstone mode (phase fluctuations of the order parameter) accompanying the spontaneous symmetry breaking of a continuous symmetry [146, 147], and radial amplitude oscillations, the Higgs mode [162].

Fluctuations of the order parameter

In order to study fluctuations of the order parameter, we reinstall the gradient and dynamic terms to the Lagrangian and expand the order parameter around its ground state equilibrium value, $\Delta = \Delta_0 \rightarrow [\Delta_0 + \eta(\mathbf{r}, t)]e^{i\phi(\mathbf{r}, t)} \approx \Delta_0 + \eta(\mathbf{r}, t) + i\Delta_0\phi(\mathbf{r}, t) + \dots \equiv \Delta_0 + \delta_a + i\delta_p + \dots$. Integration by parts gives,

$$S = \int dt d^3\mathbf{r} \left[iK_1\Delta^*(\partial_t\Delta) + K_2\Delta^*(\partial_t^2\Delta) - r|\Delta|^2 + \frac{u}{2}|\Delta|^4 - \xi^2\Delta^*(\nabla^2\Delta) \right]. \quad (4.6)$$

The equations of motion are obtained by setting $\frac{\partial S}{\partial \Delta^*} = 0$, giving

$$\left[iK_1\partial_t + K_2\partial_t^2 - r + u|\Delta|^2 - \xi^2\nabla^2 \right] \Delta = 0. \quad (4.7)$$

Again there exists the trivial solution of vanishing order parameter $\Delta = 0$. Expanding around the static equilibrium $\Delta = \Delta_0 + \delta_a + i\delta_p$, using $u\Delta_0^2 = r$, we find

$$\underbrace{(-K_1\partial_t\delta_p + K_2\partial_t^2\delta_a - \xi^2\nabla^2\delta_a + 2r\delta_a)}_{\Re} + i \underbrace{(K_1\partial_t\delta_a + K_2\partial_t^2\delta_p - \xi^2\nabla^2\delta_p)}_{\Im} + \mathcal{O}(\delta^2) = 0. \quad (4.8)$$

Since δ_a, δ_p are real-valued functions, we can look at the real (\Re) and imaginary (\Im) part of the above equation separately. Going to Fourier space via

$$\delta(\mathbf{r}, t) = \int \frac{d^3\mathbf{k}}{(2\pi)^3} \int \frac{d\omega}{2\pi} e^{i(\mathbf{k}\cdot\mathbf{r} - \omega t)} \delta(\mathbf{k}, \omega), \quad (4.9)$$

we finally obtain

$$\begin{pmatrix} 2r + k^2\xi^2 - \omega^2K_2 & i\omega K_1 \\ -i\omega K_1 & k^2\xi^2 - \omega^2K_2 \end{pmatrix} \begin{pmatrix} \delta_a \\ \delta_p \end{pmatrix} = \begin{pmatrix} 0 \\ 0 \end{pmatrix}. \quad (4.10)$$

We now see that the K_1 term (which breaks Lorentz invariance and gives rise to a time-dependence as in the Schrödinger equation) in fact *couples* the amplitude and phase fluctuations. For the Schrödinger theory, $K_2 = 0$, the roots of the secular equation Eq. 4.10 are given by $\omega^2 = (\frac{k\xi}{K_1})^2(2r + k^2\xi^2) \rightarrow \frac{2r}{K_1^2}(k\xi)^2$ at long wavelengths. These are the degenerate Bogoliubov modes of the system, where phase and amplitude fluctuations are coupled [160]. Retaining only the Lorentz invariant theory¹ (space and time derivatives are treated on an equal footing, i.e. $K_1 = 0, K_2 \neq 0$), the modes decouple. We find a gapless Bogoliubov (phase) mode with a dispersion $\omega^2 = \xi^2k^2/K_2$, the Nambu-Goldstone mode, and a *gapped* amplitude mode with $\omega^2 = 2r/K_2$ for $k \rightarrow 0$. If the system is approximately particle-hole symmetric and we retain both time derivatives, the modes couple and the massive ‘Higgs’ can decay to massless ‘Gold-

¹Particle-hole symmetry in the present context requires the equations of motion to be invariant under conjugation.

4.3 Calibration Procedure

stone' modes². In general the phase fluctuations remain gapless, whilst the amplitude mode is gapped (albeit at higher energies) with $\omega = \frac{1}{K_2} \sqrt{K_1^2 + 2K_2 r}$ for $k = 0$ [160]. Importantly, we see that the Higgs mode can be described within the time-dependent Ginzburg-Landau theory and as such is also visible in the time-dependent, mean-field BCS method used in this work.

4.2 Exciting the Higgs Mode

When investigating the Higgs mode in a superfluid system we have to address two key questions. How can one couple to the Higgs mode and excite it? And, once excited, how is it detected? We answer both of these questions in our work as described in detail in the following sections. The excitation of the Higgs mode requires a scheme that couples as directly as possible to the amplitude of the order parameter, rather than creating phase fluctuations (Nambu-Goldstone modes) or strong single-particle excitations.

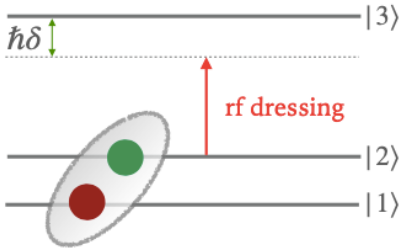


Figure 4.2: We employ rf-dressing of the paired superfluid by off-resonantly coupling to an unoccupied level $|3\rangle$

Previous theoretical proposals for exciting the Higgs mode in ultracold Fermi gases have focussed on a modulation of the interaction parameter $1/(k_F a)$ [163–165]; however, experimentally only single-particle excitations have been observed from such a modulation [166]. The key idea regarding the first question on how to couple to the superconducting order parameter *directly* relies upon reducing $|\Delta|$ through pair breaking. Here we developed a novel radiofrequency (rf) excitation scheme to achieve this. By dressing $|2\rangle$ with the initially empty level $|3\rangle$, we directly affect the pair coherence $\Delta_{\mathbf{k}}$, and modulate the pairing Δ between states $|1\rangle$ and $|2\rangle$ (see Fig. 4.2).

Experimentally, previous rf-spectroscopy studies on ultracold quantum gases have focussed on the single-particle excitations [59, 85, 106, 167]. With short rf-pulse durations $\tau < 1/\Omega_R$, the experiments were performed in the weak-coupling limit and could be interpreted in the linear response framework using Fermi's golden rule. Our proposal on the other hand operates in the long-pulse regime $\Omega_R \tau \gg 1$, and we use a far red-detuned rf-drive to diminish the coupling to single-particle excitations. To start with, for a non-interacting system we have seen that the rf-coupling gives rise to Rabi oscillations in the population of $|2\rangle$ and $|3\rangle$ as $\langle n_{k,3}(t) \rangle = \frac{\Omega_R^2}{\Omega_{\text{eff}}^2} \sin^2(\frac{1}{2}\Omega_{\text{eff}} t)$ (see section 2.5.2 for details).

4.3 Calibration Procedure

Before we discuss the results of our numerical simulations of the driven BCS model, Eq. 3.3, we need to briefly explain how the simulational parameters are chosen, in particular in connection to the experiments performed in the group of Michael Köhl, discussed in section 4.5.

²Since for $K_1 \neq 0$ the two modes couple, amplitude and phase excitations are not distinct and one cannot strictly talk about a 'Higgs' and 'Goldstone' mode in an exact sense.

Experimentally the system is initialised as a balanced superfluid in the lowest two states of the hyperfine manifold of the atoms. The interaction between the two hyperfine states is tuned with a Feshbach resonance, parameterised by their mutual s -wave scattering length, as shown in Fig. 2.3. This defines the dimensionless interaction parameter $1/(k_F a)$ which we use to initialise our simulations³.

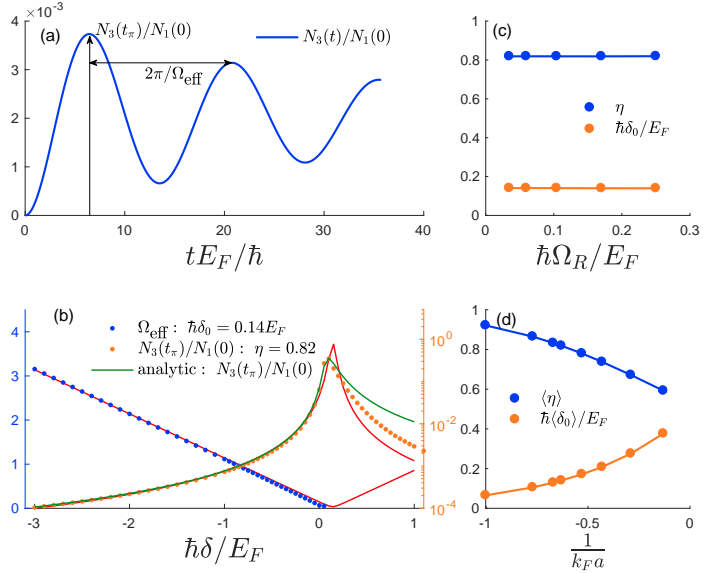


Figure 4.3: The four steps to obtain the full calibration of the model parameters. (a) shows a characteristic curve ($\frac{1}{k_F a} = -0.6305$, $\hbar\Omega_R = 0.0347E_F$, $\hbar\delta = -0.3500E_F$) of the population of $|3\rangle$ divided by the initial occupation of $|1\rangle$, $N_3(t)/N_1(0)$, which yields the effective modulation frequency Ω_{eff} and the peak transfer $N_3(t_\pi)$ (indicated by the black arrows). (b) shows the fits of (4.11) and (4.12) (red lines) to the numerical data (blue and orange dots), giving $\hbar\delta_0 = 0.1406E_F$ and $\eta = 0.8186$. The green line shows the analytic calculation of the spectrum using ansatz 4.16, which gives good agreement on the red-detuned side of the resonance. (c) The procedure is repeated for several Rabi frequencies. Their mean value, $\hbar\langle\delta_0\rangle/E_F$ and $\langle\eta\rangle$ are plotted as a function of interaction strength in (d).

The key insight into the problem of how to directly couple to the superconducting order parameter of the superfluid, is the use of an additional hyperfine level to break Cooper pairs through an rf-transfer scheme. For the present investigation it is crucial that we do *not* perturb the system much, i.e. the upper level population $N_3(t)$ should remain small throughout the entire simulation. In the experiment this is achieved by independently adjusting the power and modulation frequency of the rf-antenna, which translates into the tuning of the Rabi frequency (Ω_R) and detuning (δ) in our theoretical model. By varying these simulation parameters, we are able to modify the maximal upper level population α and the effective modulation frequency Ω_{eff} .

The calibration process is easiest explained by going through the different steps as depicted

³The gap and chemical potential are uniquely defined as depicted in Fig. 2.8, and all necessary correlators can be written in terms of the Bogoliubov amplitudes $u_{\mathbf{k}}$ and $v_{\mathbf{k}}$.

4.4 Activation of the Higgs

in Fig. 4.3. Panel (a) shows the initial brief evolution of the upper level population $N_3(t)$ for typical values of detuning and Rabi frequency. The evolution exhibits a damped oscillatory behaviour, reminiscent of the Rabi oscillations discussed in section 2.5.2. From the evolution we derive the effective modulation frequency and maximal transfer as indicated by the black arrows. We extract the first peak (maximal transfer) as $\alpha = N_3(t_\pi)/N_1(0)$. Since the oscillations are quite stable, we take the time separation T between the first and second peak in the evolution to define the effective modulation frequency as $\Omega_{\text{eff}} = 2\pi/T$. We plot these (orange and blue dots) as a function of detuning (keeping the Rabi frequency fixed) in (b), and fit the following functional form to them

$$\Omega_{\text{eff}} = \sqrt{\Omega_R^2 + (\delta - \delta_0)^2} \quad (4.11)$$

$$\frac{N_3(t_\pi)}{N_1(0)} = \eta \frac{\Omega_R^2}{\Omega_R^2 + (\delta - \delta_0)^2}. \quad (4.12)$$

Since the interacting Fermi gas is an interacting many-body problem, the fitting parameters δ_0 and η account for resonance shifts and imperfect transfer as seen in the evolution of N_3 . In the weak coupling limit the fitting functions of Eq. 4.12 go over into the non-interacting Lorentzian distribution for the maximal transfer as $(\delta_0, \eta) \rightarrow (0, 1)$. Repeating this analysis for several Rabi frequencies Ω_R , gives us the behaviour of the fitting parameters as the coupling strength between $|2\rangle$ and $|3\rangle$ is varied (c). For modest interactions strengths in the BCS regime we find them to be independent of Ω_R , and will henceforth replace them by their average value $\{\delta_0(\Omega_R), \eta(\Omega_R)\} \rightarrow \{\langle\delta_0\rangle, \langle\eta\rangle\}$. Finally, in (d) we show $\langle\delta_0\rangle$ and $\langle\eta\rangle$ as a function of interaction strength $1/(k_F a)$.

We are now in the position to construct the appropriate simulation parameters (δ and Ω_R) from the experimentally relevant parameters (α and Ω_{eff}). Inverting Eq. 4.12 we find, $\Omega_{\text{eff}} = \sqrt{\frac{\eta}{\alpha}}\Omega_R$ and $\delta = \delta_0 - \sqrt{\frac{\eta - \alpha}{\alpha}}\Omega_R$. We can thus choose the effective modulation frequency and population transfer independently.

4.4 Activation of the Higgs

In the BCS regime, a continuum of quasiparticle excitations, $E_{\mathbf{k}}$, exists above the threshold of the superconducting order parameter Δ . In this limit the rf-excitation scheme can be approximated by coupling each occupied BCS quasiparticle momentum state to the corresponding momentum state $|k, 3\rangle$ (since the rf-dressing transfers negligible momentum). Thus a modified effective two-level picture emerges where the two levels are coupled by an effective Rabi frequency $\Omega'_{R,\mathbf{k}} = \sqrt{\Omega_R^2 + \delta_{\mathbf{k}}^2}$, and the excitation probability becomes momentum dependent through the many-body detuning $\hbar\delta_{\mathbf{k}} = \hbar\delta - E_{\mathbf{k}} - \xi_{\mathbf{k}}$, as shown schematically in Fig. 4.4

As detailed in section 3.1, we numerically solve the equations of motion, Eq. 3.3, and investigate the response of the superfluid order parameter subject to the red-detuned rf-drive. Our rf excitation scheme avoids resonant coupling to the single-particle excitations, and only off-resonantly modulates the occupation of the excited states as shown in Fig. 4.5 (top panel,

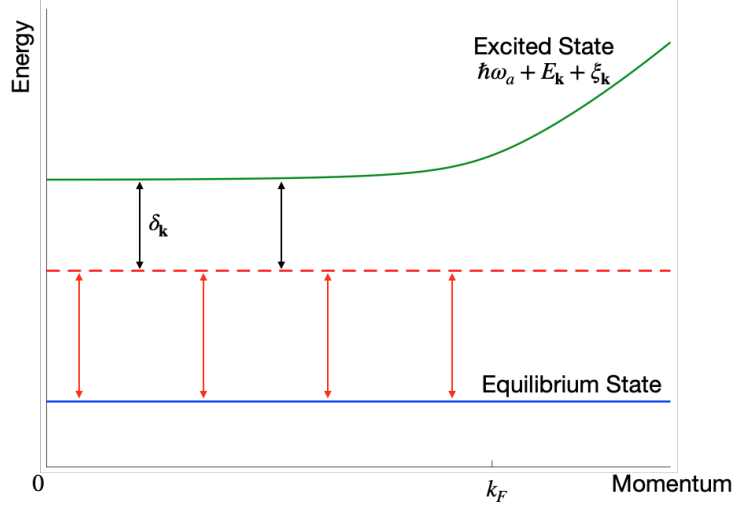


Figure 4.4: Illustration of the excitation scheme. The rf field is red-detuned from the quasiparticle excitations, and creates an off-resonant excitation to the state $|3\rangle$ with a momentum dependent detuning $\delta_{\mathbf{k}}$. The Figure is adapted with permission from [56], ©2018 Springer Nature.

green line). The coherent rf-driving of particles out of $|2\rangle$ and into level $|3\rangle$ directly affects the pair coherence and induces a modulation of the amplitude of the order parameter Δ (top panel, blue line of Fig. 4.5). The Fourier spectrum, depicted in Fig. 4.5 (lower panel), reveals the frequency content of these oscillations, and we observe a sharp peak at the gap value $2|\Delta|$ (red dashed line), a first indication hinting at the excitation of the Higgs mode. In contrast to this, the Fourier spectrum of N_3 shows no discernible feature around $\hbar\omega \sim 2|\Delta|$, but rather exhibits a much wider peak at the effective modulation frequency well below the Higgs.

4.4.1 Convergence of the Numerical Simulations

Before we analyse the activation of the Higgs mode in further detail, we here want to comment on the convergence of our numerical results obtained using a fourth-order Runge-Kutta method as discussed in section 3.1. All our simulations were performed on a discretised time and momentum grid. The simulations ran up to a final time $T = 400\hbar/E_F$ with a time step $dt = 5 \times 10^{-4}\hbar/E_F$, momentum spacing $dk/k_F = 5 \times 10^{-4}$, and energy cutoff of $E_c = 100E_F$. To assure the convergence of our results, we performed careful checks, varying each convergence parameter individually.

The identification of the Higgs mode relies crucially on the signal in the Fourier transform of $|\Delta|$. Fig. 4.6 (a) shows $|\Delta(\omega)|$ for the different convergence runs. We clearly see that the amplitude and location of the Higgs peak agrees very well and the data is well converged. Since the energy cutoff directly enters the expression for the interaction strength g , we refrain from performing the same convergence analysis in E_c as we cannot compare simulations of different E_c quantitatively with each other. Nevertheless, we found the qualitative features to be in agreement with the here presented data. The lower panel (b) shows the convergence in the upper level population $N_3(t)$. Throughout the entirety of the evolution the observable is very well converged; it is difficult to make out the different convergence curves by eye, and we

4.4 Activation of the Higgs

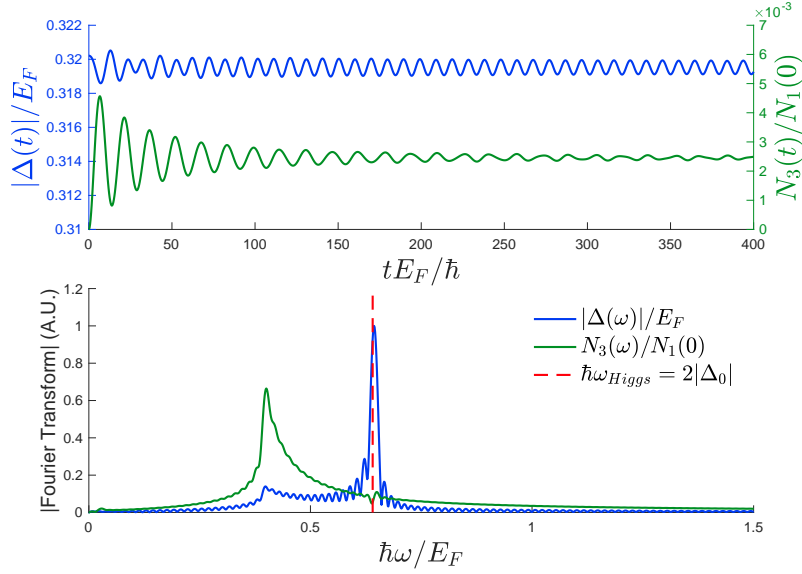


Figure 4.5: Top panel: The realtime evolution of $|\Delta(t)|$ and $N_3(t)$ for the full model (blue and green curves respectively). The upper level population exhibits damped oscillations originating from the quick dephasing of the different momentum states due to the rf transfer. The superconducting order parameter $|\Delta|$ exhibits stable, persistent oscillations in agreement with the expected activation of the Higgs amplitude mode. Lower panel: The Fourier transform of the quantities displayed in the upper panel (same colour assignments). While the third state population shows a dominant peak at the effective modulation frequency of the Rabi drive, the oscillations of the superconducting order parameter are dominated by the peak located at $\hbar\omega_{Higgs} = 2|\Delta(0)| = 2\Delta_0$ (red dashed line), suggesting the successful activation of the Higgs amplitude mode through the proposed off-resonant driving scheme. The parameters of the simulations are given by $\frac{1}{k_F a} = -0.6305$, $\hbar\Omega_R = 0.0375E_F$, $\hbar\delta = -0.3385E_F$, and $\alpha = 0.0050$.

4.4.1 Convergence of the Numerical Simulations

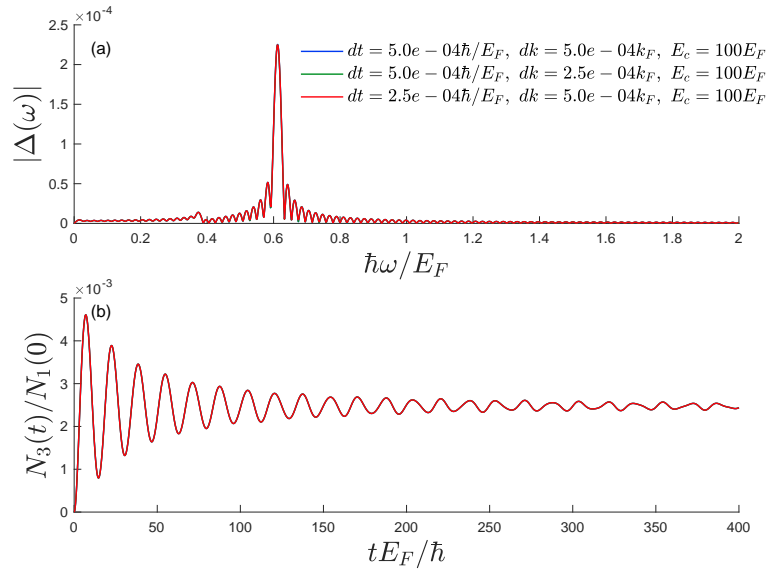


Figure 4.6: Here we show the numerical convergence of the presented results. The upper panel (a) shows the convergence of the central quantity to characterise the Higgs mode, $|\Delta(\omega)|$. We have independently varied the time step (red), and the momentum grid (green), and compared the result to our default parameters (blue). We find very good agreement in all cases. The lower panel (b) shows the corresponding evolution of $N_3(t)$, the population of the upper state. Legend and colouring are the same as in (a). The good convergence in both quantities means that we can almost only discern a single line (the others are hidden underneath).

4.4 Activation of the Higgs

can therefore confidently conclude that our simulations are converged.

4.4.2 The Effective Rabi Problem

In order to explain the excitations found in our numerical results, we here devise an effective Rabi model which will help us understand the rf-driving scheme in more detail at a microscopic level. As shown schematically in Fig. 4.4, the rf-transitions to $|3\rangle$ are red-detuned with a momentum-dependent detuning $\delta_{\mathbf{k}}$. We will use this observation to reduce the full many-body problem to a self-consistent, simplified set of equations which still retain the key features of the full model and mimic the coherent rf-transfer of particles from $|\mathbf{k}, 2\rangle$. For the derivation we first consider the pure BCS limit (by removing the upper level $|3\rangle$ from the equations 3.3) and in a second step the non-interacting, two-level Rabi transitions (by removing the $|1\rangle$ state from the equations 3.3), before combining the two into an effective model. Neglecting the upper level from the equations of motion 3.3, we obtain

$$\begin{aligned}\hbar\frac{\partial\Delta_{\mathbf{k}}}{\partial t} &= i\{-2\epsilon_{\mathbf{k}}\Delta_{\mathbf{k}} + \Delta(n_{\mathbf{k},1} + n_{-\mathbf{k},2} - 1)\} \\ \hbar\frac{\partial n_{\mathbf{k},1}}{\partial t} &= -2\Im\{\Delta^* \Delta_{\mathbf{k}}\} \\ \hbar\frac{\partial n_{-\mathbf{k},2}}{\partial t} &= -2\Im\{\Delta^* \Delta_{\mathbf{k}}\}.\end{aligned}\tag{4.13}$$

The equations are coupled implicitly through the superconducting order parameter. They will form the basis for our effective model, to which we add an additional term by hand to represent the rf-drive.

To understand which term correctly mimics the effect of the Rabi drive, we next turn to look at the non-interacting limit by neglecting interactions between levels $|1\rangle$ and $|2\rangle$. In this limit the Hilbert space of $|1\rangle$ states is completely decoupled from the $|23\rangle$ manifold and upon neglecting all dependencies on $|1\rangle$ we obtain

$$\begin{aligned}\frac{\partial\langle c_{-\mathbf{k},2}^\dagger c_{-\mathbf{k},3}\rangle}{\partial t} &= i\{\delta\langle c_{-\mathbf{k},2}^\dagger c_{-\mathbf{k},3}\rangle - \frac{\Omega_R}{2}(n_{-\mathbf{k},2} - n_{-\mathbf{k},3})\} \\ \frac{\partial n_{-\mathbf{k},2}}{\partial t} &= \Omega_R\Im\{\langle c_{-\mathbf{k},2}^\dagger c_{-\mathbf{k},3}\rangle\} \\ \frac{\partial n_{-\mathbf{k},3}}{\partial t} &= -\Omega_R\Im\{\langle c_{-\mathbf{k},2}^\dagger c_{-\mathbf{k},3}\rangle\}.\end{aligned}\tag{4.14}$$

These are just the Rabi equations in momentum space for a two-level system already discussed in section 2.5.2. The system is exactly solvable and leads to Rabi oscillations as observed in the populations of levels $|2\rangle$ and $|3\rangle$.

We will now modify Eq. 4.14 by reintroducing the interaction effect between $|1\rangle$ and $|2\rangle$ in order to obtain a consistent, effective description of the interacting many-body problem. We will do so by promoting δ and Ω_R appearing in Eq. 4.14 to momentum-dependent quantities

which incorporate the momentum dependent dispersions of the BCS state.

To do this, we begin by considering the effect of a spin-flip on the BCS wave function induced by the rf-drive. Initially particles in $|1\rangle$ and $|2\rangle$ are condensed as Cooper pairs in the superconducting ground state and removing an atom from $|2\rangle$ excites a quasiparticle with an energy $E_{\mathbf{k}}$. The addition of the particle into $|3\rangle$ costs an energy $\hbar\omega_a + \xi_{\mathbf{k}}$. Thus the total cost of making an rf-excitation is given by $E_{\mathbf{k}} + \hbar\omega_a + \xi_{\mathbf{k}}$. For a far red-detuned rf-drive, we expect to only significantly alter the quasiparticle dispersion close to the Fermi momentum (through the excitation of the Higgs mode). Thus, we expect the Rabi picture to continue to hold when extended to account for the momentum dependence of the energy bands. The effective Rabi frequency is then given by $\Omega'_{R,\mathbf{k}} = \sqrt{\Omega_R^2 + \delta_{\mathbf{k}}^2}$, whilst the momentum dependent detuning takes the energy cost of an rf-flip excitation into account, and has the form $\hbar\delta_{\mathbf{k}} = \hbar\delta - (E_{\mathbf{k}} + \xi_{\mathbf{k}})$.

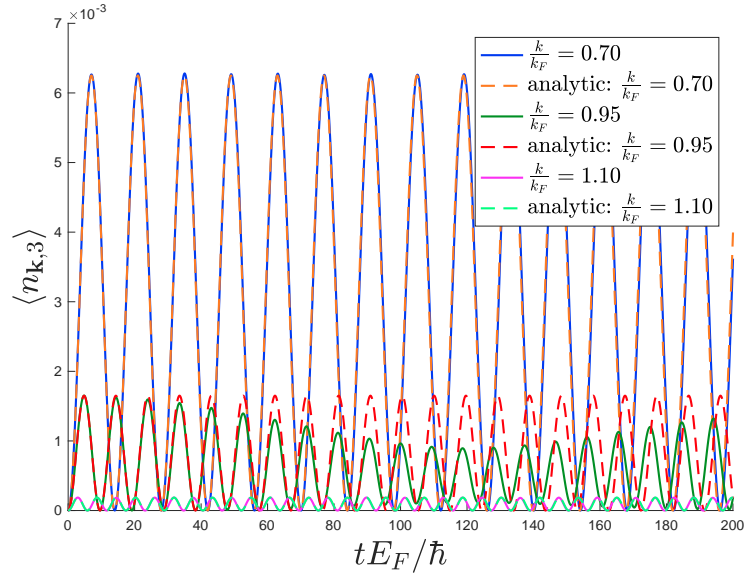


Figure 4.7: Time evolution of the momentum-resolved occupation of the upper level, $\langle n_{\mathbf{k},3} \rangle$. As suggested by the effective model and despite the non-trivial dispersion of the BCS quasiparticles, the individual momentum states undergo stable Rabi oscillations. Physically, this is because the rf-dressing transfers negligible momentum. The dashed lines show the analytic solution Eq. 4.16 and are generally in very good agreement with the full simulations (full lines). Discrepancies arise, as expected, mainly in the vicinity of the superconducting gap $|\xi_{\mathbf{k}}| \sim 0$ (e.g. $|\mathbf{k}| \approx 0.95k_F$), where the effect of the amplitude mode excitation is most pronounced. Furthermore, note that it is the momentum-dependent amplitude and frequency of the Rabi oscillations, which gives rise to the dephased, damped oscillations of $N_3(t)$. The simulation parameters used are $\frac{1}{k_F a} = -0.6305$, $\hbar\Omega_R = 0.0375E_F$, $\hbar\delta = -0.3385E_F$, and $\alpha = 0.0050$.

With the replacement $\delta \rightarrow \delta_{\mathbf{k}}$ and $\Omega_{\text{eff}} \rightarrow \Omega'_{R,\mathbf{k}}$, the analytic solutions to Eq. 4.14 become

4.4 Activation of the Higgs

$$\Im(\langle c_{-\mathbf{k},2}^\dagger c_{-\mathbf{k},3} \rangle) = -|v_{\mathbf{k}}|^2 \frac{\Omega_R}{2\Omega'_{R,\mathbf{k}}} \sin(\Omega'_{R,\mathbf{k}} t) \quad (4.15)$$

$$n_{-\mathbf{k},3}(t) = |v_{\mathbf{k}}|^2 \frac{\Omega_R^2}{\Omega'^2_{R,\mathbf{k}}} \sin^2(\Omega'_{R,\mathbf{k}} t/2), \quad (4.16)$$

in analogy to the two level system discussed in section 2.5.2. Here $|v_{\mathbf{k}}|^2$ is the probability to have an occupied Cooper pair and thus an atom in the relevant momentum state $|\mathbf{k}, 2\rangle$ as can be seen from Eq. 2.26. Intuitively the prefactor accounts for the fact that, since the momentum state $|\mathbf{k}, 2\rangle$ is being rotated into a superposition with $|\mathbf{k}, 3\rangle$, there is a certain probability $|v_{\mathbf{k}}|^2$ for the state $|\mathbf{k}, 2\rangle$ to be occupied and transfer is only possible if this probability is non-zero. Fig. 4.7 shows the Rabi oscillations of the full model and compares them to the analytic formula of Eq. 4.16. The dynamics of the full model is captured very accurately and we only notice clear deviations in the vicinity of the gap $|\xi_{\mathbf{k}}| \sim 0$, where this approximation is not expected to be valid. Outside of this small region the system exhibits coherent Rabi oscillations, which, interestingly, can be analytically captured by this two-level, momentum-dependent single particle model.

Simulation of the effective Model

Having seen that the analytic equation for the upper level population yields a very accurate description of the system away from the Fermi momentum, we reintroduce the analytic expression for the modulation term $\hbar\Omega_R \Im\{\langle c_{-\mathbf{k},2}^\dagger c_{-\mathbf{k},3} \rangle\}$, Eq. 4.16, into the BCS equations, Eq. 4.13, which yields the following effective model

$$\begin{aligned} \hbar \frac{\partial \Delta_{\mathbf{k}}}{\partial t} &= i\{-2\epsilon_{\mathbf{k}} \Delta_{\mathbf{k}} + \Delta(n_{\mathbf{k},1} + n_{-\mathbf{k},2} - 1)\} \\ \hbar \frac{\partial n_{\mathbf{k},1}}{\partial t} &= -2\Im\{\Delta^* \Delta_{\mathbf{k}}\} \\ \hbar \frac{\partial n_{-\mathbf{k},2}}{\partial t} &= -2\Im\{\Delta^* \Delta_{\mathbf{k}}\} + \hbar\Omega_R \Im\{\langle c_{-\mathbf{k},2}^\dagger c_{-\mathbf{k},3} \rangle\}. \end{aligned} \quad (4.17)$$

These equations are then solved numerically, in the same manner as discussed in chapter 3. Fig 4.8 shows the time evolution of the absolute value of the superconducting order parameter and the upper level population N_3 . The effective model does not include a third state so, in order to compare easier to the full simulations, we make use of the fact that $(N_2 + N_3)/N_1(0) = 1$ in the full model (conserved quantity) and introduce a ‘fictitious’ N_3 for the effective model according to $N_3/N_1(0) = 1 - N_2/N_1(0)$.

Fig. 4.8 (upper panel) shows the evolution of the amplitude of the order parameter together with the population of $|3\rangle$ as a function of dimensionless time. As expected we see a periodic modulation of the $|3\rangle$ population. Note however, that the N_3 oscillations are damped which is reminiscent of the fact that we excite Rabi oscillations for all momentum states, but due to the different dispersions of $|2\rangle$ and $|3\rangle$, these oscillations vary in amplitude and frequency with

momentum \mathbf{k} giving rise to dephasing. Turning to $|\Delta|$ we see that after a brief initial period we obtain very stable and clean oscillations. The Fourier content in the lower panel of Fig. 4.8 reveals these stable oscillations of $|\Delta|$ to lie at twice the superconducting order parameter value which is a strong indication that we have indeed excited the Higgs mode of the system with this proposed protocol.

The total transfer of particles into the upper level, N_3 , is very low, since we are always red-detuned from the resonance, and can therefore exclude single-particle excitations as the (primary) source of the characteristic Higgs resonance seen here in the amplitude of the order parameter. In summary, we find the effective model to be in excellent agreement with the simulations of the full model. In particular comparing the Fourier transforms in the lower panel we see - apart from slight changes in the amplitudes of the Fourier components - that the spectra look almost identical.

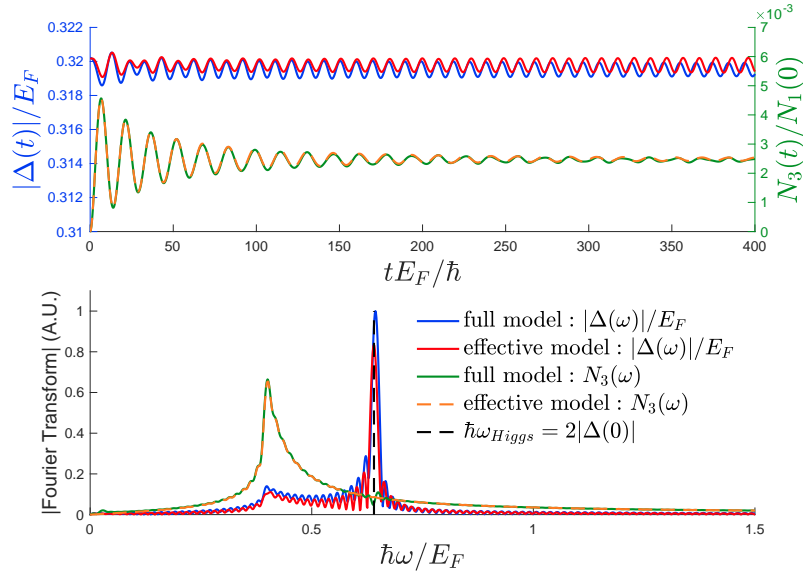


Figure 4.8: Top panel: Evolution of $|\Delta(t)|$ and $N_3(t)$ for the full model (Eq. 3.3, blue and green curve respectively) and the effective model (Eq. 4.17, red and orange line). The population shows damped oscillations originating from the quick dephasing of the different momentum states due to the Rabi transfer. The superconducting order parameter $|\Delta|$ exhibits stable, persistent oscillations in agreement with the expected activation of the Higgs amplitude mode. Note that for the effective model we show the quantity $N_3(t) = N_1(0) - N_2(t)$, as we do not have an explicit upper level in the model. Lower panel: The Fourier transform of the observables displayed in the upper panel (same colour assignments). While the third state population shows a dominant peak at the effective modulation frequency, the oscillations of the superconducting order parameter are dominated by the peak located at $\hbar\omega_{Higgs} = 2|\Delta(0)| = 2\Delta_0$, suggesting the successful activation of the Higgs amplitude mode through the proposed off-resonant driving scheme. Note that in both panels, the simplified model successfully captures the dynamics of the full model. The parameters of the simulations are given by $\frac{1}{k_F a} = -0.6305$, $\hbar\Omega_R = 0.0375E_F$, $\hbar\delta = -0.3385E_F$, and $\alpha = 0.0050$.

4.4 Activation of the Higgs

Validity of the effective Model

To understand why the extended Rabi picture fails close to the Fermi momentum, we note that exciting the Higgs mode means inducing fluctuations in the amplitude of the order parameter. Since the order parameter is also the superconducting gap, its modulation changes the dispersion of the quasiparticles $E_{\mathbf{k}} = E_{\mathbf{k}}(t)$ in time. However, this effect is only appreciable in a small region around the gap $|\xi_{\mathbf{k}}| \approx 0$, whilst the dispersion is largely static away from this region, as shown schematically in Fig. 4.9. At time t , with a superconducting order parameter of $\Delta(t)$, making an excitation to $|\mathbf{k}, 3\rangle$ will cost an energy $\mathcal{E}(t) = E_{\mathbf{k}}(t) + \xi_{\mathbf{k}} + \hbar\omega_a$, while at a later point $t + \delta t$ the same transition costs $\mathcal{E}(t + \delta t) = E_{\mathbf{k}}(t + \delta t) + \xi_{\mathbf{k}} + \hbar\omega_a \neq \mathcal{E}(t)$ since $\Delta(t + \delta t) \neq \Delta(t)$. Therefore the same transition $|\mathbf{k}, 2\rangle \rightarrow |\mathbf{k}, 3\rangle$ is driven by Rabi frequencies and amplitudes which vary in time (formally, the respective detuning $\delta_{\mathbf{k}}$ is implicitly time-dependent through $E_{\mathbf{k}}(t)$). Therefore the picture of a single, locked Rabi frequency across the full time evolution only holds as a good approximation in the regions where the quasiparticle's dispersion change is negligible (i.e. outside a small region around the Fermi momentum) as can be seen in Fig. 4.9. This ultimately leads to discrepancies between the coherent Rabi picture (Eq. 4.16) and the simulation of the full Hamiltonian (Eq. 3.3) as can be seen for $|\mathbf{k}| \approx 0.95k_F$ in Fig. 4.7, where the individual momenta can no longer be assumed to be independent and decoupled. Since the variation of the amplitude of the order parameter is of the order 10^{-3} , the discrepancy region is however very small.

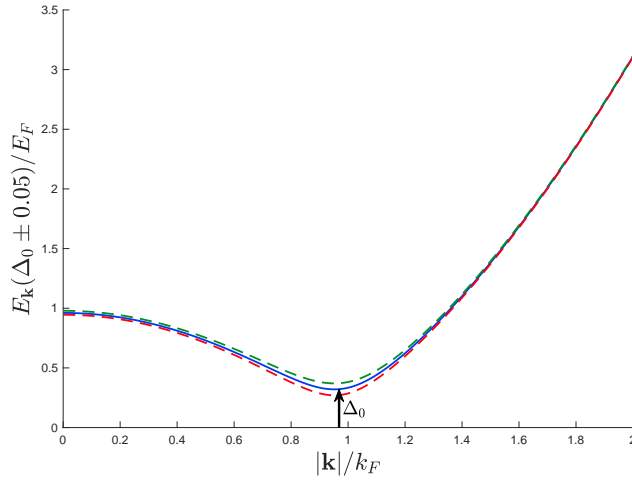


Figure 4.9: The BCS quasiparticle dispersion, $E_{\mathbf{k}}(\Delta)$, and how it changes due to the excitation of the amplitude mode. It is only significantly modulated around the gap of the dispersion, $|\xi_{\mathbf{k}}| \approx 0$. This explains intuitively, why the analytic expression 4.16, works so well outside of this region. Here, the dispersion is approximately static, so the assumption of a decoupled, momentum-resolved two-level system is valid and the Rabi picture is expected to be applicable. Note that the modulation $\Delta = \Delta_0 \pm 0.05E_F$ is exaggerated (by an order of magnitude) compared to the actual simulations for visibility.

4.4.3 The Higgs Mode as a Collective Excitation

Whilst the Fourier signal in Fig. 4.5 of $|\Delta(\omega)|$ at $\hbar\omega = 2|\Delta_0|$ hints very strongly at the activation of the Higgs mode, there exists another excitation which has this value as its lower excitation threshold. The creation of two quasiparticles on top of the BCS ground state $\gamma_{\mathbf{k},0}^\dagger \gamma_{\mathbf{k},1}^\dagger |\psi_{BCS}\rangle$ creates an excited Cooper pair (orthogonal to the initially unexcited pair in the condensate) [59]. The energy of such an excitation is $2E_{\mathbf{k}} \geq 2|\Delta|$. A priori it is thus not obvious, whether the peak seen in Fig. 4.5 is truly coming from the activation of the Higgs or from excited quasiparticles. The Higgs mode is however a *collective* mode of the system, i.e. all pairs constituting the condensate *collectively* and coherently give rise to the amplitude oscillation seen in $|\Delta(t)|$. To unambiguously identify the excitation peak as the Higgs mode we therefore look at the momentum-resolved spectral weight of $\Delta_{\mathbf{k}} = \langle c_{-\mathbf{k},2} c_{\mathbf{k},1} \rangle$,

$$A_{\mathbf{k}}(\omega) = \left| \mathcal{F} \left\{ |\Delta_{\mathbf{k}}(t)| - \frac{1}{T} \int_0^T dt |\Delta_{\mathbf{k}}(t)| \right\} \right|. \quad (4.18)$$

Fig. 4.10 shows the spectral weight $A_{\mathbf{k}}(\omega)$ on the BCS (a) and BEC (b) side of the Feshbach resonance ($1/(k_F a) < 0$, and $1/(k_F a) > 0$ respectively) for an effective modulation frequency of $\hbar\Omega_{\text{eff}} \sim 1.5\Delta_0$. The most striking feature on the BCS side of the resonance is the clear vertical excitation line at the Higgs frequency (marked by pink dots). It signals the collective, non-dispersive excitation of Cooper pairs across all momenta. Additionally we can make out two further excitation branches. One stems from the excitation of pairs of quasiparticles at an energy $2E_{\mathbf{k}}$ as discussed above (marked by cyan triangles). Indeed we see that they ‘touch’ the Higgs branch at $\xi_{\mathbf{k}} = 0$ ($\hbar\omega = 2\Delta_0$), but their contribution to the Higgs peak in $|\Delta(\omega)|$ is only marginal. From these momentum resolved plots we can now unambiguously identify the resonance at $\hbar\omega = 2\Delta_0$ as the signature of the Higgs mode. The last remaining branch (red inverted triangles) marks the effective modulation frequency of the upper level population $\Omega'_{R,\mathbf{k}}$ as shown in the previous section. Eq. 4.16 gave a very good description of the momentum resolved particle density in the upper level. Due to the interaction in the lower $|12\rangle$ manifold, it is not surprising that this induced modulation is also imprinted into the momentum-resolved spectral weight. Finally, it is worth noting that the markers on the excitation branches stem entirely from our analytical calculations of sections 2.3 (quasiparticle dispersion $2E_{\mathbf{k}}$), 4.1 (Higgs dispersion $2|\Delta_0|$) and 4.4.2 (effective modulation frequency $\Omega'_{R,\mathbf{k}}$), and do not contain any free parameters.

As we have seen in section 4.1, the Higgs mode is only stable as long as the particle-hole symmetry of the underlying Hamiltonian is sufficiently satisfied. Strictly, this is only the case deep in the BCS limit of the crossover. As we tune to stronger interactions and eventually cross over onto the BEC of the Feshbach resonance, particle-hole symmetry is lost ($K_1 \neq 0$) and the Higgs mode is expected to vanish [160]. In Fig. 4.10 (b) we show the momentum-resolved spectral weight $A_{\mathbf{k}}(\omega)$ in the BEC regime. First and foremost, the Higgs excitation is absent as expected. We have marked the $2E_{\mathbf{k}}$ and $\Omega'_{R,\mathbf{k}}$ lines (cyan upper and red lower triangles respectively) as in (a) and find again very good agreement between the simulation and our analytical calculations.

4.4 Activation of the Higgs

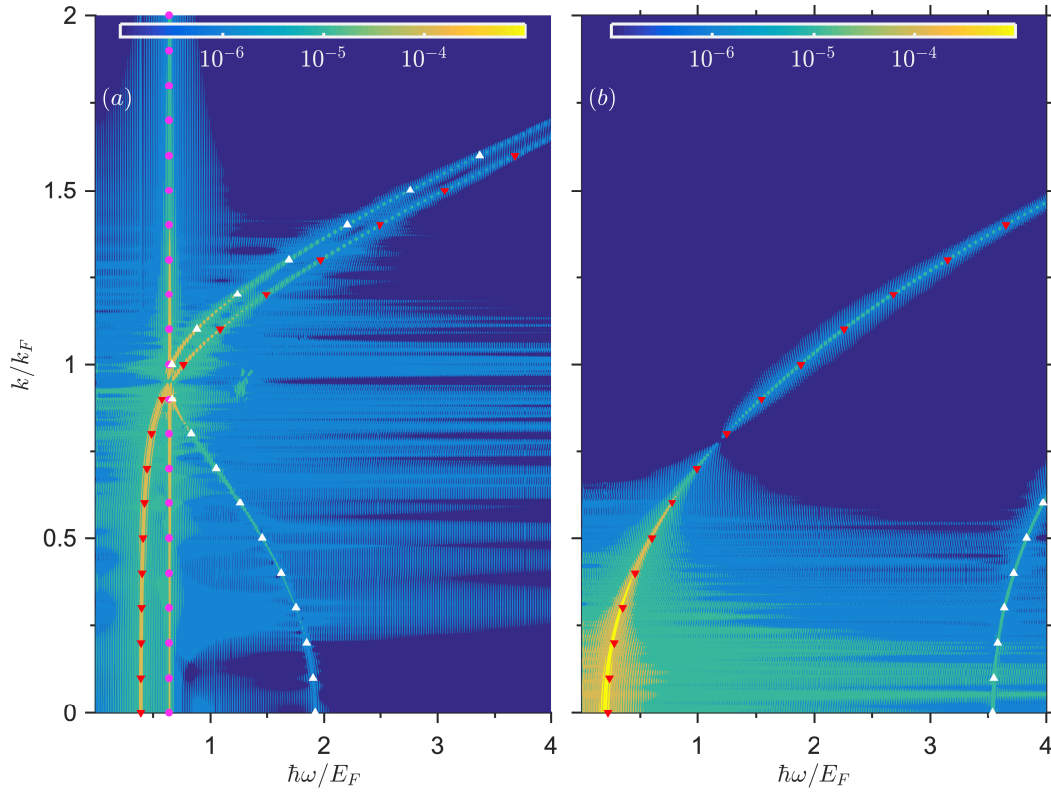


Figure 4.10: Contour plots of $\log[A_{\mathbf{k}}(\omega)]$, Eq. 4.18, in the BCS-BEC crossover. The Higgs is strongly excited on the BCS side of the resonance (a) for $1/(k_F a) = -0.6305$, $\hbar\Omega_R = 0.0375E_F$, and $\hbar\delta = -0.3385E_F$, whilst it is absent on the BEC side (b) for $1/(k_F a) = 1.0199$, $\hbar\Omega_R = 0.1129E_F$ and $\hbar\delta = 2.5294E_F$. The pink dots mark the $\hbar\omega_{\text{Higgs}} = 2\Delta_0$ excitation line (a). White triangles denote the quasiparticle $2E_{\mathbf{k}}$ branch and red, inverted triangles the effective modulation frequency of the upper level $\Omega'_{R,\mathbf{k}}$. All markers stem from analytic calculations and are *not* fits to the numerical data.

With this we can now be sure that the peaked signal in Fig. 4.5 in fact *is* coming from the Higgs mode and not from quasiparticle excitations. From the momentum-resolved contour plot Fig. 4.10 (a), we identified the peak in $|\Delta(\omega)|$ to be dominated by the Higgs excitation with a momentum-independent dispersion. Finally, how strongly the Higgs is excited depends largely on the effective modulation frequency in relation to the Higgs threshold. In the following section 4.5 we will compare the spectral weight of the Higgs (obtained from integrating $A_{\mathbf{k}}(\omega)$ along the Higgs line) to the condensate fraction as measured experimentally. We find that the amplitude of the spectral weight of the Higgs peak is maximal when the effective modulation frequency is resonant with the Higgs mode $\hbar\Omega_{\text{eff}} \approx 2|\Delta|$.

However, before turning to the experimental observation of the Higgs, we want to turn to Fig. 4.11, where we show the Fourier transform of the imaginary part of $\Delta_{\mathbf{k}}$ for an undriven system (a), and compare this to imaginary part (b), and absolute value of $\Delta_{\mathbf{k}}$ (c) for a driven system. It is common to look at the spectral function (related to the imaginary part of the correlator) to learn about the excitations of the system. The Higgs however shows up as an oscillation in the *amplitude* of the superconducting order parameter, and as such neither $\Re(\Delta_{\mathbf{k}})$ nor $\Im(\Delta_{\mathbf{k}})$ signal the excitation of the mode strongly. The vertical strong line that we see in Fig. 4.11 (a) is coming from the unitary evolution of the BCS theory under the chemical potential⁴ (for more details we refer to appendix B.2). Interestingly, the spectrum, as seen in $\Im(\Delta_{\mathbf{k}})$, is largely unchanged between the undriven (a) and driven evolution (b) of the system. This shows that we are indeed only weakly perturbing the system and the unitary evolution is the dominant contribution to the dynamics of the system. Also, herewith it becomes clear why we chose the particular functional form of $A_{\mathbf{k}}(\omega)$ in Eq. 4.18. Only by looking at the absolute value of $\Delta_{\mathbf{k}}$ are we able to reveal the collective excitation of the amplitude mode of the superfluid (c). This novel method of using the Fourier content of $|\Delta_{\mathbf{k}}|$ as a diagnostic tool to detect and characterise the excitations of the superfluid state is one of the central results of this chapter and of the publication [56].

4.5 Experimental Signature and Observation

To conclude this chapter, in this section we want to discuss the connection between the presented theoretical results and experimentally measured data, and comment on the observability of the Higgs mode in an ultracold quantum gas. This work came out of a fruitful collaboration with the experimental group of Michael Köhl, who has implemented the here proposed radiofrequency driving scheme of an atomic gas of ${}^6\text{Li}$ atoms in the BCS-BEC crossover. By inducing a periodic modulation of the superconducting order parameter through the rf-drive, they observe an excitation resonance at the characteristic Higgs frequency in a strongly interacting superfluid Fermi gas. Performing these measurements throughout the BCS-BEC crossover, they observe, for strong coupling, the broadening of peak width and the eventual disappearance of the mode when the Cooper pairs turn into tightly bound dimers on the BEC side of the Feshbach resonance. In the following we will give a brief overview over the experimental setup and results. For further details, we refer the reader to the PhD thesis of Alexandra Behrle, Tim

⁴Similar to the evolution of the wave function in the Gross-Pitaevski equation for a weakly interacting BEC [168, 169].

4.5 Experimental Signature and Observation

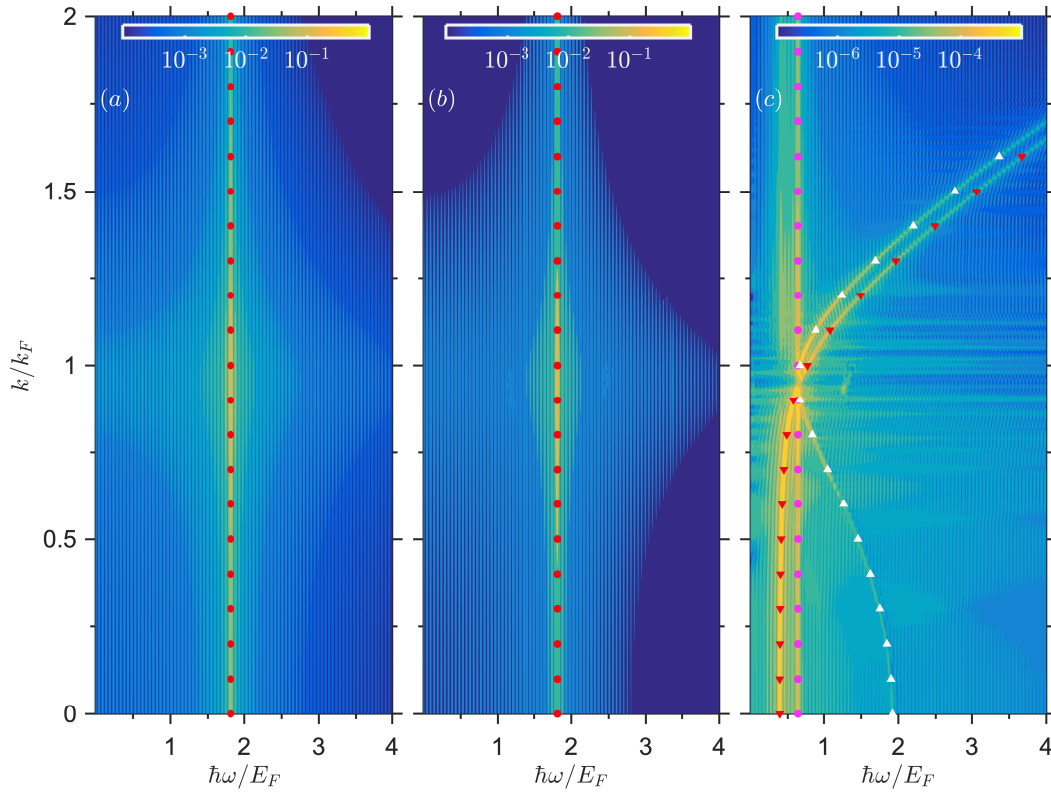


Figure 4.11: Contour plots of $\Im(\Delta_{\mathbf{k}})$ (a-b), and $|\Delta_{\mathbf{k}}|$ (c) for $\frac{1}{k_F a} = -0.6305$. We compare the results of an undriven, $\Omega_R = \delta = 0$, (a) to the driven system for $\hbar\Omega_R = 0.0375E_F$, and $\hbar\delta = -0.3385E_F$ (b-c). The red dots in (a) and (b) mark the line at $\hbar\omega = 2\mu$, where μ is the chemical potential in the initial state. Note the absence of the Higgs line in $\Im(\Delta_{\mathbf{k}})$ (a-b). It is only when the real and imaginary part are *combined* to $|\Delta_{\mathbf{k}}|$ that the Higgs (pink dots), the quasiparticles at $\hbar\omega = 2E_{\mathbf{k}}$ (white triangles) and drive excitations (red, inverted triangles) become clearly visible (c).

Harrison and Martin Link in relation to this work [170–172].

In chapter 2, we showed the hyperfine level structure of ^6Li (Fig. 2.2). In this experiment, the lowest three hyperfine levels are used to encode the different fermionic species. The interaction between the lowest two levels $|1\rangle$ and $|2\rangle$ is set by tuning the s -wave scattering length near the Feshbach resonance (section 2.2). Using a radiofrequency antenna, transitions between levels $|2\rangle$ and $|3\rangle$ are driven, where the rf-detuning from the bare Zeeman resonance, and the Rabi frequency are set by the frequency of the rf-field and the power of the rf-coil.

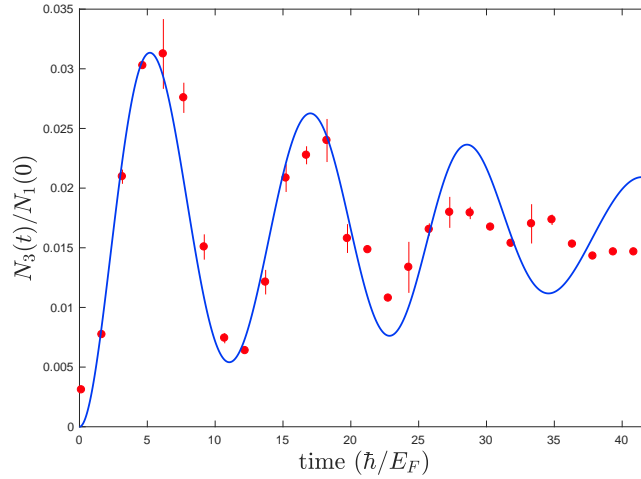


Figure 4.12: Oscillation of the atom number in state $|3\rangle$ as a function of time during the modulation. Experimental parameters: $1/(k_F a) = -0.504$, trap frequencies $2\pi \times (17, 170, 407)\text{Hz}$, total atom number $N = 2 \times 10^6$, and $\alpha = 0.04$. Theoretical parameters: $1/(k_F a) = -0.505$, and $\alpha = 0.035$. The Figure is reproduced with permission from [56], ©2018 Springer Nature.

In Fig. 4.12 we compare the evolution of the upper level population N_3 during the rf-drive between the theoretical simulations and the experimental measurements. Measurements and simulation were performed with the same effective modulation frequency Ω_{eff} and maximal atom transfer α . The theoretical simulations agree well with the experimental data for the first three oscillation periods, which implies that the dominant damping mechanism seen is a result of the dephasing of the different momentum states $\langle n_{k,3} \rangle$. Beyond this the deviations increase and we attribute this to additional damping mechanisms present in the experiment but not accounted for in the theoretical model.

Experimentally the Higgs mode is detected by measuring the energy absorption spectra for the $|12\rangle$ superfluid. After the rf-drive is applied, a fast magnetic field ramp onto the molecular (BEC) side of the Feshbach resonance adiabatically connects the Cooper pairs with tightly bound dimers [84, 86, 173], which are subsequently imaged in time-of-flight measurements. Experimentally, they extract the condensate fraction from Gaussian fits to the zero-momentum peak in the absorption image. Changes in the condensate fraction are a sensitive measure of the excitations in the system. To compare our simulations with their experimentally obtained spectra, we integrate, for each momentum state, under the respective Higgs peak in Fig. 4.10,

4.5 Experimental Signature and Observation

and sum up the contributions for all momenta.

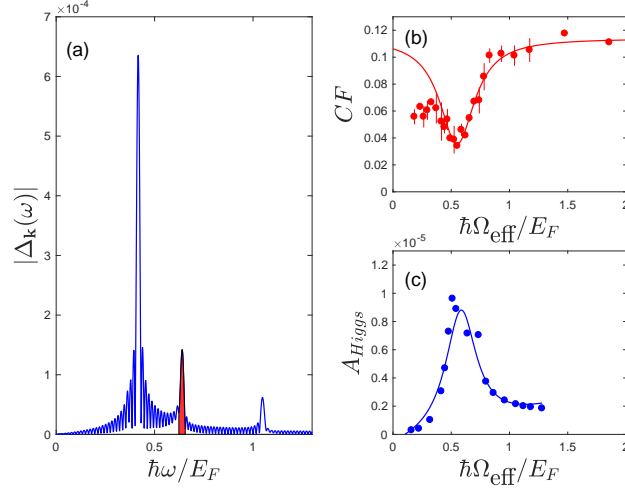


Figure 4.13: Comparison of the spectral weight of the Higgs. (a) shows a momentum slice of the numerical integration (red shaded region) under $|\Delta_{\mathbf{k}}(\omega)|$ (Fig. 4.10) performed to compute the spectral weight of the Higgs for $|\mathbf{k}| = 0.7k_F$. (b) shows the experimentally measured condensate fraction (CF), for the parameters $1/(k_F a) = -0.63$, trap frequencies $2\pi \times (91, 151, 235)\text{Hz}$, total atom number $N = 3 \times 10^6$, and $\alpha = 0.005$. (c) shows the theoretically computed spectrum of the Higgs A_{Higgs} , as a function of modulation frequency Ω_{eff} . Note that the activation of an excitation in the system is observed as a depletion of the condensate fraction (b), whilst it theoretically reveals itself as an increase in the spectral weight of the excitation (c). The theoretical parameters are $1/(k_F a) = -0.6305$, and $\alpha = 0.005$. The Figure is adapted with permission from [56], ©2018 Springer Nature.

Fig. 4.13 (a) shows an example of this integration for one particular momentum state. Upon momentum-integration, the extracted spectral weight of the Higgs is then plotted as a function of effective modulation frequency (c) and compared to the experimentally measured condensate fraction (b). We note that within this integration procedure, by following the Higgs excitation line, we find a non-vanishing contribution to the weight at high modulation frequencies, which, however, can be attributed to the excitation of quasiparticles in a homogeneous system and would vanish in a trapped system as considered experimentally. We note that even though the Higgs mode has a very sharp frequency and therefore a long lifetime (c.f. Fig. 4.10), the resulting spectra show a much broader peak (b-c), which is an artefact of the excitation procedure. The reason is, that the Higgs mode can already be excited for effective modulation frequencies away from $2|\Delta_0|^5$, since for some momentum states, the effective Rabi frequencies $\Omega'_{R,\mathbf{k}}$ will be resonant with the Higgs mode. Thus, the broadening of the spectral feature is mainly due to the particular excitation scheme and *not* a measurement of the lifetime of the Higgs mode.

⁵The Higgs mode is a collective mode of the system and even for the harmonically trapped gas exhibits a unique frequency. Numerical studies in the BCS limit have shown that in harmonically trapped systems, the Higgs mode should occur at the frequency of twice the superconducting gap evaluated at the maximum density of the gas [163, 174–177].

Overall the experimental and theoretical spectra show good agreement both in the resonance position and its width.

Whilst the theoretical simulations are necessarily limited to the weak-coupling regime, where BCS theory applies, experimentally one can now follow the Higgs excitation as the system is tuned to stronger interactions. Fig. 4.14 shows the measured spectra throughout the BCS-BEC crossover. The depletion of the condensate fraction survives as a clear mode up to surprisingly strong interactions, implying the excitation of a well-defined mode. Even at unitarity we can make out the signature of an excitation. Its width though - as expected - grows with the interaction strength. Finally, on the BEC side of the resonance the mode cannot be distinguished anymore.

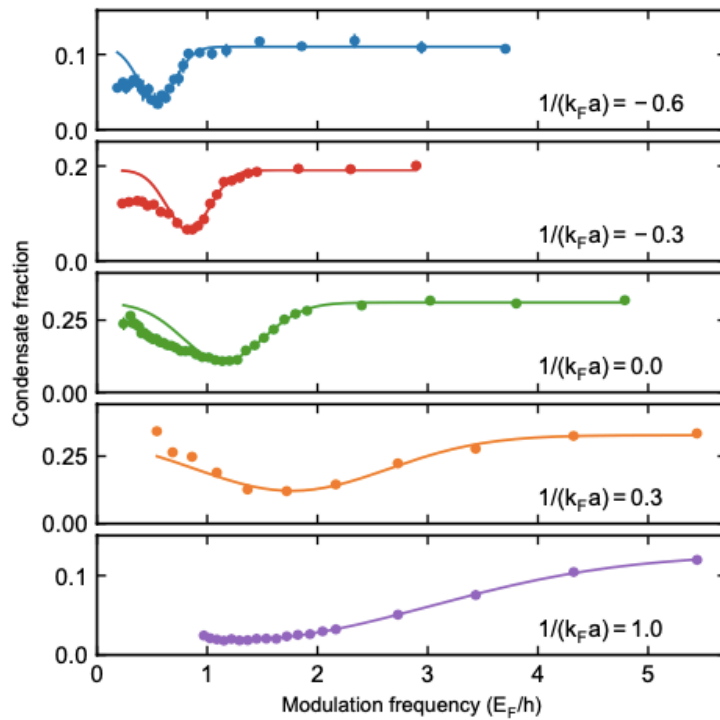


Figure 4.14: Experimental excitation spectra of the Higgs mode for different interaction strengths as labelled in the Figure. Solid lines show Gaussian fits to the high frequency side of the spectra. The resonance survives to surprisingly strong interactions (even unitarity) and gradually washes out on the BEC side. The error bars show the standard deviation of approximately four measurements. The Figure is reproduced with permission from [56], ©2018 Springer Nature.

4.6 Conclusion and Outlook

In conclusion we have devised a novel excitation scheme to directly excite the Higgs mode in a correlated fermionic superfluid. Employing an rf-modulation and dressing fermions of level $|2\rangle$ with $|3\rangle$, we have shown that we directly couple to the superconducting order parameter and induce periodic oscillations in its amplitude. We have performed numerical simulations of the underlying equations of motion within the rotating-wave approximation and found the simu-

4.6 Conclusion and Outlook

lations to be in good agreement with the experimental measurements. Our results demonstrate the effectiveness of this modulation scheme to excite the amplitude mode, and confirmed its collective nature. Finally, we devised a novel, theoretical detection method to unambiguously identify the excitation of the Higgs mode. The evolution of the momentum-resolved order parameter $\Delta_{\mathbf{k}}$, has been integral to our analysis in this chapter, with the potential to become a valuable, theoretical tool to study and characterise the excitations and response of interacting superfluids throughout the BCS-BEC crossover.

Finite-Duration Interaction Quench in Dilute Attractively Interacting Fermi Gases: Emergence of Pre-Formed Pairs

In recent years, significant experimental efforts have been devoted to dynamically generate complex states and monitor their evolution. Ultrafast optical pulses were used to photo-induce phase transitions in strongly interacting solid state materials [178–181] whilst similar successes were reported for ultracold atoms using time-dependent electromagnetic fields [68, 182]. Despite these remarkable advances, uncovering the mechanisms underlying the non-equilibrium dynamics of strongly correlated matter is still the subject of intense research. For example, in quantum many-body systems, identifying the processes governing the evolution of order parameters when interactions are tuned over time remains an open question. As order parameters are global quantities often with (quasi)local expectation values as their constituting elements, one would like to understand how the time-dependent behaviour of these different local components give rise to the complex dynamics of the global order parameter.

Quantum systems are usually very sensitive to external perturbations. Interactions between the various degrees of freedom are often similar in magnitude and can thus give rise to complex emergent phases, tuned by an external parameter. Driven away from equilibrium by a rapid quench of such a parameter, the system will subsequently undergo complex dynamics and non-trivial states may emerge in the long-time limit. We note that any experimental quench will inevitably be conducted over a finite window of time. In this work, we therefore address the non-equilibrium behaviour of dilute, attractively interacting Fermi gases subject to finite-duration ramps of their internal interaction strength. By changing the duration of the ramp time in our numerical protocol, we identify and characterise three dynamical regimes exhibiting distinct features in their long-time steady state. For short ramp durations, these systems become non-superconducting and their order parameter vanishes. We can trace its origin to the loss of phase coherence between the Cooper pairs, while the pair amplitude displays a non-thermal distribution. Importantly, the pair distribution is non-zero and the steady state still hosts Cooper pairs. Therefore, the dynamics gives rise to the emergence of a phase

5.1 Quench Dynamics in the BCS Model

disordered superconductor, made up of incoherent pairs. Intermediate ramp durations induce long-lived oscillations in the superconducting order parameter. Partial phase coherence is restored amongst the pairs, which gives rise to a finite, albeit reduced magnitude of the order parameter. Finally, for slow ramps the system adiabatically follows the ramp and phase coherence is almost fully retained. The steady state is characterised by a thermal-like pair amplitude distribution. This work demonstrates the possibility to dynamically tune the coherence between pairs, the magnitude of the superconducting order parameter, and even to stabilise a non-equilibrium steady state made of preformed pairs. The results of this chapter, whilst entirely theoretical in nature, came out of a fruitful collaboration and numerous discussions with the experimental group of Michael Köhl, and are published in [57], which we will follow in our subsequent presentation.

5.1 Quench Dynamics in the BCS Model

Following the early work of Volkov and Kogan [183] on the response of the superconducting order parameter to small initial perturbations, a resurgence of interest in this problem [163, 164, 184–194] was seen alongside the advances to cool fermionic gases below degeneracy and tune their interactions by the means of Feshbach resonances (see section 2.2) [68]. Volkov and Kogan found that in the collisionless regime, the superconducting order parameter Δ exhibits oscillations at a frequency 2Δ damped with a power law decay of $t^{-1/2}$. This was put into the broader context of sudden quenches realised in the BCS model [184, 188], where it was shown that the pairing dynamics falls into three different regimes, depending on the ratio $r = \frac{\Delta_i}{\Delta_f}$, where Δ_i (Δ_f) are the initial (final) BCS gap values. For small ratios ($r < e^{-\pi/2} \approx 0.2$) individual Cooper pair states synchronise and $\Delta(t)$ shows non-harmonic, undamped oscillations. For $e^{-\pi/2} \leq r < e^{\pi/2}$ the pairs start to dephase, giving rise to the Landau damped oscillations predicted in [183]. Finally for $r \geq e^{\pi/2} \approx 4.8$ the pairs are fully dephased, the order parameter is overdamped and vanishes. Meanwhile, Volkov and Kogan’s work was extended to larger deviations from equilibrium [187] and in [194] Yuzbashyan et al. analysed interaction quenches throughout the entire BCS-BEC crossover in a paired superfluid.

The focus thus far has been on abrupt quenches in the BCS regime, but experimentally quenches are realised within a finite window of time e.g. by exciting phononic modes in solids [195], or ramping the magnetic field in cold gases. Correspondingly, the response of superfluid Fermi gases to ramps and modulations of the three-dimensional s -wave scattering length was eventually studied in [163]. The investigation, set in the damped region of the pairing regime ($e^{-\pi/2} \leq r < e^{\pi/2}$), focussed on the excitation of Higgs mode and reported its attenuation in time according to a power law decay.

Here we consider ramps of the internal interaction strength of a three-dimensional, attractively interacting Fermi gas applicable to both solid state and cold atom systems. We are interested in the dynamics of the BCS order parameter, focussing on the overdamped pairing regime ($r > e^{\pi/2}$). Following an abrupt quench, Δ is overdamped and decays to zero without oscillations. The system is described by the s -wave BCS Hamiltonian,

$$H_{\text{BCS}} = \sum_{\mathbf{k}, \sigma=\{1,2\}} \epsilon_{\mathbf{k}} n_{\mathbf{k},\sigma} + \sum_{\mathbf{k}} \left[\Delta c_{\mathbf{k},1}^\dagger c_{-\mathbf{k},2}^\dagger + \text{h.c.} \right], \quad (5.1)$$

where $c_{\mathbf{k},\sigma}^{(\dagger)}$ are the fermionic annihilation (creation) operators, and $n_{\mathbf{k},\sigma}$ is the particle number operator of momentum \mathbf{k} and species $\sigma = \{1, 2\}$. $\epsilon_{\mathbf{k}} = \hbar^2 k^2 / (2m)$ is the single-particle dispersion and $\Delta = \frac{g}{V} \sum_{\mathbf{k}} \Delta_{\mathbf{k}}$ the superconducting order parameter already introduced in chapter 2, Eq. 2.21. For our later analysis, we additionally introduce a second quantity P , to assess the absolute pairing strength,

$$P = \frac{g}{V} \sum_{\mathbf{k}} |\Delta_{\mathbf{k}}|, \quad (5.2)$$

where $\Delta_{\mathbf{k}} = \langle c_{-\mathbf{k},2} c_{\mathbf{k},1} \rangle$ is the momentum-resolved superconducting order parameter. The expression for P only subtly differs from Δ in that it ignores the *phase* of the individual Cooper pairs and thus provides information about the presence of pairs in the system. The equilibrium phase diagram for this system was discussed in chapter 2 and has been thoroughly studied (see [59] and references therein). One of the key properties of the superconducting state is the long-range phase coherence that is established below the critical temperature. In this case $|\Delta| = |P|$, but when driven away from equilibrium, the different Cooper pairs can begin to evolve separately from each other, their phases no longer staying synchronised. In this case Δ would be reduced (possibly to zero), but pairs might still be present. Hence, in the following analysis we will carefully study both, Δ and P , to fully capture the non-equilibrium response of the superfluid.

Our quench protocol of the interaction parameter $\frac{1}{k_{Fa}} < 0$ takes the form

$$\frac{1}{k_{Fa}(t)} = \frac{1}{k_{Fa}(t_f)} + h(t, t_i, t_f) \left[1 - \sin^2 \left(\frac{\pi}{2} \frac{t - t_i}{\delta t_{ramp}} \right) \right], \quad (5.3)$$

where $h(t, t_i, t_f) = \Theta(t_f - t) \left[1 / (k_{Fa}(t_i)) - 1 / (k_{Fa}(t_f)) \right]$, $\delta t_{ramp} = t_f - t_i$ with t_i and t_f the times at which the interaction ramp begins and ends, and Θ is the Heaviside function. $\delta t_{ramp} \rightarrow 0$ corresponds to a sudden quench while an adiabatic ramp is realised in the limit of $\delta t_{ramp} \rightarrow \infty$. We choose a smooth (differentiable) sinusoidal schedule for the ramp so as to avoid complications due to the generation of additional excitations at the beginning and end of the ramp. In this study, the ramp *decreases* the interaction strength such that the superconducting order parameter is reduced ($\Delta_{0,i} > \Delta_{0,f}$). The Heisenberg equations of motion for this system are given by (c.f. Eq. 4.13):

5.2 Finite-Duration Quenches: Emergence of Pre-Formed Pairs

$$\begin{aligned}
\hbar \frac{\partial \Delta_{\mathbf{k}}}{\partial t} &= i \{-2\epsilon_{\mathbf{k}} \Delta_{\mathbf{k}} + \Delta (n_{\mathbf{k},1} + n_{-\mathbf{k},2} - 1)\} \\
\hbar \frac{\partial n_{\mathbf{k},1}}{\partial t} &= -2\Im\{\Delta^* \Delta_{\mathbf{k}}\} \\
\hbar \frac{\partial n_{-\mathbf{k},2}}{\partial t} &= -2\Im\{\Delta^* \Delta_{\mathbf{k}}\},
\end{aligned} \tag{5.4}$$

where $\Im(\dots)$ denotes the imaginary part. We numerically solve this set of equations together with the self-consistency condition for Δ , Eq. 2.21, for different ramp speeds δt_{ramp} , and will compare and contrast the dynamical behaviour of Δ in detail.

5.2 Finite-Duration Quenches: Emergence of Pre-Formed Pairs

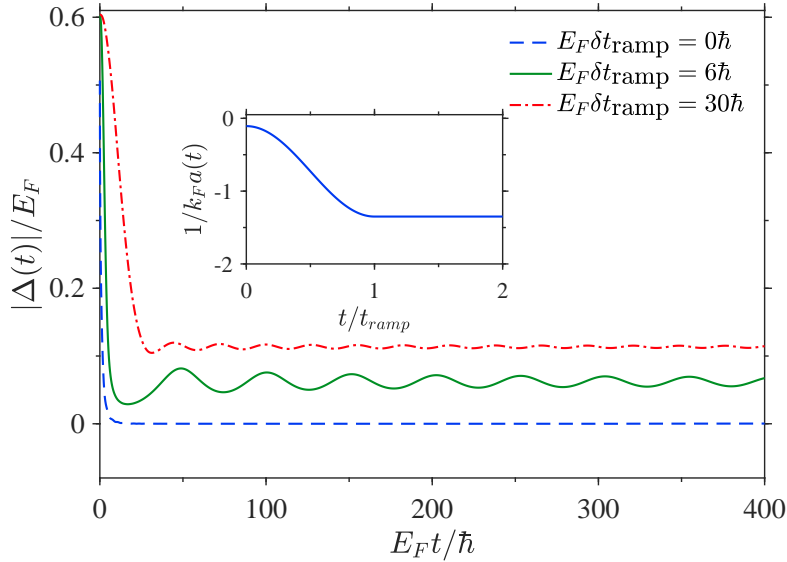


Figure 5.1: Time evolution of the superconducting order parameter $|\Delta(t)|$ as a function of time, as the interaction strength is ramped down from $1/(k_F a) = -0.1072$ to $1/(k_F a) = -1.3493$ ($|\Delta_{0,i}| = 0.60E_F$ and $|\Delta_{0,f}| = 0.11E_F$). Shown are three different ramp durations $E_F \delta t_{ramp} = \{0, 6, 30\} \hbar$, representing the three distinct dynamical regimes of the system. The inset depicts the ramp schedule for the dimensionless interaction parameter $1/(k_F a(t))$.

We will focus on the dynamical region where an interaction quench would result in the vanishing of the superconducting order parameter. As we vary the *duration* of the ramp however, we observe the emergence of three different dynamical regimes. In Fig. 5.1, we show examples of the evolution of Δ in those three distinct regimes. For fast ramps the superconducting order parameter in the long-time asymptotic limit decays to zero and superconductivity is destroyed. For intermediate ramp durations we retain a finite order parameter, which exhibits oscillations around its asymptotic value. For even slower ramps, in the adiabatic limit, the BCS gap fol-

lows the instantaneous interaction and the system remains in its ground state throughout the evolution. The final gap value agrees with the equilibrium gap at zero temperature and the oscillations are vanishingly small. Shown is a ramp duration, $E_F \delta t_{ramp} = 30\hbar$ which is not quite in the adiabatic limit, i.e. we still have small but finite oscillations on top of the overall dynamics. In the remainder of this chapter, we detail further the three regimes and the subtle mechanism responsible for the dynamics.

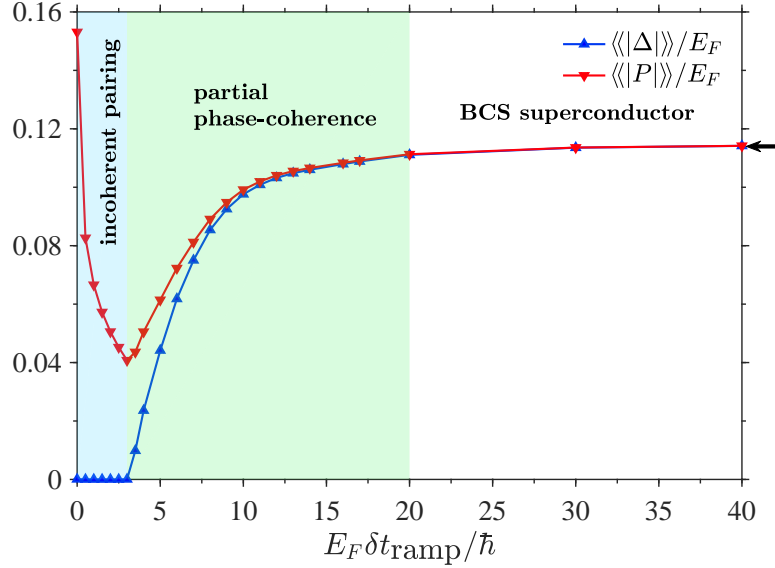


Figure 5.2: Time-averaged value of the superconducting order parameter, $\langle\langle \Delta \rangle\rangle$, and of the sum over the magnitude of the pair amplitudes, $\langle\langle |P| \rangle\rangle$, as a function of ramp duration. The interaction strength is ramped down from $1/(k_F a) = -0.1072$ ($|\Delta_{0,i}| = 0.60E_F$) to $1/(k_F a) = -1.3493$ ($|\Delta_{0,f}| = 0.11E_F$), and the time-average is taken between $100\hbar/E_F$ and $400\hbar/E_F$. These two quantities signal three different dynamical regimes. For short quenches, the system is characterised by pre-formed pairs (incoherent pairing state). For intermediate quench durations, superconductivity is maintained but with only partial phase coherence; while, for longer ramp times, phase coherence is mostly unaffected and the order parameter asymptotes to $|\Delta_{0,f}|$ (value marked by the arrow). The boundary between the partial phase coherence and BCS superconductor regimes is located at $|\langle\langle |\Delta| \rangle\rangle - \langle\langle |P| \rangle\rangle| \sim 10^{-4}E_F$.

The main results of this chapter are summarised in Fig. 5.2 which shows the different dynamical regimes as a function of ramp duration δt_{ramp} . We show the time averaged value of the order parameter $\langle\langle |\Delta| \rangle\rangle$ and the net pair amplitude $\langle\langle |P| \rangle\rangle$. We take the time average of a quantity $f(t)$ to be

$$\langle\langle f(t) \rangle\rangle = \frac{1}{\delta t} \int_{t_0}^{t_0 + \delta t} dt f(t), \quad (5.5)$$

with $E_F t_0 = 100\hbar$ the beginning of the averaging window, chosen well after the end of the ramp, and $E_F \delta t = 300\hbar$ its duration, taken suitably long to average over several oscillations

5.2 Finite-Duration Quenches: Emergence of Pre-Formed Pairs

in the post-ramp state. While $\langle\langle|\Delta|\rangle\rangle$ is found to average to zero for fast ramps up to $3\hbar/E_F$, it acquires a finite value for intermediate (and slower) ramp times. The precise ramp duration at which the crossover occurs depends on the interaction strength and the cutoff. In contrast to this, $\langle\langle|P|\rangle\rangle$, remains finite for all ramp times, indicating that the phase coherence between the Cooper pairs is crucial to the observed dynamics. As the amplitude of pairs is reduced but remains finite, the destruction of superconductivity for short ramp durations is associated with the loss of phase coherence between pairs. Therefore, phase unlocking is the main mechanism responsible for the suppression of superconductivity, and a state made of incoherent pre-formed pairs, the so-called phase disordered superconductor [196], is stabilised.

In an equilibrium thermal state, superconductivity is suppressed by thermal fluctuations increasing the pair breaking. This is fundamentally different from the mechanism observed here, which implies that stabilising a state made of pre-formed pairs is possible via a fast ramp. This state is long-lived within the scope of BCS theory, but experimentally the presence of decay mechanisms (e.g. electron-phonon coupling in solids) will affect the long-time stability of this state.

Surprisingly, $\langle\langle|P|\rangle\rangle$ exhibits a non-monotonic behaviour with the ramp duration, decreasing at first for short ramp times and then increasing subsequently. For a sudden quench, the initial BCS state is frozen and projected onto the new quasiparticle basis. In this new basis, the initial BCS state is made up of excited quasiparticle pairs which contribute to the net pair amplitude. Since these quasiparticle pairs are incoherent, their contributions to Δ dephase quickly, resulting in the suppression of the superconducting order parameter. For fast ramps this same mechanism persists until $\langle\langle|P|\rangle\rangle$ is minimal. As we increase the ramp duration further, the Cooper pairs retain part of their long-range coherence, so that they contribute to an overall finite value at later times. To understand the physical mechanism underlying these different regimes, in the following we will carefully analyse the momentum-resolved order parameter $\Delta_{\mathbf{k}}$ in the three dynamical regimes.

Quenches and Fast Ramps

As displayed in the top panel (a) of Figs. 5.3, 5.6 and 5.7, initially the distribution of pair amplitudes is given by its ground state expression $\Delta_{\mathbf{k}} = \frac{1}{2}\sqrt{1 - \xi_{\mathbf{k}}^2/E_{\mathbf{k}}^2}$ with $\xi_{\mathbf{k}} = \epsilon_{\mathbf{k}} - \mu_i$, where μ_i is the chemical potential at the initial interaction strength. For $\frac{1}{k_F a} = -0.1072$, this distribution (see curve (i)) has a relatively broad peak close to the Fermi momentum, while the distribution corresponding to the final ground state for $\frac{1}{k_F a} = -1.3493$ (see curve (ii)) is strongly peaked around the Fermi momentum and much lower in value.

To understand the time evolution of the distribution of pair amplitudes, we look at snapshots of $|\Delta_{\mathbf{k}}|$ for particular times as well as its time-average $\langle\langle|\Delta_{\mathbf{k}}|\rangle\rangle$. For the sudden ramp, shown in Fig. 5.3, the $|\Delta_{\mathbf{k}}|$ distribution at $E_F t = 3\hbar$ already agrees reasonably well with the time-averaged one, and shows relatively little dynamics in the long-time limit. However, even at long times, it does not resemble the distribution expected in equilibrium at the final interaction strength $\frac{1}{k_F a} = -1.3493$. The finite value of the pair distribution explains why we observe a finite value of $\langle\langle|P|\rangle\rangle$ in Fig. 5.2, and implies that Cooper pairs survive through the quench albeit with a smaller amplitude than in the initial state.

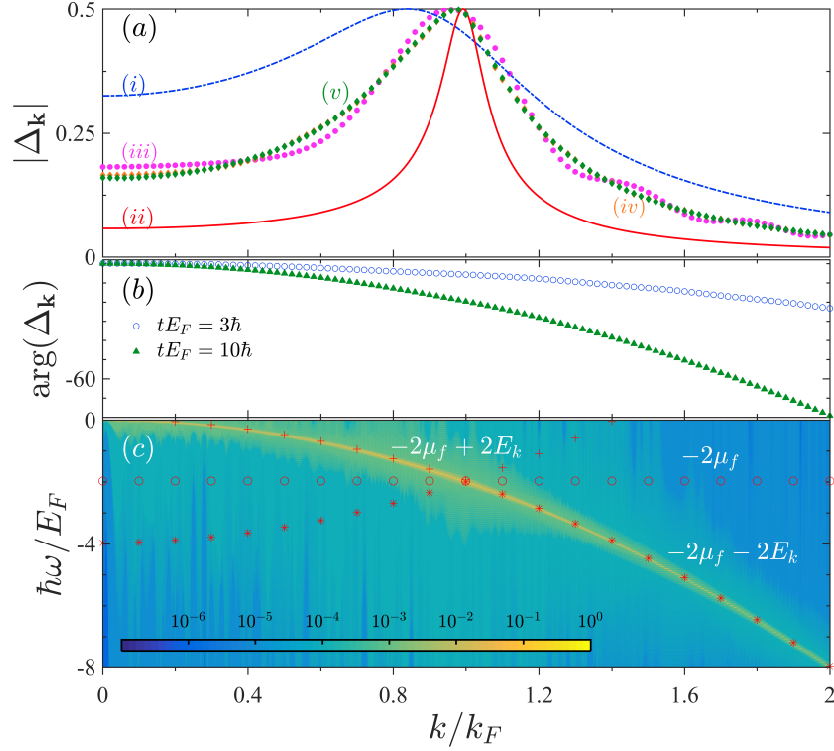


Figure 5.3: Sudden quench of the interaction strength from $1/(k_F a) = -0.1072$ to $1/(k_F a) = -1.3493$. (a) Distribution of the magnitude of the pair amplitude as a function of momentum: (i, blue) ground state at $1/(k_F a) = -0.1072$; (ii, red) ground state at $1/(k_F a) = -1.3493$; (iii, pink) snapshot at $3\hbar/E_F$; (iv, orange) snapshot at $10\hbar/E_F$; and (v, green) time-average between $100\hbar/E_F$ and $400\hbar/E_F$. This distribution is already hardly distinguishable from its steady-state configuration at $10\hbar/E_F$. It is non-thermal and signals the presence of pre-formed pairs. (b) Phase of the pair amplitude as a function of momentum. Rapid phase unlocking is responsible for the destruction of superconductivity. (c) Fourier transform of the momentum-dependent pair amplitude $|\mathcal{F}\{\Im[\Delta_{\mathbf{k}}(t)]\}|$. The sudden quench generates quasiparticle pair excitations along the parabolic line $\pm 2E_k - 2\mu_f$ (marked by the red crosses and stars respectively; red circles mark the coherent evolution at $2\mu_f$). ©2019 American Physical Society, published in [57].

5.2 Finite-Duration Quenches: Emergence of Pre-Formed Pairs

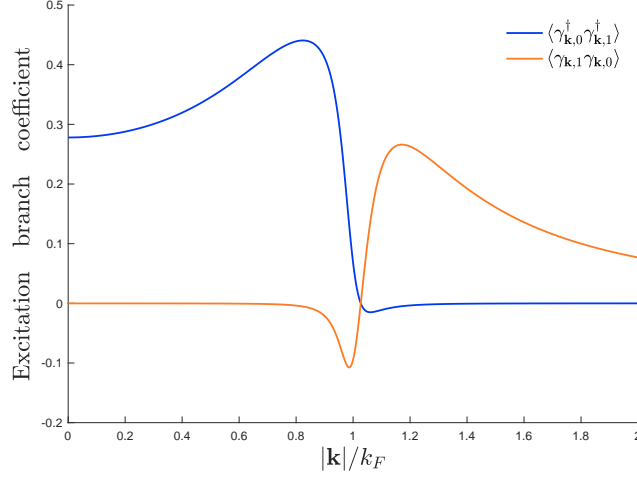


Figure 5.4: Coefficients of the quasiparticle excitation branches $\pm 2E_{\mathbf{k}}$, activated by a sudden quench from $1/(k_F a) = -0.1 \rightarrow -1.3$. $\langle \gamma_{k,0}^\dagger \gamma_{k,1}^\dagger \rangle$ is activated for $k \lesssim k_F$, while $\langle \gamma_{k,1} \gamma_{k,0} \rangle$ above the Fermi momentum, $k \gtrsim k_F$.

In the central panel of Fig. 5.3, we show the phase of each Cooper pair. Strikingly, the pairs seem to rapidly acquire a phase proportional to $2E_{\mathbf{k}}$ leading to complete dephasing such that already at $E_F t = 10\hbar$ the superconducting order parameter is zero (c.f. Fig 5.1). This can be understood by looking at the Fourier transform of the pair amplitudes. Since $\Im[\Delta_{\mathbf{k}}(t)]$ and $\Re[\Delta_{\mathbf{k}}(t)]$ provide the same information about the phase evolution, we only consider the former without loss of generality. The sudden quench generates quasiparticle pairs at $-2\mu_f \pm 2E_{\mathbf{k}}$ (see lower panel of Fig. 5.3) with μ_f the chemical potential at the final interaction strength. To understand why a quench couples predominantly to the quasiparticle excitations, we analysed the spectral weight of the quasiparticle excitation branches for an abrupt quench analytically. The details of the calculations can be found in appendix B.1 and we only quote the main result here:

$$\begin{aligned} \langle \Delta_{\mathbf{k}}(t) \rangle &= U_{\mathbf{k}}^* V_{\mathbf{k}} - 2U_{\mathbf{k}}^* V_{\mathbf{k}} (-u_{\mathbf{k}}^* V_{\mathbf{k}}^* + v_{\mathbf{k}}^* U_{\mathbf{k}}^*) (-u_{\mathbf{k}} V_{\mathbf{k}} + v_{\mathbf{k}} U_{\mathbf{k}}) \\ &\quad + U_{\mathbf{k}}^2 (u_{\mathbf{k}}^* U_{\mathbf{k}} + v_{\mathbf{k}}^* U_{\mathbf{k}}) (-u_{\mathbf{k}} V_{\mathbf{k}} + v_{\mathbf{k}} U_{\mathbf{k}}) e^{-i2E_{\mathbf{k}} t/\hbar} \\ &\quad - V_{\mathbf{k}}^2 (u_{\mathbf{k}} U_{\mathbf{k}}^* + v_{\mathbf{k}} U_{\mathbf{k}}^*) (-u_{\mathbf{k}}^* V_{\mathbf{k}}^* + v_{\mathbf{k}}^* U_{\mathbf{k}}^*) e^{i2E_{\mathbf{k}} t/\hbar}, \end{aligned} \quad (5.6)$$

where $u_{\mathbf{k}}$ ($U_{\mathbf{k}}$) and $v_{\mathbf{k}}$ ($V_{\mathbf{k}}$) are the initial (final) Bogoliubov Cooper pair amplitudes as introduced in Eq. 2.24. Crucially, for an abrupt quench we find that the dynamical response of $\Delta_{\mathbf{k}}$ is dictated by quasiparticle excitations at an energy $\pm 2E_{\mathbf{k}}$. Fig. 5.4 shows the prefactors of these quasiparticle excitation branches ($e^{\pm i2E_{\mathbf{k}} t/\hbar}$) as a function of momentum. We can conclude that a quench couples strongly to both the $\langle \gamma_{k,0}^\dagger \gamma_{k,1}^\dagger \rangle$ ($k \lesssim k_F$) and $\langle \gamma_{k,1} \gamma_{k,0} \rangle$ ($k \gtrsim k_F$) branches of the quasiparticles. Since the Cooper pairs dephase quickly and the BCS gap vanishes, the two excited, distinct parts of the quasiparticle branches appear as one continuous parabolic

excitation line (c.f. the phase evolution in the central panel (b)). This result indicates that the system dynamically organises into a non-thermal state made of pre-formed but dephased Cooper pairs.

Intermediate Ramp Times

For intermediate ramp durations, the coupling to the quasiparticles is reduced, which means that the phases do not unlock fully and a finite order parameter is retained. To check whether the reduction of the BCS gap can be understood as a thermally excited final state, we solve the finite temperature gap equation, Eq. 2.30, as discussed in chapter 2. The temperature dependence of Δ is depicted in Fig. 5.5. We now use the constructed $\Delta(T)$ to extract an effective temperature T from Fig. 5.1 by assuming that $\langle\langle|\Delta|\rangle\rangle = \Delta(T)$.

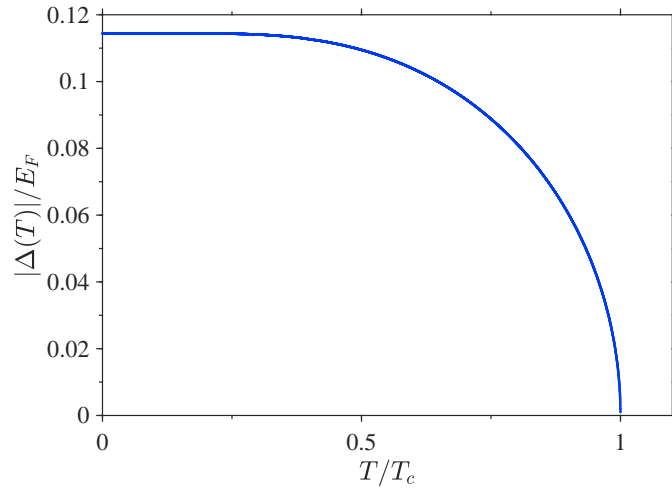


Figure 5.5: Superconducting order parameter $|\Delta(T)|$ as a function of temperature. For $T > T_c$ the system is in the normal phase, whilst below the transition temperature the order parameter acquires a finite value, signalling the emergence of an ordered (here superconducting) state and a spontaneous breaking of the underlying U(1) symmetry of the Hamiltonian.

For the ramp duration $E_F \delta t_{ramp} = 6\hbar$ (Fig. 5.6 a), both the snapshots and time-averaged distributions are clearly finite and non-thermal, since only the small and large momentum tails of $\langle\langle\Delta_{\mathbf{k}}\rangle\rangle$ agree with the thermal equilibrium distribution at $\frac{1}{k_F a} = -1.3493$.

As we see in the lower panel (c) of Fig. 5.6, the intermediate ramp creates fewer quasiparticle pairs at $-2\mu_f \pm 2E_{\mathbf{k}}$ and the contour plot of the Fourier transform of $\Im(\Delta_{\mathbf{k}})$ signals a strong component at $-2\mu_f$. In appendix B.2 we show that the unquenched BCS state evolves freely with a time-dependence $e^{-2\mu t/\hbar}$. It is this free evolution, which we also observe here in the Fourier content (lower panel). Regarding the central panel (b), at short times compared to the ramp duration, the phases remain fully locked. As the evolution goes on, in the momentum region where most quasiparticles are excited, the Cooper pairs begin accumulating individual phases. This process leads to a partial loss of phase coherence, but Cooper pairs are still sufficiently synchronised for superconductivity to survive as can be seen from Fig. 5.2.

5.2 Finite-Duration Quenches: Emergence of Pre-Formed Pairs

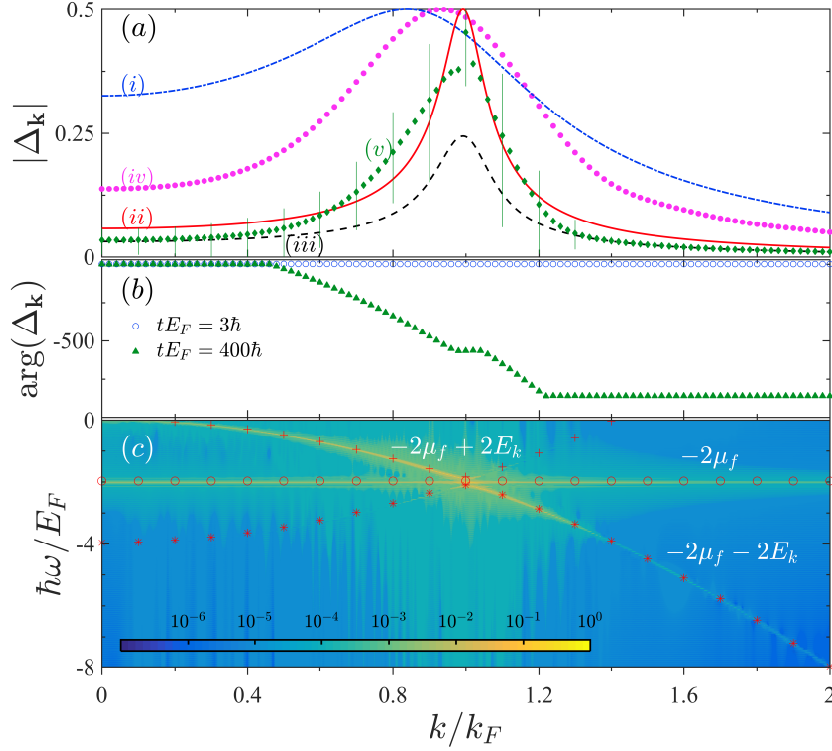


Figure 5.6: Intermediate quench performed in $E_F \delta t_{ramp} = 6\hbar$ (same interaction strengths as in Fig. 5.3). (a) Distribution of the magnitude of the pair amplitude as a function of momentum: (i, blue) and (ii, red) same as in Fig. 5.3; (iii, black) thermal distribution at $1/(k_F a) = -1.3493$, $T = 0.89T_c$ is chosen such that $\langle\langle \Delta \rangle\rangle = \Delta(T)$; (iv, pink) snapshot at $3\hbar/E_F$; (v, green) time-average between $100\hbar/E_F$ and $400\hbar/E_F$. The time-averaged distribution is non-thermal, and $|\Delta_{\mathbf{k}}|$ exhibit strong oscillations represented, together with (v), by vertical bars (peak-to-peak amplitude of the oscillations). (b) Phase of the pair amplitude as a function of momentum. (c) Fourier transform of the momentum-dependent pair amplitude $|\mathcal{F}\{\Im[\Delta_{\mathbf{k}}(t)]\}|$. While this quench generates quasiparticle pair excitations, all $\Delta_{\mathbf{k}}(t)$ signals have a strong in-phase component at $2\mu_f$. ©2019 American Physical Society, published in [57].

Slow Ramp Times and the Adiabatic Regime

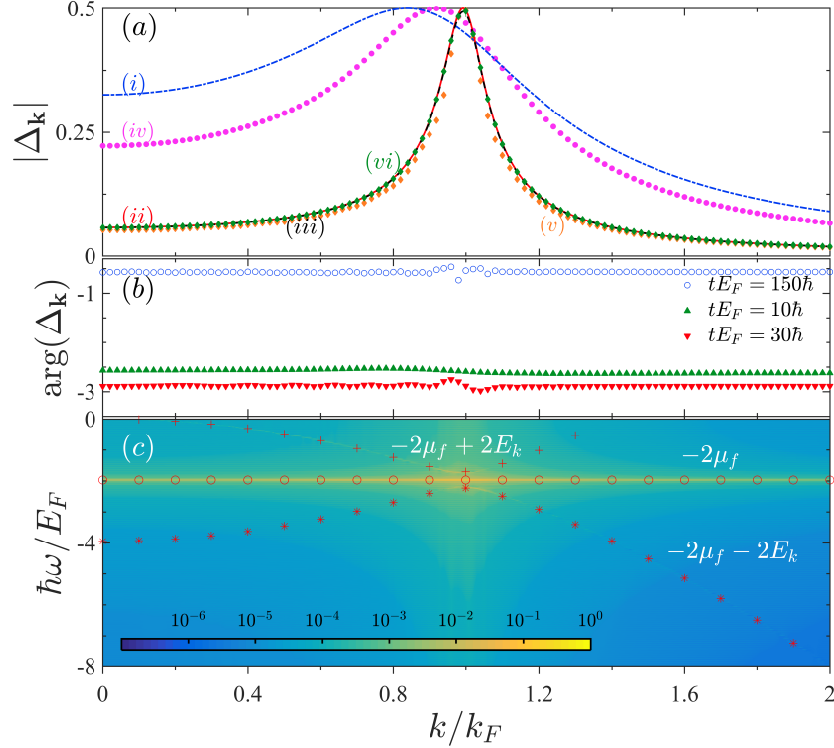


Figure 5.7: Slow quench performed in $E_F\delta t_{ramp} = 30\hbar$ (same interaction strengths as in Fig. 5.3). (a) Distribution of the magnitude of the pair amplitude as a function of momentum: (i, blue) and (ii, red) same as in Fig. 5.3; (iii, black) thermal distribution at $1/(k_F a) = -1.3493$, $T = 0.35T_c$ is chosen such that $\langle\langle\Delta\rangle\rangle = \Delta(T)$; (iv, pink) snapshot at $10\hbar/E_F$; (v, orange) snapshot at $30\hbar/E_F$; (vi, green) time-average between $100\hbar/E_F$ and $400\hbar/E_F$. The steady-state distribution is thermal (b) Phase of the pair amplitude as a function of momentum. Phase coherence is only slightly lost near k_F . (c) Fourier transform of the momentum-dependent pair amplitude $|\mathcal{F}\{\Im[\Delta_{\mathbf{k}}(t)]\}|$. Quasiparticle pairs are only generated near k_F (red crosses and stars). $\Delta_{\mathbf{k}}$ is dominated by the coherent phase evolution at $-2\mu_f$. ©2019 American Physical Society, published in [57].

Finally, for $E_F\delta t_{ramp} \geq 20\hbar$, we find that the dynamics enters a new, thermal regime, where we can assign a meaningful temperature to the system. As can be seen from Fig. 5.7, for a slow ramp of $E_F\delta t_{ramp} = 30\hbar$ the pair amplitude distribution at the end of the ramp strongly resembles that of a thermal system in equilibrium at $T = 0.35T_c$. Here, quasiparticle pairs are solely generated in a small momentum region around k_F (see lower panel (c) of Fig. 5.7), and the phase coherence remains intact and is largely undisturbed by the ramp. As illustrated in the central panel (b) of Fig. 5.7, during the ramp the phase starts to mildly unlock close to k_F , coinciding with the momenta at which quasiparticle pairs are being activated. However phase locking is still the dominant factor and long-range phase coherence is maintained throughout

5.3 Numerical Convergence

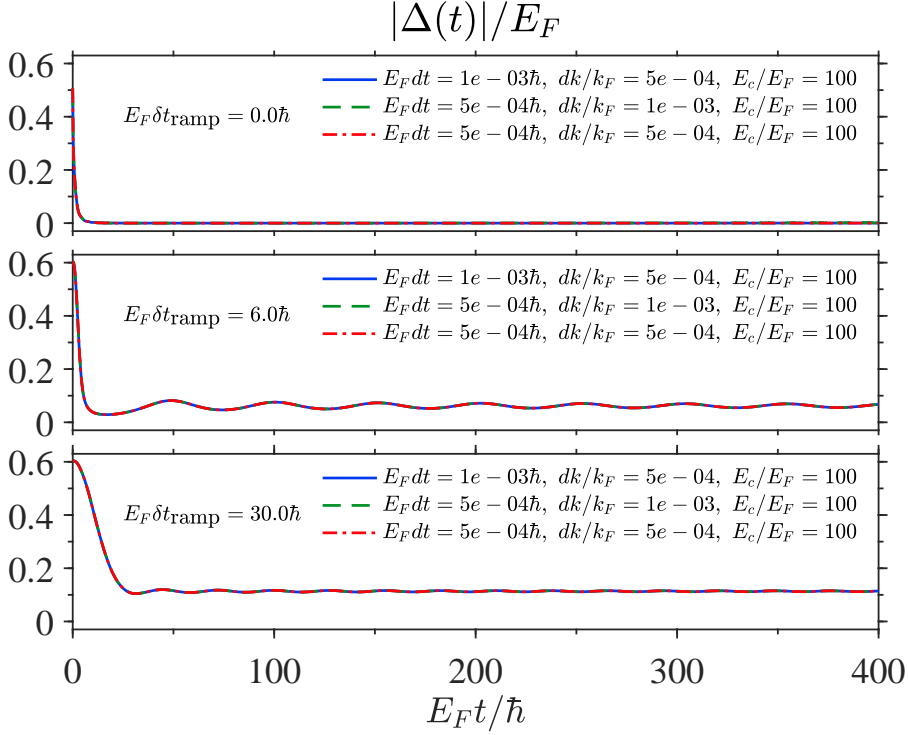


Figure 5.8: Convergence of $|\Delta(t)|$ with time step dt , and momentum spacing dk . The different panels show simulations for $E_F\delta t_{\text{ramp}} = \{0, 6, 30\}\hbar$ respectively. Deviations in dt and dk are smaller than the linewidth and we conclude that the simulations are well converged. Since the energy cutoff directly affects the renormalised interaction strength, the numerical values will quantitatively differ. However, we checked that even despite this, the disagreement is small and the overall *behaviour* agrees qualitatively well.

the system.

The BCS state evolves freely with a frequency $2\mu/\hbar$. For very slow (nearly adiabatic) ramps as considered here, the Cooper pairs can follow the instantaneous value of the interaction strength and therefore stay coherent with each other. The evolution is predominantly dictated by the chemical potential, with only minor deviations near the Fermi edge, where few quasiparticle pairs are excited. In summary, the ramp duration controls the strength of the coupling to the quasiparticle excitations, and thereby the phase coherence of the Cooper pairs making up the superfluid state.

5.3 Numerical Convergence

The simulations were performed using the same numerical approach as for the Higgs mode (chapter 4). In Fig. 4.6 we have explicitly shown the convergence of the simulation for the time step dt , and the momentum spacing dk . Since here we are *not* driving the system continuously, and perform rather slow interaction changes in the majority of cases, we can expect the data to be equally well converged. Nevertheless, Fig. 5.8 and 5.9, show the convergence of $|\Delta(t)|$ and

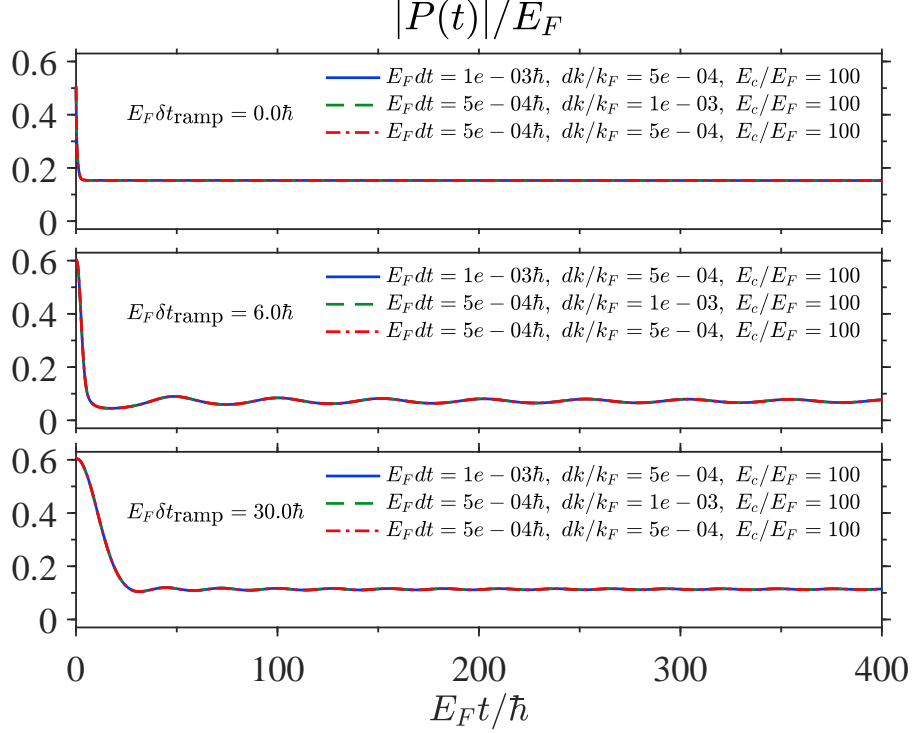


Figure 5.9: Convergence of $|P(t)|$ with time step dt , and momentum spacing dk . The different panels show simulations for $E_F \delta t_{\text{ramp}} = \{0, 6, 30\} \hbar$ respectively. Deviations in dt and dk are smaller than the linewidth and we conclude that the simulations are well converged. Since the energy cutoff directly affects the renormalised interaction strength, the numerical values will quantitatively differ. However, we checked that even despite this, the disagreement is small and the overall *behaviour* agrees qualitatively well.

$|P(t)|$ for the different parameters in the simulation. The time step dt and momentum spacing dk are very well converged, the deviations being smaller than the linewidth of the curves. As discussed in section 4.4.1, it is important to remember that the contact interaction was renormalised for the purpose of our numerical simulations, whereby the interaction becomes directly related to the energy cutoff E_c . Therefore a direct, quantitative comparison of the different convergence data in E_c is not possible. More importantly what we should look for is a qualitative agreement in the overall physics. We have checked this and indeed found this to be the case, the dynamics inside the different quench regimes are well reproduced for a larger energy cutoff E_c . We can therefore be confident that our results are robust and converged with respect to all relevant parameters.

5.4 Conclusion and Outlook

To summarise, we analysed the non-equilibrium dynamics of dilute, attractively interacting Fermi gases described within BCS theory subject to finite-duration ramps of the internal interaction strength. We identified three different dynamical regimes depending on the duration

5.4 Conclusion and Outlook

of the interaction ramp. For abrupt and sufficiently fast quenches, the superconducting order parameter decays to zero without oscillations and superconductivity is destroyed, but pairs are still present in the system. The Fourier content of the momentum-resolved order parameter $\Delta_{\mathbf{k}}$ sheds light upon the physical origin underlying the dynamical response of the system. Fast ramps strongly couple to the quasiparticle excitations of the superfluid, which quickly dephase. This leads to a loss of phase coherence between the Cooper pairs, and demonstrates the possibility to dynamically create a steady state of pre-formed pairs without global phase coherence. For intermediate ramp times, partial phase coherence amongst the pairs is retained due to a diminished coupling to quasiparticle excitations. The superconducting order parameter is consequently lowered in amplitude and exhibits long-lived oscillations around its asymptotic value, while the pair amplitude follows a non-thermal distribution. Finally, for slow ramps, the Cooper pairs in the system can follow the instantaneous interaction strength and the system adiabatically connects to the final equilibrium state. The gap is smoothly lowered to its new value with oscillations largely absent in the final state. This work paves the way to employ slow quenches to create steady states with novel properties absent in thermal equilibrium.

Radiofrequency Spectroscopy of Ultracold Fermions: Probing the Excitations of the Fermi-Hubbard Model

Radiofrequency (rf) spectroscopy has established itself as a powerful experimental probe to study the equilibrium properties of ultracold atomic gases [111, 114]. Based on the idea of coherent transfer between different internal states of the atom (e.g. different hyperfine levels of the electronic ground state manifold), rf-spectroscopy has been successfully applied to measure (unitarity-limited) ‘clock’ shifts around a Feshbach resonance [108, 197, 198], and study pairing and molecule formation on the BEC side of the Feshbach resonance [199–202], as well as the excitation spectrum and underlying pairing gap of interacting Fermi gases [85, 115, 203]. More recently, a spatially resolved rf-technique has been developed [204], circumventing complications of density inhomogeneities in harmonically trapped gases, while the momentum-resolved rf-spectroscopy introduced in [106] gives direct access to the spectral function.

Commonly, the obtained rf-spectra are interpreted within the framework of linear response. Here, the rf-field is assumed to only weakly perturb the system, thus probing the unperturbed, equilibrium system. In this limit, satisfied for rf-pulses short compared to the Rabi period, the transfer rate is related to a response function. In the absence of final state interactions, the expression simplifies and the transferred particle rate can be shown to be directly related to the single-particle spectral function [109, 113, 114, 205], as observed in [106].

Here we investigate the response of an interacting ultracold Fermi gas driven away from equilibrium by radiofrequency radiation. We use the one-dimensional, attractively interacting Fermi-Hubbard model, introduced in section 2 and discussed in further detail in section 3.4, to model the evolution of the degenerate quantum gas, confined to an optical lattice. The chapter is organised as follows. We will explore the ensuing dynamics and discuss the emerging regimes, depending on the driving frequency of the rf-field. The rf-field couples fermions of species $|2\rangle$ in the initial, correlated manifold, with a third fermionic species $|3\rangle$, here modelled as a free upper band. Starting from our intuition of the non-interacting system, we begin by discussing a weakly interacting Fermi-Hubbard model in section 6.1. With current experimental setups in

6.1 Weakly attractive Fermi-Hubbard model

mind, we use a combination of analytic Bethe ansatz and linear response theory calculations, as well as numerically quasi-exact t-MPS simulations, to comprehensively explore the evolution of the system during the drive. To that end, we monitor both the (momentum-resolved) population of the upper level $|3\rangle$ as well as the pair correlations in the initial $|12\rangle = |1\rangle \otimes |2\rangle$ manifold. Our investigations reveal two distinct dynamical regimes in the evolution of the mentioned observables: an oscillatory regime akin to the Rabi-physics of the non-interacting system, and a linear response regime, indicating the rf-coupling to a continuous band of excitations in the final state. By carefully monitoring the dynamics of the momentum-resolved populations, we are able to gain a detailed understanding of the underlying excitation spectrum of the system, and can infer which excitations the rf-field is most strongly coupled to. Throughout this study, we compare our numerical findings to exact results obtained from Bethe ansatz.

Subsequently, we turn to a strongly interacting system in section 6.2 where we compare and contrast our findings to the weakly interacting model. We have performed a careful convergence analysis of the presented results and included the convergence checks into the Figures showing the main results. Unless otherwise stated, our results were obtained from time-dependent matrix product state simulations with a bond dimension of $D = 500$, truncation error $\epsilon = 10^{-12}$, and Suzuki-Trotter time step $dt = 0.005\hbar/J$.

The present work aims to explore the intricate nature of the rf-transfer and paint a detailed picture of the potential for using rf-spectroscopy to study fermionic gases in experimentally realistic settings. As such, our discussions are relevant to rf-spectroscopy studies, and are also amenable to investigations of multi-orbital, interacting quantum many-body systems [206, 207]. The central results of this chapter are currently being prepared for publication.

6.1 Weakly attractive Fermi-Hubbard model

Consider the Fermi-Hubbard model introduced in chapter 2, which is coupled to an upper, free band by a weak radiofrequency modulation. In this way, the setup is similar to the already discussed Higgs mode in the BCS-BEC crossover (c.f. chapter 4), but here we consider a one-dimensional quantum lattice model. Bearing in mind our discussions of the t-MPS algorithm in chapter 3, this allows us to *exactly* treat the interacting many-body problem *beyond* the mean-field approximation and without invoking a rotating-wave approximation. Rather, we here study the fully interacting, time-dependent problem.

It is instructive to briefly recall the physics of the non-interacting system discussed in section 2.5.2. The rf-field couples different hyperfine levels of the quantum gas and, depending on the driving frequency, we observe (off)resonant Rabi oscillations in the momentum-resolved upper level population $\langle n_{k,3}(t) \rangle$, Eq. 2.60. Turning on the interactions, in the initial state of the $|12\rangle$ manifold, $U = -2J$, this simple two-level picture gives rise to a complex pattern of intricate dynamics, as the amplitude and form of the rf-transfer become very sensitive to the various drive parameters. We begin in 6.1.1 by considering the time dependence of the momentum-resolved transfer to level $|3\rangle$, an observable which illustrates best the different dynamical regimes observed. We discuss in which situations Rabi-like or linear response behaviours are observed. Section 6.1.3 addresses the momentum distribution of the three levels, whilst 6.1.4 discusses the pairing evolution between levels $|1\rangle$ and $|2\rangle$. Finally, we conclude this section by commenting,

in 6.1.5, on the evolution of the experimentally most accessible quantity, the spectrum of the upper level population N_3 .

6.1.1 Momentum-resolved Transfer to the third level

Fig. 6.1 shows the evolution of the momentum-resolved population $\langle n_{k,3}(t) \rangle$ for a range of driving frequencies ω_{rf} and three selected, representative momentum values: a value near zero momentum ($ka = 0.0909\pi$), one near the Fermi edge ($ka = 0.4242\pi$), and one about halfway in between ($ka = 0.2424\pi$). Generally, the transfer strongly depends on both the respective momentum and driving frequency ω_{rf} . For small frequencies, $\hbar\omega_{\text{rf}} \sim 50J$, the transfer is dominated by fast, off-resonant Rabi oscillations with relatively little transfer (blue curve in all panels). Note that $\hbar\omega_{\text{rf}} = V_3 = 50J$ was the resonance for the non-interacting system, and corresponds now, for $U = -2J$, to red-detuned driving with respect to the maximal integrated transfer as observed in N_3 occurring at $\hbar\omega_{\text{rf}} = 51.1J$. Upon increasing ω_{rf} , the oscillations become slower and larger in amplitude, while the damping increases, which we attribute to the interaction induced level mixing. At frequencies between $\hbar\omega_{\text{rf}} = 50.9J$ and $51.1J$, the transfer increases substantially, as shown in the insets.

Following the maximum transfer lines in Fig. 6.1 (green and orange lines), we observe a small shift of the maximum transfer to larger frequencies with increasing momentum. We attribute this maximal transfer to a resonance and note that the response of the system changes drastically, when driven above the resonance frequency, $\hbar\omega_{\text{rf}} \gtrsim 51.7J$. After an initial slow rise, the evolution displays a linear trend with superposed oscillations over a significant time interval. These features persist even for higher driving frequencies, but the transfer rate appears to be decreasing for increasing ω_{rf} . Unexpectedly, a second peak occurs at a second set of driving frequencies, whose values depend on the considered momentum. We also want to draw attention to a few specific driving frequencies in (a) at $\hbar\omega_{\text{rf}} = 52.5J$, (b) at $\hbar\omega_{\text{rf}} = 53.4J$, and (c) at $\hbar\omega_{\text{rf}} = 54.6J$. Contrary to its generally observed behaviour, the slope and transfer surpass previous values at lower driving frequencies, which signals a second resonance in the transfer. Lastly, once driven very far above the resonance at $\hbar\omega_{\text{rf}} = 51.1J$, one recovers again a fast oscillating signal with low net transfer, reminiscent of far blue-detuned Rabi oscillations.

We have seen how the evolution of the population of $|3\rangle$ changes from a (off)resonant Rabi-like regime, into a transfer which exhibits a strong linear background, before becoming again Rabi-like for very high driving frequencies above the resonance. To obtain a more quantitative picture, we therefore fit $\langle n_{k,3}(t) \rangle$ over an interval of $0 \leq Jt/\hbar \leq 15$ as

$$\langle n_{k,3}(t) \rangle = m(k, \omega_{\text{rf}}) t + c(k, \omega_{\text{rf}}), \quad (6.1)$$

where $m(k, \omega_{\text{rf}})$ is the slope and $c(k, \omega_{\text{rf}})$ its intercept. Examples of the fits are displayed in Fig. 6.1, and the resulting slopes are shown in Fig. 6.2. Within linear response theory (c.f. chapter 3), we expect the slope to scale with the square of the driving amplitude. Thus here we report the rescaled slopes m/Ω_{23}^2 for various momenta and two Rabi frequencies $\hbar\Omega_{23} = 0.01J, 0.1J$. Since close to resonance the evolution of the system does not show any linear background trend, we refrain from fitting here and instead show the maximum transfer value to level $|3\rangle$ over the

6.1 Weakly attractive Fermi-Hubbard model

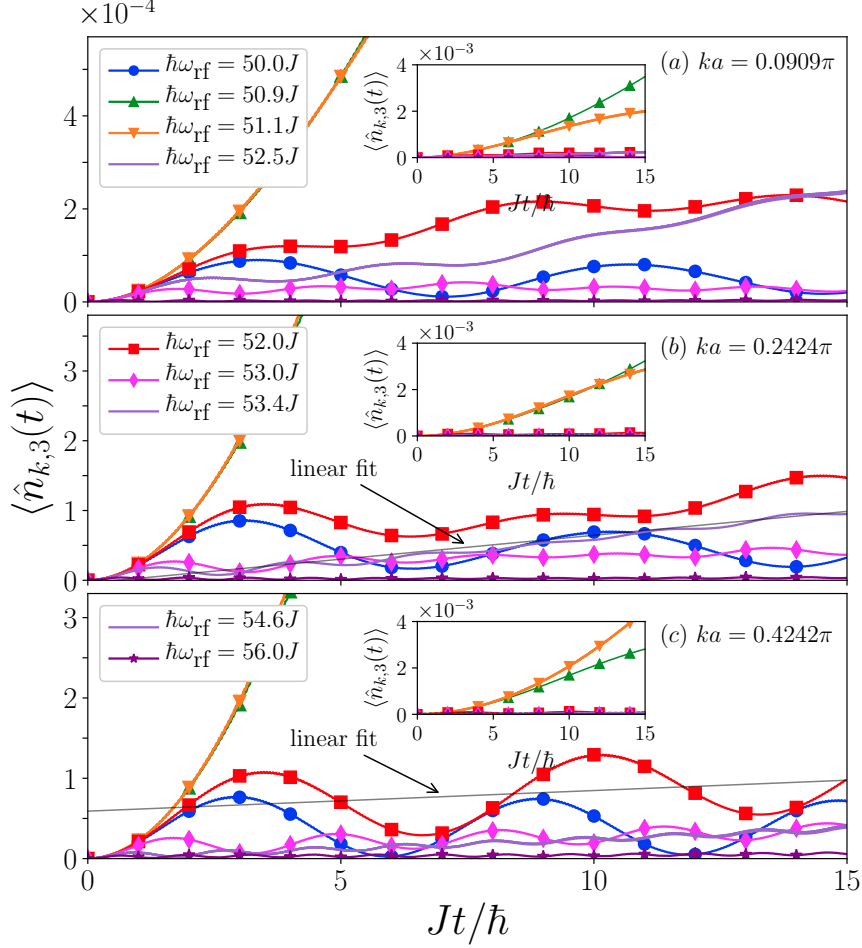


Figure 6.1: Time-dependence of the upper band population $\langle n_{k,3}(t) \rangle$ for selected momentum states at various driving frequencies ω_{rf} (labels distributed over the three panels, where only the solid line without markers changes from panel to panel as indicated) across the main resonance for a system of $L = 32$ sites at half-filling for interaction strength $U = -2J$. Level $|3\rangle$ is $V_3 = 50J$ in energy above levels $|1\rangle$ and $|2\rangle$, and the Rabi frequency is $\hbar\Omega_{23} = 0.01J$. The time-evolution can be separated into two regimes: a Rabi-like regime, occurring in the limits of driving far below or above, and near the main resonance, and a linear response regime. Full grey lines are examples of linear fits, the extracted slopes are then used to construct the spectrum shown in Fig. 6.2. (a) $ka = 0.0909\pi$; (b) $ka = 0.2424\pi$; (c) $ka = 0.4242\pi$. The insets show the same curves as a zoomed out view, to put the curve's relative transfer into perspective. To ensure convergence of our results, we have separately varied the bond dimension ($D = 400$), truncation error ($\epsilon = 10^{-13}$), and time step ($Jdt = 0.002\hbar$). The corresponding curves are overlaid for driving frequencies $\hbar\omega_{\text{rf}} = 51.1J$ (a-c), $\hbar\omega_{\text{rf}} = 52.5J$ (a), and $\hbar\omega_{\text{rf}} = 54.6J$ (c). The numerical error is therefore below the linewidth shown.

interval $0 \leq Jt/\hbar \leq 15$. The corresponding region is marked in blue shading for clarity.

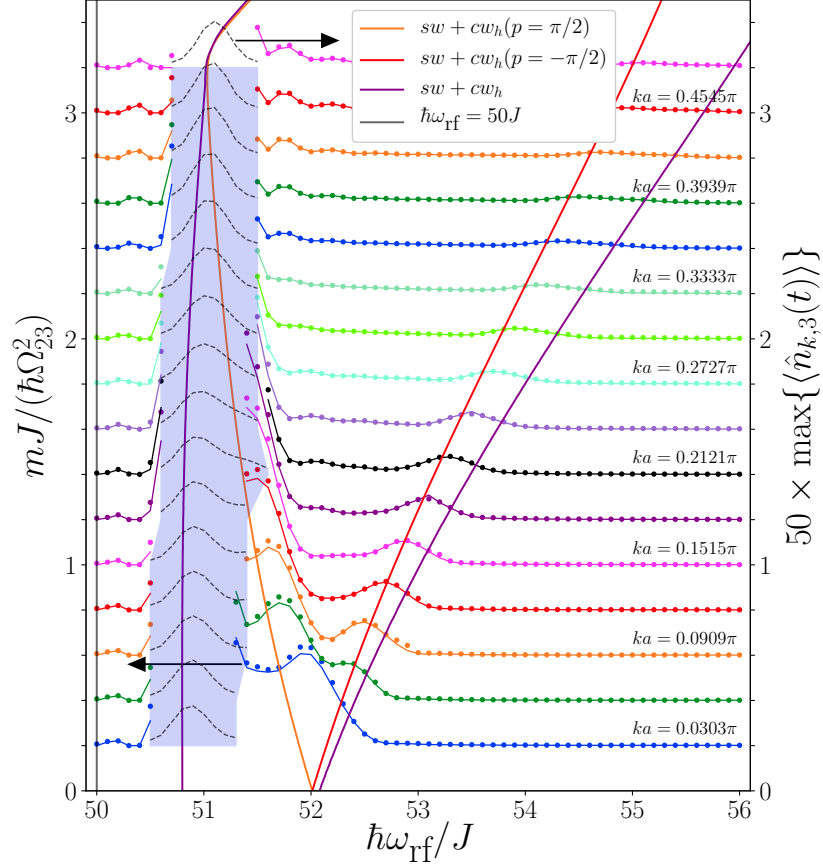


Figure 6.2: Rescaled momentum-resolved transfer rate to level $|3\rangle$, $m(k, \omega_{\text{rf}})/\Omega_{23}^2$, for a system of $L = 32$ sites at half-filling for interaction strength $U = -2J$. Level $|3\rangle$ is $V_3 = 50J$ in energy above levels $|1\rangle$ and $|2\rangle$. The dots represent the rescaled slopes for a weaker driving amplitude of $\hbar\Omega_{23} = 0.01J$, and the lines for $\hbar\Omega_{23} = 0.1J$ (left axis, see lower arrow). We find a collapse of the different Rabi frequencies, exemplifying the good agreement between the data sets. The shaded region corresponds to the frequency interval over which the time-evolution is not linear and the fitting procedure is not attempted. In this region, instead of reporting the slope, we show the maximum atom transfer in the time interval $0 \leq Jt \leq 15\hbar$ (black dashed lines, right axis, c.f. upper arrow). The momentum values are equally spaced and stacked vertically by an amount $ka(L+1)/(5\pi)$. The bold solid lines are the lower and upper limits of the spin-charge continuum (purple), and two ‘spin-wave’ excitations (orange and red lines) obtained from Bethe ansatz in section 3.4.

We observe well defined spectral features in the response, which can be understood by remembering that linear response predicts that the rescaled slope is proportional to the single-

6.1 Weakly attractive Fermi-Hubbard model

particle correlation function, $A(k, \omega_{\text{rf}})$ (see Eq. 3.47). We can therefore loosely interpret Fig. 6.2 as displaying $A(k, \omega_{\text{rf}})$ for the attractively interacting Hubbard model. Section 3.4 discussed the Bethe ansatz solution of the Fermi-Hubbard model and its excitation spectrum. We solved the thermodynamic Bethe ansatz equations for the elementary and physical excitations. Since the rf-drive couples to both charge and spin degrees of freedom, we have overlaid the extracted spectrum with the analytical spin-charge continuum excitations, taking the dispersion of the upper level into account such that $\hbar\omega_{\text{rf}} = (\epsilon_{n,k}^{\text{Bethe}} - \epsilon_{0,k}^{\text{Bethe}}) + \hbar\omega_{k,3}$. Here $(\epsilon_{n,k}^{\text{Bethe}} - \epsilon_0^{\text{Bethe}})$ is the energy of a given excitation above the ground state. The purple lines mark the lower and upper edge of the two-excitation spin-charge continuum (c.f. Fig. 3.10 lower-right panel), while the other two lines correspond to excitations within the continuum that the rf-field couples strongly to. These are either mostly of ‘spin-wave’ character, together with a gapless excitation of the opposite (charge) sector (orange and red lines)¹.

We first notice that, for driving frequencies below the spin-charge continuum, the rf-photon effectively sees the lower edge of the excitation continuum and the evolution is characterised by off-resonant Rabi oscillations. The frequencies marking the onset of the rapid rise of the maximum atom transfer are in very good agreement with the lower edge of the spin-charge continuum. For driving frequencies well within the continuum, the transfer rate is finite and we extracted a finite slope. Here the drive couples to a continuous band of excitations and Rabi oscillations from a discrete two-level system give rise to a *linear* regime [208]. We can therefore deduce that the transfer rate is a very sensitive measure to some excitations making up the continuum. Following the ‘spin-wave’ excitation line, we observe a pronounced peak in the spectrum (red and orange lines in Fig. 6.2).

Driving frequencies above the upper edge of the continuum yield a reduced slope and the response is again fast oscillating, with a low net amplitude. In this case, the energy conservation condition of Eq. 3.47 cannot be strictly fulfilled in this two-particle excitation sector, the rf-photon provides too much energy to resonantly excite spin and charge degrees of freedom leading to insufficient coupling and very weak net transfer rates. With yet higher energies of the rf-photon we would expect to eventually enter and resonantly couple to the $2n$ -particle ($n > 1$) excitation sectors.

Fig. 6.3 shows an example of the evolution of $\langle n_{k,3}(t) \rangle$ for a particular momentum of $ka = 0.0909\pi$, around the ‘spin-wave’ peak, in this case, at $\hbar\omega_{\text{rf}} = 52.5J$. As the rf-drive couples strongly to this excitation, we see that the character of the dynamics changes as the resonance is approached. Whilst the transfer is very similar from one driving frequency to the next provided $\hbar\omega_{\text{rf}} \neq 52.5J$, as the driving frequency gets closer to resonance, the transfer rate noticeably increases and the curves fan out around $Jt \sim 8\hbar$. This behaviour is observed across all momenta, when following the two excitation lines.

¹For the remainder of this chapter we will refer to these excitations as having ‘spin-wave’ character. Formally they are constructed by two elementary spin-wave, ϵ_{sw} , and charge-wave, ϵ_{cw} excitations. The spin-charge continuum is built from all momentum combinations of the two elementary excitations. The ‘spin-wave’ excitations highlighted here are built from specific, gapless charge wave excitations $\epsilon_q^{sw} + \epsilon_{q=\pi/(2a)}^{cw}$

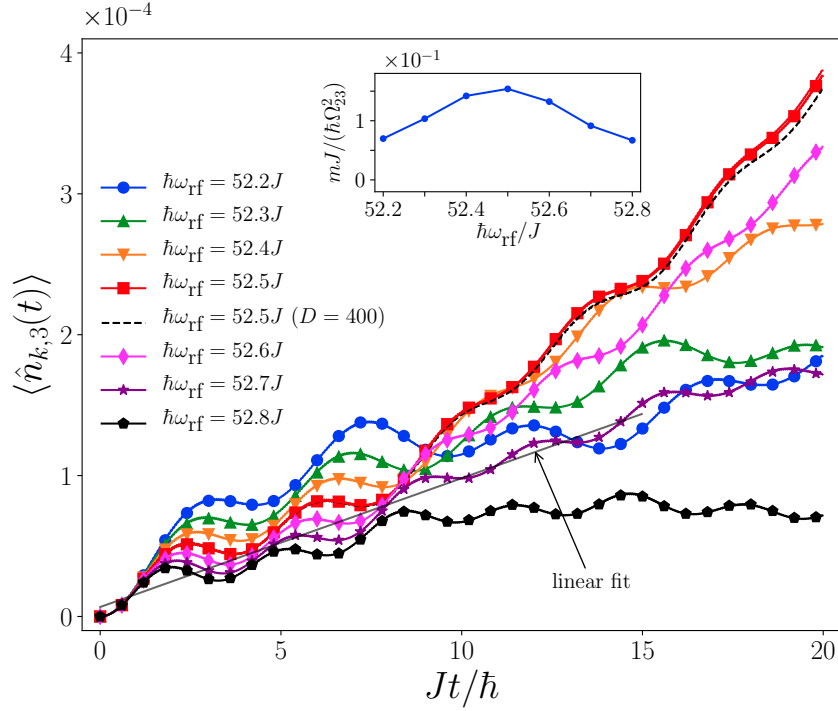


Figure 6.3: Time-dependence of $\langle n_{k,3}(t) \rangle$ at $ka = 0.0909\pi$ near the resonance at $\hbar\omega_{\text{rf}} = 52.5J$ for a half-filled system of size $L = 32$ with interaction strength $U = -2J$ and $\hbar\Omega_{23} = 0.01J$. The system coupling to a ‘spin-wave’ excitation translates into an increase of the transfer rate near the resonance and in the fanning out of the curves around $Jt \sim 8\hbar$. The full grey line is an example of linear fit, the extracted slope is reported in the inset showing a momentum slice of the single-particle excitation spectrum. To ensure convergence of our results, we have separately varied the bond dimension ($D = 400$), truncation error ($\epsilon = 10^{-13}$), and time step ($Jdt = 0.002\hbar$). The corresponding curves are overlaid for a driving frequency of $\hbar\omega_{\text{rf}} = 52.5J$. The convergence for the time step and truncation error are plotted in the same color (and the respective error is below the linewidth), while the bond dimension is explicitly shown as a black dashed line.

6.1 Weakly attractive Fermi-Hubbard model

6.1.2 Finite Size Effects

Here, we briefly comment on the influence of the considered system size onto the presented results, and discuss discrepancies one could expect to arise as finite size effects. The analytic Bethe ansatz calculations were performed in the thermodynamic limit, whilst the simulational complexity of the problem has limited us to study systems of size up to $L = 32$. Here we consider a smaller system, $L = 20$, and outline deviations to the results presented above. In general, the results obtained for a half-filled system of both system sizes are in very good agreement with one another. We recover the same dynamic regimes of Rabi-like and linear response behaviour in the upper level population and detect the same features in the spectral response from the fitted slopes.

However, for the smaller system, we find additional peaks. At half-filling and a system size of $L = 32$, we found the fanning out of the curves to occur only along two well defined excitation lines of spin-wave character, as shown in Fig. 6.3. Meanwhile, for a smaller system, this behaviour is more prominent and a recurring pattern in the spectrum inside the spin-charge continuum. We highlighted this in Fig. 6.4 for selected momentums state $ka = 0.4762\pi$. Focussing first on the lower three panels (b-d), we see that the time-evolution of $\langle n_{k,3}(t) \rangle$ is split into two regimes: for early times ('A') the different curves overlap and collapse onto each other, while at later times ('B') the curves separate and fan out. The top panel (a) depicts the extracted slopes from two different fits in the different regions, m_A and m_B . While m_A is generally a smoothly varying, decreasing function of ω_{rf} , m_B presents oscillations throughout the spin-charge continuum (the upper limit of which is marked by the purple vertical line). While the peak for $\hbar\omega_{\text{rf}} = 54.9J$ corresponds to a 'spin-wave' excitation in the continuum (red dashed line in top panel), the reason behind the existence of the other peaks is not as obvious. Additionally, the fanning out in the other peaks (b-c), highlighted in blue and green shading in the top panel (a), occurs at a later time as compared to panel (d). Meanwhile, the fanning out in (d) happens later than for the larger system size discussed in the previous section, and similar structures are absent at other driving frequencies within the spin-charge continuum. Similar behaviours were observed in [209] where the time scale marking the beginning of the fanning out was shown to be related to the inverse finite-size gap. Hence we expect to observe such a fanning out also in the larger system, but at times larger than $tJ \gtrsim 25\hbar$.

6.1.3 Evolution of the Momentum Distributions

In the following we will discuss the momentum distributions $\langle n_{k,\sigma} \rangle$ to gain further insight into the way the rf-drive excites the system. It is particularly informative to study the response of $\langle n_{k,1} \rangle$, since atoms in level $|1\rangle$ do not couple directly to the rf-field; rather their dynamics is entirely induced by the interaction with $|2\rangle$. As we have seen for the momentum-resolved transfer, we expect the changes in $\langle n_{k,2} \rangle$ and $\langle n_{k,3} \rangle$ to depend strongly on the momentum and rf-frequency. However, the redistribution in level $|1\rangle$ is largely confined to momentums states close to the Fermi edge. For weak Rabi coupling, $\hbar\Omega_{23} = 0.01J$, the net transfer is very small and the absolute momentum density $\langle n_{k,\sigma} \rangle$, with $\sigma = \{1, 2\}$, is only minimally altered during the evolution. For $\sigma = \{1, 2\}$ and $U = -2.0J$, the initial distributions follow a step-like Fermi-Dirac profile smoothed out by the effect of interaction, and with a $\sim 80\%$ drop in occupation

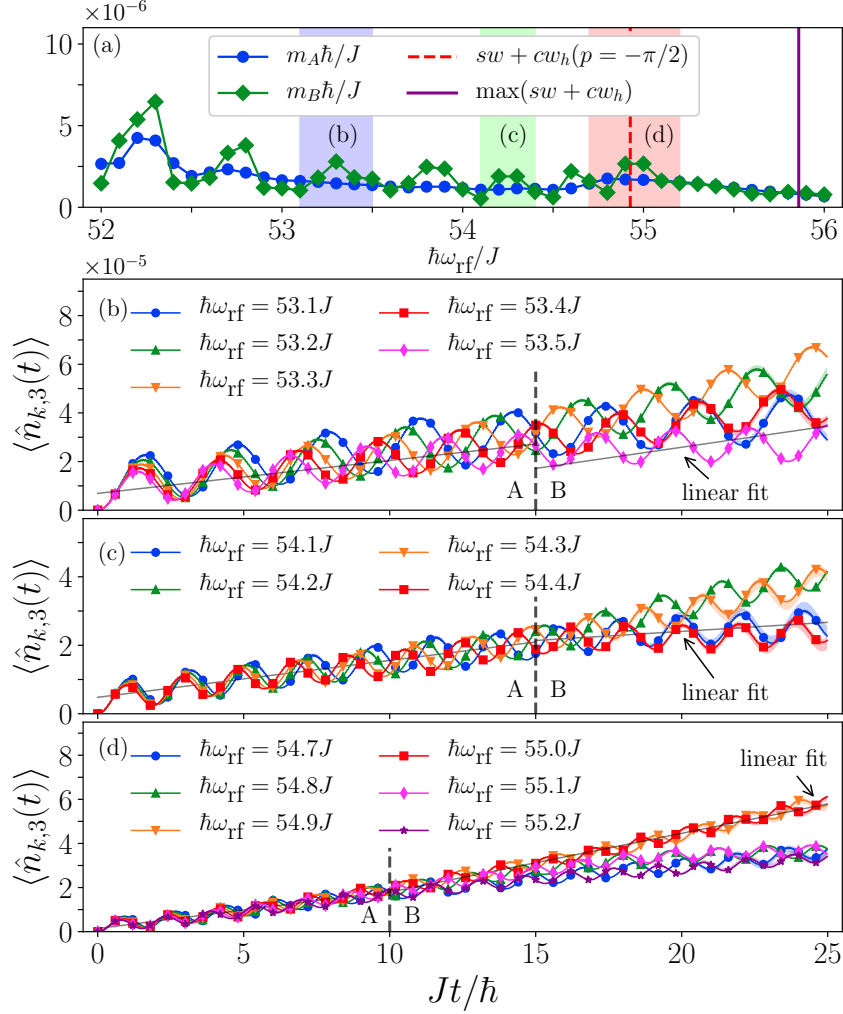


Figure 6.4: (a) Rescaled momentum-dependent transfer rates to level $|3\rangle$, m_A and m_B , for a system of size $L = 20$, $\hbar\Omega_{23} = 0.01J$ and $U = -2.0J$ for $ka = 0.4762\pi$. $\langle n_{k,3}(t) \rangle$ for the driving frequencies corresponding to the shaded regions (b), (c) and (d) is shown in the corresponding panels. In (a) the red dashed vertical line marks the position of the ‘spin-wave’ excitation and the purple dashed vertical line marks the upper limit of the spin-charge continuum. The solid grey lines (b-d) are examples of linear fits while the vertical dashed lines mark the boundary between the two fitting regions ‘A’ and ‘B’. To ensure convergence of our results, we have separately varied the bond dimension ($D = 600$), truncation error ($\epsilon = 10^{-13}$), and time step ($Jdt = 0.002\hbar$). The maximal and minimal deviation is shown as a shaded region around the corresponding curve (same colour respectively). As expected, we note that the overall error grows in time, but up to $Jt \lesssim 20\hbar$ the numerical error is still below the linewidth of the curves.

6.1 Weakly attractive Fermi-Hubbard model

around the Fermi edge. We will therefore discuss the *deviations* of the momentum distribution $\langle n_{k,\sigma}(t) - n_{k,\sigma}(0) \rangle$, as they reveal the detailed effect of the driving on the individual momentum states. In the following, we present the different regimes for driving frequencies below (red), above (blue), and on resonance to explain this structure in detail².

Red Detuning

Fig. 6.5 shows the momentum distribution for a drive, far red-detuned $\hbar\omega_{\text{rf}} = 50J$ from the resonance at $\hbar\omega_{\text{rf}} = 51.1J$. In the top panel (a) we see that $|1\rangle$ is only significantly affected close to the Fermi edge. Over time occupied states below the Fermi surface are depleted, and particles are redistributed into empty states above the Fermi edge. In comparison, (b) shows the response of $\sigma = 2$, and we note that all momenta below the Fermi edge are depleted, as would be expected from the vertical transitions induced by the rf-drive. Finally, (c) shows the distribution for $|3\rangle$, as shown in real-time in Fig. 6.1. The initial transfer is larger for smaller momenta. This can be explained by looking at the excitation spectrum as shown in the inset. The driving frequency (black vertical line) is red-detuned from all excitations, giving rise to an effective, momentum dependent detuning from the lower continuum edge (shaded region in the inset). The lower edge of the continuum (purple line in the inset) has a small curvature to higher energies (as alluded to when discussing Fig. 6.1), thereby effectively increasing the detuning with momentum. This leads to faster oscillations with lower amplitude for momentum states towards the Fermi edge, consistent with the intuition gained when considering the driving of a non-interacting system in section 2.5.2. Since the momentum is conserved by the rf-transfer and states below the Fermi surface are significantly more populated in the initial state, the population of the upper level momentum states is only appreciable below the Fermi edge $ka \lesssim \pi/2$, which we confirm from our simulations shown in (c).

Resonance

For resonant driving, Fig. 6.6, we see the assymmetric depletion of $\langle n_{k,2} \rangle$ (b) just below the Fermi edge, while $\langle n_{k,1} \rangle$ (a), purely an interaction effect, shows an almost symmetric response around the same momentum value. Correspondingly, the population of $|3\rangle$ (c) is restricted to the same momentum range as the depletion of $|2\rangle$. The Rabi oscillations in $\langle n_{k,3} \rangle$ appear to be largely in phase, but with an amplitude that is increasing towards larger momenta.

With reference to the inset, the curvature of the lower continuum implies that, whilst we are driving $ka \sim 0.4\pi$ resonantly (orange vertical line in lower panel), the drive is already slightly above the lower continuum edge for lower momentum states. This leads to a reduced, but finite transfer rate for lower momenta, and explains the enhanced transfer close to the Fermi edge. Compared to off-resonant driving frequencies as shown in Figs. 6.5 or 6.8, the transfer is significantly larger by up to two orders of magnitude, and the (a)symmetric depletion of $|1\rangle$ ($|2\rangle$) is strongly pronounced and clearly visible.

²Since we are dealing with an excitation *continuum*, red and blue detuning here refer to the many-body resonance as seen in the obtained spectrum for the total upper level population N_3 discussed in section 6.1.5

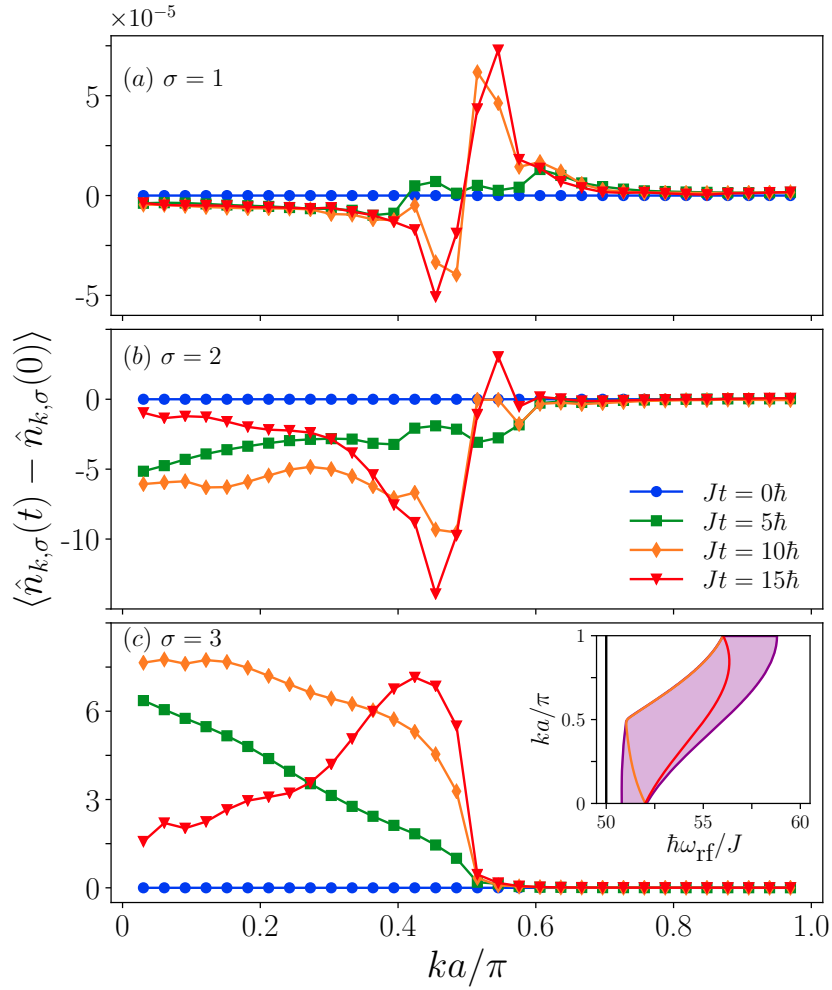


Figure 6.5: Evolution of the momentum distributions $\langle n_{k,\sigma} \rangle$, for $U = -2J$, $\hbar\Omega_{23} = 0.01J$, and $\hbar\omega_{\text{rf}} = 50.0J$ for $\sigma = \{1, 2, 3\}$ in panels (a-c) respectively. We show the deviation of the momentum distribution at different times as marked in the legend in (b). The inset in (c) shows the spin-charge excitation continuum (purple region bounded by purple lines), along with two particular excitations of ‘spin-wave’ character (orange and red lines). The black vertical line marks the driving frequency ω_{rf} .

6.1 Weakly attractive Fermi-Hubbard model

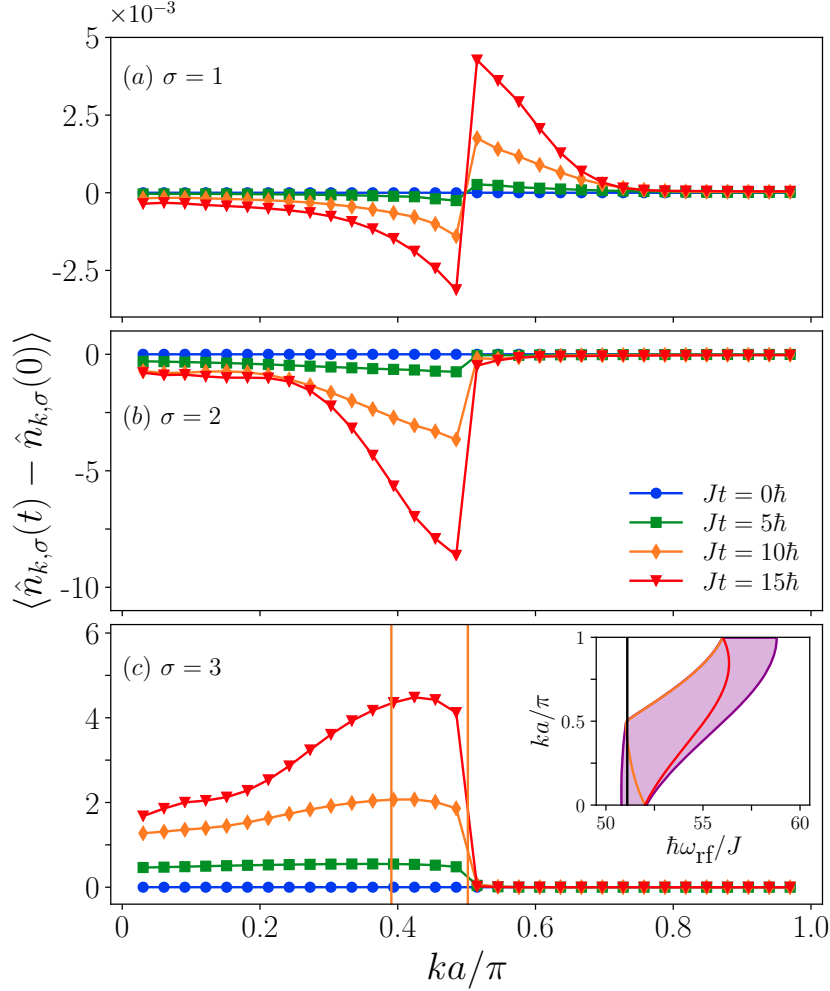


Figure 6.6: Evolution of the momentum distributions $\langle n_{k,\sigma} \rangle$, for $U = -2J$, $\hbar\Omega_{23} = 0.01J$, and $\hbar\omega_{\text{rf}} = 51.1J$ for $\sigma = \{1, 2, 3\}$ in panels (a-c) respectively. We show the deviation of the momentum distribution at different times as marked in the legend in (b). The inset in (c) shows the spin-charge excitation continuum (purple region bounded by purple lines), along with two particular excitations of ‘spin-wave’ character (orange and red lines). The black vertical line marks the driving frequency ω_{rf} (inset), while the orange vertical lines (c) mark the momenta, at which the driving frequency ω_{rf} is resonant with the ‘spin-wave’ excitation (orange line, inset). To ensure convergence of our results, we have separately varied the bond dimension ($D = 400$), truncation error ($\epsilon = 10^{-13}$), and time step ($Jdt = 0.002\hbar$). The maximal and minimal deviation is shown as a shaded region around the corresponding curve (same colour respectively), and if not discernible, the numerical error is below the linewidth.

Above the Resonance

For Figs. 6.7 and 6.8, the driving frequency, ω_{rf} , lies well within or even at the upper edge of the excitation continuum. Interestingly, $\langle n_{k,3} \rangle$ (c) reveals a very distinct response not seen before. The momentum distribution develops a strong two-peak structure at $ka \sim \{0.18\pi, 0.63\pi\}$ in Fig. 6.7.

From the inset in (c) we see that we are driving particular excitations of ‘spin-wave’ character at two distinct momenta resonantly, marked by the red and orange vertical lines in the lower panel. These are in good agreement with the peaks observed, and we can thereby interpret the peaks as a signature of the activation of these excitations in the system. Note also, that the lower onset of the lower peak at $ka \sim 0.18\pi$ is indeed set by the onset of the spin-charge excitation continuum (purple vertical line). Being inside the linear regime, these peaks grow monotonically in time. With increasing ω_{rf} the two-peak structure shifts to larger momenta, even above the Fermi edge for a far blue detuned drive at $\hbar\omega_{\text{rf}} = 56.0J$ in Fig. 6.8. The vertical lines marking the different ‘resonant’ momentum states for the ‘spin-wave’ excitations and the onset of the spin-charge continuum, are in qualitative good agreement, but we do see a shift to larger momenta in this estimate. The precise location of these momentum states is difficult to estimate, as it depends on the occupation of the initial, correlated state we are transferring out of, and crucially also the matrix elements of the corresponding transitions. Since these are very difficult to extract from Bethe ansatz, we can instead *use* this momentum distribution measurement to learn about which states are coupled strongly and thereby infer information about the underlying matrix elements and which excitations the rf-field couples to predominantly.

The upper two panels (a-b), show the particle redistribution for $\sigma = \{1, 2\}$. The density redistribution has two effects. The dominant one stems from the physical transfer between levels $|2\rangle$ and $|3\rangle$. This can be clearly seen in panel (b) for $\langle n_{k,2}(t) \rangle$ as the occupation decreases below the Fermi edge. The redistribution of populations due to the interaction and scattering between the atoms is the only channel that also affects the momentum density distribution of level $|1\rangle$. For these two driving frequencies well above the resonance, the occupation in $\langle n_{k,1} \rangle$ also reveals signatures of the resonant coupling to excitations of ‘spin-wave’ character. In Fig. 6.7 (a), one sees that a secondary peak is developing just above the Fermi edge, near the momentum value corresponding to the crossing of the upper (orange) excitation line with ω_{rf} (black vertical line in the inset). This driving noticeably perturbs the system beyond a simple occupation redistribution around the Fermi edge. The situation is similar for a far off-resonant modulation $\hbar\omega_{\text{rf}} = 56J$ shown in Fig. 6.8. Here, the secondary peak develops near the crossing of the lower (red) excitation line with ω_{rf} .

We saw that below and at resonance our drive couples either to all momentum states (approximately) equally or only to states close to the Fermi surface. In a simplified picture, this effectively shrinks the Fermi sphere isotropically and does not alter its overall shape much, hence the redistribution of $|1\rangle$ is only restricted to momenta around k_F . Above the resonance on the other hand, we couple to states deep inside the Fermi sphere. This requires a *substantial* redistribution of particles and leads to significant heating of the system. We can see from panel (a) in Figs. 6.7 and 6.8 that here, the redistribution of $|1\rangle$ extends beyond the immediate vicinity of k_F across the entire Brillouin zone, giving rise to heating effects.

6.1 Weakly attractive Fermi-Hubbard model

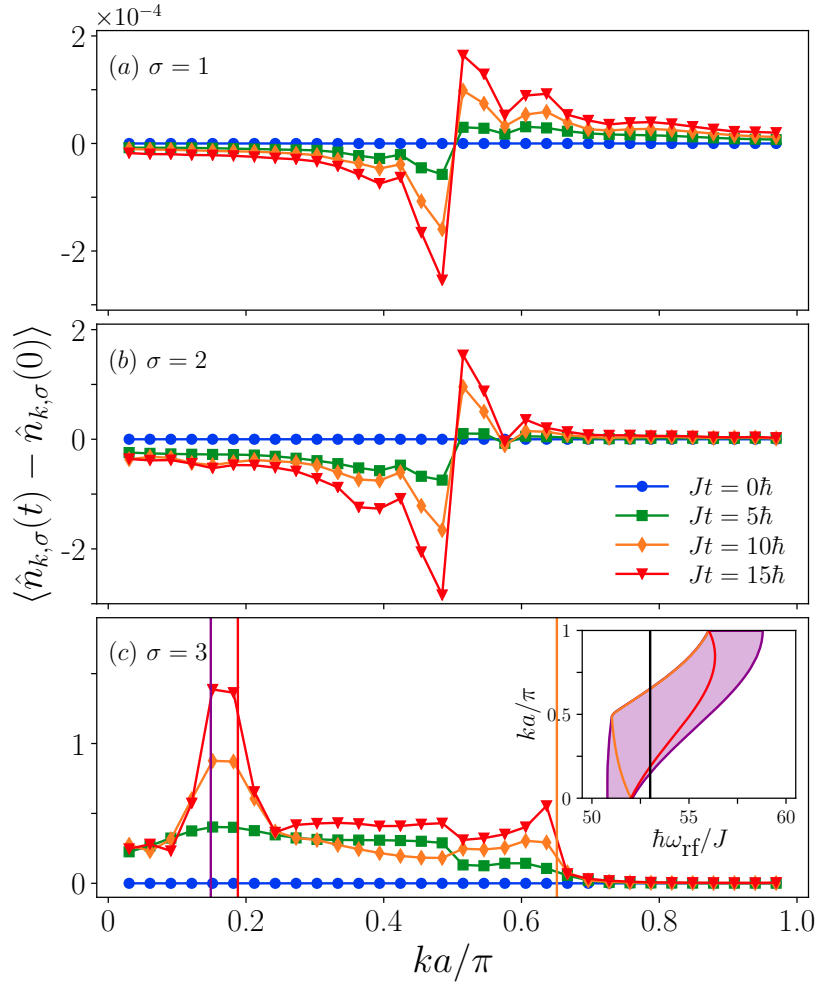


Figure 6.7: Evolution of the momentum distributions $\langle n_{k,\sigma} \rangle$, for $U = -2J$, $\hbar\Omega_{23} = 0.01J$, and $\hbar\omega_{\text{rf}} = 53.0J$ for $\sigma = \{1, 2, 3\}$ in panels (a-c) respectively. We show the deviation of the momentum distribution at different times as marked in the legend in (b). The inset in (c) shows the spin-charge excitation continuum (purple region bounded by purple lines), along with two particular excitations of ‘spin-wave’ character (orange and red lines). The black vertical line marks the driving frequency ω_{rf} (inset), while the coloured vertical lines in the lower panel (c) mark the momenta, at which the driving frequency ω_{rf} is resonant with either the ‘spin-wave’ excitations (red and orange), or the upper spin-charge continuum edge (purple).

6.1.3 Evolution of the Momentum Distributions

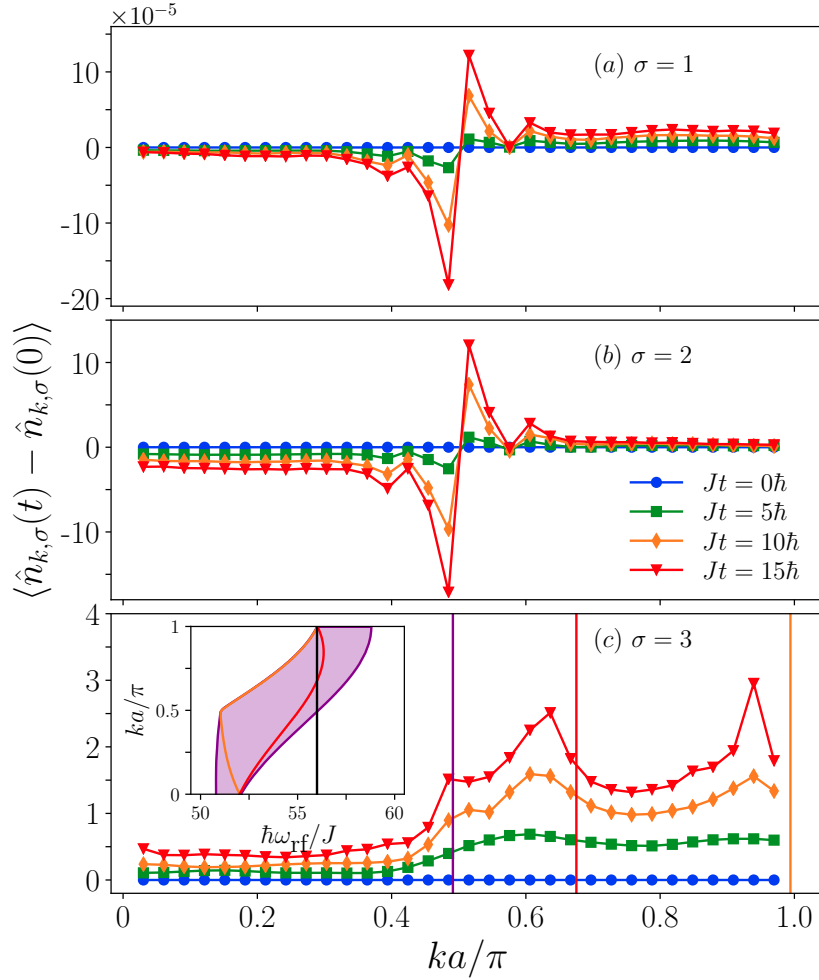


Figure 6.8: Evolution of the momentum distributions $\langle n_{k,\sigma} \rangle$, for $U = -2J$, $\hbar\Omega_{23} = 0.01J$, and $\hbar\omega_{\text{rf}} = 56.0J$ for $\sigma = \{1, 2, 3\}$ in panels (a-c) respectively. We show the deviation of the momentum distribution at different times as marked in the legend in (b). The inset in (c) shows the spin-charge excitation continuum (purple region bounded by purple lines), along with two particular excitations of ‘spin-wave’ character (orange and red lines). The black vertical line marks the driving frequency ω_{rf} (inset), while the coloured vertical lines in the lower panel (c) mark the momenta, at which the driving frequency ω_{rf} is resonant with either the ‘spin-wave’ excitations (red and orange), or the upper spin-charge continuum edge (purple).

6.1 Weakly attractive Fermi-Hubbard model

6.1.4 Evolution of the Pair Distribution

As introduced in chapter 2, the ground state of the Fermi-Hubbard model for attractive interactions presents superconducting correlations. Hence, as a natural extension of the previous investigation, here we want to comment on how the rf-drive influences the superconducting pairing in the $|12\rangle$ manifold. Quite generally we find that, in contrast to the momentum distribution discussed above, mostly small momenta $k \sim 0$ of the pair distribution are affected and changed by the rf-drive. We therefore only show the evolution on resonance, since here we observe the strongest signal, as the perturbation to the system is largest. The evolution of the superconducting pair correlations is analysed by monitoring the pair structure factor

$$P_k(t) = \frac{1}{L} \sum_{i,j} e^{ik(r_i - r_j)} \langle (\hat{\Delta}_i^\dagger \hat{\Delta}_j + \text{h.c.}) \rangle, \quad (6.2)$$

where the expectation value is taken with respect to the time-evolved wave function $|\Psi(t)\rangle$, $\hat{\Delta}_i = c_{i,1}c_{i,2}$, is the pair annihilation operator at site i , and we employed periodic boundary conditions for the Fourier transform, i.e. $k = \frac{2n\pi}{L}$, with $n = [-\frac{L}{2} + 1, \dots, \frac{L}{2}]$.

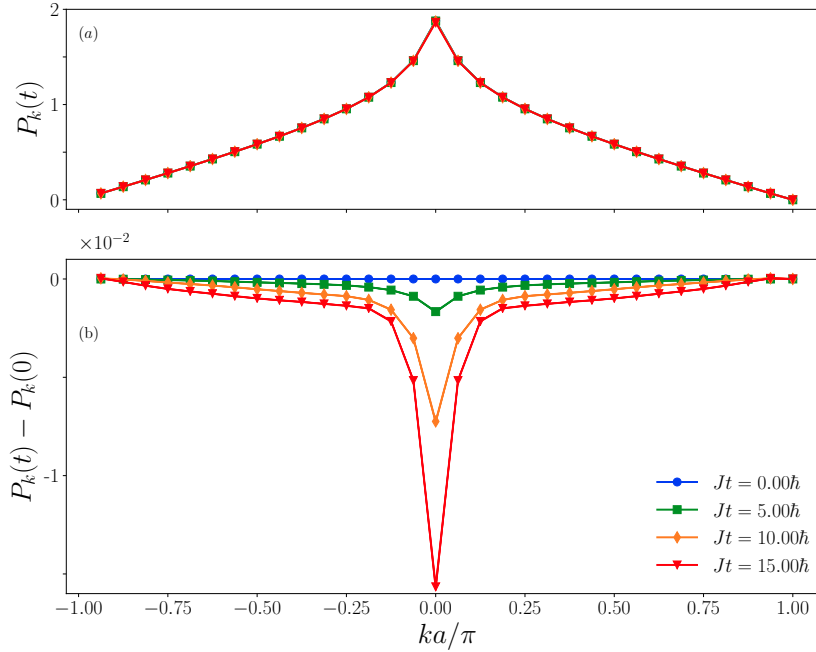


Figure 6.9: Evolution of the pair distribution $P_k(t)$ for the attractive Hubbard model of size $L = 32$ at half-filling for $U = -2J$, $\hbar\Omega_{23} = 0.01J$ and $\hbar\omega_{\text{rf}} = 51.1J$. To ensure convergence of our results, we have separately varied the bond dimension ($D = 400$), truncation error ($\epsilon = 10^{-13}$), and time step ($Jdt = 0.002\hbar$). The corresponding curves are overlaid in the same colours as the shown data. The numerical error is therefore below the linewidth.

Fig. 6.9 shows the pair correlator for different points in time for resonant driving frequency

$\hbar\omega_{\text{rf}} = 51.1J$. Considering first the absolute pair correlation, $P_k(t)$, in panel (a), the dynamics induced by the weak driving amplitude is not discernible by eye (despite being on resonance), and we instead depict its deviation from the initial state, $P_k(t) - P_k(0)$, in the lower panel (b). We have a weak background depletion across all momenta, which is however overshadowed by a strong reduction at $k = 0$. This is in stark contrast to the observed features of $\langle n_{k,\sigma} \rangle$ of the previous section. Throughout the evolution, even on resonance, the pair correlation amplitude is monotonically lowered for all momenta. Similarly to previous observations, the change in the pairing correlations is nearly two orders of magnitude larger on resonance as compared to off-resonant driving frequencies.

The rf-drive creates coherent superpositions of $|2\rangle$ and $|3\rangle$ particles and thereby injects energy into the system, creating excitations in the $|12\rangle$ manifold. Since we are considering a closed quantum system, our model does not include any coupling to the environment and thus lacks any dissipation channels. Hence, the system *cannot* relax back into the ground state, causing heating of the lattice. Furthermore, as the atoms are transferred back from $|3\rangle$ to $|2\rangle$, they are no longer fully coherent with the $|1\rangle$ atom they originally formed a pair with. This decoherence is accumulating in time and we conclude that the rf-drive induces decoherence and causes heating, leading to a suppression of the superconducting pair correlations $P_k(t)$, as observed in (b).

6.1.5 Total Transfer to the third state

Experimentally, the most accessible observable is the total transfer to the third state, $N_3(t)$. We discuss in this section, which information can already be extracted from measurements of this quantity. Fig. 6.10 shows the total transfer of the upper level for different driving frequencies. We expect to recover the physics discussed previously in section 6.1.1, since $N_3(t)$ is just the summed quantity of the momentum-resolved populations of $|3\rangle$. Indeed, well below the resonance $N_3(t)$ shows Rabi oscillations around a small value. On resonance, $\hbar\omega_{\text{rf}} = 51.1J$, the transfer is maximal (see inset), exhibiting slow, large amplitude oscillations, while above this resonance the evolution is characterised by a steady, linear increase in $N_3(t)$ (with oscillations superposed on top). Referring back to the spectrum in Fig. 6.2, here we are driving excitations inside the spin-charge continuum and hence couple to a continuous band of states.

We extract the slopes in the linear response region by fitting a damped, sinusoidal function with a linear background $mt + A \cos(\omega t)e^{-\gamma t} + c$, (where m , A , ω , γ , and c are all fitting parameters) to $N_3(t)$. The obtained spectrum in Fig. 6.11 shows the rescaled slope, m/Ω_{23}^2 , as a function of driving frequency ω_{rf} . For blue detuning of the rf-field from this resonance, the curves for the two Rabi frequencies, $\hbar\Omega_{23} = 0.01J, 0.1J$, collapse very well onto each other, as already seen in Fig. 6.2, displaying the correct scaling behaviour expected in the linear regime, and confirming the validity of using the linear response approach. Discrepancies between the curves arise closer to the resonance, where the transfer becomes significantly larger and is dominated by slow Rabi oscillations. Our fits do not cover this regime for two reasons. Firstly, the transfer is large (relative to other driving frequencies), so the approximation of a weak perturbation no longer holds stringently. Secondly, if there is an overall linear background trend, the dominant slow Rabi dynamics would require long evolutions for us to observe them, which are however

6.1 Weakly attractive Fermi-Hubbard model

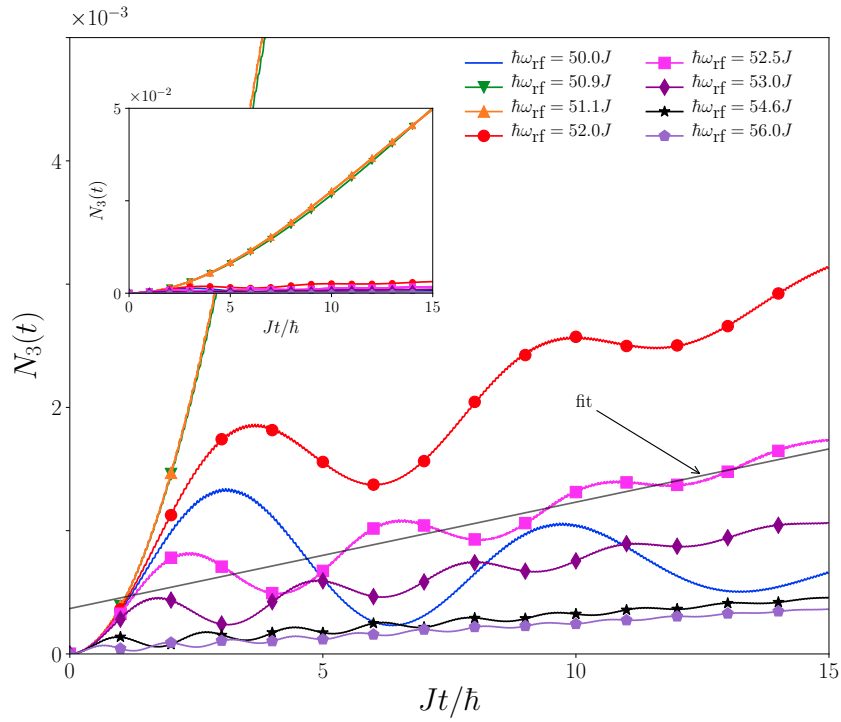


Figure 6.10: Time-dependence of the total transfer to the third state, $N_3(t)$, for the attractive Hubbard model of size $L = 32$ at half-filling for $U = -2J$, $\hbar\Omega_{23} = 0.01J$ and several driving frequencies ω_{rf} . The main plot focuses on the curves for off-resonance driving, whilst the inset shows the curves to scale to focus on the resonantly driven situations. The grey solid line is the linear portion of a fit to the time-dependence for $\hbar\omega_{\text{rf}} = 52.5J$. To ensure convergence of our results, we have separately varied the bond dimension ($D = 400$), truncation error ($\epsilon = 10^{-13}$), and time step ($Jdt = 0.002\hbar$). The corresponding curves for driving frequencies $\hbar\omega_{\text{rf}} = 51.1J$ and $52.5J$ are overlaid in the same colours as the shown data. The numerical error is therefore below the linewidth.

numerically prohibitive. We therefore refrain from fitting the response close to the resonance (hence the absence of data points in the blue and orange curves) and additionally show the (scaled) maximal transfer of $N_3(t)$ for $Jt \leq 15\hbar$ and both driving amplitudes. It is peaked at $\hbar\omega_{\text{rf}} = 51.1J$ so our resonant driving corresponds to a maximal net integrated transfer.

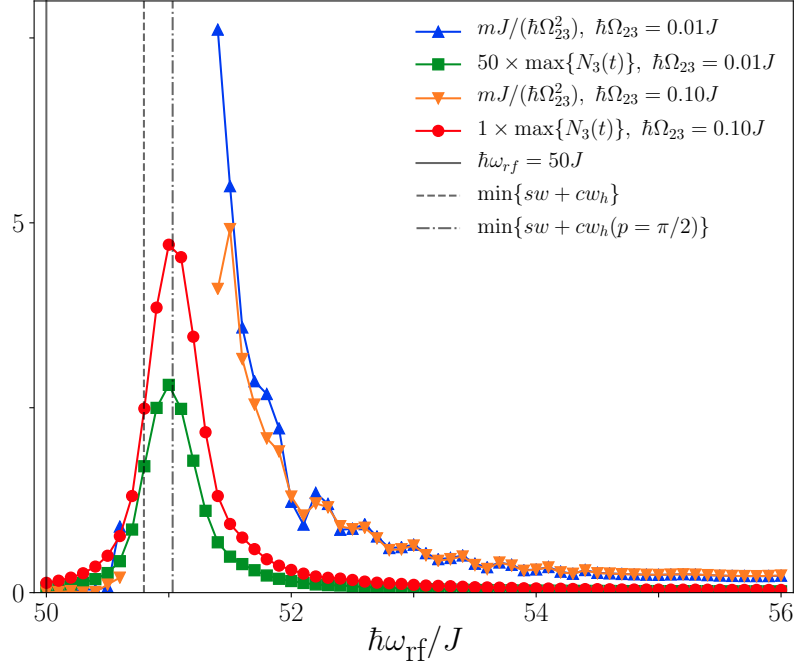


Figure 6.11: Radiofrequency transfer rate (scaled by the squared Rabi frequency) and scaled maximum net transfer between $0 \leq Jt \leq 15\hbar$ for a system of size $L = 32$, $U = -2J$, and $\hbar\Omega_{23} = 0.01J, 0.1J$. The grey solid line indicates the resonance position for a non-interacting system, the grey dashed line marks the lower edge of the spin-charge excitation continuum, whilst the grey dash-dotted line highlights the minimum energy of the ‘spinwave’-type excitations, $\epsilon_q^{sw} + \epsilon_{q=\pi/(2a)}^{cw}$.

Eq. 3.47 indicates that $\langle \dot{N}_3(t) \rangle \sim \sum_k A(k, \omega_{\text{rf}})$, and indeed the onset of the spectral response in $N_3(t)$ as extracted from our fits, agrees well with the lower onset of the spin-charge excitation continuum (grey dashed line). The width of the resonance as observed here in N_3 is however much wider, compared to the momentum resolved spectra, which we attribute to the dispersive nature of the underlying excitation continuum. In particular, a strong coupling to the excitations of ‘spin-wave’ character (orange and red lines in Fig. 6.2) gives rise to the long tail in the N_3 spectrum.

6.2 Strongly attractive Fermi-Hubbard model

Having discussed the dynamical response of a weakly interacting Fermi gas subject to a weak rf-perturbation, in this section we will compare and contrast the observed behaviour,

6.2 Strongly attractive Fermi-Hubbard model

when the initial state is *strongly* interacting. To this end we choose the same weak modulation amplitude $\hbar\Omega_{23} = 0.01J$ and an interaction strength of $U = -8.0J$.

6.2.1 Momentum-resolved Transfer to the third state

Examples of the momentum-resolved evolution of the upper level is shown in 6.12 for the representative momenta $ka = 0.1818\pi$ (a) and $ka = 0.4242\pi$ (b). For low $\hbar\omega_{\text{rf}} < 55J$ we again find a dominant Rabi-like character in the evolution (fast oscillations with low transfer amplitude). However, looking at the individual curves to locate any resonance behaviour, we note that there is no consistent frequency beyond which we enter the linear regime. This is a first indication that the spin-charge excitation continuum is strongly dispersive for large interactions. Indeed, following the curve of largest transfer, we see it moving for increasing momentum to higher energies, from $\hbar\omega_{\text{rf}} \sim 55.25J$ to $\hbar\omega_{\text{rf}} \sim 56.0J$ (orange line in the two panels respectively). Driving the system close to maximal transfer, the population evolves with large amplitude oscillations in its response as shown in the respective insets. At nearby frequencies, the evolution is strongly damped, while on resonance the frequency of oscillation is too slow for us to comment on the dephasing in this case. Once the rf field is driving resonantly into the excitation continuum, the response is dominated by a net linear trend underlying the whole dynamics, with oscillations largely diminished. The crossover into this linear regime occurs rather quickly, which is not surprising, since we expect a stronger interaction induced level mixing [208].

We extract the slopes from linear fits to the momentum-resolved data and compare the obtained spectra to the analytic Bethe ansatz calculations in Fig. 6.13. The general picture that emerged for $U = -2J$ in the previous section holds here as well. The transfer is Rabi-dominated when driving below or above the spin-charge continuum. The shaded region denotes evolutions which have a strong Rabi character and which we do not attempt to fit. Also for strong interactions the excitation lines are very clearly defined and in good agreement with the exact calculations. One can clearly make out the dispersive ‘spin-wave’ band (orange line) joining the lower continuum edge at large momenta (purple line), which also coincides with the maximal momentum-resolved transfer in the upper level population (blue shaded region). In general, the regime of non-zero effective transfer is given by the upper and lower edges of the excitation continuum.

Let us now address some differences to the weakly interacting system studied above. Firstly, Fig. 6.13 extends across the entire Brillouin zone, since we have fitted the $\langle n_{k,3} \rangle$ curves all the way to the upper edge of the first Brillouin zone at $ka = \pi$. The reason lies in the broader momentum distribution of the initial ground state, and will be discussed in more detail in the following paragraph. Secondly, the curvature of the lower edge of the spin-charge continuum is very pronounced, which implies a much broader resonance peak in the N_3 spectrum, shown in Fig. 6.19. Furthermore, it accounts for the widely differing resonance onsets in the momentum resolved curves for $\langle n_{k,3}(t) \rangle$. In agreement with our findings for weak interactions, we confirm, that this driving scheme also couples strongly to the ‘spin-wave’ degrees of freedom (red and orange line) in the system. Beyond the upper edge, we recover weak, oscillatory transfer, reminiscent of far-detuned Rabi oscillations.

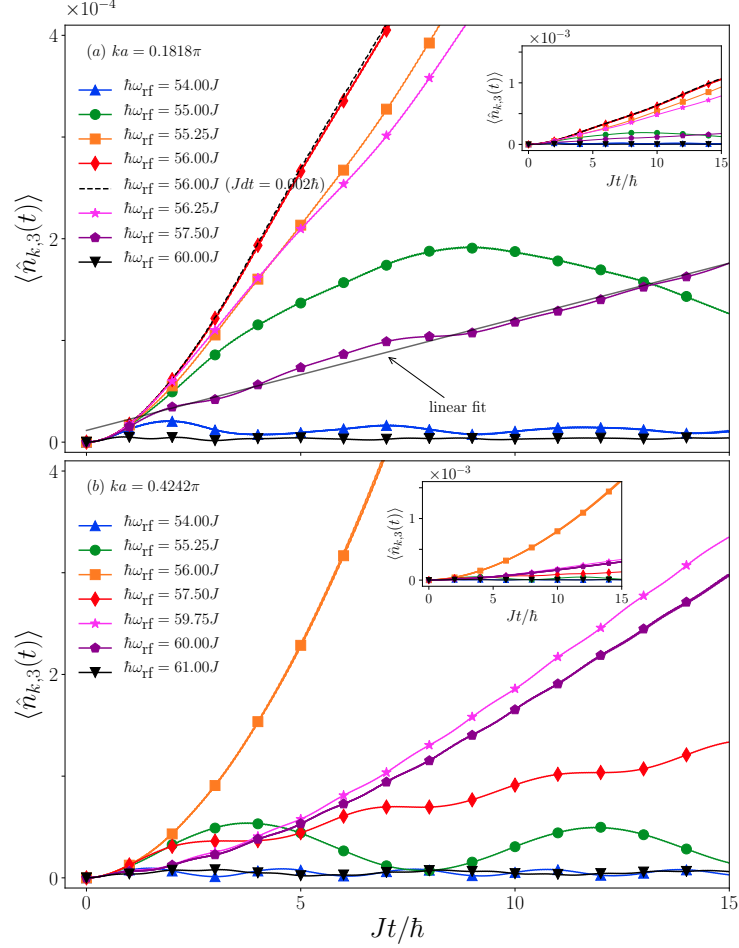


Figure 6.12: Time-dependence of the upper band population $\langle n_{k,3}(t) \rangle$ for selected momentum states at various driving frequencies ω_{rf} across the main resonance for a system of $L = 32$ sites at half-filling for interaction strength $U = -8J$. Level $|3\rangle$ lies an energy $V_3 = 50J$ above the $|12\rangle$ manifold, and the Rabi coupling is given by $\hbar\Omega_{23} = 0.01J$. The time-evolution can be separated into two regimes: a linear response, and a Rabi-like regime. The full grey line in (a) is an example of a linear fit to extract the slope used for constructing the spectrum shown in Fig. 6.13. The momenta shown are (a) $ka = 0.1818\pi$ and (b) $ka = 0.4242\pi$. The insets show the same curves as a zoomed out view, to put the curve's relative transfer into perspective. To ensure convergence of our results, we have separately varied the bond dimension ($D = 400$), truncation error ($\epsilon = 10^{-13}$), and time step ($Jdt = 0.002\hbar$). In (a) we show the convergence for $\hbar\omega_{\text{rf}} = 54.0J, 56.0J$, in the same colour as the data (ϵ , and D), with the time-step convergence shown explicitly as a black dashed line (for $\hbar\omega_{\text{rf}} = 56.0J$). In the lower panel (b) the convergence curves for $\hbar\omega_{\text{rf}} = 56.0J, 60.0J$ are overlaid in the same colours as the shown data. Where only a single lines is discernible, the numerical error is below the linewidth of the curve.

6.2 Strongly attractive Fermi-Hubbard model

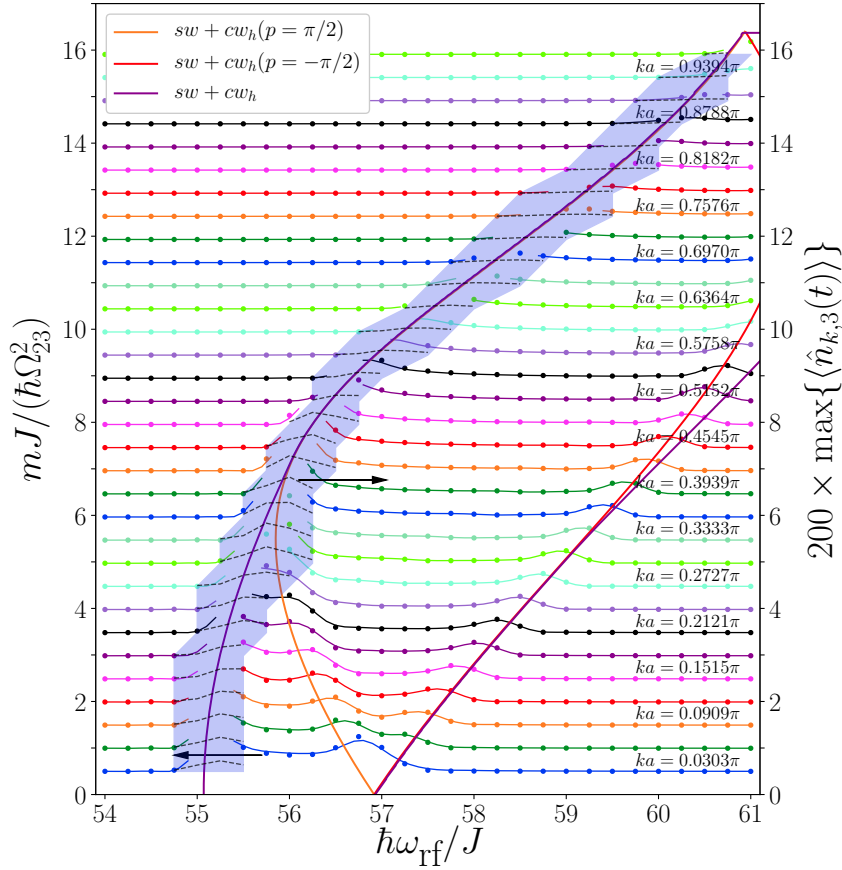


Figure 6.13: Rescaled momentum-resolved transfer rate to level $|3\rangle$, $m(k, \omega_{\text{rf}})/\Omega_{23}^2$, for a system of $L = 32$ sites at half-filling for interaction strength $U = -8J$. Level $|3\rangle$ is $V_3 = 50J$ in energy above levels $|1\rangle$ and $|2\rangle$. The dots represent the rescaled slopes for $\hbar\Omega_{23} = 0.01J$, and the lines for $\hbar\Omega_{23} = 0.1J$ (left axis, see lower arrow). The collapse of the different Rabi frequency curves highlights the good agreement between the data sets. The shaded region corresponds to the frequency interval over which the time-evolution is not linear and the fitting procedure is not attempted. In this region, instead of reporting the slope, we show the maximum atom transfer in the time interval $0 \leq Jt \leq 15\hbar$ (black dashed lines, right axis, c.f. upper arrow). The momentum values are equally spaced and stacked vertically by an amount $ka(L + 1)/(2\pi)$. The bold solid lines are the lower and upper limits of the spin-charge continuum (purple), and two ‘spin-wave’ excitations (orange and red lines) obtained from Bethe ansatz.

6.2.1 Momentum-resolved Transfer to the third state

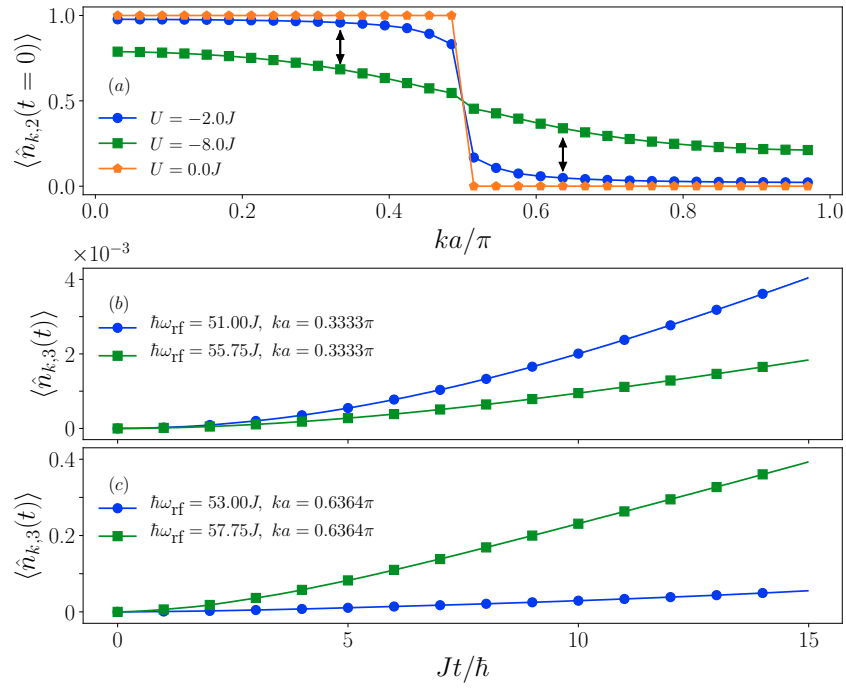


Figure 6.14: (a) ground state distribution of $\langle n_{k,2}(0) \rangle$ for $U = 0J, -2J, -8J$. The lower two panels show the time-dependence of $\langle n_{k,3}(t) \rangle$ at (b) $ka = 0.3333\pi$ and (c) $ka = 0.6364\pi$ near their respective resonances for a half-filled system of size $L = 32$ and $\hbar\Omega_{23} = 0.01J$.

6.2 Strongly attractive Fermi-Hubbard model

As we hinted above, the reason that we are able to extract a meaningful slope from the momentum-resolved evolution of the population of $|3\rangle$ *throughout* the Brillouin zone, lies in its larger initial occupation for $ka \geq \pi/2$, as depicted in Fig. 6.14 (a). Here we compare the initial ground state momentum distribution $\langle n_{k,2}(0) \rangle$ for the two interaction strengths considered, along with the non-interacting system. For a free system, the distribution follows the Fermi-Dirac equation and displays the sharp step-function behaviour at the Fermi momentum $k_F = \pi/(2a)$. Whilst the $U = -2J$ distribution already shows a softening around the Fermi edge at $ka \sim \pi/2$ compared to the non-interacting Fermi-Dirac distribution, for strong interactions this edge is completely smeared out and rather resembles a slowly decaying function of momentum. For the marked momenta below ($ka = 0.3333\pi$) and above ($ka = 0.6364\pi$) the Fermi surface, we plot the full time evolution in the lower two panels (b) and (c) respectively at their respective maximal transfer frequencies. While the transfer is larger for $U = -2J$ below the Fermi edge (b), the situation is reversed above it (c). This corroborates our assertion, that the vastly different occupation of $\langle n_{k,2}(t=0) \rangle$ in the different regions of the Brillouin zone, strongly affects the observed transfer to the upper level.

6.2.2 Evolution of the Momentum Distribution

In the following we discuss the evolution of the momentum distributions $\langle n_{k,\sigma} \rangle$, focussing on two driving frequencies: on resonance at $\hbar\omega_{\text{rf}} = 56.0J$ (Fig. 6.15), and far above it (Fig. 6.16).

In accordance with our observations for the weakly interacting system, Fig. 6.15 shows the appearance of the characteristic two-peak structure in the lowest panel (c) for state $|3\rangle$. The orange vertical line marks the momenta to which the rf-drive is coupling resonantly to the ‘spin-wave’ excitation line shown in the inset (orange line). The extracted momentum state is in very good agreement with the enhanced transfer seen in $\langle n_{k,3}(t) \rangle$. Focussing on the central panel (b), initially the rf-drive depletes $|2\rangle$ below the Fermi edge homogeneously, but eventually the (near) resonant coupling to momentum states between $ka \sim 0.2\pi$ and $ka \sim 0.4\pi$ becomes the dominant transfer mechanism in the evolution for $Jt \gtrsim 10\hbar$. The opposite in turn holds for the population gain in level $|3\rangle$. Notably in contrast to a weakly interacting system however, the larger momenta are also significantly depleted (b), but are seemingly *not* transferred into the corresponding momentum states for $\sigma = 3$. This strongly supports our interpretation, that the transfer to the upper level is largely going through the resonant momentum channels arising from the coupling to the ‘spin-wave’ excitations (orange and red lines in the inset of the lower panel). Meanwhile the population of $|1\rangle$ shows population redistributions across all momenta. Since the dynamics in $|1\rangle$ is purely induced by the interaction $U = -8.0J$, it is not surprising that the effect is seen more strongly here. Finally, it is important to point out that the overall transfer in all levels is significantly reduced compared to the weaker interaction, by nearly an order of magnitude. We argue that the strong interaction leads to an increased rate of dephasing, and thus hinders coherent transfer.

For large driving frequencies above the resonance, Fig. 6.16, the two peaks move into the upper half of the Brillouin zone, where states $ka \sim 0.4\pi$ and $ka \sim 0.9\pi$ are driven particularly strongly. The vertical lines (c) indicating the resonant momentum states for ‘spin-wave’ excitations and the continuum onset (red, orange and purple vertical lines respectively in the lower

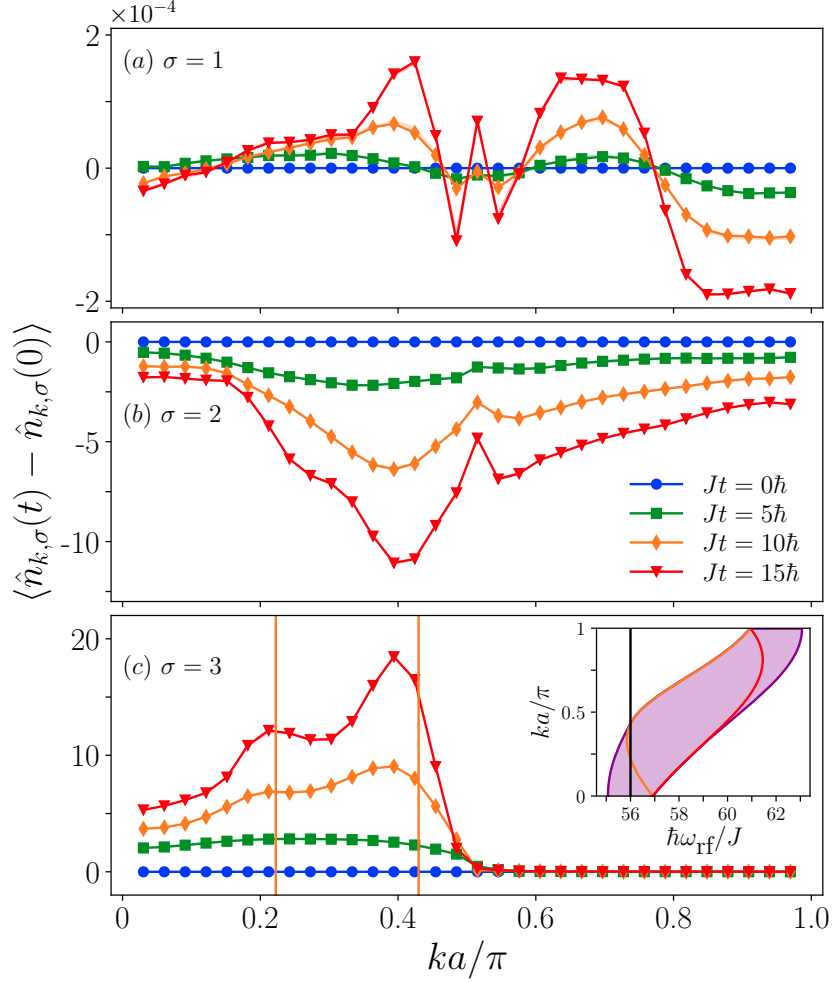


Figure 6.15: Evolution of the momentum distributions $\langle n_{k,\sigma} \rangle$, for $U = -8J$, $\hbar\Omega_{23} = 0.01J$, and $\hbar\omega_{\text{rf}} = 56.0J$ for $\sigma = \{1, 2, 3\}$ in panels (a-c) respectively. We show the deviation of the momentum distribution at different times as marked in the legend in (b). The inset in (c) shows the spin-charge excitation continuum (purple region bounded by purple lines), along with two particular excitations of ‘spin-wave’ character (orange and red lines). The black vertical line marks the driving frequency ω_{rf} (inset), while the vertical, orange lines in the lower panel (c) mark the momenta, at which the driving frequency ω_{rf} is resonant with the ‘spin-wave’ excitation (orange line, inset). The shown data was obtained for a bond dimension $D = 500$, truncation error $\epsilon = 10^{-12}$, and time step $Jdt = 0.001\hbar$. To ensure convergence of our results, we have separately varied the bond dimension ($D = 600$), truncation error ($\epsilon = 10^{-13}$), and time step ($Jdt = 0.0005\hbar$). The maximal and minimal deviation is shown as a shaded region around the corresponding curve (same colour respectively).

6.2 Strongly attractive Fermi-Hubbard model

panel) are in very good agreement with the peaks in the distribution. The $\langle n_{k,3} \rangle$ evolution (c) monotonically increases with time, predominantly at the resonant momentum states, oscillations are damped out, and the strong interactions place the drive well inside the linear regime. Meanwhile $\langle n_{k,2} \rangle$ does *not* show the complimentary depletion. Instead it is exclusively emptied for all momenta $k \leq k_F$ (b). This points to a strong redistribution of particles, as confirmed by panel (a). Particles are moved from below to above the Fermi surface and the system is heated in the process.

6.2.3 Evolution of the Pair Distribution

Fig. 6.17 shows the pair distribution of Eq. 6.2 for strong interactions and maximal net transfer $\hbar\omega_{\text{rf}} = 56.0J$. The large transfer is reflected in the pair correlation as a strong monotonic depletion of the pairs close to $k \sim 0$. Contrasting this to weak interactions, Fig. 6.9, here pairs are tightly bound together on a site, making it harder to break them. Thus, we cannot observe any appreciable reduction in the pair coherence for non-zero momentum states, as was the case for $U = -2J$.

6.2.4 Total Transfer to the third state

Finally, we conclude our discussion of the strongly interacting system by looking at the total upper level population $N_3(t)$, shown in Fig. 6.18 for various driving frequencies. For red-detuned driving frequencies below the continuum edge, $\hbar\omega_{\text{rf}} \lesssim 55.0J$, the integrated transfer oscillates around a small long-time value. Beyond this, the oscillatory behaviour gradually gives way to the linear regime once the coupling to the spin-charge continuum allows for sufficient level mixing. The onset of the linear regime is more gradual compared to weak interactions, since the lower edge of the excitation continuum is curved more strongly (c.f. Fig. 6.13). For $\hbar\omega_{\text{rf}} \sim 56.0J$ the net transfer is maximal. Strong interactions lead to an enhanced dephasing, and as a result the oscillations on top of the linear increase are strongly damped out, or not observable at all. To access the spectrum of N_3 , we fit this region with a linear function, as exemplified by the grey dashed line in Fig. 6.18, and show the obtained spectrum in Fig. 6.19.

The spectral response is peaked around $\hbar\omega_{\text{rf}} \sim 56.0J$ and is much wider than in the weakly attractive case, because of the strong curvature of the lower excitation band as seen in the single particle spectral function, Fig. 6.13 (orange and purple line). For clarity we have marked the lower onset of the spin-charge continuum (grey dashed line) as well as the minimum energy of the excitations with ‘spin-wave’ character (grey dash-dotted line). Whilst the former sets the *onset* of the spectral response of N_3 , the latter dictates its resonance position, i.e. the frequency where the integrated transfer is maximal. We report an overall very good agreement with the spectral features obtained from our fitting procedure. The resonance position is shifted from the non-interacting result of $\hbar\omega_{\text{rf}} = 50.0J$ to significantly higher energies as a result of the strong interactions and the opening of a gap in the excitation spectrum. It is important to note that here we are able to perform our fitting analysis throughout and across the resonance region because the strong interaction allows for sufficient mixing of the levels already at the lower edge of the excitation continuum, facilitating the emergence of the linear regime. For far red-detuned drivings, the response is still oscillatory and Rabi-like (very weak transfer), but closer to the resonance, scattering and interactions obscure this picture and give rise to saturation

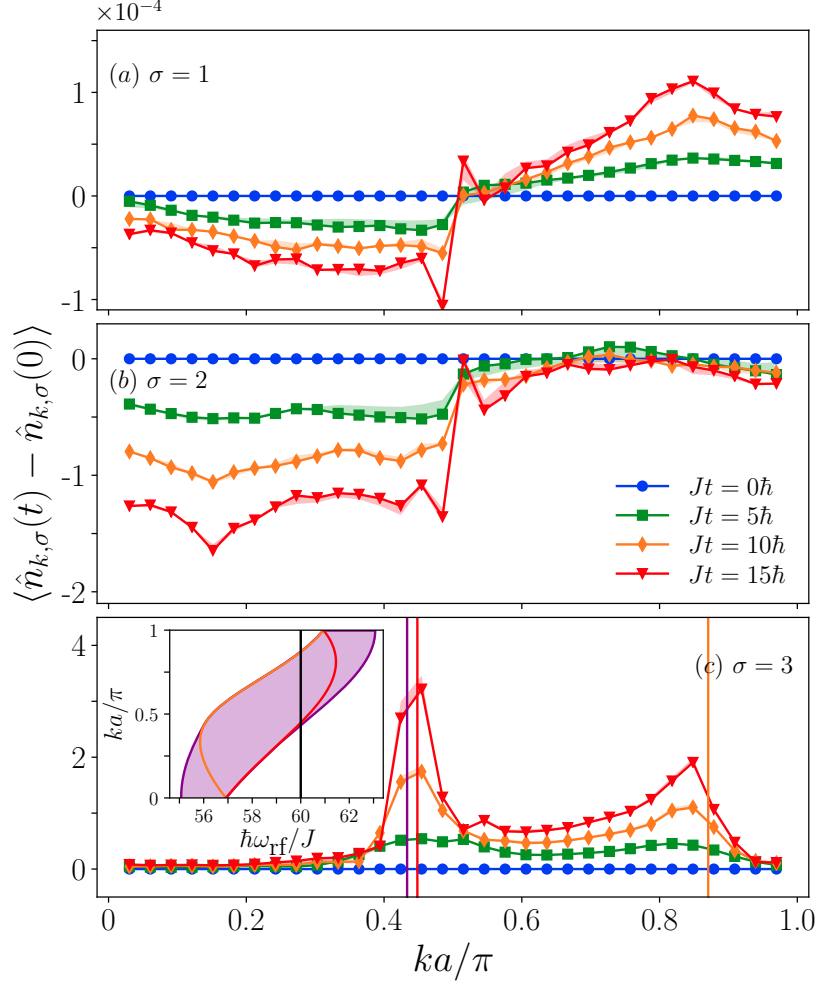


Figure 6.16: Evolution of the momentum distributions $\langle n_{k,\sigma} \rangle$, for $U = -8J$, $\hbar\Omega_{23} = 0.01J$, and $\hbar\omega_{\text{rf}} = 60.0J$ for $\sigma = \{1, 2, 3\}$ in panels (a-c) respectively. We show the deviation of the momentum distribution at different times as marked in the legend in (b). The inset in (c) shows the spin-charge excitation continuum (purple region bounded by purple lines), along with two particular excitations of ‘spin-wave’ character (orange and red lines). The black vertical line marks the driving frequency ω_{rf} (inset), while the coloured vertical lines in the lower panel (c) mark the momenta, at which the driving frequency ω_{rf} is resonant with either the ‘spin-wave’ excitations (red and orange), or the upper spin-charge continuum edge (purple). The shown data was obtained for a bond dimension $D = 500$, truncation error $\epsilon = 10^{-12}$, and time step $Jdt = 0.001\hbar$. To ensure convergence of our results, we have separately varied the bond dimension ($D = 600$), truncation error ($\epsilon = 10^{-13}$), and time step ($Jdt = 0.0005\hbar$). The maximal and minimal deviation is shown as a shaded region around the corresponding curve (same colour respectively).

6.2 Strongly attractive Fermi-Hubbard model

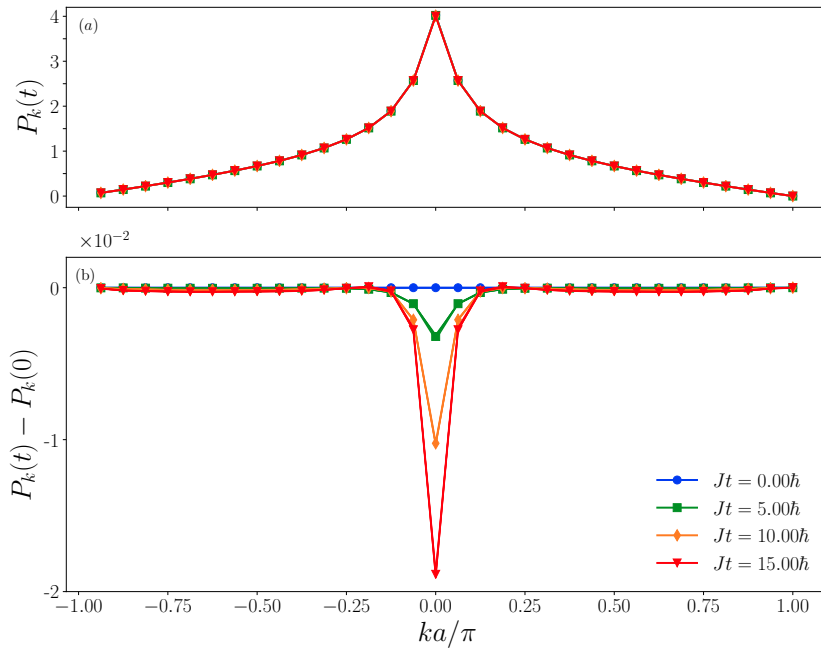


Figure 6.17: Evolution of the pair distribution $P_k(t)$ for the attractive Hubbard model of size $L = 32$ at half-filling for $U = -8J$, $\hbar\Omega_{23} = 0.01J$ and $\hbar\omega_{\text{rf}} = 56.0J$. To ensure convergence of our results, we have separately varied the bond dimension ($D = 400$), truncation error ($\epsilon = 10^{-13}$), and time step ($Jdt = 0.002\hbar$). These are shown in the same colour as the data, the numerical error is therefore below the linewidth.

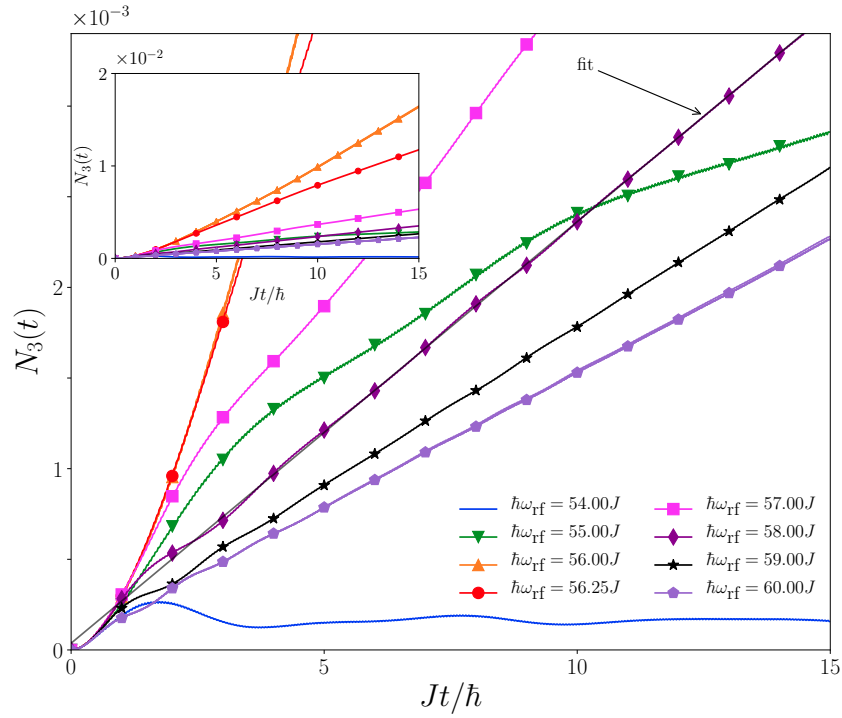


Figure 6.18: Time-dependence of the total transfer to the third state, $N_3(t)$, for the attractive Hubbard model of size $L = 32$ at half-filling for $U = -8J$, $\hbar\Omega_{23} = 0.01J$ and several driving frequencies ω_{rf} . The main plot focuses on the curves for off-resonant driving, whilst the inset shows a zoomed-out picture of the same curves and thereby highlights the comparatively much larger transfer for resonant driving of the system. The grey solid line is the linear portion of a fit to the time-dependence for $\hbar\omega_{\text{rf}} = 58.0J$. To ensure convergence of our results, we have separately varied the bond dimension ($D = 400$), truncation error ($\epsilon = 10^{-13}$), and time step ($Jdt = 0.002\hbar$). These are shown in the same colour as the data, the numerical error is therefore below the linewidth.

6.3 Conclusions

(maximal transfers of up to 60%) and non-oscillatory behaviour, which gradually gives way to the linear response regime, shown in Fig. 6.18.

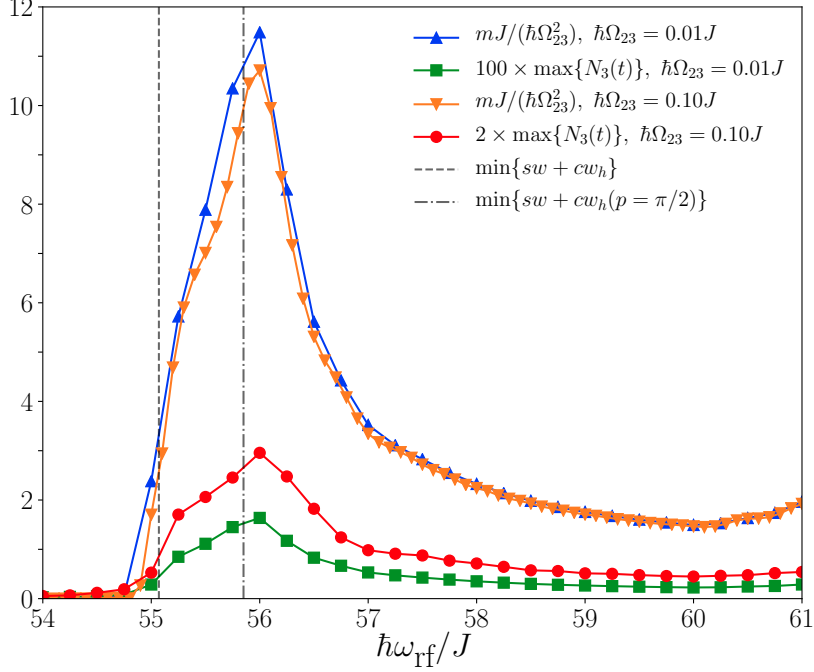


Figure 6.19: Radiofrequency transfer rate (scaled by the squared Rabi frequency) and scaled (for visibility) maximum net transfer between $0 \leq Jt \leq 15\hbar$ for a system of size $L = 32$, $U = -8J$, and $\hbar\Omega_{23} = 0.01J, 0.1J$. The grey dashed line marks the lower edge of the spin-charge excitation continuum, whilst the grey dash-dotted line highlights the minimum energy of the ‘spin-wave’-type excitations.

6.3 Conclusions

In this chapter we studied a half-filled, attractive Fermi-Hubbard model confined to a one-dimensional optical lattice geometry. The rf-field drives the system away from equilibrium by inducing transitions to a free, upper band. We numerically simulate the fully interacting, time-dependent model using the time-dependent matrix product state algorithm. Our simulations are supplemented by response theory calculations and exact solutions of the Hubbard model via Bethe ansatz. Depending on the driving frequency of the rf-field, the system’s evolution explores two different dynamical regimes, one with a strong Rabi-character and another in the linear regime. Whilst the former exhibits (off)resonant many-body oscillations in the upper level population, the latter emerges when the drive couples to a continuum of states in the final state. Notably, even though the driven system is not always in the linear response regime, we are still able to extract the underlying spectra to a reasonable accuracy.

Our simulations allow us to access the complete time-evolution of the system throughout

the drive, where we observe complex, intricate dynamics. The obtained spectra are in very good agreement with exact Bethe ansatz calculations. In particular the momentum-resolved upper level population $\langle n_{k,3}(t) \rangle$ provided a lot of insight into the underlying excitation structure of the system, and the way the rf-drive couples to these excitations. As such, rf-spectroscopy is an invaluable tool to probe the system as it offers direct access to the single-particle spectral function in the weak-coupling regime.

We explored the intricate nature of the rf-transfer and have given a detailed account of its potential to study atomic gases in experimentally realistic settings. Due to the generality of our model, these discussions are relevant to rf-spectroscopy studies, but are also amenable to investigations of e.g. multi-orbital, interacting quantum many-body systems [206, 207].

Decay and Revival of a Transient Fermi Condensate

The non-equilibrium properties of correlated quantum matter have been established as a rich and active research field in recent years. This research effort has been driven on the theoretical side in part by novel numerical algorithms e.g. the advent of t-MPS giving access to the full time evolution through quasi-exact simulations of the full many-body problem. From the experimental perspective, rapid progress in quantum optics and the field of ultracold quantum gases has led to a surge of interest to manipulate quantum states on very short time scales [68, 182].

The paradigm of these studies is often a rapid change of an internal parameter of the system's Hamiltonian, leading to the creation of a highly excited quantum state, whose relaxation dynamics is studied subsequently. For such quench experiments it is necessary to perform excitations on a very short time scale, since the non-trivial quantum dynamics is usually short-lived in any realistic setting. However, fast excitation time scales immediately imply a broad excitation spectrum, which in turn couples to a wealth of excitations in the material, complicating the interpretation of the data.

Cold atoms offer a unique opportunity to perform and study these quantum quenches in a particularly clean realisation due to their isolation from the environment. Moreover, the low temperatures and dilute nature of these gases imply dynamical time scales on the order of micro- or even milliseconds [182], which makes the *full* time evolution of the system experimentally accessible [43]. Finally, the absence of complications such as phonons or impurities, makes these systems ideal to experimentally study non-equilibrium quench phenomena cleanly. For example, low-energy collective modes [56, 210, 211] or the formation dynamics of a pair condensate [212] have been observed. However, an interaction quench in a superfluid on time scales faster than the trap period and its ensuing quantum dynamics has not been studied yet.

7.1 Non-Equilibrium Dynamics through Population Quenches

In this chapter we study the response of a Fermi condensate in the strongly-interacting regime to a fast quench of the interaction strength (relative to the trap dynamics), by a com-

plete population transfer. Whereas the previous project of chapter 6 was aimed at unravelling the intricate dynamics induced by an rf-drive and how it manifests in various, experimentally relevant observables, here we employ a *strong* rf-drive to achieve a near perfect π -pulse to flip the populations between two internal states.

While final state interactions can be neglected in certain systems due to a suitable arrangement of the Feshbach resonance of the Zeeman levels [115], generally this is not the case. The obtained rf-spectra are then changed both quantitatively and qualitatively, which complicates their interpretation significantly [110, 213–216]. By taking final state interactions explicitly into account, the population transfer effectively realises a quantum quench setup, which can be experimentally performed on time scales faster than typical magnetic field ramps, as it avoids the complications arising from e.g. eddy currents in the magnetic coils. In this chapter we simulate the lattice model discussed in chapter 6, to gain insights into the condensate dynamics of a fully interacting fermionic gas. To make connections to a realistic experimental setup, we study the Fermi-Hubbard model in the low density limit to minimise lattice effects, and where a continuum approximation is usually valid. Additionally we take the final state interactions and time-dependence of the rf-drive explicitly into account.

Theoretically we observe an initial increase in the final state pair correlation function, dominated by the transfer drive. Surprisingly, as the width of the momentum state pair correlator grows, the zero-momentum pair correlation reaches its maximal value and then starts to decrease. We attribute this to fast decoherence processes determined by the final state. Finally, our simulations reveal the excitation of a collective mode of the harmonically trapped system, and the interplay between density inhomogeneity and pairing dynamics.

The chapter is organised as follows. In section 7.2 we detail the calibration procedure to obtain suitable driving parameters to achieve a population π -pulse. Section 7.3 then discusses the subsequent evolution of the system as seen in the density of the trapped system, while section 7.4 focuses on its pairing dynamics. We conclude with a brief discussion of the numerical convergence of the presented results in section 7.5 and their connection to a current experiment in the group of Michael Köhl in section 7.6. We conclude with a brief summary in section 7.7. Parts of this chapter have been submitted for publication [58].

7.2 Calibration

In contrast to a rapid change of the s -wave scattering length a , here we are aiming to change the populations significantly to induce the quench dynamics. To this end we use a strong Rabi coupling of $\hbar\Omega_{23} = 1J$ in our simulations. Furthermore, to make connection to realistic quantum gas setups, we study a large system of $L = 80$ sites which is harmonically confined and the full Hamiltonian given by

$$H(t) = -J \sum_{\langle i,j \rangle, \sigma} c_{i,\sigma}^\dagger c_{j,\sigma} + V_3 \sum_{i=1}^L n_{i,3} + H_{int} + H_{trap} + H'(t) \quad (7.1)$$

where $n_i = n_{i,1} + n_{i,2} + n_{i,3}$ is the total density of fermions on site i , and the interaction, trapping, and driving Hamiltonians are given by

7.2 Calibration

$$H_{int} = \sum_{i=1}^L \sum_{\sigma < \tau} U_{\sigma,\tau} n_{i,\sigma} n_{i,\tau}, \quad (7.2)$$

$$H_{trap} = V_{trap} \sum_{i=1}^L \left(i - \frac{L+1}{2} \right)^2 n_i, \quad (7.3)$$

$$H'(t) = \hbar\Omega_{23} \cos(\omega_{rf}t) \sum_{i=1}^L (c_{i,3}^\dagger c_{i,2} + \text{h.c.}). \quad (7.4)$$

In the low density limit, we can associate the trapping potential to a trapping frequency of a harmonically confined continuum model, given by $\hbar\omega/J = 2\sqrt{V_{trap}/J}$ and the corresponding time scale reads $JT/\hbar = \pi/\sqrt{V_{trap}/J}$ [217].

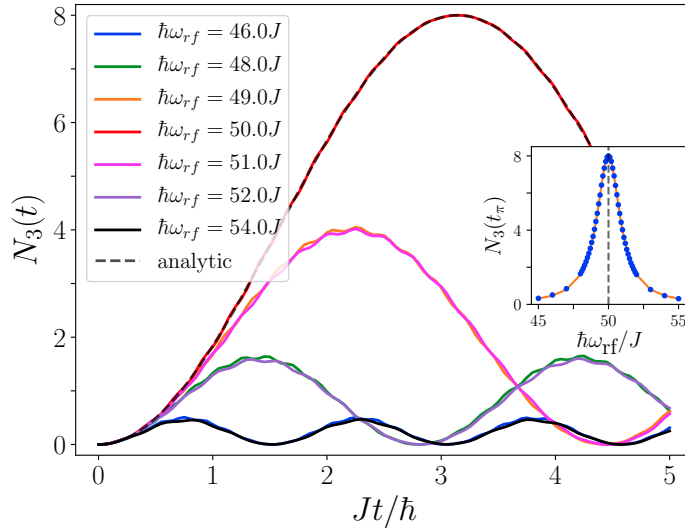


Figure 7.1: Evolution of the population of $|3\rangle$ for a homogeneous ($V_{trap} = 0J$) system of $L = 40$ sites. The initial and final state interactions are all equal $U_{12} = U_{13} = U_{23} = -6J$, the Rabi coupling is large, $\hbar\Omega_{23} = 1J$, and we choose a filling of $n = 0.4$ ($N_1 = N_2 = 8$ initially). We show the evolution for driving frequencies ω_{rf} centred around the non-interacting resonance of $\hbar\omega_{rf} = 50J = V_3$. The inset shows the extracted maximal transfer $N_3(t_\pi)$ after a duration t_π of the rf-transfer ($\Omega_{\text{eff}}t_\pi = \pi$, for details we refer the reader to section 2.5.2). The grey dashed line in the main plot displays the analytic Rabi formula Eq. 2.60, whilst its prefactor is depicted in the inset (orange line). The vertical, grey dashed line in the inset marks the non-interacting resonance at $\hbar\omega_{rf} = 50J$. The numerical simulations were performed with a bond dimension of $m = 300$, truncation error $\epsilon = 10^{-12}$, and a Trotter-Suzuki time-step of $Jdt = 0.002\hbar$.

Before considering the fully interacting, inhomogeneous system, it is instructive to discuss an interacting system with the *same* initial and final state interaction. Since the rf-drive evolves

the initial state $|2\rangle$ into a *coherent* superposition state $\cos(\theta)|2\rangle + \sin(\theta)e^{i\phi}|3\rangle$, the transfer is not affected by interactions between these two species. Furthermore, if their mutual interactions with $|1\rangle$ is the same, the excitation spectra of a system in the $|12\rangle = |1\rangle \otimes |2\rangle$ or the $|13\rangle = |1\rangle \otimes |3\rangle$ manifold are *identical* (apart from the hyperfine offset V_3 in the model) and therefore we expect the rf-drive to induce Rabi oscillations in the populations, exactly like in a non-interacting system.

Fig. 7.1 shows the evolution of the upper level population $N_3(t)$ as a function of time for various driving frequencies ω_{rf} . They exhibit clean (off)resonant Rabi oscillations, symmetric about the non-interacting resonance frequency of $\hbar\omega_{\text{rf}} = 50J = V_3$. The black dashed line marks the analytic Rabi calculation and confirms the previous assertion. We extract the maximal transfer after a π -pulse of duration $t_\pi = \pi/\Omega_{\text{eff}}$, $N_3(t_\pi)$, which is shown in the inset of the figure (blue dots). We recognise the clear Lorentzian lineshape of the Rabi spectrum (for clarity we have plotted the analytic Rabi formula in orange underneath).

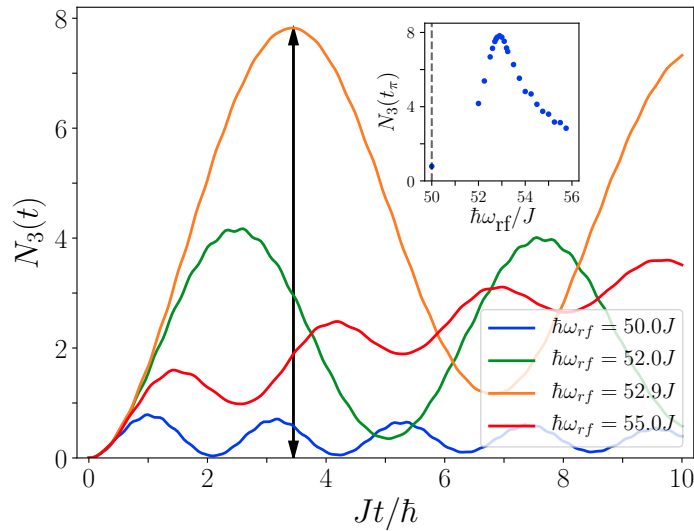


Figure 7.2: Evolution of the population of $|3\rangle$ for an inhomogeneous ($V_{\text{trap}} = 0.001J$) system of $L = 80$ sites. The initial and final state interactions are $U_{12} = -6J$ and $U_{13} = U_{23} = -2J$, the Rabi coupling is large, $\hbar\Omega_{23} = 1J$, and we choose a filling of $n = 0.2$ ($N_1 = N_2 = 8$ initially). We show the evolution of $N_3(t)$ for different driving frequencies ω_{rf} . The inset shows the extracted maximal transfer $N_3(t_\pi)$ after a duration t_π of the rf-transfer. The grey dashed line marks the non-interacting resonance position and we notice a clear shift to $\hbar\omega_{\text{rf}} = 52.9J$ due to the interaction. The numerical simulations were performed with a bond dimension of $m = 300$, truncation error $\epsilon = 10^{-12}$, and a Trotter-Suzuki time-step of $Jdt = 0.002\hbar$.

We now proceed with the same analysis for a harmonically trapped system ($V_{\text{trap}} = 0.001J$), with Rabi frequency $\hbar\Omega_{23} = 1J$, and *unequal* initial and final state interactions $U_{12} = -6J$ and $U_{13} = U_{23} = -2J$. Fig. 7.2 shows $N_3(t)$ and we first notice that it is possible to realise a near complete population transfer and thereby effectively achieve an interaction quench in the

7.3 Density Dynamics and Breathing Mode Excitation

Fermi-Hubbard model from $U = -6J \rightarrow -2J$ when driving the system on ‘resonance’ (orange line). For red-detuned driving frequencies $\hbar\omega_{\text{rf}} < 52.9$, we observe fast, low amplitude oscillations, whilst blue-detuned driving gives a strong linear background with oscillations on top. Drawing upon our results from the previous chapter 6, this signals the coupling to a continuum of states. The inset shows the retrieved spectrum for the upper level transfer. The resonance position is shifted from the non-interacting result (grey dashed line) to $\hbar\omega_{\text{rf}} = 52.9J$, and we can read off the duration of the π -pulse to be $Jt = 3.45\hbar$.

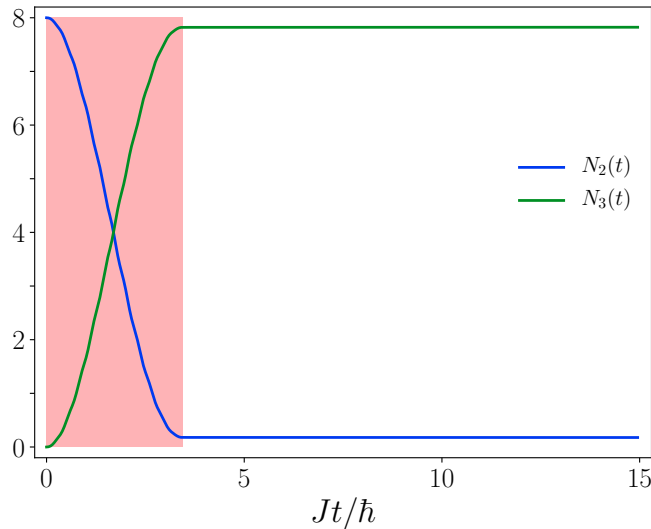


Figure 7.3: Evolution of the population of $|2\rangle$ and $|3\rangle$ for an inhomogeneous ($V_{\text{trap}} = 0.001J$) system of $L = 80$ sites. The initial and final state interactions are $U_{12} = -6J$ and $U_{13} = U_{23} = -2J$, the Rabi coupling is large, $\hbar\Omega_{23} = 1J$, and we choose an initial filling of $n = 0.2$ ($N_1(0) = N_2(0) = 8$). The rf-coupling is turned on for a duration of $Jt = 3.45\hbar$ (red shaded region). We see that the populations nearly completely swap between $|2\rangle$ and $|3\rangle$, but remain stable and constant once the drive is turned off. In this way we achieve a nearly complete population transfer and thereby realise a quantum quench setup. The numerical simulations were performed with a bond dimension of $m = 300$, truncation error $\epsilon = 10^{-12}$, and a Trotter-Suzuki time-step of $Jdt = 0.002\hbar$.

Fig. 7.3 shows the simulation of a π -pulse with the calibration parameters obtained from the previous analysis. The red shaded region marks the duration of the rf-drive, which is turned off after a time $Jt_\pi = 3.45\hbar$. The population of $|2\rangle$ is nearly completely transferred to $|3\rangle$ and, as it should be, remains constant throughout the remainder of the evolution (since the rf-coupling is turned off). In the following we will now discuss the response of the Fermi gas to this type of quench setup.

7.3 Density Dynamics and Breathing Mode Excitation

We now turn to the site resolved densities $\langle n_{i,1} \rangle$ and $\langle n_{i,3} \rangle$ as well as the emerging doublon density $\langle n_{i,1}n_{i,3} \rangle$ in the system, displayed in Fig. 7.4. Starting from an initially empty band,

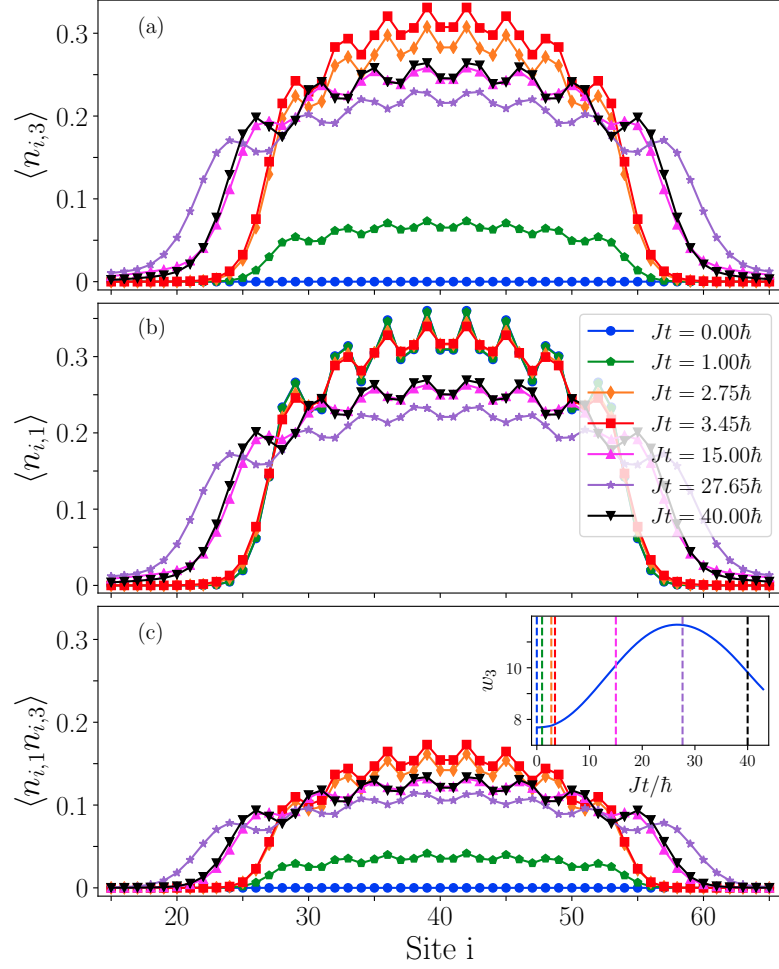


Figure 7.4: Evolution of the density distributions in the trapped system (same parameters as in Fig. 7.3). (a) Snapshots of the density distribution of the third state starting from the empty state at time $Jt = 0\hbar$. (b) Response of $\langle n_{i,1} \rangle$, not addressed by the rf-pulse. Despite the population remaining constant throughout the evolution, we observe interaction induced density redistributions. (c) Snapshots of the doublon distribution, $\langle n_{i,1}n_{i,3} \rangle$, state starting from an initially empty occupation. The times shown in all panels are displayed in the legend of (b). The inset in (c) displays the width $w_3(t)$, Eq. 7.5, of the density shown in the upper panel (a), where the vertical dashed lines mark the presented snapshots in the main part of the plot (with the corresponding colour coding). The numerical simulations were performed with a bond dimension of $m = 300$, truncation error $\epsilon = 10^{-12}$, and a Trotter-Suzuki time-step of $Jdt = 0.002\hbar$.

7.3 Density Dynamics and Breathing Mode Excitation

$|3\rangle$ is rapidly populated during the π -pulse. Due to the presence of the harmonic trap, we have reduced boundary effects and the particles are restricted to the central region of the lattice. We hence only show the populated core of the system. The top panel (a) shows the evolution $\langle n_{i,3}(t) \rangle$. Interestingly, once the transfer is completed and the rf-coupling turned off at $Jt = 3.45\hbar$ (red line), the dynamics does not halt. Instead, we observe ‘breathing’ oscillations in the density with a broad distribution at time $Jt = 27.65\hbar$ which steepens again thereafter. The dynamics is clearly seen in the width of the density distribution of the third level, defined by

$$w_3(t) = \sqrt{\frac{1}{N_3(t)} \sum_i \left(i - \frac{L+1}{2}\right)^2 n_{i,3}(t)}. \quad (7.5)$$

As shown in the inset of the lower panel (c), the width displays non-trivial oscillation dynamics, signalling the excitation of the collective monopole mode of the trap, induced by the rf-quench. For a trapping potential $V_{\text{trap}} = 0.001J$, we can estimate its oscillation period to be given by $JT \sim 100\hbar$, which agrees with the widest density distribution reached at a quarter period of $T/4 \sim 25\hbar/J$.

The central panel in turn shows the dynamics in the lower level population $\langle n_{i,1} \rangle$. Since level $|1\rangle$ is not coupled by the rf-drive to the final state $|3\rangle$, any dynamics observed is purely an interaction induced effect. Furthermore, since the rf-pulse is performed on a time scale much faster than the trap dynamics, we expect $\langle n_{i,1} \rangle$ to show no disturbance or dynamics at short times. Referring to (b), we can indeed confirm this. The density remains stable and ‘frozen’ in its initial ground state distribution, but as time evolves we observe a very similar breathing mode dynamics as in $\langle n_{i,3} \rangle$. The excitation of the breathing mode naturally affects all species coupled with each other through the interaction and in this way the π -pulse also induces breathing oscillations in $|1\rangle$.

Finally, (c) shows the doublon density $\langle n_{i,1}(t)n_{i,3}(t) \rangle$. Due to the attractive interaction in the final state, $U_{13} = -2J$, we would naively expect the quench to transfer the population from $|2\rangle$ to $|3\rangle$ which subsequently would form new pairing correlations in the $|13\rangle$ manifold. Before turning to these pairing correlations, we here look at the doublon occupation. Albeit being reduced in magnitude compared to the other two densities discussed, after the initial increase due to the drive, the doublons exhibit shape oscillations of the same nature as shown previously.

Density Distributions in Momentum Space

Since the rf-pulse drives vertical transitions in momentum space, we conclude this section by briefly commenting on the response of the momentum distributions. As we are transferring particles out of $|2\rangle$, we expect the initial ground state distribution to be depleted to (near) zero over the course of the rf-drive. Looking at Fig. 7.5 (b) we see that this is indeed the case, the initially broad distribution of $\langle n_{k,2}(t=0) \rangle$ is transferred into a narrower $\langle n_{k,3} \rangle$ distribution by the end of the drive, due to the weaker interaction in the final state (c). Additionally, the upper level exhibits a steepening towards low momenta and a subsequent relaxation thereof. This slow dynamics occurs on the same time scale as the monopole mode of the system, corroborating our previous findings in real space.

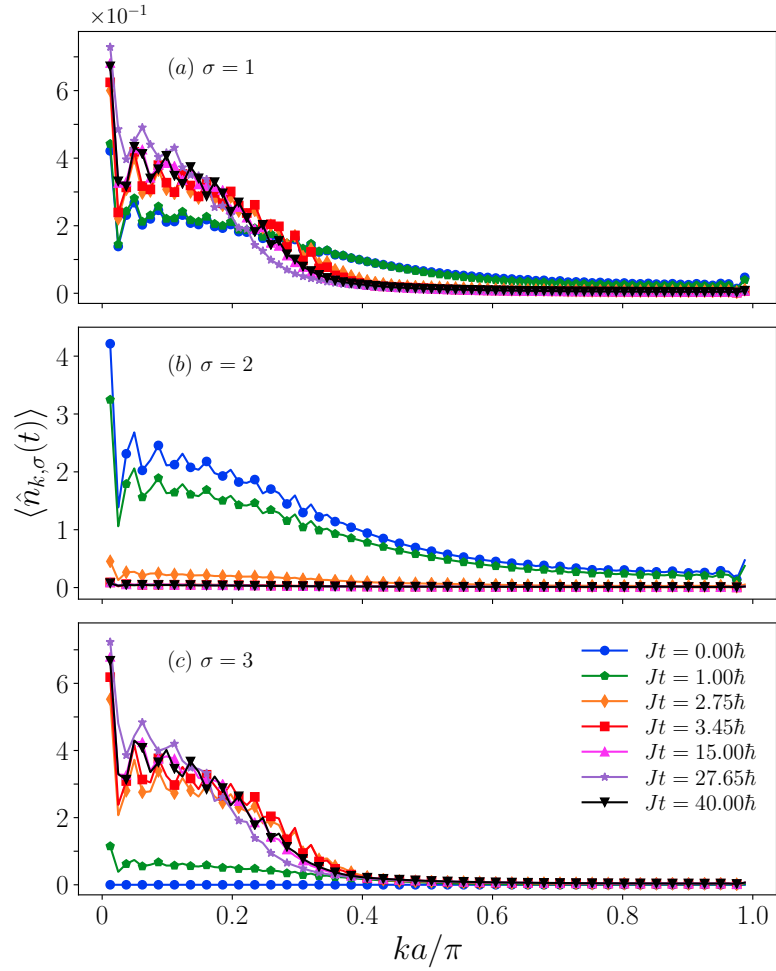


Figure 7.5: Snapshots of the evolution of the momentum densities $\langle n_{k,\sigma} \rangle$ in the trapped system (same parameters as in Fig. 7.3) for $\sigma = \{1, 2, 3\}$ shown in (a-c) respectively. The times shown in all panels are displayed in the legend of (c). Also note, that we have only marked every other numerical data point for better readability. The numerical simulations were performed with a bond dimension of $m = 300$, truncation error $\epsilon = 10^{-12}$, and a Trotter-Suzuki time-step of $Jdt = 0.002\hbar$.

7.4 Characterising the Pairing State

Intuitively, when the real-space density distribution is at its widest point in the evolution at $Jt = 27.65\hbar$ (see e.g. the lower panel of Fig. 7.4), the atomic cloud stops expanding and begins to turn inwards towards the center of the trap. At this turning point the momentum distribution should show an accumulation of fermions in the lower momentum states and a relatively narrow distribution, which we can confirm by looking at the purple curve ($Jt = 27.65$) of Fig. 7.5 (c). Subsequently, as the cloud draws inwards, the particles gain momentum and $\langle n_{k,3} \rangle$ shows a redistribution towards higher momentum states and becomes wider ($Jt = 40\hbar$, black line).

Finally, $\langle n_{k,1}(t) \rangle$ already shows interaction induced redistribution effects *during* the drive. Due to the relatively weak final state interactions between $|1\rangle$ and $|3\rangle$, the momentum distribution steepens and becomes narrower, eventually matching the $\sigma = 3$ distribution and mimicking the ensuing trap induced dynamics as already discussed. This suggests that particles in $|1\rangle$ and $|3\rangle$ are correlated and prompts us to look into the emerging pair coherence in the following section.

7.4 Characterising the Pairing State

The attractive interaction in the final state allows for pairing between species $|1\rangle$ and $|3\rangle$. Hence the natural extension of the previous investigation is to see, whether the system is able to establish pairing coherence after the population is flipped. To that end we show in Fig. 7.6 the pair momentum distribution given by

$$P_k(t) = \frac{1}{L} \sum_{m,n} e^{ik(m-n)} \langle \hat{\Delta}_m^\dagger \hat{\Delta}_n \rangle, \quad (7.6)$$

where $\hat{\Delta}_m = c_{m,1}c_{m,3}$ is the pair annihilation operator at site m , and $k = \frac{2n\pi}{L}$ is the momentum, with $n = \{-\frac{L}{2} + 1, \dots, \frac{L}{2}\}$.

In momentum space the pair distribution follows the same dynamics as already observed in $\langle n_{k,\sigma} \rangle$. Pair coherence is growing in the initial part of the evolution due to the growth in population of the final state (a). Subsequently, the slow trap dynamics gives rise to an oscillatory behaviour in the distribution between a narrow distribution with a zero-peak and one which is wider and has a shifted peak at non-zero momentum. The dashed lines highlight particular momenta, for which we show the full time evolution in (b) (correspondingly the time snapshots are marked by black dots here). The most notable feature is the evolution of the $k = 0$ amplitude $\Re(P_{k=0})$ (related to the experimental condensate fraction), which shows an initial strong increase during the time of the rf-drive due to the occupation of the third state. Interestingly, $\Re(P_{k=0})$ appears to be decreasing *before* the rf-pulse has ended, signaling the loss of phase coherence over long distances, which can no longer be balanced by the population transfer into the upper level. The long-time dynamics can again be attributed to the excitation of the monopole mode. The resurgence of the zero-momentum pair amplitude coincides with the density distribution being at its widest point. The large spread of the particles in the trap allows for longer range coherence, which in turn directly yields an increase in $P_{k=0}$. Whilst low momentum amplitudes of P_k qualitatively present a similar picture, for large momenta the

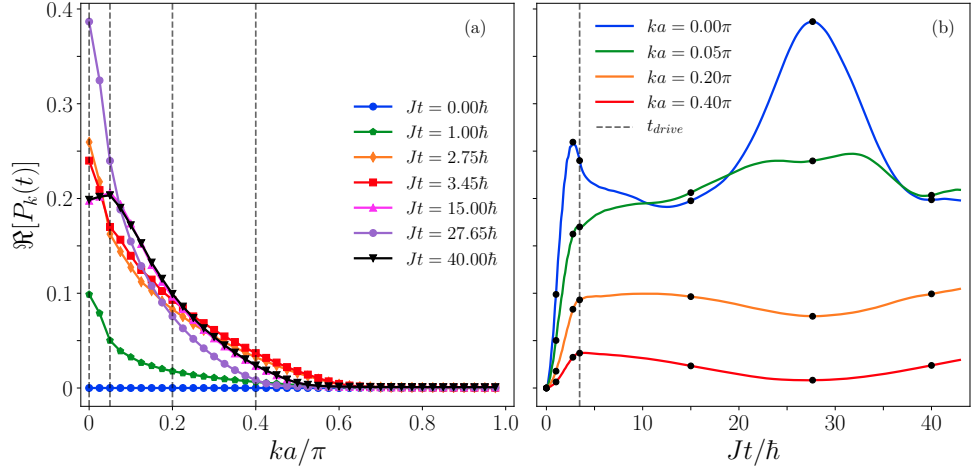


Figure 7.6: (a) Snapshots of the evolution of the pair momentum correlator $P_k(t)$ in the trapped system (same parameters as in Fig. 7.3). Since P_k is symmetric about the $k = 0$ axis, we only show one half of the Brillouin zone here. Similarly to the momentum distribution, here pair coherence builds up during the transfer, with an additional slow dynamics at later times resulting from the excitation of the collective trap mode of the system. The vertical dashed lines (grey) mark the momenta depicted in their entire evolution in (b). In turn the snapshots of (a) are marked by black dots in (b), and the end of the rf-pulse is denoted by the grey dashed line. The numerical simulations were performed with a bond dimension of $m = 300$, truncation error $\epsilon = 10^{-12}$, and a Trotter-Suzuki time-step of $Jdt = 0.002\hbar$.

long-time dynamics is reversed. After approximately a quarter of the trap period $t \sim T/4$, the pair amplitude reaches its *minimal* value.

To understand the role played by the long range coherences a little better, we show in Fig. 7.7 (a) the pair correlation as a function of time for several distances. Whilst it initially increases as a result of the growing population of $|3\rangle$, the long-range coherences start to decrease again even *before* the π -pulse is completed. Since both, decoherence and density redistributions, affect the observed pair correlation, we show in (b) the same pair correlation function renormalised by the doublon densities on the given sites. This has the effect of disentangling the doublon density redistributions from the pair coherence. We see that now all distances show an immediate decrease throughout the rf-pulse. This affirms that it is the loss of coherence between pairs, which cannot be compensated by the rf-transfer, which causes the early decrease of $P_{k=0}$, seen in Fig. 7.6 (b). We furthermore observe slow dynamics in the long-time limit of the pair correlators. These long pair coherences, measured by the zero momentum peak, are thus influenced by the monopole oscillations in the density and hence also show the oscillations with the monopole frequency.

7.5 Summary and Convergence of Results

To conclude this investigation we show a summary of our results in Fig. 7.8. The shaded region in the lower panel (b) marks the duration of the rf-drive. We show the density dynamics in real-space in (a) and can clearly identify the monopole mode as the slow dynamics in the

7.5 Summary and Convergence of Results

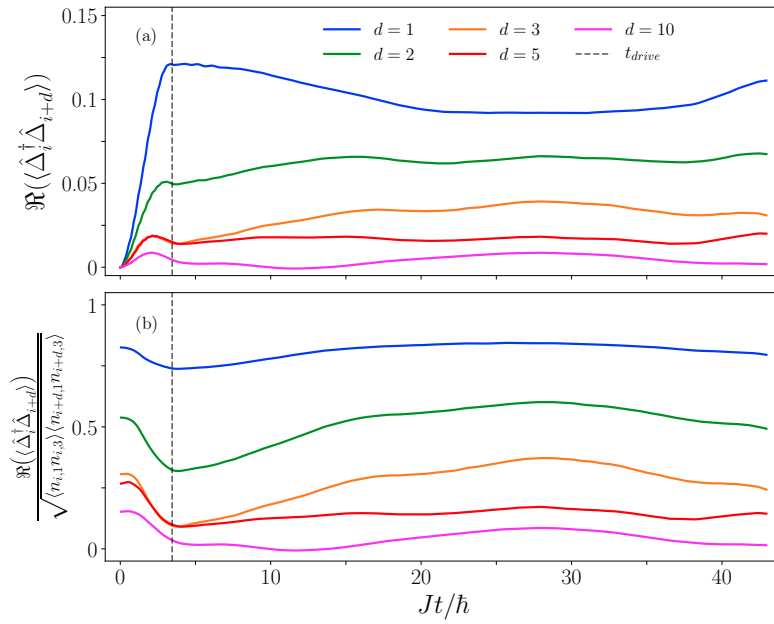


Figure 7.7: (a) Evolution of the pair correlation function for different distances d , starting from the central site $i = 41$ (same parameters as in Fig. 7.3). During the rf-pulse the pair correlations initially all increase, with the longer distance correlators showing a subsequent decrease before the rf-pulse ends. (b) The doublon density renormalised pair correlation function. The initial growth in pair correlations is absent, and instead the coherence decreases during the rf-pulse. The shown distances correspond to the values marked in the legend in (a). The vertical dashed lines (grey) mark the end of the rf-pulse. The numerical simulations were performed with a bond dimension of $m = 300$, truncation error $\epsilon = 10^{-12}$, and a Trotter-Suzuki time-step of $Jdt = 0.002\hbar$.

density profile of $|3\rangle$. Next to the $k = 0$ amplitude of $\Re(P_k)$ (related to the experimental condensate fraction, discussed in the following section), we show its width in momentum space (b),

$$w_{pair} = \sqrt{\frac{1}{P(t)} \sum_k k^2 P_k(t)}, \quad (7.7)$$

where $P(t) = \sum_k P_k$ is the total number of pairs in $|3\rangle$. The oscillations of the width of the pair momentum peak and its amplitude are out of phase. As we have seen, the density dynamics induced by the trap is crucial, hence we disentangle the pair coherence from the density distribution using the following expression

$$C_{k=0}^{pair} = \frac{1}{L_{\text{eff}}} \sum_{20 < i, j < 61} \frac{\langle \hat{\Delta}_i^\dagger \hat{\Delta}_j \rangle}{\sqrt{\langle n_{i,1} n_{i,3} \rangle \langle n_{j,1} n_{j,3} \rangle}}, \quad (7.8)$$

where we have restricted the summation over the central core of the lattice $20 < i, j < 61$ where the density profile of the upper level is appreciably large. $L_{\text{eff}} = 40$ is then the effective size of this central region. This quantity measures the time-evolution of the pair coherence beyond pure density redistribution effects (orange curve), and undergoes a strong decrease at early times, causing the decay of the low momentum amplitude in the pair distribution.

Finally, we plot the width of the density distribution of the third level (red curve), Eq. 7.5, and observe the clear signature of a monopole oscillation as the cloud expands and subsequently draws inwards again.

For all discussed curves we have performed a careful convergence analysis. By varying the Trotter-Suzuki time-step $Jdt = 0.001\hbar$, bond dimension $D = 200$, and truncation error $\epsilon = 10^{-10}$ of the t-MPS simulations independently, we estimated the maximal and minimal variation from the shown data. This defines an effective convergence region within which the numerical error is estimated to lie. For each observable in Fig. 7.8, we have depicted this convergence region by a shaded envelope around the given curve (in the same color). For most curves the shading is not discernible as the numerical error is smaller than the linewidth of the curves. We therefore conclude that our data is sufficiently well converged.

7.6 Connection to Experiment

The described method of performing a quantum quench by applying an rf π -pulse to completely transfer the populations between two internal states of the fermions has been realised in the group of Michael Köhl for a three-dimensional fermionic superfluid in the BCS-BEC crossover in the strongly interacting regime. In previous experiments rf-pulses were mainly used to explore the equilibrium phases of a fermionic quantum gas [85, 106, 166, 167, 218] and only recently the excitation of a Higgs mode [56] has been demonstrated.

Experimentally, as detailed in chapter 4, an ultracold quantum gas of $\sim 10^6$ ${}^6\text{Li}$ atoms is prepared in a balanced mixture of the lowest two hyperfine states $|1\rangle$ and $|2\rangle$ of the electronic ground state (c.f. Fig. 2.2). The gas is harmonically trapped and a homogeneous magnetic

7.6 Connection to Experiment

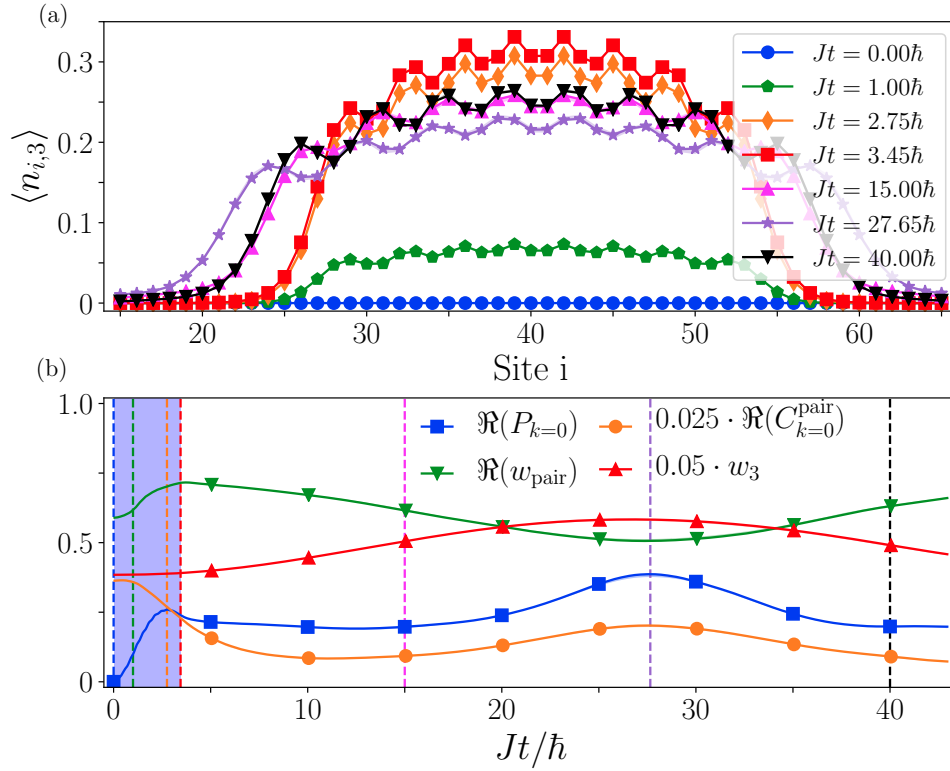


Figure 7.8: (a) Snapshots of the density distribution of the third state in the trap starting from the empty state at time $t = 0$. (b) Time-evolution of various observables: the zero-momentum amplitude of the pair coherence $\Re(P_{k=0})$, w_{pair} is the width of the pair correlation function in momentum space, $C_{k=0}^{\text{pair}}$ is the net pair coherence rescaled by the doublon density, and w_3 the width of the density distribution of state $|3\rangle$. (see main text for the definition of the observables). The blue, shaded area marks the duration of the rf-pulse. The dashed vertical lines mark the times shown in panel (a). For the convergence we have independently varied the bond dimension ($m = 200$), truncation error ($\epsilon = 10^{-10}$) and Trotter-Suzuki time-step $Jdt = 0.001\hbar$. The maximal and minimal deviation is plotted as a shaded region around each curve. Where such a region is not discernible, the numerical error is below the linewidth shown.

field in the range of 880G – 1000G tunes the s -wave scattering length a near the Feshbach resonance at 834G (c.f. section 2.2, realising a quantum gas in the strongly interacting regime $-0.7 \lesssim 1/(k_F a) \lesssim -0.1$). By transferring the population from $|2\rangle$ to $|3\rangle$ the s -wave scattering length is changed from a_{12} to a_{13} , quenching the system from a strongly-interacting initial to a weakly-interacting final state in the BCS regime (c.f. Fig 2.3).

Once the π -pulse is completed and after a certain hold time, the dipole trap is turned off and a rapid magnetic field sweep onto the BEC side of the Feshbach resonance is performed. A ballistic expansion maps the initial momentum distribution onto real-space, which is recorded by an absorption image.

With a Fermi energy of $E_F \simeq h \times (29 \pm 3)$ kHz in the trap centre, and a typical π -pulse duration of $\tau \simeq 28\mu s = 4.8\hbar/E_F$, the rf-pulse is still slow compared to the internal dynamics of the BCS model, but fast as compared to the time scale of the trap. It is therefore not expected to excite the collective amplitude mode of the superconducting order parameter (for reference we refer the reader back to chapter 4). Instead, the experiment reveals the excitation of a collective mode of the harmonic trap and, surprisingly, dynamics reminiscent of collapse and revival in the superfluid condensate fraction [219]. The time scales observed for the collapse and revival of the condensate are very long and comparable to the trap period rather than to the intrinsic time scales of the superfluid. The experiment, conducted by the group of Michael Köhl, excited a collective monopole mode and revealed the non-trivial interplay between trap and pairing dynamics, in particular oscillations in the condensate fraction have not been reported in previous experiments [210, 211, 220–223].

The experimental results are in qualitative agreement with the theoretical calculations presented above, which confirms that the observed dynamics is a result of the interplay between density inhomogeneity and pairing dynamics.

7.7 Conclusion

Here we have studied the dynamical response of an interacting, three-species Fermi-Hubbard model to an rf π -pulse. Taking final state interactions into account, the near-perfect population transfer realised a quantum quench setup. To make connection to experiments, we included the harmonic trapping of the fermionic gas in our description of our model and worked in the low density regime. We found different dynamics ensuing as a result of the population transfer. While the pair correlation in the final state initially increases due to the population of the upper level, it exhibits a surprising decrease even before the π -pulse is completed, which we attribute to fast decoherence processes determined by the final state. Additionally, all discussed observables, most notable the particle density show another, slow dynamical time scale in their evolution. We find that the rf-quench activates the collective monopole mode of the trap and discuss its non-trivial effect on the pairing dynamics. Our simulations are in good, qualitative agreement with rf-quench experiments performed in the BCS-BEC crossover in the group of Michael Köhl.

Conclusion

In this thesis we have presented a comprehensive investigation of the non-equilibrium dynamics of interacting Fermi gases. We focussed on two different fermionic models, a three-dimensional Fermi gas in the BCS-BEC crossover, and a one-dimensional Fermi-Hubbard model confined to an optical lattice geometry. Both models have been studied in the past and in this thesis we build upon these results, by extending the Hilbert space to include an initially unpopulated state corresponding to a third fermionic species. By coupling this final level to an initially occupied state using radiofrequency (rf) modulation to redistribute the population between the three fermionic species, we drove the system away from equilibrium and probed its excitation spectrum. In this thesis we have explored the rf-modulation as a tool with three-fold purpose.

Firstly, we developed a novel excitation technique based upon the rf-transfer. We studied a three-dimensional, homogeneous Fermi gas in the BCS-BEC crossover. By transferring a small fraction of particles between the initial, correlated ground state and the empty final state, we excited the Higgs mode of the system, a collective excitation of the superconducting state. This mode is usually short-lived, but in the BCS regime it is stabilised by an effective Lorentz invariance of the equations of motion provided by the particle-hole symmetry of the Hamiltonian near the Fermi momentum. As it is a scalar excitation it does not couple directly to gauge fields and is therefore difficult to excite and observe experimentally. In this chapter, we have devised a novel excitation mechanism based on far red-detuned rf-modulation of the Fermi gas and theoretically showed the *direct* coupling to the superconducting order parameter. We revealed the collective nature of the Higgs mode from Fourier spectra of the momentum-resolved superconducting order parameter, which served as an unambiguous final proof of its excitation, and confirmation of the proposed excitation scheme. Finally, we have compared our simulations in the BCS regime to an experiment conducted in the group of Michael Köhl and found excellent agreement between the two. Our investigations provide a route to use rf-techniques beyond spectroscopic tools to dynamically excite and stabilise complex quantum many-body states away from equilibrium.

In a closely related study, we explored the influence of the duration of quantum quenches upon the ensuing quantum dynamics. Here we tuned the *s*-wave scattering length of an interacting two-species Fermi gas described by the mean-field BCS Hamiltonian. As we lowered the

interaction strength over time, we uncovered three distinct dynamical regimes in the subsequent dynamics of the superconducting order parameter. For fast quenches, the order parameter vanished, while the pair amplitude remained finite. This illustrated the delicate nature of the superconducting state, and the importance of long-range phase coherence between Cooper pairs. By rapidly changing the interaction, the Cooper pairs of the initial state were projected onto the new basis of the final Hamiltonian. We showed that this rapid quench predominantly generated excited Cooper pairs in the new basis, which quickly dephased. The observed final state was therefore characterised by incoherent, pre-formed pairs. Increasing the quench duration we found that intermediate ramps gave rise to a reduced, but finite order parameter with long-lived oscillations in the final state. The competition between the free evolution driven by the system’s chemical potential and the dephasing mechanism of the excited Cooper pairs was the origin of this dynamical regime, where the dephasing has not been sufficient to fully erode the superconducting state. For slow quenches in the (near) adiabatic regime, the system followed the instantaneous interaction strength and the final state was shown to be given by a finite temperature thermal state with a static, reduced superconducting order parameter. Our results thus show how the coherence of Cooper pairs can be dynamically tuned by the quench duration, and demonstrate a new avenue to engineer non-trivial quantum states away from equilibrium.

Secondly, we used the rf-transfer as a spectroscopic tool to uncover the intricate excitation spectrum of the attractive, one-dimensional Fermi-Hubbard model. Our quasi-exact time-dependent matrix product state simulations, revealed two distinct dynamical regimes in the evolution of the system. One was characterised by (off)resonant oscillations of the upper level’s population whilst the other, through coupling to a continuous band of final states, was dominated by a net linear rise. By monitoring the population of the final state in time, we gained detailed information of the excitation spectrum, in particular about the coupling strength to different excitations in the initial state. Using linear response calculations in the weak coupling regime, we related the transfer rate to the spectral function of the initial system. Surprisingly, despite not always being in the linear response regime, we were able to extract the underlying excitation spectrum with reasonable accuracy. We compared our numerical findings to exact results from Bethe ansatz, and find overall good agreement between the different methods. However, the t-MPS simulations allowed us to go beyond the spectral response and study in detail the full out-of-equilibrium evolution, enabling us to characterise the two distinct dynamical regimes. In this way we presented a comprehensive overview of the nature of the rf-transfer and how it affects a quantum many-body system at the microscopic level.

Thirdly, we explored the possibility of employing rf-modulation to perform quench experiments on time scales difficult to attain using more traditionally used magnetic ramp techniques. We proposed a scheme which exploits the differences in the s -wave scattering length near a Feshbach resonance. By completely transferring particles from a strongly interacting initial state to a weakly interacting final state, we realised a *population quench* of the system on a time-scale of a few hopping periods. We performed t-MPS simulations of a large system in the low density limit, explicitly taking the final state interactions and time-dependence of the rf-drive into account. Our simulations revealed the excitation of a collective trap mode and we observed its

fingerprint in various experimentally accessible observables. The pairing dynamics was shown to be governed by two different dynamical time scales. For early times the evolution was determined by the π -pulse of the rf-drive, and its competition with decoherence processes set by the final state. In the long time limit, a second time scale appeared on the order of the trap mode, and we reported breathing oscillations in the density distribution. These results show how an rf-pulse can be used as a quantum quench method to excite a quantum system, and induce intricate dynamics.

Together these studies constitute a detailed account of the response of correlated Fermi gases away from equilibrium in experimentally realistic settings. Our study of the Higgs mode highlighted the applicability of the rf-drive to dynamically stabilise complex quantum states out-of-equilibrium. Here, we have focussed on balanced superfluids, but an interesting line of inquiry to pursue would be the long-sought exotic superconducting Fulde-Ferrell-Larkin-Ovchinnikov (FFLO) state [224, 225]. It is characterised by Cooper pairs with a finite centre-of-mass momentum due to an *imbalance* in the population of the two fermionic species. This gives rise to a spatially modulated order parameter $\Delta \sim \Delta_0 e^{i\mathbf{q}\cdot\mathbf{r}}$, with $|\mathbf{q}| \sim |k_{F,\uparrow} - k_{F,\downarrow}|$ and $k_{F,\sigma}$ is the Fermi momentum of spin species σ , where the excess fermions are mainly pinned to the nodes of the order parameter. While the one-dimensional analog of the FFLO state has been found in DMRG simulations of the attractive Hubbard model [226, 227], it has not yet been observed experimentally. A possible route, building upon the presented work, is to extend the rf-driving scheme to create an imbalance between the fermionic populations, and *dynamically* stabilise the FFLO state. Quantum gas microscopy with single atom resolution then offers a promising experimental probe to detect the density modulations imprinted by the FFLO state [228–234].

Lastly, building upon the discussed three-species fermionic systems to model pump-probe experiments [178, 180, 181] would be another route for extension and application. The generality of the considered lattice models, and the numerical algorithm allows for enough flexibility to design and tailor the final state and pump excitation scheme as required. These extensions would allow us to trace the dynamics of the system as it evolves from the created non-equilibrium state and help build a deeper understanding of the microscopic relaxation processes in correlated many-body quantum systems.

Appendix **A**

Appendix for Chapter 2

A.1 Bound state of two particles interacting attractively

To check whether a solution to Eq. 2.16 exists, we need to solve the integral

$$\frac{1}{\Omega} \int_{\epsilon < E_R} d\epsilon \frac{\rho_n(\epsilon)}{2\epsilon + |E|}, \quad (\text{A.1})$$

where Ω is the volume of the system, $\rho_n(\epsilon)$ the density of states in n dimensions, $\epsilon = \frac{\hbar^2 q^2}{2m}$ the energy of a free particle of mass m , and $E_R = \frac{\hbar^2}{mR^2}$ the energy cutoff [59]. The density of states in n dimensions, $\rho_n(\epsilon)$ reads

$$\rho_n(\epsilon) = \frac{m\Omega}{\hbar^2} \begin{cases} \frac{1}{\pi} \sqrt{\frac{\hbar^2}{2m\epsilon}}, & n = 1 \\ \frac{1}{2\pi}, & n = 2 \\ \frac{1}{2\pi^2} \sqrt{\frac{2m\epsilon}{\hbar^2}}, & n = 3 \end{cases}. \quad (\text{A.2})$$

1D

$$\begin{aligned} \frac{1}{\Omega} \int_{\epsilon < E_R} d\epsilon \frac{\rho_n(\epsilon)}{2\epsilon + |E|} &= \frac{1}{\pi} \sqrt{\frac{m}{2\hbar^2}} \int_0^{E_R} \frac{d\epsilon}{\sqrt{\epsilon}(2\epsilon + |E|)} \\ &= \frac{2}{\pi} \sqrt{\frac{m}{2\hbar^2}} \int_0^{\sqrt{E_R}} \frac{dx}{(2x^2 + |E|)} \\ &= \frac{2}{\pi} \sqrt{\frac{m}{4\hbar^2|E|}} \int_0^{\sqrt{2E_R/|E|}} \frac{dz}{(z^2 + 1)} \\ &= \frac{2}{\pi} \sqrt{\frac{m}{4\hbar^2|E|}} \arctan(\sqrt{2E_R/|E|}) \\ &\xrightarrow{|E| \ll E_R} \sqrt{\frac{m}{4\hbar^2|E|}}. \end{aligned} \quad (\text{A.3})$$

A.1 Bound state of two particles interacting attractively

2D

$$\begin{aligned} \frac{1}{\Omega} \int_{\epsilon < E_R} d\epsilon \frac{\rho_n(\epsilon)}{2\epsilon + |E|} &= \frac{m}{2\pi\hbar^2} \int_0^{E_R} \frac{d\epsilon}{2\epsilon + |E|} \\ &= \frac{m}{4\pi\hbar^2} \ln \left(\frac{2E_R + |E|}{|E|} \right). \end{aligned} \quad (\text{A.4})$$

3D

$$\begin{aligned} \frac{1}{\Omega} \int_{\epsilon < E_R} d\epsilon \frac{\rho_n(\epsilon)}{2\epsilon + |E|} &= \frac{1}{2\pi^2} \left(\frac{m}{\hbar^2} \right)^{\frac{3}{2}} \int_0^{E_R} \frac{\sqrt{2\epsilon} d\epsilon}{2\epsilon + |E|} \\ &= \frac{1}{2\pi^2} \left(\frac{m}{\hbar^2} \right)^{\frac{3}{2}} \int_0^{\sqrt{2E_R}} \frac{x^2 dx}{x^2 + |E|} \\ &= \frac{1}{2\pi^2} \left(\frac{m}{\hbar^2} \right)^{\frac{3}{2}} \int_{\sqrt{|E|}}^{\sqrt{2E_R+|E|}} dz \frac{\sqrt{z^2 - |E|}}{z} \\ &= \frac{\sqrt{|E|}}{2\pi^2} \left(\frac{m}{\hbar^2} \right)^{\frac{3}{2}} \int_1^{\sqrt{1+2E_R/|E|}} dy \frac{\sqrt{y^2 - 1}}{y} \\ &= \frac{\sqrt{|E|}}{2\pi^2} \left(\frac{m}{\hbar^2} \right)^{\frac{3}{2}} \int_0^{\cosh^{-1}(\sqrt{1+2E_R/|E|})} d\theta \frac{\sinh^2(\theta)}{\cosh(\theta)} \\ &= \frac{\sqrt{|E|}}{2\pi^2} \left(\frac{m}{\hbar^2} \right)^{\frac{3}{2}} \int_0^{\theta_R} d\theta \left(\cosh(\theta) - \frac{1}{\cosh(\theta)} \right) \\ &= \frac{\sqrt{|E|}}{2\pi^2} \left(\frac{m}{\hbar^2} \right)^{\frac{3}{2}} \left[\sinh(\theta_R) - 2 \int_0^{\theta_R} \frac{e^\theta d\theta}{e^{2\theta} + 1} \right] \\ &= \frac{\sqrt{|E|}}{2\pi^2} \left(\frac{m}{\hbar^2} \right)^{\frac{3}{2}} \left[\sinh(\theta_R) - 2 \int_1^{\gamma_R} \frac{d\gamma}{\gamma^2 + 1} \right] \\ &= \frac{\sqrt{|E|}}{2\pi^2} \left(\frac{m}{\hbar^2} \right)^{\frac{3}{2}} \left[\sinh(\theta_R) - 2 \left(\arctan(\gamma_R) - \frac{\pi}{4} \right) \right] \\ &= \frac{\sqrt{|E|}}{2\pi^2} \left(\frac{m}{\hbar^2} \right)^{\frac{3}{2}} \left[\sqrt{\cosh^2(\theta_R) - 1} - 2 \arctan(e^{\theta_R}) + \frac{\pi}{2} \right] \\ &= \frac{\sqrt{|E|}}{2\pi^2} \left(\frac{m}{\hbar^2} \right)^{\frac{3}{2}} \left[\sqrt{2E_R/|E|} - 2 \arctan(e^{\theta_R}) + \frac{\pi}{2} \right] \\ &\stackrel{|E| \ll E_R, \theta_R \gg 1}{\longrightarrow} \frac{\sqrt{|E|}}{2\pi^2} \left(\frac{m}{\hbar^2} \right)^{\frac{3}{2}} \left[\sqrt{2E_R/|E|} - \pi + \frac{\pi}{2} \right] \\ &= \frac{1}{2\pi^2} \left(\frac{m}{\hbar^2} \right)^{\frac{3}{2}} \left[\sqrt{2E_R} - \frac{\pi}{2} \sqrt{|E|} \right]. \end{aligned} \quad (\text{A.5})$$

We therefore see, that the above integral diverges for dimensions $n = \{1, 2\}$, whilst it is finite in three dimensions. Thus in three dimensions there is a threshold for the interaction potential, below which there exists no bound state for two particles interacting attractively for $|E| \rightarrow 0$.

A.2 Self-consistent solution of the BCS gap and number equation

Here we outline the steps involved in solving the gap and number equations of section chapter 2, following [59]. The superconducting gap and particle number equations read

$$\Delta = \frac{g}{V} \sum_{\mathbf{k}} \langle c_{-\mathbf{k},2} c_{\mathbf{k},1} \rangle = \frac{g}{V} \sum_{\mathbf{k}} u_{\mathbf{k}}^* v_{\mathbf{k}} = -\frac{g}{V} \sum_{\mathbf{k}} \frac{\Delta}{2E_{\mathbf{k}}} \quad (\text{A.6})$$

$$n = \frac{1}{V} \sum_{\mathbf{k},\sigma} \langle n_{\mathbf{k},\sigma} \rangle = \frac{2}{V} \sum_{\mathbf{k}} |v_{\mathbf{k}}|^2 = \frac{1}{V} \sum_{\mathbf{k}} \left(1 - \frac{\xi_{\mathbf{k}}}{E_{\mathbf{k}}}\right). \quad (\text{A.7})$$

Using the renormalisation procedure outline in section 2.1 and rewriting the sums in their integral form, results in

$$\begin{aligned} -\frac{1}{g} &= \int \frac{d^3\mathbf{k}}{(2\pi)^3} \frac{1}{2E_{\mathbf{k}}} \\ -\frac{n}{4\pi\hbar^2 a} &= \int \frac{d^3\mathbf{k}}{(2\pi)^3} \left(\frac{1}{2E_{\mathbf{k}}} - \frac{1}{2\epsilon_{\mathbf{k}}} \right) \\ -\frac{1}{k_F a} &= \frac{2}{\pi} \sqrt{\frac{\Delta}{E_F}} \int_0^\infty dx x^2 \left[\frac{1}{\sqrt{(x^2 - \mu/\Delta)^2 + 1}} - \frac{1}{x^2} \right], \end{aligned} \quad (\text{A.8})$$

while the number equation becomes

$$\begin{aligned} n &= \int \frac{d^3\mathbf{k}}{(2\pi)^3} \left(1 - \frac{\xi_{\mathbf{k}}}{E_{\mathbf{k}}}\right) \\ 1 &= \frac{3}{2} \left(\frac{\Delta}{E_F}\right)^{3/2} \int_0^\infty dx x^2 \left[1 - \frac{x^2 - \mu/\Delta}{\sqrt{(x^2 - \mu/\Delta)^2 + 1}} \right], \end{aligned} \quad (\text{A.9})$$

where we have used the expression of the Fermi momentum in terms of the particle density, $k_F = (3\pi^2 n)^{1/3}$ in the last line of the previous equation. We can now solve Eq. A.9 numerically to obtain Δ/E_F as a function of μ/Δ , which can in turn be used in Eq. A.8 to compute $1/(k_F a)$. Inverting the relations, we thus evaluated the superconducting gap and chemical potential in the BCS-BEC crossover as a function of the dimensionless interaction parameter $1/(k_F a)$.

Appendix B

Appendix for Chapter 5

B.1 Quasiparticle weight in a sudden Quench

Here we detail the calculation to try and understand why an abrupt quench of the interaction strength couples strongly to the quasiparticle excitations of the system. We are interested in the evolution of the momentum-resolved superconducting order parameter $\Delta_{\mathbf{k}}(t)$ in the case of an abrupt interaction quench, i.e. we have a Hamiltonian H_i (time-independent) for $t < 0$, then change the internal interaction at $t = 0$ so that the system is described by H_f for $t \geq 0$. We start in the ground state of the initial Hamiltonian $|\psi(0^-)\rangle = |\psi_{BCS}\rangle = \prod_{\mathbf{k}}(u_{\mathbf{k}} + v_{\mathbf{k}}c_{\mathbf{k},1}^\dagger c_{-\mathbf{k},2}^\dagger)|0\rangle \equiv |\psi_0\rangle$. The Hamiltonian of the system is diagonalisable at each point in time, making the Bogoliubov amplitudes time-dependent. For notational purposes we choose capital letters for $t \geq 0$, such that the Bogoliubov transformation at some positive time reads

$$\begin{pmatrix} \gamma_{\mathbf{k},0} \\ \gamma_{\mathbf{k},1}^\dagger \end{pmatrix} = \begin{pmatrix} U_{\mathbf{k}} & -V_{\mathbf{k}} \\ V_{\mathbf{k}}^* & U_{\mathbf{k}} \end{pmatrix} \begin{pmatrix} c_{\mathbf{k},1} \\ c_{-\mathbf{k},2}^\dagger \end{pmatrix} \text{ and } \begin{pmatrix} c_{\mathbf{k},1} \\ c_{-\mathbf{k},2}^\dagger \end{pmatrix} = \begin{pmatrix} U_{\mathbf{k}}^* & V_{\mathbf{k}} \\ -V_{\mathbf{k}}^* & U_{\mathbf{k}} \end{pmatrix} \begin{pmatrix} \gamma_{\mathbf{k},0} \\ \gamma_{\mathbf{k},1}^\dagger \end{pmatrix}. \quad (\text{B.1})$$

In terms of the quasiparticle operators the momentum-resolved gap reads

$$\begin{aligned} \langle \Delta_{\mathbf{k}}(t) \rangle &= \langle c_{-\mathbf{k},2}(t)c_{\mathbf{k},1}(t) \rangle \\ &= \langle (-V_{\mathbf{k}}\gamma_{\mathbf{k},0}^\dagger(t) + U_{\mathbf{k}}^*\gamma_{\mathbf{k},1}(t))(U_{\mathbf{k}}\gamma_{\mathbf{k},0}(t) + V_{\mathbf{k}}\gamma_{\mathbf{k},1}^\dagger(t)) \rangle \\ &= U_{\mathbf{k}}^*V_{\mathbf{k}}(1 - \langle \gamma_{\mathbf{k},0}^\dagger(t)\gamma_{\mathbf{k},0}(t) \rangle - \langle \gamma_{\mathbf{k},1}^\dagger(t)\gamma_{\mathbf{k},1}(t) \rangle) \\ &\quad + U_{\mathbf{k}}^{*2}\langle \gamma_{\mathbf{k},1}(t)\gamma_{\mathbf{k},0}(t) \rangle - V_{\mathbf{k}}^2\langle \gamma_{\mathbf{k},0}^\dagger(t)\gamma_{\mathbf{k},1}^\dagger(t) \rangle, \end{aligned} \quad (\text{B.2})$$

where the expectation value is understood to be taken with respect to the initial ground state $|\psi_0\rangle$. Since the Hamiltonian is diagonal in the quasiparticle operators, their time-dependence is straightforwardly derived from Heisenberg's equation of motion and is given by,

$$\begin{aligned}
\frac{d\gamma_{\mathbf{k},\sigma}^\dagger \gamma_{\mathbf{k},\sigma}}{dt} &= \frac{i}{\hbar} [H_f, \gamma_{\mathbf{k},\sigma}^\dagger \gamma_{\mathbf{k},\sigma}] = 0 \\
\frac{d\gamma_{\mathbf{k},0}^\dagger \gamma_{\mathbf{k},1}^\dagger}{dt} &= \frac{i}{\hbar} [H_f, \gamma_{\mathbf{k},0}^\dagger \gamma_{\mathbf{k},1}^\dagger] = \frac{i}{\hbar} 2E_{\mathbf{k}} \gamma_{\mathbf{k},0}^\dagger \gamma_{\mathbf{k},1}^\dagger .
\end{aligned} \tag{B.3}$$

Thus $\gamma_{\mathbf{k},0}^\dagger(t)\gamma_{\mathbf{k},1}^\dagger(t) = \gamma_{\mathbf{k},0}^\dagger\gamma_{\mathbf{k},1}^\dagger e^{i2E_{\mathbf{k}}t/\hbar}$ and $\gamma_{\mathbf{k},1}(t)\gamma_{\mathbf{k},0}(t) = \gamma_{\mathbf{k},1}\gamma_{\mathbf{k},0} e^{-i2E_{\mathbf{k}}t/\hbar}$. We thus find at this stage

$$\langle \Delta_{\mathbf{k}}(t) \rangle = \langle U_{\mathbf{k}}^* V_{\mathbf{k}} (1 - \gamma_{\mathbf{k},0}^\dagger \gamma_{\mathbf{k},0} - \gamma_{\mathbf{k},1}^\dagger \gamma_{\mathbf{k},1}) + U_{\mathbf{k}}^{*2} \gamma_{\mathbf{k},1} \gamma_{\mathbf{k},0} e^{-i2E_{\mathbf{k}}t/\hbar} - V_{\mathbf{k}}^2 \gamma_{\mathbf{k},0}^\dagger \gamma_{\mathbf{k},1}^\dagger e^{i2E_{\mathbf{k}}t/\hbar} \rangle . \tag{B.4}$$

We now use the BCS wave function to work out the explicit expectation values (note the difference between upper and lower case Bogoliubov amplitudes denoting final and initial Hamiltonians):

$$\begin{aligned}
\langle \gamma_{\mathbf{k},0}^\dagger \gamma_{\mathbf{k},0} \rangle &= (-u_{\mathbf{k}}^* V_{\mathbf{k}}^* + v_{\mathbf{k}}^* U_{\mathbf{k}}^*) (-u_{\mathbf{k}} V_{\mathbf{k}} + v_{\mathbf{k}} U_{\mathbf{k}}) \\
\langle \gamma_{\mathbf{k},1}^\dagger \gamma_{\mathbf{k},1} \rangle &= (-u_{\mathbf{k}}^* V_{\mathbf{k}}^* + v_{\mathbf{k}}^* U_{\mathbf{k}}^*) (-u_{\mathbf{k}} V_{\mathbf{k}} + v_{\mathbf{k}} U_{\mathbf{k}}) \\
\langle \gamma_{\mathbf{k},0}^\dagger \gamma_{\mathbf{k},1}^\dagger \rangle &= (u_{\mathbf{k}} U_{\mathbf{k}}^* + v_{\mathbf{k}} U_{\mathbf{k}}^*) (-u_{\mathbf{k}}^* V_{\mathbf{k}}^* + v_{\mathbf{k}}^* U_{\mathbf{k}}^*) \\
\langle \gamma_{\mathbf{k},1} \gamma_{\mathbf{k},0} \rangle &= (u_{\mathbf{k}}^* U_{\mathbf{k}} + v_{\mathbf{k}}^* U_{\mathbf{k}}) (-u_{\mathbf{k}} V_{\mathbf{k}} + v_{\mathbf{k}} U_{\mathbf{k}}) .
\end{aligned} \tag{B.5}$$

Putting everything together we finally obtain

$$\begin{aligned}
\langle \Delta_{\mathbf{k}}(t) \rangle &= U_{\mathbf{k}}^* V_{\mathbf{k}} - 2U_{\mathbf{k}}^* V_{\mathbf{k}} (-u_{\mathbf{k}}^* V_{\mathbf{k}}^* + v_{\mathbf{k}}^* U_{\mathbf{k}}^*) (-u_{\mathbf{k}} V_{\mathbf{k}} + v_{\mathbf{k}} U_{\mathbf{k}}) \\
&\quad + U_{\mathbf{k}}^{*2} (u_{\mathbf{k}} U_{\mathbf{k}} + v_{\mathbf{k}} U_{\mathbf{k}}) (-u_{\mathbf{k}} V_{\mathbf{k}} + v_{\mathbf{k}} U_{\mathbf{k}}) e^{-i2E_{\mathbf{k}}t/\hbar} \\
&\quad - V_{\mathbf{k}}^2 (u_{\mathbf{k}} U_{\mathbf{k}}^* + v_{\mathbf{k}} U_{\mathbf{k}}^*) (-u_{\mathbf{k}}^* V_{\mathbf{k}}^* + v_{\mathbf{k}}^* U_{\mathbf{k}}^*) e^{i2E_{\mathbf{k}}t/\hbar} .
\end{aligned} \tag{B.6}$$

The prefactors of the two time-dependent excitation branches (quasiparticle excitations) are shown in Fig. 5.4.

B.2 Free Evolution of the BCS Equations

Separating the equations of motion, Eq. 5.1, into real and imaginary parts via $\Delta = |\Delta| e^{-i\phi} = \Delta^R - i\Delta^I$ and $\Delta_{\mathbf{k}} = |\Delta_{\mathbf{k}}| e^{-i\phi_{\mathbf{k}}} = \Delta_{\mathbf{k}}^R - i\Delta_{\mathbf{k}}^I$, we find

B.2 Free Evolution of the BCS Equations

$$\begin{aligned}
\hbar \frac{\partial \Delta_{\mathbf{k}}^R}{\partial t} &= -2\epsilon_{\mathbf{k}} \Delta_{\mathbf{k}}^I + \Delta^I (n_{\mathbf{k},1} + n_{-\mathbf{k},2} - 1) \\
\hbar \frac{\partial \Delta_{\mathbf{k}}^I}{\partial t} &= 2\epsilon_{\mathbf{k}} \Delta_{\mathbf{k}}^R - \Delta^R (n_{\mathbf{k},1} + n_{-\mathbf{k},2} - 1) \\
\hbar \frac{\partial n_{\mathbf{k},\sigma}}{\partial t} &= 2 \left(\Delta^R \Delta_{\mathbf{k}}^I - \Delta^I \Delta_{\mathbf{k}}^R \right).
\end{aligned} \tag{B.7}$$

Note that from the last equation we can see that if $\tan(\phi) = \frac{\Delta^I}{\Delta^R} = \frac{\Delta_{\mathbf{k}}^I}{\Delta_{\mathbf{k}}^R} = \tan(\phi_{\mathbf{k}})$, i.e. the phases are completely locked, and $n_{\mathbf{k},\sigma}$ is constant in time.

Pseudo-spin representation

A convenient way to represent the BCS problem is in terms of pseudo-spin variables $\mathbf{s}_{\mathbf{k}}$. These are defined as

$$s_{\mathbf{k}}^- = \langle \hat{s}_{\mathbf{k}}^- \rangle = s_{\mathbf{k}}^x - i s_{\mathbf{k}}^y \equiv \Delta_{\mathbf{k}} = \langle c_{-\mathbf{k},2} c_{\mathbf{k},1} \rangle \tag{B.8}$$

$$s_{\mathbf{k}}^z = \langle \hat{s}_{\mathbf{k}}^z \rangle \equiv \frac{1}{2} (n_{\mathbf{k},1} + n_{-\mathbf{k},2} - 1), \tag{B.9}$$

i.e. $\hat{s}_{\mathbf{k}}^{\pm}$ are related to the creation/annihilation of a (zero-momentum) Cooper pair at momenta ($\mathbf{k} \uparrow, -\mathbf{k} \downarrow$). The equations of motion for the spin variables then read

$$\begin{aligned}
\hbar \frac{\partial s_{\mathbf{k}}^x}{\partial t} &= 2\Delta^I s_{\mathbf{k}}^z - 2\epsilon_{\mathbf{k}} s_{\mathbf{k}}^y \\
\hbar \frac{\partial s_{\mathbf{k}}^y}{\partial t} &= 2\epsilon_{\mathbf{k}} s_{\mathbf{k}}^x - 2\Delta^R s_{\mathbf{k}}^z \\
\hbar \frac{\partial s_{\mathbf{k}}^z}{\partial t} &= 2\Delta^R s_{\mathbf{k}}^y - 2\Delta^I s_{\mathbf{k}}^x.
\end{aligned} \tag{B.10}$$

These can be compactly written as a precession equation of the spins around a self-consistent artificial magnetic field $\hbar \dot{\mathbf{s}}_{\mathbf{k}} = \mathbf{b}_{\mathbf{k}} \times \mathbf{s}_{\mathbf{k}}$, where $\mathbf{b}_{\mathbf{k}} = (2\Delta^R, 2\Delta^I, 2\epsilon_{\mathbf{k}})^T$. The BCS Hamiltonian can in turn be rewritten in terms of the spin operators as

$$H = \sum_{\mathbf{k}} \mathbf{b}_{\mathbf{k}} \cdot \hat{\mathbf{s}}_{\mathbf{k}}, \tag{B.11}$$

and the equations of motion (see above) remind us of the optical Bloch equations [235]. We can also see that the ground state of the quantum-mechanically averaged "classical" spin Hamiltonian, is simply the state, where each spin anti-aligns with its local magnetic field (note that $\|\mathbf{s}_{\mathbf{k}}\| = 1/2$):

$$\mathbf{s}_{\mathbf{k},GS} = \langle GS | \hat{\mathbf{s}}_{\mathbf{k}} | GS \rangle = -\frac{\mathbf{b}_{\mathbf{k}}}{2\|\mathbf{b}_{\mathbf{k}}\|} = -\frac{1}{4\sqrt{|\Delta_0|^2 + \epsilon_{\mathbf{k}}^2}} \begin{pmatrix} 2\Delta^R \\ 2\Delta^I \\ 2\epsilon_{\mathbf{k}} \end{pmatrix} = \frac{1}{2E_{\mathbf{k}}} \begin{pmatrix} \Delta_0 \\ 0 \\ -\epsilon_{\mathbf{k}} \end{pmatrix}, \quad (\text{B.12})$$

where $\Delta(t=0) = \Delta^R(0) - i\Delta^I(0) = -\Delta_0$ and initially $H \rightarrow H - \mu N$, i.e. $\epsilon_{\mathbf{k}} \rightarrow \xi_{\mathbf{k}} = \epsilon_{\mathbf{k}} - \mu$ (this is also how the chemical potential enters the evolution of the wave function as we will see in the following). This agrees with our result from diagonalising the Hamiltonian after a Bogoliubov transformation.

Ansatz for the phase evolution

When the system evolves freely, the phases of Δ and $\Delta_{\mathbf{k}}$ are completely synchronised as $\phi(t) = \phi_{\mathbf{k}}(t) = \omega t = 2\mu t/\hbar$. The following calculation aims to recover this result from the equations of motion directly. We choose the ansatz $\Delta(t) = -|\Delta(0)|e^{-i\omega t}$ and $\Delta_{\mathbf{k}}(t) = |\Delta_{\mathbf{k}}(0)|e^{-i\omega t}$ (the extra minus sign in Δ comes from the interaction $g < 0$ which we also see in the numerical simulations). The ansatz for the spins then reads

$$\begin{aligned} s_{\mathbf{k}}^x(t) &= \Delta_{\mathbf{k},0} \cos(\omega t) \\ s_{\mathbf{k}}^y(t) &= \Delta_{\mathbf{k},0} \sin(\omega t) \\ s_{\mathbf{k}}^z(t) &= s_{\mathbf{k}}^z(0) = \frac{1}{2}(n_{\mathbf{k},1}(0) + n_{-\mathbf{k},2}(0) - 1) = \frac{1}{2}(2|v_{\mathbf{k}}|^2 - 1) = -\frac{\xi_{\mathbf{k}}}{2E_{\mathbf{k}}} \\ \Delta^R(t) &= -\Delta_0 \cos(\omega t) \\ \Delta^I(t) &= -\Delta_0 \sin(\omega t), \end{aligned} \quad (\text{B.13})$$

where $\Delta_0 = |\Delta(t=0)|$, and $\Delta_{\mathbf{k},0} = |\Delta_{\mathbf{k}}(t=0)| = |u_{\mathbf{k}}^* v_{\mathbf{k}}| = \frac{\Delta_0}{2E_{\mathbf{k}}}$. Since this ansatz assumes synchronised phases, the number densities and hence also $s_{\mathbf{k}}^z$ are constant in time. Plugging this ansatz then into the precession equations yields the coupled equations

$$\begin{aligned} -\hbar\omega\Delta_{\mathbf{k},0} \sin(\omega t) &= -2\Delta_0 s_{\mathbf{k}}^z(0) \sin(\omega t) - 2\epsilon_{\mathbf{k}}\Delta_{\mathbf{k},0} \sin(\omega t) \\ \hbar\omega\Delta_{\mathbf{k},0} \cos(\omega t) &= 2\epsilon_{\mathbf{k}}\Delta_{\mathbf{k},0} \cos(\omega t) + 2\Delta_0 s_{\mathbf{k}}^z(0) \cos(\omega t), \end{aligned} \quad (\text{B.14})$$

the equation for $s_{\mathbf{k}}^z$ is already satisfied by the nature of the ansatz. These equations give the dispersion of ω which we find to be

$$\hbar\omega = 2\frac{\Delta_0 s_{\mathbf{k}}^z(0)}{\Delta_{\mathbf{k},0}} + 2\epsilon_{\mathbf{k}} = -2\xi_{\mathbf{k}} + 2\epsilon_{\mathbf{k}} = 2\mu. \quad (\text{B.15})$$

Interestingly the phase evolution is dictated by the chemical potential, even though it is not explicitly included in the equations of motion and only enters through the initialisation via the

B.2 Free Evolution of the BCS Equations

amplitudes $u_{\mathbf{k}}, v_{\mathbf{k}}$.

List of Tables

2.1	Examples of degenerate Fermi Gases	5
3.1	Example of common tensor diagram elements.	36

List of Figures

2.1	Scattering properties of atomic gases	9
2.2	Hyperfine structure of ${}^6\text{Li}$	10
2.3	Feshbach resonance in ${}^6\text{Li}$	11
2.4	Fermionic Pairs in the BCS-BEC crossover	11
2.5	Phase Diagram of the BCS-BEC crossover	12
2.6	Quasiparticle Dispersion	18
2.7	Cooper pair amplitudes	19
2.8	Δ and μ in the BCS-BEC crossover	20
2.9	Band Structure of a periodic lattice	24
2.10	Hopping amplitude	26
2.11	The rf-driven, three-species Fermi-Hubbard model	29
2.12	Schematic of the rf-drive	31
2.13	Rabi Oscillations for the non-interacting system	32
3.1	Left canonical MPS	38
3.2	Right canonical MPS	41
3.3	Local measurement in the MPS formalism	41
3.4	Measuring correlation functions within MPS	42
3.5	Application of an MPO to an MPS	42
3.6	Ground state search	45
3.7	Bond evolution operator	46
3.8	Single time step evolution	47
3.9	Block Structure of MPS Tensors with good quantum numbers	49
3.10	Bethe excitation spectrum for $U = -2J$	56
3.11	Bethe excitation spectrum for $U = -8J$	57
4.1	Mexican hat potential	60
4.2	Principle of Excitation Mechanism	62
4.3	Calibrating the model	63
4.4	Illustration of excitation scheme in momentum space	65
4.5	Δ and N_3 of the full model	66
4.6	Higgs Convergence	67
4.7	$\langle n_{\mathbf{k},3} \rangle$: Comparison of full simulation and analytics	69
4.8	Time evolution and Fourier content of $\Delta(t)$ and $N_3(t)$ for full and simplified model	71
4.9	Modulation of the BCS dispersion due to the Higgs	72
4.10	Contour plot of $ \Delta_{\mathbf{k}} $ in the BCS-BEC crossover	74
4.11	Contour Plot $\Im(\Delta_{\mathbf{k}})$ in BCS-BEC crossover	76
4.12	Theory-Experiment Comparison: $N_3(t)$	77
4.13	Theory-Experiment Comparison: Spectral Weight	78

4.14	Fate of the Higgs in the Crossover	79
5.1	Examples of Slow Quenches in the BCS model	84
5.2	Emergent phases for finite ramp duration in the BCS model	85
5.3	Sudden Quench	87
5.4	Sudden Quench: Excitation Branches	88
5.5	Finite temperature superconducting order parameter	89
5.6	Intermediate Quench	90
5.7	Slow Quench	91
5.8	Convergence of $ \Delta(t) $	92
5.9	Convergence of $ P(t) $	93
6.1	$\langle n_{k,3}(t) \rangle$ for selected states at weak interactions	98
6.2	Spectrum of $\langle n_{k,3} \rangle$ for $U = -2J$	99
6.3	$\langle n_{k,3} \rangle$ near a ‘spin-wave’ excitation	101
6.4	Finite Size Effects	103
6.5	Momentum distribution for $\hbar\omega_{\text{rf}} = 50.0J$	105
6.6	Momentum distribution for $\hbar\omega_{\text{rf}} = 51.1J$	106
6.7	Momentum distribution for $\hbar\omega_{\text{rf}} = 53.0J$	108
6.8	Momentum distribution for $\hbar\omega_{\text{rf}} = 56.0J$	109
6.9	Evolution of the Pair Correlation $P_k(t)$	110
6.10	$N_3(t)$ for $U = -2.0J$	112
6.11	N_3 Spectra for $U = -2.0J$	113
6.12	$\langle n_{k,3}(t) \rangle$ for selected states at strong interactions	115
6.13	Spectrum of $\langle n_{k,3} \rangle$ for $U = -8J$	116
6.14	Ground state distributions of $\langle n_{k,2}(0) \rangle$	117
6.15	Momentum distribution for $\hbar\omega_{\text{rf}} = 56.0J$	119
6.16	Momentum distribution for $\hbar\omega_{\text{rf}} = 60.0J$	121
6.17	Evolution of the Pair Correlation $P_k(t)$	122
6.18	$N_3(t)$ for $U = -8.0J$	123
6.19	N_3 Spectrum for $U = -8.0J$	124
7.1	Rabi transfer for same initial and final state interactions	128
7.2	Rabi transfer for different initial and final state interactions	129
7.3	Population quench through π -pulse	130
7.4	Density profiles during and after a π -pulse	131
7.5	Momentum density during and after a π -pulse	133
7.6	Pair Correlator in momentum space after a π -pulse	135
7.7	Pair Coherences	136
7.8	Convergence and Summary of the results	138

Bibliography

- [1] Charles Kittel and Ching-Yao Fong. *Quantum theory of solids*, volume 5. Wiley New York, 1963.
- [2] Neil W Ashcroft and N David Mermin. *Solid State Physics*, Cornell University, 1976.
- [3] Thierry Giamarchi. *Quantum physics in one dimension*, volume 121. Clarendon Press, 2003.
- [4] Alexander Altland and Ben D. Simons. *Condensed Matter Field Theory*. Cambridge University Press, 2 edition, 2010.
- [5] Subir Sachdev. *Quantum Phase Transitions*. Cambridge University Press, 2 edition, 2011.
- [6] Alexander Weiß and Holger Fehske. *Exact Diagonalization Techniques*, pages 529–544. Springer Berlin Heidelberg, Berlin, Heidelberg, 2008.
- [7] Nicholas Metropolis, Arianna W Rosenbluth, Marshall N Rosenbluth, Augusta H Teller, and Edward Teller. Equation of state calculations by fast computing machines. *The journal of chemical physics*, 21(6):1087–1092, 1953.
- [8] Robert H Swendsen and Jian-Sheng Wang. Nonuniversal critical dynamics in Monte Carlo simulations. *Phys. Rev. Lett.*, 58(2):86, 1987.
- [9] Matthias Troyer and Uwe-Jens Wiese. Computational complexity and fundamental limitations to fermionic quantum Monte Carlo simulations. *Phys. Rev. Lett.*, 94(17):170201, 2005.
- [10] Lode Pollet. Recent developments in quantum Monte Carlo simulations with applications for cold gases. *Reports on progress in physics*, 75(9):094501, 2012.
- [11] Antoine Georges, Gabriel Kotliar, Werner Krauth, and Marcelo J Rozenberg. Dynamical mean-field theory of strongly correlated fermion systems and the limit of infinite dimensions. *Rev. Mod. Phys.*, 68(1):13, 1996.
- [12] Thomas Maier, Mark Jarrell, Thomas Pruschke, and Matthias H Hettler. Quantum cluster theories. *Rev. Mod. Phys.*, 77(3):1027, 2005.
- [13] Steven R. White. Density matrix formulation for quantum renormalization groups. *Phys. Rev. Lett.*, 69:2863–2866, Nov 1992.
- [14] A. J. Daley, C. Kollath, U. Schollwöck, and G. Vidal. Time-dependent density-matrix renormalization-group using adaptive effective Hilbert spaces. *J. Stat. Mech.: Theor. Exp.*, P04005, 2004.
- [15] Guifré Vidal. Efficient Simulation of One-Dimensional Quantum Many-Body Systems. *Phys. Rev. Lett.*, 93:040502, Jul 2004.
- [16] Ulrich Schollwöck. The density-matrix renormalization group in the age of matrix product states. *Annals of Physics*, 326(1):96 – 192, 2011. January 2011 Special Issue.
- [17] H Kamerlingh Onnes. Leiden Comm. 1911. *120b, 122b, 124c*.
- [18] M. Tinkham. *Introduction to Superconductivity*. Courier Corporation, 2004.
- [19] Satyendra Nath Bose. Plancks Gesetz und Lichtquantenhypothese. *Zeitschrift für Physik*,

- 26(1):178–181, 1924.
- [20] Albert Einstein. Quantentheorie des einatomigen idealen Gases. *Sitzungsberichte der Preußischen Akademie der Wissenschaften, Physikalisch-Mathematische Klasse, Berlin*, 1924.
- [21] Albert Einstein. Quantentheorie des idealen einatomigen Gases, zweite abhandlung. *Sitzungsberichte der Preußischen Akademie der Wissenschaften, Physikalisch-Mathematische Klasse, Berlin*, pages 3–14, 1925.
- [22] John Bardeen and David Pines. Electron-phonon interaction in metals. *Phys. Rev.*, 99(4):1140, 1955.
- [23] L. N. Cooper. Bound Electron Pairs in a Degenerate Fermi Gas. *Phys. Rev.*, 104:1189–1190, Nov 1956.
- [24] J. R. Schrieffer. *Theory of Superconductivity*. CRC Press, 2018.
- [25] J. G. Bednorz and K. A. Müller. Possible high- T_c superconductivity in the Ba-La-Cu-O system. *Zeitschrift für Physik B Condensed Matter*, 64(2):189–193, 1986.
- [26] J. Georg Bednorz and K. Alex Müller. Perovskite-type oxides—The new approach to high- T_c superconductivity. *Rev. Mod. Phys.*, 60:585–600, Jul 1988.
- [27] B. Keimer, S. A. Kivelson, M. R. Norman, S. Uchida, and J. Zaanen. From quantum matter to high-temperature superconductivity in copper oxides. *Nature*, 518(7538):179–186, 2015.
- [28] Wolfgang Ketterle and N.J. Van Druten. Evaporative Cooling of Trapped Atoms. volume 37 of *Advances In Atomic, Molecular, and Optical Physics*, pages 181 – 236. Academic Press, 1996.
- [29] Harold J Metcalf and Peter Van der Straten. Laser cooling and trapping of neutral atoms. *The Optics Encyclopedia: Basic Foundations and Practical Applications*, 2007.
- [30] M. H. Anderson, J. R. Ensher, M. R. Matthews, C. E. Wieman, and E. A. Cornell. Observation of Bose-Einstein Condensation in a Dilute Atomic Vapor. *Science*, 269(5221):198–201, 1995.
- [31] K. B. Davis, M. O. Mewes, M. R. Andrews, N. J. van Druten, D. S. Durfee, D. M. Kurn, and W. Ketterle. Bose-Einstein Condensation in a Gas of Sodium Atoms. *Phys. Rev. Lett.*, 75:3969–3973, Nov 1995.
- [32] Brian DeMarco and Deborah S Jin. Onset of Fermi degeneracy in a trapped atomic gas. *Science*, 285(5434):1703–1706, 1999.
- [33] M. R. Matthews, B. P. Anderson, P. C. Haljan, D. S. Hall, C. E. Wieman, and E. A. Cornell. Vortices in a Bose-Einstein Condensate. *Phys. Rev. Lett.*, 83:2498–2501, Sep 1999.
- [34] K. W. Madison, F. Chevy, W. Wohlleben, and J. Dalibard. Vortex Formation in a Stirred Bose-Einstein Condensate. *Phys. Rev. Lett.*, 84:806–809, Jan 2000.
- [35] Michael Köhl, Henning Moritz, Thilo Stöferle, Kenneth Günter, and Tilman Esslinger. Fermionic Atoms in a Three Dimensional Optical Lattice: Observing Fermi Surfaces, Dynamics, and Interactions. *Phys. Rev. Lett.*, 94:080403, Mar 2005.
- [36] Simon Braun, Mathis Friesdorf, Sean S. Hodgman, Michael Schreiber, Jens Philipp

Bibliography

- Ronzheimer, Arnau Riera, Marco del Rey, Immanuel Bloch, Jens Eisert, and Ulrich Schneider. Emergence of coherence and the dynamics of quantum phase transitions. *Proceedings of the National Academy of Sciences*, 112(12):3641–3646, 2015.
- [37] Philipp Hauke, Fernando M Cucchietti, Luca Tagliacozzo, Ivan Deutsch, and Maciej Lewenstein. Can one trust quantum simulators? *Reports on Progress in Physics*, 75(8):082401, 2012.
- [38] J. Ignacio Cirac and Peter Zoller. Goals and opportunities in quantum simulation. *Nature Physics*, 8(4):264–266, 2012.
- [39] Markus Greiner, Olaf Mandel, Theodor W Hänsch, and Immanuel Bloch. Collapse and revival of the matter wave field of a Bose–Einstein condensate. *Nature*, 419(6902):51–54, 2002.
- [40] W. S. Bakr, A. Peng, M. E. Tai, R. Ma, J. Simon, J. I. Gillen, S. Fölling, L. Pollet, and M. Greiner. Probing the Superfluid-to-Mott Insulator Transition at the Single-Atom Level. *Science*, 329(5991):547–550, 2010.
- [41] David Chen, Matthew White, Cecilia Borries, and Brian DeMarco. Quantum Quench of an Atomic Mott Insulator. *Phys. Rev. Lett.*, 106:235304, Jun 2011.
- [42] S. Trotzky, Y-A. Chen, A. Flesch, I. P. McCulloch, U. Schollwöck, J. Eisert, and I. Bloch. Probing the relaxation towards equilibrium in an isolated strongly correlated one-dimensional Bose gas. *Nature Physics*, 8(4):325–330, 2012.
- [43] Marc Cheneau, Peter Barmettler, Dario Poletti, Manuel Endres, Peter Schauß, Takeshi Fukuhara, Christian Gross, Immanuel Bloch, Corinna Kollath, and Stefan Kuhr. Light-cone-like spreading of correlations in a quantum many-body system. *Nature*, 481(7382):484–487, 2012.
- [44] Ulrich Schneider, Lucia Hackermüller, Jens Philipp Ronzheimer, Sebastian Will, Simon Braun, Thorsten Best, Immanuel Bloch, Eugene Demler, Stephan Mandt, David Rasch, and Achim Rosch. Fermionic transport and out-of-equilibrium dynamics in a homogeneous Hubbard model with ultracold atoms. *Nature Physics*, 8(3):213–218, 2012.
- [45] Tilman Esslinger. Fermi-Hubbard Physics with Atoms in an Optical Lattice. *Annual Review of Condensed Matter Physics*, 1(1):129–152, 2010.
- [46] Immanuel Bloch, Jean Dalibard, and Sylvain Nascimbène. Quantum simulations with ultracold quantum gases. *Nature Physics*, 8(4):267–276, 2012.
- [47] Abigail Klopffer. Topics in non-equilibrium physics. *Nature Physics*, 11(2):103–103, 2015.
- [48] M. C. Marchetti, J. F. Joanny, S. Ramaswamy, T. B. Liverpool, J. Prost, Madan Rao, and R. Aditi Simha. Hydrodynamics of soft active matter. *Rev. Mod. Phys.*, 85:1143–1189, Jul 2013.
- [49] Corinna Kollath, Andreas M. Läuchli, and Ehud Altman. Quench Dynamics and Nonequilibrium Phase Diagram of the Bose-Hubbard Model. *Phys. Rev. Lett.*, 98:180601, Apr 2007.
- [50] Norbert Schuch, Michael M. Wolf, Frank Verstraete, and J. Ignacio Cirac. Entropy Scaling and Simulability by Matrix Product States. *Phys. Rev. Lett.*, 100:030504, Jan 2008.
- [51] Peter Barmettler, Matthias Punk, Vladimir Gritsev, Eugene Demler, and Ehud Altman. Re-

- laxation of Antiferromagnetic Order in Spin-1/2 Chains Following a Quantum Quench. *Phys. Rev. Lett.*, 102:130603, Apr 2009.
- [52] S. Langer, F. Heidrich-Meisner, J. Gemmer, I. P. McCulloch, and U. Schollwöck. Real-time study of diffusive and ballistic transport in spin- $\frac{1}{2}$ chains using the adaptive time-dependent density matrix renormalization group method. *Phys. Rev. B*, 79:214409, Jun 2009.
- [53] J. P. Ronzheimer, M. Schreiber, S. Braun, S. S. Hodgman, S. Langer, I. P. McCulloch, F. Heidrich-Meisner, I. Bloch, and U. Schneider. Expansion Dynamics of Interacting Bosons in Homogeneous Lattices in One and Two Dimensions. *Phys. Rev. Lett.*, 110:205301, May 2013.
- [54] J. Eisert, M. Friesdorf, and C. Gogolin. Quantum many-body systems out of equilibrium. *Nature Physics*, 11(2):124–130, 2015.
- [55] John Hubbard. Electron correlations in narrow energy bands. *Proceedings of the Royal Society of London. Series A. Mathematical and Physical Sciences*, 276(1365):238–257, 1963.
- [56] A Behrle, T Harrison, J Kombe, K Gao, M Link, J-S Bernier, C Kollath, and M Köhl. Higgs mode in a strongly interacting fermionic superfluid. *Nature Physics*, 14(8):781–785, 2018.
- [57] Johannes Kombe, Jean-Sébastien Bernier, Michael Köhl, and Corinna Kollath. Finite-duration interaction quench in dilute attractively interacting Fermi gases: Emergence of preformed pairs. *Phys. Rev. A*, 100:013604, Jul 2019.
- [58] T Harrison, M Link, A Behrle, K Gao, A Kell, J Kombe, J-S Bernier, C Kollath, and M Köhl. Decay and revival of a transient trapped Fermi condensate. *arXiv:1411.4831*, 2020.
- [59] W. Ketterle and M. Zwierlein. Making, probing and understanding ultracold Fermi gases. *Rivista del Nuovo Cimento*, 164, 01 2008.
- [60] William D Phillips. Nobel Lecture: Laser cooling and trapping of neutral atoms. *Rev. Mod. Phys.*, 70(3):721, 1998.
- [61] Claude N Cohen-Tannoudji. Nobel Lecture: Manipulating atoms with photons. *Rev. Mod. Phys.*, 70(3):707, 1998.
- [62] Steven Chu. Nobel Lecture: The manipulation of neutral particles. *Rev. Mod. Phys.*, 70(3):685, 1998.
- [63] Lev Davidovich Landau and Evgenii Mikhailovich Lifshitz. *Quantum mechanics: non-relativistic theory*, volume 3. Elsevier, 2013.
- [64] Kerson Huang and C. N. Yang. Quantum-Mechanical Many-Body Problem with Hard-Sphere Interaction. *Phys. Rev.*, 105:767–775, Feb 1957.
- [65] Herman Feshbach. Unified theory of nuclear reactions. *Annals of Physics*, 5(4):357–390, 1958.
- [66] E Tiesinga, BJ Verhaar, and HTC Stoof. Threshold and resonance phenomena in ultracold ground-state collisions. *Phys. Rev. A*, 47(5):4114, 1993.
- [67] S. Inouye, M. R. Andrews, J. Stenger, H. J. Miesner, D. M. Stamper-Kurn, and W. Ketterle. Observation of Feshbach resonances in a Bose–Einstein condensate. *Nature*, 392(6672):151–154, 1998.

Bibliography

- [68] Immanuel Bloch, Jean Dalibard, and Wilhelm Zwerger. Many-body physics with ultra-cold gases. *Rev. Mod. Phys.*, 80:885, 2008.
- [69] G. Zürn, T. Lompe, A. N. Wenz, S. Jochim, P. S. Julienne, and J. M. Hutson. Precise Characterization of ^6Li Feshbach Resonances Using Trap-Sideband-Resolved RF Spectroscopy of Weakly Bound Molecules. *Phys. Rev. Lett.*, 110:135301, Mar 2013.
- [70] M. Parish. *The BCS-BEC Crossover*, chapter 9, pages 179–197. World Scientific, 2015.
- [71] V. N. Popov. Theory of a Bose gas produced by bound states of Fermi particles. *Sov. Phys. JETP*, 50:1034, 1966.
- [72] L. V. Keldysh and A. N. Kozlov. Collective properties of excitons in semiconductors. *Sov. Phys. JETP*, 27(3):521, 1968.
- [73] D. M. Eagles. Possible pairing without superconductivity at low carrier concentrations in bulk and thin-film superconducting semiconductors. *Phys. Rev.*, 186(2):456, 1969.
- [74] A. J. Leggett. Diatomic molecules and cooper pairs. In Andrzej Pękalski and Jerzy A. Przystawa, editors, *Modern Trends in the Theory of Condensed Matter*, pages 13–27, Berlin, Heidelberg, 1980. Springer Berlin Heidelberg.
- [75] M. Randeria and E. Taylor. Crossover from Bardeen-Cooper-Schrieffer to Bose-Einstein condensation and the unitary Fermi gas. *Annual Review of Condensed Matter Physics*, 5(1):209–232, 2014.
- [76] Giancarlo Calvanese Strinati, Pierbiagio Pieri, Gerd Röpke, Peter Schuck, and Michael Urban. The BCS–BEC crossover: From ultra-cold Fermi gases to nuclear systems. *Physics Reports*, 738:1–76, 2018.
- [77] M. Randeria, W. Zwerger, and M. Zwierlein. *The BCS–BEC Crossover and the Unitary Fermi Gas*, pages 1–32. Springer Berlin Heidelberg, Berlin, Heidelberg, 2012.
- [78] Herbert Fröhlich. Interaction of electrons with lattice vibrations. *Proceedings of the Royal Society of London. Series A. Mathematical and Physical Sciences*, 215(1122):291–298, 1952.
- [79] Herbert Fröhlich. Electrons in lattice fields. *Advances in Physics*, 3(11):325–361, 1954.
- [80] David Pines. Superconductivity in the periodic system. *Phys. Rev.*, 109(2):280, 1958.
- [81] NN Bogoljubov, Vladimir Veniaminovic Tolmachov, and DV Sirkov. A new method in the theory of superconductivity. *Fortschritte der Physik*, 6(11-12):605–682, 1958.
- [82] JG Valatin. Comments on the theory of superconductivity. *Il Nuovo Cimento (1955-1965)*, 7(6):843–857, 1958.
- [83] Markus Greiner, Olaf Mandel, Tilman Esslinger, Theodor W. Hänsch, and Immanuel Bloch. Quantum phase transition from a superfluid to a Mott insulator in a gas of ultracold atoms. *Nature*, 415(6867):39–44, 2002.
- [84] C. A. Regal, M. Greiner, and D. S. Jin. Observation of Resonance Condensation of Fermionic Atom Pairs. *Phys. Rev. Lett.*, 92:040403, Jan 2004.
- [85] C Chin, M Bartenstein, A Altmeyer, S Riedl, S Jochim, J Hecker Denschlag, and R Grimm. Observation of the pairing gap in a strongly interacting Fermi gas. *Science*, 305(5687):1128–1130, 2004.
- [86] M. W. Zwierlein, C. A. Stan, C. H. Schunck, S. M. F. Raupach, A. J. Kerman, and W. Ket-

- terle. Condensation of Pairs of Fermionic Atoms near a Feshbach Resonance. *Phys. Rev. Lett.*, 92:120403, Mar 2004.
- [87] J. Kinast, S. L. Hemmer, M. E. Gehm, A. Turlapov, and J. E. Thomas. Evidence for Superfluidity in a Resonantly Interacting Fermi Gas. *Phys. Rev. Lett.*, 92:150402, Apr 2004.
- [88] T. Bourdel, L. Khaykovich, J. Cubizolles, J. Zhang, F. Chevy, M. Teichmann, L. Tarruell, S. J. J. M. F. Kokkelmans, and C. Salomon. Experimental Study of the BEC-BCS Crossover Region in Lithium 6. *Phys. Rev. Lett.*, 93:050401, Jul 2004.
- [89] M. W. Zwierlein, J. R. Abo-Shaeer, A. Schirotzek, C. H. Schunck, and W. Ketterle. Vortices and superfluidity in a strongly interacting Fermi gas. *Nature*, 435(7045):1047–1051, 2005.
- [90] M. Aidelsburger, M. Atala, M. Lohse, J. T. Barreiro, B. Paredes, and I. Bloch. Realization of the Hofstadter Hamiltonian with Ultracold Atoms in Optical Lattices. *Phys. Rev. Lett.*, 111:185301, Oct 2013.
- [91] Charles Kittel and Paul McEuen. *Introduction to solid state physics*, volume 8. Wiley New York, 1976.
- [92] D. Jaksch and P. Zoller. The cold atom Hubbard toolbox. *Annals of Physics*, 315(1):52 – 79, 2005. Special Issue.
- [93] Richard P. Feynman. Simulating physics with computers. *International Journal of Theoretical Physics*, 21(6):467–488, 1982.
- [94] Seth Lloyd. Universal Quantum Simulators. *Science*, 273(5278):1073–1078, 1996.
- [95] Enric Jané, Guifre Vidal, Wolfgang Dür, Peter Zoller, and J. Ignacio Cirac. Simulation of quantum dynamics with quantum optical systems. *Quantum Inf. Comput.*, 3:15–37, 2003.
- [96] G. Modugno, F. Ferlaino, R. Heidemann, G. Roati, and M. Inguscio. Production of a Fermi gas of atoms in an optical lattice. *Phys. Rev. A*, 68:011601, Jul 2003.
- [97] Henning Moritz, Thilo Stöferle, Kenneth Günter, Michael Köhl, and Tilman Esslinger. Confinement Induced Molecules in a 1D Fermi Gas. *Phys. Rev. Lett.*, 94:210401, Jun 2005.
- [98] D. Jaksch, C. Bruder, J. I. Cirac, C. W. Gardiner, and P. Zoller. Cold Bosonic Atoms in Optical Lattices. *Phys. Rev. Lett.*, 81:3108–3111, Oct 1998.
- [99] W. Hofstetter, J. I. Cirac, P. Zoller, E. Demler, and M. D. Lukin. High-Temperature Superfluidity of Fermionic Atoms in Optical Lattices. *Phys. Rev. Lett.*, 89:220407, Nov 2002.
- [100] Rudolf Grimm, Matthias Weidemüller, and Yurii B Ovchinnikov. Optical dipole traps for neutral atoms. In *Advances in atomic, molecular, and optical physics*, volume 42, pages 95–170. Elsevier, 2000.
- [101] Claude Cohen-Tannoudji, Jacques Dupont-Roc, and Gilbert Grynberg. *Atom-photon interactions: basic processes and applications*. Wiley-VCH, 1998.
- [102] C. Cohen-Tannoudji, J. Dupont-Roc, and G. Grynberg. *The Dressed Atom Approach*, chapter 6, pages 407–514. John Wiley & Sons, Ltd, 2008.
- [103] Edwin T Jaynes and Frederick W Cummings. Comparison of quantum and semiclassical radiation theories with application to the beam maser. *Proceedings of the IEEE*, 51(1):89–109, 1963.
- [104] Gregory H. Wannier. The Structure of Electronic Excitation Levels in Insulating Crystals.

Bibliography

- Phys. Rev.*, 52:191–197, Aug 1937.
- [105] W. Kohn. Analytic Properties of Bloch Waves and Wannier Functions. *Phys. Rev.*, 115:809–821, Aug 1959.
- [106] JT Stewart, JP Gaebler, and DS Jin. Using photoemission spectroscopy to probe a strongly interacting Fermi gas. *Nature*, 454(7205):744–747, 2008.
- [107] JP Gaebler, JT Stewart, TE Drake, DS Jin, A Perali, P Pieri, and GC Strinati. Observation of pseudogap behaviour in a strongly interacting Fermi gas. *Nature Physics*, 6(8):569–573, 2010.
- [108] Gordon Baym, CJ Pethick, Zhenhua Yu, and Martin W Zwierlein. Coherence and clock shifts in ultracold Fermi gases with resonant interactions. *Phys. Rev. Lett.*, 99(19):190407, 2007.
- [109] M Punk and W Zwerger. Theory of rf-spectroscopy of strongly interacting fermions. *Phys. Rev. Lett.*, 99(17):170404, 2007.
- [110] A Perali, P Pieri, and GC Strinati. Competition between final-state and pairing-gap effects in the radio-frequency spectra of ultracold Fermi atoms. *Phys. Rev. Lett.*, 100(1):010402, 2008.
- [111] R. Haussmann, M. Punk, and W. Zwerger. Spectral functions and rf response of ultracold fermionic atoms. *Phys. Rev. A*, 80:063612, Dec 2009.
- [112] Qijin Chen, Yan He, Chih-Chun Chien, and K Levin. Theory of radio frequency spectroscopy experiments in ultracold Fermi gases and their relation to photoemission in the cuprates. *Reports on Progress in Physics*, 72(12):122501, oct 2009.
- [113] C. Berthod, M. Köhl, and T. Giamarchi. Second-order response theory of radio-frequency spectroscopy for cold atoms. *Phys. Rev. A*, 92:013626, Jul 2015.
- [114] Päivi Törmä. Physics of ultracold Fermi gases revealed by spectroscopies. *Physica Scripta*, 91(4):043006, mar 2016.
- [115] Christian H. Schunck, Yong-il Shin, André Schirotzek, and Wolfgang Ketterle. Determination of the fermion pair size in a resonantly interacting superfluid. *Nature*, 454(7205):739–743, 2008.
- [116] Jon H. Shirley. Solution of the Schrödinger Equation with a Hamiltonian Periodic in Time. *Phys. Rev.*, 138:B979–B987, May 1965.
- [117] Carl Runge. Über die numerische Auflösung von Differentialgleichungen. *Mathematische Annalen*, 46(2):167–178, 1895.
- [118] Wilhelm Kutta. Beitrag zur näherungsweise Integration totaler Differentialgleichungen. *Z. Math. Phys.*, 46:435–453, 1901.
- [119] Steven R. White and Adrian E. Feiguin. Real-Time Evolution Using the Density Matrix Renormalization Group. *Phys. Rev. Lett.*, 93:076401, Aug 2004.
- [120] M B Hastings. An area law for one-dimensional quantum systems. *Journal of Statistical Mechanics: Theory and Experiment*, 2007(08):P08024–P08024, aug 2007.
- [121] Michele Dolfi, Bela Bauer, Sebastian Keller, Alexandr Kosenkov, Timothée Ewart, Adrian Kantian, Thierry Giamarchi, and Matthias Troyer. Matrix product state applications for

- the ALPS project. *Computer Physics Communications*, 185(12):3430 – 3440, 2014.
- [122] Johannes Hauschild and Frank Pollmann. Efficient numerical simulations with Tensor Networks: Tensor Network Python (TeNPy). *SciPost Phys. Lect. Notes*, page 5, 2018.
- [123] *ITensor Library (version 2.1.1)* <http://itensor.org>.
- [124] Matthew Fishman, Steven R. White, and E. Miles Stoudenmire. The ITensor Software Library for Tensor Network Calculations. *arXiv:2007.14822*.
- [125] F. Verstraete, V. Murg, and J.I. Cirac. Matrix product states, projected entangled pair states, and variational renormalization group methods for quantum spin systems. *Advances in Physics*, 57(2):143–224, 2008.
- [126] J Ignacio Cirac and Frank Verstraete. Renormalization and tensor product states in spin chains and lattices. *Journal of Physics A: Mathematical and Theoretical*, 42(50):504004, dec 2009.
- [127] Román Orús. A practical introduction to tensor networks: Matrix product states and projected entangled pair states. *Annals of Physics*, 349:117 – 158, 2014.
- [128] Jens Eisert. *Entanglement and tensor network states*, volume 3 of *Modeling and Simulation*, page 520 p. Forschungszentrum Jülich Zentralbibliothek, Verlag, Jülich, Sep 2013.
- [129] Johannes Hauschild and Frank Pollmann. Efficient numerical simulations with Tensor Networks: Tensor Network Python (TeNPy). *SciPost Phys. Lect. Notes*, page 5, 2018.
- [130] J. Eisert, M. Cramer, and M. B. Plenio. Colloquium: Area laws for the entanglement entropy. *Rev. Mod. Phys.*, 82:277–306, Feb 2010.
- [131] M. Suzuki. Decomposition formulas of exponential operators and Lie exponentials with some applications to quantum mechanics and statistical physics. *J. Math. Phys.*, 26(4):601, 1985.
- [132] M. Suzuki. General theory of fractal path integrals with applications to many-body theories and statistical physics. *J. Math. Phys.*, 32(2):400, 1991.
- [133] H. F. Trotter. On the product of semi-groups of operators. *Proc. Amer. Math. Soc.*, 10:545–551, 1959.
- [134] M. Suzuki. Relationship between d-Dimensional Quantum Spin Systems and (d+1)-Dimensional Ising Systems – Equivalence, Critical Exponents and Systematic Approximants of the Partition Function and Spin Correlations. *Prog. Theor. Phys.*, 56:1454, 1976.
- [135] Elliott H. Lieb and Derek W. Robinson. The finite group velocity of quantum spin systems. *Communications in Mathematical Physics*, 28(3):251–257, 1972.
- [136] Tobias J. Osborne. Efficient Approximation of the Dynamics of One-Dimensional Quantum Spin Systems. *Phys. Rev. Lett.*, 97:157202, Oct 2006.
- [137] Ulrich Schollwöck. *DMRG: Ground States, Time Evolution, and Spectral Functions*, volume 3 of *Modeling and Simulation*, page 520 p. Forschungszentrum Jülich Zentralbibliothek, Verlag, Jülich, Sep 2013.
- [138] Pasquale Calabrese and John Cardy. Entanglement entropy and quantum field theory. *Journal of Statistical Mechanics: Theory and Experiment*, 2004(06):P06002, jun 2004.
- [139] C. Kollath, U. Schollwöck, and W. Zwerger. Spin-Charge Separation in Cold Fermi Gases:

Bibliography

- A Real Time Analysis. *Phys. Rev. Lett.*, 95:176401, Oct 2005.
- [140] M. Cramer, A. Flesch, I. P. McCulloch, U. Schollwöck, and J. Eisert. Exploring Local Quantum Many-Body Relaxation by Atoms in Optical Superlattices. *Phys. Rev. Lett.*, 101:063001, Aug 2008.
- [141] T. Giamarchi, A. Iucci, and C. Berthod. Introduction to Many Body physics, 2013.
- [142] Elliott H. Lieb and F. Y. Wu. Absence of Mott Transition in an Exact Solution of the Short-Range, One-Band Model in One Dimension. *Phys. Rev. Lett.*, 20:1445–1448, Jun 1968.
- [143] Fabian HL Essler, Holger Frahm, Frank Göhmann, Andreas Klümper, and Vladimir E Korepin. *The one-dimensional Hubbard model*. Cambridge University Press, 2005.
- [144] Minoru Takahashi. One-Dimensional Hubbard Model at Finite Temperature. *Progress of Theoretical Physics*, 47(1):69–82, 01 1972.
- [145] N. M. Bogolyubov and V. E. Korepin. Correlation functions of the one-dimensional Hubbard model. *Theoretical and Mathematical Physics*, 82(3):231–243, 1990.
- [146] J. Goldstone. Field theories with «Superconductor »solutions. *Il Nuovo Cimento (1955-1965)*, 19(1):154–164, 1961.
- [147] Jeffrey Goldstone, Abdus Salam, and Steven Weinberg. Broken Symmetries. *Phys. Rev.*, 127:965–970, Aug 1962.
- [148] PB Littlewood and CM Varma. Gauge-invariant theory of the dynamical interaction of charge density waves and superconductivity. *Phys. Rev. Lett.*, 47(11):811, 1981.
- [149] R Sooryakumar and MV Klein. Raman scattering by superconducting-gap excitations and their coupling to charge-density waves. *Phys. Rev. Lett.*, 45(8):660, 1980.
- [150] Ryusuke Matsunaga, Yuki I Hamada, Kazumasa Makise, Yoshinori Uzawa, Hiroataka Terai, Zhen Wang, and Ryo Shimano. Higgs amplitude mode in the BCS superconductors $\text{Nb}_{1-x}\text{Ti}_x\text{N}$ induced by terahertz pulse excitation. *Phys. Rev. Lett.*, 111(5):057002, 2013.
- [151] Daniel Sherman, Uwe S. Pracht, Boris Gorshunov, Shachaf Poran, John Jesudasan, Madhavi Chand, Pratap Raychaudhuri, Mason Swanson, Nandini Trivedi, Assa Auerbach, Marc Scheffler, Aviad Frydman, and Martin Dressel. The Higgs mode in disordered superconductors close to a quantum phase transition. *Nature Physics*, 11(2):188–192, 2015.
- [152] Ch Rüegg, Bruce Normand, Masashige Matsumoto, Albert Furrer, Desmond F McMorrow, Karl W Krämer, H-U Güdel, Severina N Gvasaliya, Hannu Mutka, and Martin Boehm. Quantum magnets under pressure: controlling elementary excitations in TlCuCl_3 . *Phys. Rev. Lett.*, 100(20):205701, 2008.
- [153] WP Halperin and E Varoquaux. Helium Three (eds W. Halperin and L. Pitaevskii), 1990.
- [154] Ulf Bissbort, Sören Götze, Yongqiang Li, Jannes Heinze, Jasper S. Krauser, Malte Weinberg, Christoph Becker, Klaus Sengstock, and Walter Hofstetter. Detecting the Amplitude Mode of Strongly Interacting Lattice Bosons by Bragg Scattering. *Phys. Rev. Lett.*, 106:205303, May 2011.
- [155] Manuel Endres, Takeshi Fukuhara, David Pekker, Marc Cheneau, Peter Schauß, Christian Gross, Eugene Demler, Stefan Kuhr, and Immanuel Bloch. The ‘Higgs’ amplitude mode

- at the two-dimensional superfluid/Mott insulator transition. *Nature*, 487(7408):454–458, 2012.
- [156] Thai M Hoang, Hebbe M Bharath, Matthew J Boguslawski, Martin Anquez, Bryce A Robins, and Michael S Chapman. Adiabatic quenches and characterization of amplitude excitations in a continuous quantum phase transition. *Proceedings of the National Academy of Sciences*, 113(34):9475–9479, 2016.
- [157] Julian Léonard, Andrea Morales, Philip Zupancic, Tobias Donner, and Tilman Esslinger. Monitoring and manipulating Higgs and Goldstone modes in a supersolid quantum gas. *Science*, 358(6369):1415–1418, 2017.
- [158] Lev Davidovich Landau and V L Ginzburg. On the theory of superconductivity. *Zh. Eksp. Teor. Fiz.*, 20:1064, 1950.
- [159] L P Gor’kov. Microscopic derivation of the Ginzburg–Landau equations in the theory of superconductivity. *Sov. Phys. JETP*, 36(9):1364–1367, 1959.
- [160] David Pekker and CM Varma. Amplitude/Higgs modes in condensed matter physics. *Annual Review of Condensed Matter Physics*, 6(1):269–297, 2015.
- [161] Ryo Shimano and Naoto Tsuji. Higgs mode in superconductors. *Annual Review of Condensed Matter Physics*, 11:103–124, 2020.
- [162] Peter W Higgs. Broken symmetries and the masses of gauge bosons. *Phys. Rev. Lett.*, 13(16):508, 1964.
- [163] RG Scott, F Dalfovo, LP Pitaevskii, and S Stringari. Rapid ramps across the BEC-BCS crossover: A route to measuring the superfluid gap. *Phys. Rev. A*, 86(5):053604, 2012.
- [164] Emil A. Yuzbashyan and Maxim Dzero. Dynamical Vanishing of the Order Parameter in a Fermionic Condensate. *Phys. Rev. Lett.*, 96:230404, Jun 2006.
- [165] S. Hannibal, P. Kettmann, M. D. Croitoru, A. Vagov, V. M. Axt, and T. Kuhn. Quench dynamics of an ultracold Fermi gas in the BCS regime: Spectral properties and confinement-induced breakdown of the Higgs mode. *Phys. Rev. A*, 91:043630, Apr 2015.
- [166] M. Greiner, C. A. Regal, and D. S. Jin. Probing the Excitation Spectrum of a Fermi Gas in the BCS-BEC Crossover Regime. *Phys. Rev. Lett.*, 94:070403, Feb 2005.
- [167] Michael Feld, Bernd Fröhlich, Enrico Vogt, Marco Koschorreck, and Michael Köhl. Observation of a pairing pseudogap in a two-dimensional Fermi gas. *Nature*, 480(7375):75–78, 2011.
- [168] Eugene P Gross. Structure of a quantized vortex in boson systems. *Il Nuovo Cimento (1955-1965)*, 20(3):454–477, 1961.
- [169] Lev P Pitaevskii. Vortex lines in an imperfect Bose gas. *Sov. Phys. JETP*, 13(2):451–454, 1961.
- [170] A. Behrle. *Driving a Strongly Interacting Superfluid out of Equilibrium*. PhD thesis, Rheinische Friedrich-Wilhelms-Universität Bonn, 2017.
- [171] T. Harrison. *Measuring the Gap and Investigating Non-equilibrium in the BEC-BCS Crossover*. PhD thesis, Rheinische Friedrich-Wilhelms-Universität Bonn, 2017.
- [172] M. Link. *Exploring Non-Equilibrium in ultracold Fermi Gases and Machine Learning in*

Bibliography

- Physics*. PhD thesis, Rheinische Friedrich-Wilhelms-Universität Bonn, 2020. to be published soon.
- [173] Cheng Chin, Rudolf Grimm, Paul Julienne, and Eite Tiesinga. Feshbach resonances in ultracold gases. *Rev. Mod. Phys.*, 82:1225–1286, Apr 2010.
- [174] G. M. Bruun. Low-Energy Monopole Modes of a Trapped Atomic Fermi Gas. *Phys. Rev. Lett.*, 89:263002, Dec 2002.
- [175] A. Korolyuk, J. J. Kinnunen, and P. Törmä. Density response of a trapped Fermi gas: A crossover from the pair vibration mode to the Goldstone mode. *Phys. Rev. A*, 84:033623, Sep 2011.
- [176] A. Korolyuk, J. J. Kinnunen, and P. Törmä. Collective excitations of a trapped Fermi gas at finite temperature. *Phys. Rev. A*, 89:013602, Jan 2014.
- [177] Jun Tokimoto, Shunji Tsuchiya, and Tetsuro Nikuni. Higgs mode in a trapped superfluid Fermi gas. *Journal of Low Temperature Physics*, 187(5):765–770, 2017.
- [178] D. N. Basov, Richard D. Averitt, Dirk van der Marel, Martin Dressel, and Kristjan Haule. Electrodynamics of correlated electron materials. *Rev. Mod. Phys.*, 83:471–541, Jun 2011.
- [179] J. Orenstein. *Physics Today*, 65:44, 2012.
- [180] J. Zhang and R.D. Averitt. Dynamics and Control in Complex Transition Metal Oxides. *Annual Review of Materials Research*, 44(1):19–43, 2014.
- [181] Claudio Giannetti, Massimo Capone, Daniele Fausti, Michele Fabrizio, Fulvio Parmigiani, and Dragan Mihailovic. Ultrafast optical spectroscopy of strongly correlated materials and high-temperature superconductors: a non-equilibrium approach. *Advances in Physics*, 65(2):58–238, 2016.
- [182] Anatoli Polkovnikov, Krishnendu Sengupta, Alessandro Silva, and Mukund Vengalattore. Colloquium: Nonequilibrium dynamics of closed interacting quantum systems. *Rev. Mod. Phys.*, 83:863–883, Aug 2011.
- [183] AF Volkov and Sh M Kogan. Collisionless relaxation of the energy gap in superconductors. *Sov. Phys. JETP*, 38:1018, 1974.
- [184] R. A. Barankov, L. S. Levitov, and B. Z. Spivak. Collective Rabi Oscillations and Solitons in a Time-Dependent BCS Pairing Problem. *Phys. Rev. Lett.*, 93:160401, Oct 2004.
- [185] G. L. Warner and A. J. Leggett. Quench dynamics of a superfluid Fermi gas. *Phys. Rev. B*, 71:134514, Apr 2005.
- [186] M. H. Szymańska, B. D. Simons, and K. Burnett. Dynamics of the BCS-BEC Crossover in a Degenerate Fermi Gas. *Phys. Rev. Lett.*, 94:170402, May 2005.
- [187] E.A. Yuzbashyan, O. Tsypliyatyev, and B.L. Altshuler. Relaxation and Persistent Oscillations of the Order Parameter in Fermionic Condensates. *Phys. Rev. Lett.*, 96:097005, 2006.
- [188] R. A. Barankov and L. S. Levitov. Synchronization in the BCS Pairing Dynamics as a Critical Phenomenon. *Phys. Rev. Lett.*, 96:230403, Jun 2006.
- [189] T. Papenkort, V. M. Axt, and T. Kuhn. Coherent dynamics and pump-probe spectra of BCS superconductors. *Phys. Rev. B*, 76:224522, Dec 2007.

- [190] M. Dzero, E. A. Yuzbashyan, B. L. Altshuler, and P. Coleman. Spectroscopic Signatures of Nonequilibrium Pairing in Atomic Fermi Gases. *Phys. Rev. Lett.*, 99:160402, Oct 2007.
- [191] V. Gurarie. Nonequilibrium Dynamics of Weakly and Strongly Paired Superconductors. *Phys. Rev. Lett.*, 103:075301, Aug 2009.
- [192] Dzero, M., Yuzbashyan, E. A., and Altshuler, B. L. Cooper pair turbulence in atomic Fermi gases. *Europhys. Lett.*, 85(2):20004, 2009.
- [193] Victor Galitski. Nonperturbative quantum dynamics of the order parameter in the BCS pairing model. *Phys. Rev. B*, 82:054511, Aug 2010.
- [194] E. A. Yuzbashyan, M. Dzero, V. Gurarie, and M. S. Foster. Quantum quench phase diagrams of an s -wave BCS-BEC condensate. *Phys. Rev. A*, 91:033628, Mar 2015.
- [195] M. A. Sentef, A. F. Kemper, A. Georges, and C. Kollath. Theory of light-enhanced phonon-mediated superconductivity. *Phys. Rev. B*, 93:144506, Apr 2016.
- [196] V. J. Emery and S. A. Kivelson. Importance of phase fluctuations in superconductors with small superfluid density. *Nature*, 374:434, 1995.
- [197] C. A. Regal and D. S. Jin. Measurement of Positive and Negative Scattering Lengths in a Fermi Gas of Atoms. *Phys. Rev. Lett.*, 90:230404, Jun 2003.
- [198] S. Gupta, Z. Hadzibabic, M. W. Zwierlein, C. A. Stan, K. Dieckmann, C. H. Schunck, E. G. M. van Kempen, B. J. Verhaar, and W. Ketterle. Radio-Frequency Spectroscopy of Ultracold Fermions. *Science*, 300:1723, 2003.
- [199] P. Törmä and P. Zoller. Laser Probing of Atomic Cooper Pairs. *Phys. Rev. Lett.*, 85:487–490, Jul 2000.
- [200] Cindy A. Regal, Christopher Ticknor, John L. Bohn, and Deborah S. Jin. Creation of ultracold molecules from a Fermi gas of atoms. *Nature*, 424(6944):47–50, 2003.
- [201] J. Kinnunen, M. Rodríguez, and P. Törmä. Signatures of Superfluidity for Feshbach-Resonant Fermi Gases. *Phys. Rev. Lett.*, 92:230403, Jun 2004.
- [202] M. Bartenstein, A. Altmeyer, S. Riedl, R. Geursen, S. Jochim, C. Chin, J. Hecker Denschlag, R. Grimm, A. Simoni, E. Tiesinga, C. J. Williams, and P. S. Julienne. Precise Determination of ${}^6\text{Li}$ Cold Collision Parameters by Radio-Frequency Spectroscopy on Weakly Bound Molecules. *Phys. Rev. Lett.*, 94:103201, Mar 2005.
- [203] J. Kinnunen, M. Rodríguez, and P. Törmä. Pairing Gap and In-Gap Excitations in Trapped Fermionic Superfluids. *Science*, 305(5687):1131–1133, 2004.
- [204] Y. Shin, C. H. Schunck, A. Schirotzek, and W. Ketterle. Tomographic rf Spectroscopy of a Trapped Fermi Gas at Unitarity. *Phys. Rev. Lett.*, 99:090403, Aug 2007.
- [205] Yan He, Qijin Chen, and K. Levin. Radio-frequency spectroscopy and the pairing gap in trapped Fermi gases. *Phys. Rev. A*, 72:011602, Jul 2005.
- [206] Philipp Werner, Hugo U. R. Strand, Shintaro Hoshino, Yuta Murakami, and Martin Eckstein. Enhanced pairing susceptibility in a photodoped two-orbital Hubbard model. *Phys. Rev. B*, 97:165119, Apr 2018.
- [207] Julián Rincón, Elbio Dagotto, and Adrian E. Feiguin. Photoinduced Hund excitons in the breakdown of a two-orbital Mott insulator. *Phys. Rev. B*, 97:235104, Jun 2018.

Bibliography

- [208] Claude Cohen-Tannoudji, Bernard Diu, Frank Laloe, and Bernard Dui. *Quantum Mechanics (2 vol. set)*. Wiley-Interscience, 2006.
- [209] Francesco Massel, Mikko J. Leskinen, and Päivi Törmä. Hopping Modulation in a One-Dimensional Fermi-Hubbard Hamiltonian. *Phys. Rev. Lett.*, 103:066404, Aug 2009.
- [210] A. Altmeyer, S. Riedl, C. Kohstall, M. J. Wright, R. Geursen, M. Bartenstein, C. Chin, J. Hecker Denschlag, and R. Grimm. Precision Measurements of Collective Oscillations in the BEC-BCS Crossover. *Phys. Rev. Lett.*, 98:040401, Jan 2007.
- [211] Meng Khoon Tey, Leonid A. Sidorenkov, Edmundo R. Sánchez Guajardo, Rudolf Grimm, Mark J. H. Ku, Martin W. Zwierlein, Yan-Hua Hou, Lev Pitaevskii, and Sandro Stringari. Collective Modes in a Unitary Fermi Gas across the Superfluid Phase Transition. *Phys. Rev. Lett.*, 110:055303, Jan 2013.
- [212] M. W. Zwierlein, C. H. Schunck, C. A. Stan, S. M. F. Raupach, and W. Ketterle. Formation Dynamics of a Fermion Pair Condensate. *Phys. Rev. Lett.*, 94:180401, May 2005.
- [213] Z. Yu and G. Baym. Spin-correlation functions in ultracold paired atomic-fermion systems: Sum rules, self-consistent approximations, and mean fields. *Phys. Rev. A*, 73:063601, Jun 2006.
- [214] Sourish Basu and Erich J. Mueller. Final-State Effects in the Radio Frequency Spectrum of Strongly Interacting Fermions. *Phys. Rev. Lett.*, 101:060405, Aug 2008.
- [215] Pierbiagio Pieri, Andrea Perali, and Giancarlo Calvanese Strinati. Enhanced paraconductivity-like fluctuations in the radiofrequency spectra of ultracold Fermi atoms. *Nature Physics*, 5(10):736–740, 2009.
- [216] P. Pieri, A. Perali, G. C. Strinati, S. Riedl, M. J. Wright, A. Altmeyer, C. Kohstall, E. R. Sánchez Guajardo, J. Hecker Denschlag, and R. Grimm. Pairing-gap, pseudogap, and no-gap phases in the radio-frequency spectra of a trapped unitary ${}^6\text{Li}$ gas. *Phys. Rev. A*, 84:011608, Jul 2011.
- [217] Wladimir Tschischik, Roderich Moessner, and Masudul Haque. Breathing mode in the Bose-Hubbard chain with a harmonic trapping potential. *Phys. Rev. A*, 88:063636, Dec 2013.
- [218] C. H. Schunck, Y. Shin, A. Schirotzek, M. W. Zwierlein, and W. Ketterle. Pairing Without Superfluidity: The Ground State of an Imbalanced Fermi Mixture. *Science*, 316(5826):867–870, 2007.
- [219] G. J. Milburn and C. A. Holmes. Dissipative Quantum and Classical Liouville Mechanics of the Anharmonic Oscillator. *Phys. Rev. Lett.*, 56:2237–2240, May 1986.
- [220] Enrico Vogt, Michael Feld, Bernd Fröhlich, Daniel Pertot, Marco Koschorreck, and Michael Köhl. Scale Invariance and Viscosity of a Two-Dimensional Fermi Gas. *Phys. Rev. Lett.*, 108:070404, Feb 2012.
- [221] Stefan K. Baur, Enrico Vogt, Michael Köhl, and Georg M. Bruun. Collective modes of a two-dimensional spin-1/2 Fermi gas in a harmonic trap. *Phys. Rev. A*, 87:043612, Apr 2013.
- [222] M. Holten, L. Bayha, A. C. Klein, P. A. Murthy, P. M. Preiss, and S. Jochim. Anomalous Breaking of Scale Invariance in a Two-Dimensional Fermi Gas. *Phys. Rev. Lett.*,

- 121:120401, Sep 2018.
- [223] T. Peppler, P. Dyke, M. Zamorano, I. Herrera, S. Hoinka, and C. J. Vale. Quantum Anomaly and 2D-3D Crossover in Strongly Interacting Fermi Gases. *Phys. Rev. Lett.*, 121:120402, Sep 2018.
 - [224] Peter Fulde and Richard A. Ferrell. Superconductivity in a Strong Spin-Exchange Field. *Phys. Rev.*, 135:A550–A563, Aug 1964.
 - [225] AI Larkin and Yu N Ovchinnikov. Inhomogeneous state of superconductors. *Sov. Phys. JETP*, 20:762–769, 1965.
 - [226] A. E. Feiguin and F. Heidrich-Meisner. Pairing states of a polarized Fermi gas trapped in a one-dimensional optical lattice. *Phys. Rev. B*, 76:220508, Dec 2007.
 - [227] L. Riegger, G. Orso, and F. Heidrich-Meisner. Interaction quantum quenches in the one-dimensional Fermi-Hubbard model with spin imbalance. *Phys. Rev. A*, 91:043623, Apr 2015.
 - [228] Jacob F. Sherson, Christof Weitenberg, Manuel Endres, Marc Cheneau, Immanuel Bloch, and Stefan Kuhr. Single-atom-resolved fluorescence imaging of an atomic Mott insulator. *Nature*, 467(7311):68–72, 2010.
 - [229] Chen-Lung Hung and Cheng Chin. *In Situ Imaging of Atomic Quantum Gases*, chapter Chapter 6, pages 101–120.
 - [230] G. J. A. Edge, R. Anderson, D. Jervis, D. C. McKay, R. Day, S. Trotzky, and J. H. Thywissen. Imaging and addressing of individual fermionic atoms in an optical lattice. *Phys. Rev. A*, 92:063406, Dec 2015.
 - [231] Ahmed Omran, Martin Boll, Timon A. Hilker, Katharina Kleinlein, Guillaume Salomon, Immanuel Bloch, and Christian Gross. Microscopic Observation of Pauli Blocking in Degenerate Fermionic Lattice Gases. *Phys. Rev. Lett.*, 115:263001, Dec 2015.
 - [232] Lawrence W. Cheuk, Matthew A. Nichols, Melih Okan, Thomas Gersdorf, Vinay V. Ramasesh, Waseem S. Bakr, Thomas Lompe, and Martin W. Zwierlein. Quantum-Gas Microscope for Fermionic Atoms. *Phys. Rev. Lett.*, 114:193001, May 2015.
 - [233] Maxwell F. Parsons, Florian Huber, Anton Mazurenko, Christie S. Chiu, Widagdo Setiawan, Katherine Wooley-Brown, Sebastian Blatt, and Markus Greiner. Site-Resolved Imaging of Fermionic ${}^6\text{Li}$ in an Optical Lattice. *Phys. Rev. Lett.*, 114:213002, May 2015.
 - [234] Elmar Haller, James Hudson, Andrew Kelly, Dylan A. Cotta, Bruno Peaudecerf, Graham D. Bruce, and Stefan Kuhr. Single-atom imaging of fermions in a quantum-gas microscope. *Nature Physics*, 11(9):738–742, 2015.
 - [235] Felix Bloch. Nuclear induction. *Phys. Rev.*, 70(7-8):460, 1946.